Dynamical Aspects of Confined Media, Bulk Binary Mixtures and Other Complex Systems

Thesis Submitted for the Degree of

Doctor of Philosophy (Science)

of

Jadavpur University

By

Atanu Baksi

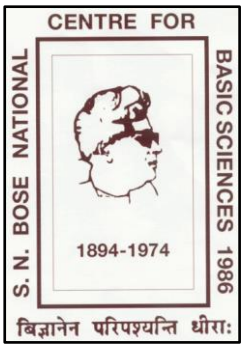

Department of Chemical, Biological and Macromolecular Sciences,

S. N. Bose National Centre for Basic Sciences,

Block-JD, Sector-III, Salt Lake

Kolkata-700106, India

January 2021

CENTRE FOR BASIC SCIENCES 1986
S.N. BOSE NATIONAL
1894-1974
विज्ञानेन परिपश्यन्ति धीराः

सत्येन्द्र नाथ बसु राष्ट्रीय मौलिक विज्ञान केन्द्र
SATYENDRA NATH BOSE NATIONAL
CENTRE FOR BASIC SCIENCES
সত্যেন্দ্র নাথ বসু জাতীয় মৌল বিজ্ঞান কেন্দ্র

CERTIFICATE FROM THE SUPERVISOR

This is to certify that the thesis entitled "**Dynamical Aspects of Confined Media, Bulk Binary Mixtures and Other Complex Systems**" submitted by **Mr. Atanu Baksi** (Index No. 250|15|Phys.|24), who got her name registered on 05/11/2015 for the award of Ph.D. (Science) degree of Jadavpur University, is absolutely based upon her own work under the supervision of **Prof. Ranjit Biswas** and that neither this thesis nor any part of it has been submitted for either any degree/diploma or any other academic award anywhere before.

Ranjit Biswas 21.01.21

Dr. Ranjit Biswas

Senior Professor,

Department of Chemical, Biological and Macromolecular Sciences

S. N. Bose National Centre for Basic Sciences

Block-JD, Sector-III, Salt Lake,

Kolkata-700106, West Bengal, India

DR. RANJIT BISWAS
Senior Professor
Dept. of Chemical, Biological & Macromolecular Sciences
S. N. Bose National Centre for Basic Sciences
Block - JD, Sector-III, Salt Lake, Kolkata - 700 106, India

Dedicated To

my

Grandfather

Late Bishnupada Manna

And

My Family

Acknowledgement

I wish to express my deepest gratitude to my PhD supervisor Prof. Ranjit Biswas for giving me the freedom to work independently. I would also like to thank him for guiding me whenever required, whether it be in research or in life. I have learnt a lot from him, most importantly I have learnt how to survive and enjoy the competitive research. His excellent guidance and continuous encouragement motivated me to perform my best. His patience and support helped me to overcome many crisis situations (including this challenging COVID-19 pandemic) and finish this Thesis. His kind and affectionate attitude is worth cherishing for my life.

I would like to convey my sincere gratitude to Prof. Pradip Kumar Ghorai, Department of Chemical Sciences, IISER Kolkata for all his help in learning simulations and technicalities. He was always a saviour for me in my early PhD days.

My sincere thanks to all the members of my Thesis committee Prof. Asoke Prasun Chattopadhyay (Kalyani University), Prof. Manoranjan Kumar (SNBNCBS), Prof. Manik Pradhan (SNBNCBS) for devoting their valuable time for me.

I would like to acknowledge the immense help of all the associates of the Computer Services Cell for their prompt and efficient actions in any computer and computational clusters related issues. I would like to thank all faculty members of SNBNCBS, research scholars and non-teaching staffs for their kind help and co-operation.

I am grateful to CSIR (India) and S. N. Bose National Centre for Basic Sciences for providing the research fellowship and all academic help.

I heartily thank my present lab mates: Juriti, Kajal, Dhrubajyoti, Narayan, Jayanta, Amrita for their constant encouragement and cooperation. I am also grateful to them for providing a friendly atmosphere inside our lab. I am also thankful to the past members of my lab: Dr. Tuhin Pradhan, Dr. Hemant Kashyap, Dr. Harun Al. Rasid Gazi, Dr. Biswajit Guchhait, Dr. Snehasis Daschakraborty, Dr. Tamisra Pal, Dr. Sandipa Indra, Dr. Suman Das, Dr. Kallol Mukherjee, Dr. Anuradha Das, Dr. Ejaj Tarif, Dr. Shirshendu Dinda for their support in various academic and non-academic purposes. I am especially thankful to Juriti Rajbangshi for helping me in learning new simulation software.

I convey my regards to Dr. Parijat Das (Biswas) for her caring attitude and great hospitality at home, and affection to little Rwitoban and Arshaman.

I am very much thankful to my personal group of friends Juriti, Samrat, Dhimadri, Anuvab, Bihalan, Pallabi, Prantik, Sayoni, Debabrata, Mithun for giving me positive energy in all ups and downs throughout my PhD life.

I am highly indebted to my teacher Mr. Chinmoy Patra for all his efforts. I want to offer my great respect to Prof. Aritra Banerjee, (Calcutta University) for being a constant support throughout my PhD times.

I want to thank and express my deep feelings to my father Mr. Anukul Kumar Baksi and mother Mrs. Anuradha Baksi for all their love and support. I also want to express my love to my all of my family members specially my nephew little Koustav. I want to show my gratitude towards my ‘mesomosai’ Doctor Manas Mandal who always stood by me like a father figure. I could not thank him enough.

Finally, I would like to thank all those people, who have directly or indirectly helped me at various stages of my research work.

Abstract

In this Thesis, dynamical aspects of different complex bulk and confined systems have been studied via molecular dynamics (MD) simulations. Systems studied range from single component hydrogen bonded (H-bonded) ambient liquids and multi-component liquid mixtures to neat liquids and liquid mixtures under charged and neutral confinements, and metastable systems such as deep eutectic solvents (DESs). To be specific, these complex systems are neat water and neat alcohols, and aqueous binary mixtures of alcohols – all in bulk and under confinement in spherical reverse micelles. Results from initial studies on biodegradable water containing DES have also been included. Numerical and simulation studies in this Thesis focus on orientational and translational structure in the condensed phase, and the resultant anomaly in presence of confinement and specific interactions, various motional features and relaxation processes. The microscopic heterogeneity aspects in both solution structure and dynamics have been thoroughly examined, and attempts have been made to compare results with the available experimental data. Fidelity of simulations performed here have been rigorously examined via comparing to available experimental data such as density, and reproducing known simulation data. We have investigated in this Thesis another important phenomenon: whether nano-sized confinements alter the preferential solvation around a neutral dipolar solvent dissolved in aqueous binary mixtures of small amphiphilic molecules.

The first part of the Thesis is connected to the investigation of how confinement affects different aspects such as translation mobility, heterogeneity, H-bond lifetime and rotational dynamics of water. These simulation studies carefully examine the well-known and celebrated core-shell model of confined water, where core water resembles bulk water and the interfacial water molecules are believed to be completely dynamically different from those that are more near to the centre (core). We find that this two-state model representation of confined water is inadequate even for large reverse micelles, and core water is far from bulk-like.

Another simulation study on water-methanol binary mixtures reveals that both preferential solvation and hydrogen bond relaxation times in bulk are affected in a confinement. More specifically, this study reveals confinement accentuates the preferential solvation phenomenon and facilitates di-mixing of mixture components. In addition, the present study reveals that the

tetrahedral H-bond network of neat liquid water becomes severely affected upon addition of methanol, which becomes further distorted under confinement. Confinement severely affects the inter-species hydrogen bonds and makes the corresponding continuous H-bonds much shorter-lived. Interestingly, structural hydrogen bond relaxation timescales become longer in confined binary mixtures than those in bulk binary mixtures.

Next, we have studied aqueous tertiary butanol solutions as a model system to explore the molecular origin of the dynamic anomaly found in aqueous amphiphilic solutions. While the anomalous composition dependence of different thermodynamic properties of these aqueous solutions in the water-rich region has been attributed to the perturbation of the tetrahedral network structure of water (structural anomaly), an abrupt change in the amphiphile concentration dependence of reactive and non-reactive relaxation rates measured employing foreign solutes in such media signals perturbation on solution dynamics. Several time-resolved measurements have indicated that this anomalous perturbation on dynamics or 'dynamical anomaly' appears at an amphiphile concentrations approximately twice larger than that at which structural anomaly occurs. In this work, we have investigated the microscopic origins of both the structural and the dynamical anomaly via performing molecular dynamics simulations of aqueous solutions of TBA at several compositions in the water-rich region. Our simulations reveal abrupt changes in H-bond dynamics and tetrahedral order parameter at amphiphile concentrations similar to those reported in experiments that measure thermodynamic properties and relaxation rates. This work, therefore, provides microscopic insights that cogently explain the corresponding experimental observations.

An analytical study employing experimental dielectric relaxation (DR) data has been performed in order to investigate the origin behind the near-independence of rates of electron transfer reaction (ETR) on medium viscosity. ETR is known to couple to high frequency solvent response (in the tera Hertz regime). This study reveals that the rotational solvent friction, $\Gamma_R(\kappa, z)$, at high frequency is the determining factor for ETR, which becomes nearly equal for solvents of widely varying viscosity.

List of Publications

1. “Dynamic Susceptibility and Structural Heterogeneity of Large Reverse Micellar Water: An Examination of the Core−Shell Model via Probing the Layer-wise Features”
   Atanu Baksi, Pradip Kr. Ghorai, * and Ranjit Biswas*
   J. Phys. Chem. B ***124***, 14, 2848−2863, 2020.

2. “Does Confinement Modify Preferential Solvation and H-bond Fluctuation Dynamics? A Molecular Level Investigation Through Simulations of Bulk and Confined Three-Component Mixture”
   Atanu Baksi, Ranjit Biswas*
   J. Phys. Chem. B ***124***, 51, 11718–11729, 2020.

3. “Dynamical Anomaly of Aqueous Amphiphilic Solutions: Connection to Solution H-bond Fluctuation Dynamics?”
   Atanu Baksi, Ranjit Biswas*
   J. Phys. Chem. B 2021 (Under review)

4. “Why Some Reactions Occurring in Widely Different Viscous Media Possess the Similar Reaction Rate? An Analytical Investigation Employing Experimental Dielectric Relaxation Data”
   Atanu Baksi, Ranjit Biswas*
   J. Chem. Sc. (to be submitted)

5. “Glucose-Water-Urea Deep Eutectics: How Water Structure and Dynamics Alters in a Crowded Environment”
   Atanu Baksi, Juriti Rajbangshi, Ranjit Biswas*
   Phys. Chem. Chem. Phys. (to be submitted)

6. **“Microscopic Structure and Dynamics of Betaine-Water-Urea Naturally Abundant Deep Eutectics: A Molecular Dynamics Study”
   Juriti Rajbangshi, ***Atanu Baksi***, Ranjit Biswas*
   (Manuscript in preparation)

7. **“Effect of Confinement on Structural and Temporal Heterogeneity of Aqueous Methanol Solutions: A Molecular Dynamics Simulation Study”
   Atanu Baksi, Ranjit Biswas*
   (Manuscript in preparation)

**not included in this Thesis

Contents

Chapter 1: Introduction…….....1

Chapter 2: Dynamic Susceptibility and Structural Heterogeneity of Large Reverse Micellar Water: An Examination of the Core−Shell Model via Probing the Layer-wise Features.....12

2.1 Introduction……...12

2.2 Simulation Details…….16

2.2.1 Construction of aqueous reverse micelles…….…….....16

2.2.2 Technical aspects for simulations of aqueous reverse micelles…….....18

2.2.3 Fidelity Check……..…….…….....19

2.2.4 Sorting out particles for exploring layer-wise and over-all motional features….....20

2.2.5 Bulk water simulation…….……20

2.3 Results and Discussion…….…..21

2.3.1 Structural parameters…….…….21

2.3.1.1 The orientation of water dipoles…….…….21

2.3.1.2 Tetrahedral order parameter (Q_i) and the distribution of the number of hydrogen bonds per water molecule ($P(N_{HB})$) ….....……...24

2.3.2 Dynamics……...….....31

2.3.2.1 Mean-Squared Displacements (MSDs) and Translational Mobilities: ‘Over-all’ and Layer-wise……31

2.3.2.2 Velocity autocorrelation function: Origin of difference in mobilities…….…..….....34

2.3.2.3 Dynamic Heterogeneity (DH): Non-Gaussian features and slow timescales…….....37

2.3.2.4 Single-particle displacement distributions: Bimodality, translational jumps and common displacements across layers……...40

2.3.2.5 Dynamic susceptibility of confined water in different layers: Long temporal correlations, and overlap across layers……43

2.3.2.6 Collective single particle -reorientation relaxations: Agreement with experiments…….….45

2.4 Conclusion…….….50

Appendix 2.A……...52

Appendix 2.B……...68

References…….…...74

Chapter 3: Does Confinement Modify Preferential Solvation and H-bond Fluctuation Dynamics? A Molecular Level Investigation Through Simulations of Bulk and Confined Three-Component Mixture……..79

3.1 Introduction……79

3.2 Simulation Details……..82

3.2.1 Systems……...82

3.2.2 Bulk System Simulations……...82

3.2.3 Confined system simulations…….....83

3.2.4 fidelity Check…….....83

3.3 Results and Discussion……..84

3.3.1 Environment around C153 in the bulk and confined binary mixtures……...84

3.3.1.1 Effects of confinement on preferential solvation…….……...85

3.3.2 Hydrogen bond structure and dynamics of the system……...88

3.3.2.1 Effects of confinement on the H-bond structure of aqueous methanol solutions……...88

3.3.2.1.1 Tetrahedral order parameter distribution, $P(Q)$……..……..90

3.3.2.1.2 Number of Hydrogen bonds per molecule……...94

3.3.2.2 Intra- and Inter-species H-bond fluctuation dynamics: Structural and Continuous……...96

3.4 Conclusion……102

Appendix 3.A……103

Appendix 3.B…….....109

References…….….117

Chapter 4: Dynamical Anomaly of Aqueous Amphiphilic Solutions: Connection to Solution H-bond Fluctuation Dynamics? …….....120

4.1 Introduction……..120

4.2 Simulation Details.……...……125

4.3 Results and Discussion.…….……...127

4.3.1 Radial Distribution Function (RDF) and Coordination Number (CN)…….…..….127

4.3.2 Number of H-bonds and Participation Papulation …….……..132

4.3.3 Tetrahedral order parameter…….……..…….…….....138

4.3.4 Spatial Distribution Function (SDF)……..…….…….....140

4.3.5 Hydrogen Bond Relaxation Dynamics.……...…….....142

4.4 Conclusion.....144

Appendix 4.A……145

Appendix 4.B……151

References……..160

Chapter 5: Why Some Reactions Occurring in Widely Different Viscous Media Possess the Similar Reaction Rate? An Analytical Investigation Employing Experimental Dielectric Relaxation Data …….…….....164

5.1 Introduction…….……164

5.2 Theoretical Formalism and Method of Calculation …….……...166

5.3 Numerical Results and Discussion …….…….....171

5.3.1 Frequency dependent Rotational kernel, $\Gamma_R(k \to 0, z)$ employing experimental DR data.…….……...171

5.3.2 Reorientational time correlation Function of rank $\ell = 1$, $C_1(t)$……. 174

5.4 Conclusion.....179

References……. 180

Chapter 6: Concluding Remarks and Future Problems……..182

6.1 Concluding Remarks …….…….....182

6.2 Future Problems ……..183

6.2.1 Effect of confinement on structural and temporal heterogeneity of aqueous methanol solutions: A Molecular Dynamics Simulation study ……..183

6.2.2 How hydrogen Bond Lifetime distribution and corresponding fluctuations behaves around 'dynamically' anomalous composition of aqueous amphiphilic solutions: A simulation study employing aqueous TMU solution as a model system. …….....183

6.2.3 Effect of cylindrical nanoconfinement on preferential solvation and microscopic di-mixing in aqueous alcohol solutions: A simulation study for understanding basics of targeted drug activation. ……..184

6.2.4 Effect of size of alcohols on water tetrahedral Hydrogen bond structure: A Molecular Dynamic Study exploring water structure at very local level.…….184

References……..185

Addendum I ……186

Chapter 1

Introduction

Profound understanding about interaction and dynamics of solvent media is of utmost importance in industrial applications as a majority of the chemical reactions in condensed phases are solvent controlled. Well-known solvent-influenced reactions such as charge transfer reactions[1–7], isomerisation[8–12], tautomerization[13–16], radical recombination reactions[17–20], proton transfer reactions[21–27] require a thorough knowledge about the dynamic behaviour of the solvent media to understand the course of these reactions and to get a clue for controlling the reaction rates. It is known that medium polarity is one of the main control parameters for reaction rates and the polarity can be easily modified through addition of co-solvents at different proportions. In industrial applications, the most used co-solvent is water, because of its cost-effectiveness, high polarity, low viscosity, and its high miscibility with other solvents.

Binary mixtures of water and small amphiphiles e.g., methanol (MeOH), ethanol (EtOH), tertiary butanol (TBA), dimethyl sulphoxide (DMSO), tetramethylurea (TMU), 1,4-dioxane (Diox) have been studied in many experimental[28–34] and simulation[28,35–39] investigations. These amphiphiles bear great importance in chemistry and biology. Amphiphiles are those which possess a combination of hydrophilic (water-attracting) and hydrophobic (water-repelling) moieties. But the most extensively studied aqueous binary mixtures are with small alcohols like methanol, ethanol, tertiary butyl alcohol. Water is known to interact with the amphiphiles through hydrogen bonding with polar headgroups and hydrophobic interaction. Water allows certain amphiphiles up to certain concentrations to agglomerate via hydrophobic interaction without leading to macroscopic phase separation. For these reasons, binary mixtures, while possessing wide-spread industrial applications, offer exciting systems for examining and discovering basic science aspects.

It is a well-known fact[40] that, in thermodynamic measurements, the entropy of mixing of alcohol with water (especially methanol or ethanol) does not decrease as much as predicted via random mixing of these two systems. Corresponding studies[41–61] exploring the origin of thermodynamic anomalies have led to much debate and discussion. However, the exact nature of the inherent structural changes connected to these anomalies is not unambiguously known yet. There exist two different views: one of them predicts the water tetrahedral hydrogen bonding structure gets perturbed upon addition of amphiphiles but retains its bulk-like structure around amphiphilic solute even at a very high concentration (for example, methanol: water = 7:3)[62] of alcohol. The other proposition[63–66] is that upon addition of alcohol, water tetrahedral structure gets enhanced up to a critical amphiphile concentration and then bulk tetrahedrality starts breaking down. Therefore, despite the existence of a large number of studies, more detailed molecular level insights on the origin of these anomalies are still warranted and worth exploring.

Our living world consists of mostly water and complex aqueous solutions. Most of the life processes are controlled by slight changes in the chemical nature of the solvent, for example, pH of the solvent. All drugs employed for human applications are designed by considering the local environment of the target site. These drugs and their carriers have both hydrophobic and hydrophilic groups within themselves at different proportions. So, preferential solvation of these drugs and drug carriers is one of the key issues in drug activation processes within living cells. It is also important to consider that chemical processes in living cells occur in confined spaces with a typical size of ~1 nm[67]. The effects of confinement on preferential solvation are, therefore, an interesting and important aspect but yet not explored in detail. Besides aqueous nanoconfinements modifying the H-bonded tetrahedral network of water, the dynamics of water also becomes considerably slowed down[68–71]. Confined aqueous environments, especially aqueous reverse micelles, have been studied extensively[69,72–84] and the hugely slowed down timescale has been found to originate from the interfacial layers where the curvature and surfactant effects play the most prominent role. It was also reported in several studies[68,80,81,85] that confined water could be described through a two-state model, the celebrated core-shell model. This model describes interfacial water to be drastically slowed down in comparison with those constituting the central pool which resembles the bulk water. Although some previous studies[79,80,86] mentioned and doubted the validity of the celebrated

two-state model for confined water, a thorough simulation study exploring the detailed aspect of confined water dynamics with a focus on this issue is still lacking.

Apart from structural anomalies[28–30,32,33] found in aqueous alcohol mixtures at very low alcohol concentrations (typically $x_{alcohol} < 0.1$), there exists another interesting dynamical feature. Several time-resolved fluorescence studies have revealed an abrupt change in the slope of the composition dependent probe lifetimes and/or probe rotation times at moderate alcohol concentrations which is approximate twice the alcohol concentrations where the structural anomaly has been found. This feature seems to be quite generic[28,30,33] for aqueous alcohol binary mixtures but there exist no detailed simulation studies focusing on this dynamic anomaly. Understanding the origin of this sharp change in the slope of the composition dependent probe rotation or lifetime requires detailed composition dependent study of the inter- and the intra-species hydrogen bond fluctuation dynamics.

It is obvious that in-silico experiments (computer simulations) provide a microscopic view of the structure and dynamics of the environment in which reactive and non-reactive dynamics occur in condensed phases. The structure is often explored by marking the relative spatial and angular arrangements of the molecules in a situation where the mean free path is typically in the order of a molecular diameter, the dynamics is monitored via probing various relaxation processes that may or may not be temporally correlated beyond their characteristic diffusion times. The frictional resistance offered by the medium and its temporal profile is often the key for understanding rates of relaxation processes because of their inherent inter-dependence. This assumes more importance because experiments can measure only the reaction rates but not the friction directly, while simulations or appropriate analytical frameworks can track down the microscopic friction connecting the rates measured in experiments.

This Thesis consists of 6 chapters, the first being the Introduction. In chapter 2 we present molecular dynamics simulation results on layer-wise structural and spatio-temporal heterogeneity features of confined water inside rigid spherical reverse micelles of 55 Å inner diameter. These confined aqueous pools were divided into four fictitious concentric layers of 5 Å thickness, and a central core layer. Reverse micellar confinements were constructed by

using model potentials mimicking AOT (charged) and IGEPAL (neutral) surfactant molecules for encapsulating SPC/E water[87]. Density profiles for confined water were obtained and compared to validate the present simulations. Analyses of simulation results revealed a strong impact of the confinement on bulk water structure and dynamics. The chemical nature of the confinement was found to influence both structure and dynamics. Interfacial water molecules were found to be the most severely affected ones and successive progression toward the center revealed a tendency for the restoration of the bulk limit, although the bulk values were never fully recovered. A close inspection of the simulated results revealed an overlap among the layer-wise structural and dynamical features. These observations suggest a break-down of the two-state core-shell model even for large RMs where an ample amount of 'free' water is available. The simulated collective reorientational relaxations of reverse micellar water agree well with the existing time-resolved 2D-IR measurements[76].

Exploring the local environment around a dissolved solute in a bulk aqueous solution of alcohol and assessing the impact of confinement on preferential solvation is the main theme of chapter 3. This type of study can provide critical information regarding the miscibility of an amphiphilic drug after delivery at a designated nanoscopic site and the subsequent release. The molecular dynamics simulation results reported in this chapter is an in-depth investigation of composition-dependent solvation structure around a dissolved hydrophobic solute, coumarin 153 (C153) in ambient binary mixtures of methanol and water in both bulk and under confinement. The confinement is a spherical AOT reverse micelle with a diameter of 55 Å. Inter- and Intra-species H-bond fluctuation dynamics have been monitored and compared with those from the corresponding bulk binary mixtures. A systematic comparison of both solvation structure and H-bond dynamics between confined and bulk binary mixtures reveals modulation of both preferential solvation and H-bond relaxation times inside a nanoscopic environment. More specifically, confinement accentuates the preferential solvation phenomenon and facilitates di-mixing of mixture components. In addition, these results reveal that the tetrahedral H-bond network of neat liquid water becomes severely affected upon addition of methanol, which becomes further distorted under confinement. It is found that confinement severely affects the inter-species hydrogen bonds and makes the corresponding continuous hydrogen bonds much shorter-lived. Interestingly, structural hydrogen bond relaxation timescales become longer in confined binary mixtures than those in bulk binary mixtures.

Chapter 4 attempts to describe and understand the dynamical anomaly in aqueous amphiphilic solutions. It is known that amphiphilic molecules can perturb the structure and dynamics of water in aqueous solutions. These amphiphiles include water-soluble alcohols, cycloethers, alkylated urea, and several others. While the anomalous composition dependence of different thermodynamic properties of these aqueous solutions in the water-rich region has been attributed to the perturbation of the tetrahedral network structure of water (structural anomaly)[88,89], an abrupt change in the amphiphile concentration dependence of reactive and non-reactive relaxation rates measured[28,30,32,33] employing foreign solutes in such media signals perturbation on solution dynamics. Several time-resolved measurements[28–34] have indicated that this anomalous perturbation on dynamics or 'dynamical anomaly' appears at an amphiphile concentration larger than that at which structural anomaly occurs. In this work, we have investigated the microscopic origins of both the structural and the dynamical anomaly by considering aqueous solutions of tertiary butanol (TBA) as a model system and performing molecular dynamics simulations at several compositions in the water-rich region. The dynamical anomaly has been followed via monitoring the composition dependent fluctuations of the intra- and inter-species H-bond dynamics, whereas the structural anomaly has been traced via simulating tetrahedral order parameter (Q), radial and spatial distribution functions, number of hydrogen bonds per water and TBA molecules, and populations of TBA and water participating in H- bonding. Our simulations reveal abrupt changes in H-bond dynamics and tetrahedral order parameter at amphiphile concentrations similar to those where spectroscopic measurements have reported sudden changes in thermodynamic properties and relaxation rates. This work, therefore, provides microscopic insights that cogently explain the corresponding composition dependent steady state and time-resolved spectroscopic measurements.

Chapter 5 explores the interconnection between solvent friction and ultrafast reactions. Reaction rate processes such as electron transfer reactions (ETRs) are found to be medium viscosity independent. Usually, reaction rates are governed by wavenumber and frequency dependent solvent friction where both rotational ($\Gamma_R(\kappa, z)$) and translational ($\Gamma_T(\kappa, z)$) frictional components are involved. However, reactions occurring at ultrafast timescale (for example, ETRs) are expected to couple to high frequency regime of the medium friction. This high frequency regime, often in the tera-Hertz (THz) regime,[90,91] involves collective inertial

motions and fast rotations of the solvent particles. This chapter presents results by employing an analytical work that provides an avenue to estimate the high frequency frictional response of a number of liquids possessing widely different viscosities. The aim here is to understand the near-insensitivity of ETRs to the long wavelength macroscopic medium viscosity. Rotational Kernel ($\Gamma_R(\kappa, z)$) has been calculated using the analytical expression[90,92–95] that connects friction to the experimental dielectric relaxation (DR) data. Three different systems, an ionic liquid ($BMIMPF_6$, $\eta \sim 310$ cP)[96], a dipolar solvent (ethanol, $\eta \sim 1.09$ cP)[97,] and a high viscous deep eutectic solvent (Acetamide+ LiBr, $\eta \sim 1950$ cP)[98] have been chosen to test the idea. Partial or full DR data are available[98–100] for these systems. Results from our analytical study have shown that $\Gamma_R(\kappa, z)$ estimated from available experiment DR data for the ionic liquid and deep eutectic solvent (DES) considered here cannot adequately illustrate the viscosity independence of high frequency rotational frictional response. Missing dispersion ($\varepsilon_\infty - n^2$) in the available experimental DR data of the DES system has been found to be critical for a sound and straightforward analysis. The collective solvent intermolecular modes[101] (CIMs) with a resonating frequency centered around 100 cm^{-1} has been used to attribute this missing dispersion amplitude.[99] Subsequently, the calculated $\Gamma_R(\kappa, z)$ for these three drastically different viscous media show high frequency frictional responses that exhibit near-insensitivity to medium viscosity. This explains the finding that ultrafast reactions often decouple significantly from medium viscosity.

Chapter 6 provides a brief over-all conclusion and lists several problems that might be studied in the near future. These representative problems are only showing a small glimpse of the vast research field consisting of hydrogen bond dynamics of the aqueous amphiphilic mixture. We present some initial results about our next ongoing project where we plan to explore hydrogen bond structure and dynamics of a naturally abundant deep eutectic system[102] (NADES) mixture of glucose+ urea+ water in 6:4:1 weight ratio in Addendum I. Besides exploring the detailed microstructure of this NADES, our major goal is to investigate how water dynamics changes in such a crowded and hydrogen-bonded environment of DES.

References

[1] B. Bagchi, Annu. Rev. Phys. Chem. **40**, 115 (1989).

[2] R. Biswas, N. Rohman, T. Pradhan, and R. Buchner, J. Phys. Chem. B **112**, 9379 (2008).

[3] K. Dahl, R. Biswas, N. Ito, and M. Maroncelli, J. Phys. Chem. B **109**, 1563 (2005).

[4] A. Das and R. Biswas, J. Phys. Chem. B **119**, 10102 (2015).

[5] M. Maroncelli, J. MacInnis, and G.R. Fleming, Science **243**, 1674 (1989).

[6] T. Pradhan and R. Biswas, J. Phys. Chem. A **111**, 11514 (2007).

[7] Y. Wang and K. Eisenthal, J. Chem. Phys. **77**, 6076 (1982).

[8] P. Barbara, Acc. Chem. Res. **21**, 195 (1988).

[9] R. Biswas, K. Dahl, and M. Maroncelli, J. Phys. Chem. B **106**, 11593 (2002).

[10] A. Heikal, S. Chong, J. Baskin, and A. Zewail, Chem. Phys. Lett. **242**, 380 (1995).

[11] J.M. Jean, D.C. Todd, S.J. Rosenthal, A.J. Ruggiero, and G.R. Fleming, in *Ultrafast Phenom. VII*, edited by C.B. Harris, E.P. Ippen, G.A. Mourou, and A.H. Zewail (Springer, Berlin, Heidelberg, 1990), pp. 441–443.

[12] Y. Onganer, M. Yin, D.R. Bessire, and E.L. Quitevis, J. Phys. Chem. **97**, 2344 (1993).

[13] A. Douhal, S. Kim, and A. Zewail, Nature **378**, 260 (1995).

[14] T. Ishida, F. Hirata, and S. Kato, J. Chem. Phys. **110**, 3938 (1999).

[15] D. McMorrow and T.J. Aartsma, Chem. Phys. Lett. **125**, 581 (1986).

[16] J. Powling and H. Bernstein, J. Am. Chem. Soc. **73**, 4353 (1951).

[17] T. Chuang, G. Hoffman, and K. Eisenthal, Chem. Phys. Lett. **25**, 201 (1974).

[18] R.M. Noyes, Prog. React. Kinet. **1**, 129 (1961).

[19] Z. Schulten and K. Schulten, J. Chem. Phys. **66**, 4616 (1977).

[20] A.G. Zawadzki and J.T. Hynes, J. Phys. Chem. **93**, 7031 (1989).

[21] D.J. Cram, B. Rickborn, C.A. Kingsbury, and P. Haberfield, J. Am. Chem. Soc. **83**, 3678 (1961).

[22] I. Giebels, M. van den Broek, M. Kropman, and H. Bakker, J. Chem. Phys. **112**, 5127 (2000).

[23] P.M. Kiefer and J.T. Hynes, J. Phys. Chem. A **106**, 1834 (2002).

[24] E. Pines and G.R. Fleming, J. Phys. Chem. **95**, 10448 (1991).

[25] E. Pines, B.-Z. Magnes, M.J. Lang, and G.R. Fleming, Chem. Phys. Lett. **281**, 413 (1997).

[26] W.H. Thompson and J.T. Hynes, J. Phys. Chem. A **105**, 2582 (2001).

[27] A. Warshel, J. Phys. Chem. **86**, 2218 (1982).

[28] S. Indra, B. Guchhait, and R. Biswas, J. Chem. Phys. **144**, 124506 (2016).

[29] S. Indra and R. Biswas, J. Chem. Sci. **128**, 753 (2016).

[30] T. Pradhan, H.A.R. Gazi, and R. Biswas, J. Chem. Phys. **131**, 054507 (2009).

[31] S. Indra and R. Biswas, J. Chem. Phys. **142**, 204501 (2015).

[32] T. Pradhan, P. Ghoshal, and R. Biswas, J. Chem. Sci. **120**, 275 (2008).

[33] T. Pradhan, P. Ghoshal, and R. Biswas, J. Phys. Chem. A **112**, 915 (2008).

[34] H.A.R. Gazi and R. Biswas, J. Phys. Chem. A **115**, 2447 (2011).

[35] S. Banerjee, S. Roy, and B. Bagchi, J. Phys. Chem. B **114**, 12875 (2010).

[36] S. Banerjee, R. Ghosh, and B. Bagchi, J. Phys. Chem. B **116**, 3713 (2012).

[37] S. Banerjee, J. Furtado, and B. Bagchi, J. Chem. Phys. **140**, 194502 (2014).

[38] A. Baksi and R. Biswas, J. Phys. Chem. B **124**, 11718 (2020).

[39] F.H. Stillinger, *The Physical Chemistry of Aqueous System* (1974).

[40] E. Boucher and J. MURRELL, *Properties of Liquids and Solutions* (Wiley, 1982).

[41] S. Banerjee and B. Bagchi, J. Chem. Phys. **139**, 164301 (2013).

[42] T.M. Bender and R. Pecora, J. Phys. Chem. **92**, 1675 (1988).

[43] D. Bowron and J. Finney, J. Phys. Chem. B **111**, 9838 (2007).

[44] M. Brai and U. Kaatze, J. Phys. Chem. **96**, 8946 (1992).

[45] S. Dixit, J. Crain, W. Poon, J.L. Finney, and A.K. Soper, Nature **416**, 829 (2002).

[46] G. Dutt, S. Doraiswamy, and N. Periasamy, J. Chem. Phys. **94**, 5360 (1991).

[47] G. Euliss and C. Sorensen, J. Chem. Phys. **80**, 4767 (1984).

[48] H.A.R. Gazi and R. Biswas, J. Phys. Chem. A **115**, 2447 (2011).

[49] Y. Koga, J. Phys. Chem. **100**, 5172 (1996).

[50] P.G. Kusalik, A.P. Lyubartsev, D.L. Bergman, and A. Laaksonen, J. Phys. Chem. B **104**, 9533 (2000).

[51] D. Laage, G. Stirnemann, and J.T. Hynes, J. Phys. Chem. B **113**, 2428 (2009).

[52] T. Pradhan, P. Ghoshal, and R. Biswas, J. Phys. Chem. A **112**, 915 (2008).

[53] T. Pradhan, P. Ghoshal, and R. Biswas, J. Chem. Sci. **120**, 275 (2008).

[54] Y. Rezus and H. Bakker, J. Phys. Chem. A **112**, 2355 (2008).

[55] S. Roy, S. Banerjee, N. Biyani, B. Jana, and B. Bagchi, J. Phys. Chem. B **115**, 685 (2011).

[56] T. Sato and R. Buchner, J. Chem. Phys. **119**, 10789 (2003).

[57] A. Soper and J. Finney, Phys. Rev. Lett. **71**, 4346 (1993).

[58] G. Stirnemann, F. Sterpone, and D. Laage, J. Phys. Chem. B **115**, 3254 (2011).

[59] K.-J. Tielrooij, J. Hunger, R. Buchner, M. Bonn, and H.J. Bakker, J. Am. Chem. Soc. **132**, 15671 (2010).

[60] K. Ydoshida and T. Yamaguchi, Z. Für Naturforschung A **56**, 529 (2001).

[61] K. Yoshida, T. Yamaguchi, A. Kovalenko, and F. Hirata, J. Phys. Chem. B **106**, 5042 (2002).

[62] S. Dixit, J. Crain, W. Poon, J.L. Finney, and A.K. Soper, Nature **416**, 829 (2002).

[63] F. Franks and D.J.G. Ives, Q. Rev. Chem. Soc. **20**, 1 (1966).

[64] H.S. Frank and M.W. Evans, J. Chem. Phys. **13**, 507 (1945).

[65] M. D'angelo, G. Onori, and A. Santucci, J. Chem. Phys. **100**, 3107 (1994).

[66] A. Soper and J. Finney, Phys. Rev. Lett. **71**, 4346 (1993).

[67] H. Middendorf, Phys. B Condens. Matter. **226**, 113 (1996).

[68] V.R. Hande and S. Chakrabarty, Phys. Chem. Chem. Phys. **18**, 21767 (2016).

[69] A. Baksi, P.Kr. Ghorai, and R. Biswas, J. Phys. Chem. B **124**, 2848 (2020).

[70] B. Guchhait, R. Biswas, and P.K. Ghorai, J. Phys. Chem. B **117**, 3345 (2013).

[71] J. Faeder and B. Ladanyi, J. Phys. Chem. B **104**, 1033 (2000).

[72] S. Abel, F. Sterpone, S. Bandyopadhyay, and M. Marchi, J. Phys. Chem. B **108**, 19458 (2004).

[73] H.-S. Tan, I.R. Piletic, and M. Fayer, J. Chem. Phys. **122**, 174501 (2005).

[74] D.E. Moilanen, E.E. Fenn, D. Wong, and M. Fayer, J. Phys. Chem. B **113**, 8560 (2009).

[75] S.A. Roget, P.L. Kramer, J.E. Thomaz, and M.D. Fayer, J. Phys. Chem. B **123**, 9408 (2019).

[76] M.D. Fayer, Acc. Chem. Res. **45**, 3 (2012).

[77] D.E. Moilanen, E.E. Fenn, D. Wong, and M.D. Fayer, J. Am. Chem. Soc. **131**, 8318 (2009).

[78] D.E. Moilanen, N.E. Levinger, D. Spry, and M. Fayer, J. Am. Chem. Soc. **129**, 14311 (2007).

[79] D.E. Moilanen, E.E. Fenn, D. Wong, and M.D. Fayer, J. Chem. Phys. **131**, 014704 (2009).

[80] I.R. Piletic, D.E. Moilanen, D. Spry, N.E. Levinger, and M. Fayer, J. Phys. Chem. A **110**, 4985 (2006).

[81] E.E. Fenn, D.B. Wong, and M. Fayer, Proc. Natl. Acad. Sci. USA **106**, 15243 (2009).

[82] M.D. Fayer and N.E. Levinger, Annu. Rev. Anal. Chem. **3**, 89 (2010).

[83] J. Chowdhary and B.M. Ladanyi, J. Phys. Chem. A **115**, 6306 (2011).

[84] J. Chowdhary and B.M. Ladanyi, J. Phys. Chem. B **113**, 15029 (2009).

[85] T.H. van der Loop, M.R. Panman, S. Lotze, J. Zhang, T. Vad, H.J. Bakker, W.F. Sager, and S. Woutersen, J. Chem. Phys. **137**, 044503 (2012).

[86] P.A. Pieniazek, Y.-S. Lin, J. Chowdhary, B.M. Ladanyi, and J. Skinner, J. Phys. Chem. B **113**, 15017 (2009).

[87] H. Berendsen, J. Grigera, and T. Straatsma, J. Phys. Chem. B **91**, 6269 (1987).

[88] K. Liltorp, P. Westh, and Y. Koga, Can. J. Chem. **83**, 420 (2005).

[89] Y. Koga, Can. J. Chem. **77**, 2039 (1999).

[90] S. Roy and B. Bagchi, J. Chem. Phys. **99**, 1310 (1993).

[91] B. Bagchi and A. Chandra, in *Adv. Chem. Phys.* (John Wiley & Sons, Ltd, 1991), pp. 1–126.

[92] B. Bagchi and R. Biswas, in *Adv. Chem. Phys.* (John Wiley & Sons, Ltd, 1999), pp. 207–433.

[93] S. Roy and B. Bagchi, J. Chem. Phys. **99**, 9938 (1993).

[94] N. Nandi, S. Roy, and B. Bagchi, J. Chem. Phys. **102**, 1390 (1995).

[95] R. Biswas and B. Bagchi, J. Phys. Chem. **100**, 1238 (1996).

[96] H.K. Kashyap and R. Biswas, J. Phys. Chem. B **112**, 12431 (2008).

[97] B. González, N. Calvar, E. Gómez, and Á. Domínguez, J. Chem. Thermodyn. **39**, 1578 (2007).

[98] K. Mukherjee, A. Das, S. Choudhury, A. Barman, and R. Biswas, J. Phys. Chem. B **119**, 8063 (2015).

[99] A. Stoppa, J. Hunger, R. Buchner, G. Hefter, A. Thoman, and H. Helm, J. Phys. Chem. B **112**, 4854 (2008).

[100] J.T. Kindt and C.A. Schmuttenmaer, J. Phys. Chem. **100**, 10373 (1996).

[101] S. Daschakraborty and R. Biswas, J. Chem. Phys. **137**, 114501 (2012).

[102] E. Tarif, J. Mondal, and R. Biswas, J. Phys. Chem. B **123**, 9378 (2019).

Chapter 2

Dynamic Susceptibility and Structural Heterogeneity of Large Reverse Micellar Water: An Examination of the Core-Shell Model via Probing the Layer-wise Features

2.1 Introduction

Water continues to fascinate researchers through its inseparable relationship to life, and its anomalous thermodynamic and solvent properties. Many of its exquisite properties as solvent stems from the extensive hydrogen bonding that extends to three dimensions for establishing a robust network in condensed phases. The inherent tendency to preserve this H-bond network in bulk, and its continual structural evolution in picosecond timescale determines much of its exotic response when subjected to unfavourable conditions[1]. Confinement of water in nanometre length-scales is expected to modify the structural features and H-bond dynamics which may open up a route to access the inaccessible temperature region (~150-235 K, known as "no man's land") for bulk supercooled water.[2,3] Confined water exists in nature in diverse forms: in salt hydrates as water crystallites, in clay and shell minerals as encapsulated water within their porous structures; and inside living cells as an alert transporter and reaction regulator. In living cells, the confinement size can vary between ~1 nm and ~100 nm[4]. Water molecules residing within half-a-nanometre of a biomolecular surface play a critical role in regulating important processes such as hydrophobic collapse leading to protein folding, and transport of ions and other molecules across biological channels.[2,4] These water molecules can be regarded as interfacial water molecules of biosystems, and relevant studies[5–9] have revealed that these water molecules are dynamically different from those of the neat bulk.

Aqueous reverse micelles are regarded as biomimetics because they offer a model to study membrane-enclosed confined water often encountered in biological systems.[1,6] The amphiphilic character of surfactant molecules facilitates the formation of nano-sized cavities in an aqueous environment and can generate size-tuneable confined interfaces through altering

the surfactant-to-water concentration ratio[1]. A significant number of studies of aqueous micellar and reverse micellar solutions reported[10–17] in addition to bulk-like relaxation, considerably slowed down dynamics of confined water. This observation led to the idea of "core-shell" model[18–21] of confined water which proposed that properties of confined aqueous pool of any size could be understood in terms of, with size-dependent proportions, water molecules that are directly interacting with the interior of the confining surface ("water shell"), and those constituting the central region (core) behaving like bulk water. Later experimental and simulation study[18,22,23] debated this two-state model of confined water and proposed that such a simplified description might be valid in the limit of large pool-size. These studies also suggested that confined water properties, in general, should vary with the distance from the interface because of the heterogeneity in interactions present in these systems. This interaction heterogeneity is present in addition to the structural heterogeneity at the interface, which arises from geometrical irregularities during the formation of self-assemblies where surfactant molecules, under suspension in oil-water systems, self-organize through a delicate balance between the hydrophobic and hydrophilic interactions. Another question that has been debated in several studies is whether the confinement itself or the chemical nature (ionic or neutral) of the confinement[24,25] dictates the structure and dynamics of confined water. In addition, a few studies[11,20] investigated the impact of the shape of the confinement and reported interesting results. Very recently, the structure and dynamics of water molecules in contact with a variety of interfaces have been studied to explore the impact of the interface on orientational as well as H-bond network structure of bulk water.[26–32]

Several experimental studies[33–37] have confirmed the spatio-temporal heterogeneity of the confined aqueous pool in reverse micelles. Although some attempts have already been made to provide a microscopic view of this micro-heterogeneity via simulations, those are sporadic and only a few structural and temporal parameters were chosen for investigation. A systematic and thorough study reflecting how a wide variety of spatial and temporal aspects of confined water gradually changes as a function of distance from the interface and assumes bulk-like values in the central region is still lacking. A piece of critical information in this regard is missing, that is, how this modification of spatio-temporal properties is affected by the chemical nature of the confining interface? This, and a re-examination of the validity of the core-shell model[18,38] in the limit of large aqueous reverse micellar pools constitute the basic premise of the present study. Note here that we have deliberately removed the structural heterogeneity at the interface arising from geometrical defects from self-aggregation; we are examining the

heterogeneity in liquid structure arising from interactions with the interface and rigid spherical confinement, and the subsequent impact on motional features of water molecules inside such confinements.

We present here extensive simulated results on structural and dynamical aspects of water molecules in different concentric layers, each 5 Å thick, starting from the interface, for charged and neutral aqueous reverse micelles with pool diameter of 55 Å. This choice of layer thickness (5 Å) is motivated by the fact that water molecules residing within such distances of biomolecular interfaces are believed to be critically important for life[2]. These layer-wise results are then compared against the corresponding 'over-all' properties (obtained after averaging over the contributions from all confined water molecules), and the corresponding bulk features. This is done in order to demonstrate how confined water properties change as one moves away from the interface toward the centre of the aqueous pool, and approach to those for bulk water. For constructing reverse micelles, we have used model interaction potentials designed for the charged surfactant molecule, sodium bis(2-Ethylhexyl) sulfosuccinate (AOT), and the neutral one poly(oxyethylene)nonylphenyl (Igepal CO-520 or, in short, IGEPAL). The chemical structures of these surfactants are shown in Scheme 2.1. We have represented water by the well-known SPC/E model. Our analyses of layer-wise properties indicate interface water molecules are the most perturbed ones both structurally and dynamically, and tend toward bulk-like properties via successive changes through layers but not achieving quite the bulk values. This is the observation for both the neutral and charged aqueous reverse micelles. These results, therefore, provide a possible resolution to the debate regarding the applicability of the core-shell model for understanding experimental results for large aqueous pools. The impact of the confinement dominates over the chemical nature of the surfactant, a finding that corroborates well with the conclusions from time-resolved 2D-IR measurements.[39] Some dynamical properties have, however, been found to strongly differentiate between the charged and neutral interfaces, reflecting the fact that the impact of the chemical nature of interfaces depends on the identity of the dynamical quantity under investigation.

a.

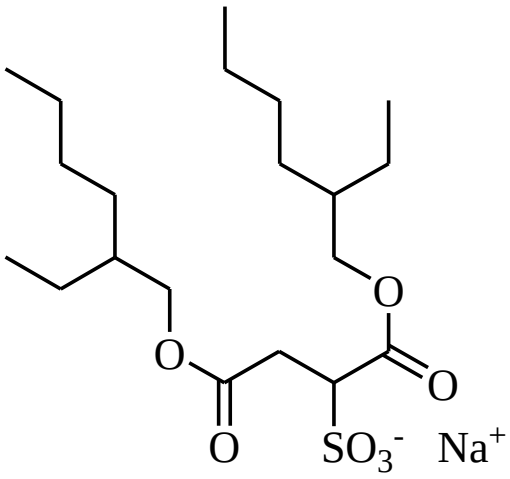

b.

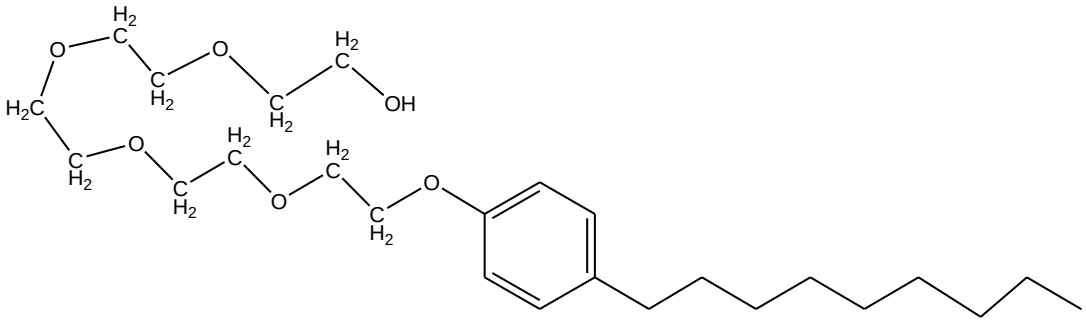

Scheme 2.1: Atomic representations of (a) AOT and (b) IGEPAL molecule. Atoms indicated here are considered explicitly in our simulation.

This brings into the context an early theoretical study[40] dewetting and formation of water-vapour interface near a hard wall. Subsequent simulation studies of water dispersed in the interstitial space between two large parallel hard oblate ellipsoidal plates predicted water vapour when the repulsive plates were ~10 Å apart, and bulk-like water when they were kept at larger distances.[41] Further analytical and simulation studies of water near non-polar solutes[42] and water inside non-polar cavities[43,44] suggested dewetting, and cavity water structures resembling those reported in gas phase spectroscopic experiments.[45] These non-polar cavities were with diameter ~10-12 Å and hence considerably smaller than the aqueous pool diameter (55 Å) considered in the present simulations. Note also that water molecules confined in these small non-polar cavities[43,44] interact with confining non-polar wall via an interaction potential which contains a slowly varying, relatively softer, attractive component (via the well-depth ε). Therefore, these nonpolar cavities are not the same as cavity made of purely repulsive hard spheres. Consequently, no results exist in the literature for water confined within RM made of purely repulsive hard spheres for a comparative study with water structure and dynamics predicted by the present simulations.

2.2 Simulation Details

2.2.1 Construction of aqueous reverse micelles

Following the model of earlier works[13,46,47] our present RM structure was constructed, where the interior of the aqueous RM was approximated as a rigid spherical cavity. The hydrogen (H) atoms of methyl (-CH_3) and ethylene (-CH_2) groups of the surfactant molecules were treated implicitly. However, for IGEPAL the H atoms of the polyethylene ((-CH_2)$_n$) and hydroxyl ($-$OH) groups that would remain inside the water pool were modelled explicitly to better represent the IGEPAL RM interior. The rigid Na^+ ions were placed inside the cavities randomly. Structures of these model aqueous RM systems are shown in Figure 2.A.1 and Figure 2.A.2 of Appendix 2.A. No nonpolar dispersion medium outside the RM was considered. Interactions between different surfactant molecules were not considered, and periodic boundary condition not used. The SPC/E water[48] filled up the spherical cavity so constructed. Note the SPC/E water molecules are non-polarizable, and with fixed bond lengths and angles. These water molecules interacted through a pairwise additive sum of the site – site

interaction potential. This includes both 12-6 Lennard-Jones (LJ), and electrostatic interactions between fixed partial charges:

$$E_{ij}(r) = 4\varepsilon_{ij}\left[\left(\frac{\sigma_{ij}}{r}\right)^{12} + \left(\frac{\sigma_{ij}}{r}\right)^{6}\right] + \frac{q_i q_j}{4\pi\varepsilon_0 r}$$

The Dreiding force field for the LJ interaction potentials of the surfactants was used.[49] The partial charges for AOT were taken from the CHARMM force field used elsewhere.[50] Partial charges for IGEPAL molecule were calculated by using the HF/6-31 + G(d) basis set maintaining the charge neutrality. The LJ interaction between different sites was approximated by the Lorentz-Berthelot combination rules[51] and the corresponding electrostatic interaction via the direct Coulomb summation technique. Partial atomic charges and the LJ parameters for AOT and IGEPAL surfactant molecules are summarized in Table 2.B.1- 2.B.4 (Appendix 2.B). We used 218 surfactant and 2060 water molecules to construct a stable aqueous RM pools of 55 Å inner diameter for both the cases.

Note here that the maximum number of water molecules that could be packed inside these RM cavities after allowing for the volumes occupied by the surfactant head-groups (SO_3^- for AOT and $(-OCH_2)_n$ for IGEPAL) inside the cavities created by 218 surfactant molecules (please see Figure 2.A.1 and Figure 2.A.2 of Appendix 2.A). The average number density of water molecules inside these RMs therefore is 0.0236 $Å^{-3}$, and lower than the average number density of bulk neat water (0.0334 $Å^{-3}$). Experimental measurements[52,53] of size dependent compressibilities of charged and neutral aqueous RMs have reported much higher compressibilities for confined water than that for bulk. This suggests that average water densities inside these RMs are lower than that of the bulk, and therefore, the number of water molecules considered here follows qualitatively the experimental trend.

2.2.2 Technical aspects for simulations of aqueous reverse micelles

MD trajectories were propagated using the Velocity- Verlet algorithm[51] with a time step of 2 fs. The temperature was maintained at 300K by using the Nose-Hoover thermostat[54,55] with a time constant of 0.5 ps. The cut-off radius for short-range interaction was 15 Å. Trajectories were saved at every 1 ps time gap throughout the production run of 20 ns, after equilibration of 40 ns in the NVT ensemble. For calculating the reorientation relaxations, separate trajectories of 2 ns were generated in the same ensemble with the pre-equilibrated systems. In this case, trajectories were saved employing 10 fs time gap to minimise the possibility of losing the faster component of the reorientation relaxation of water molecules.

2.2.3 Fidelity check

Radial density profiles of confined water shown in Figure 2.1 compares the radial distributions of water molecules (number of water molecules per unit volume) inside the charged (AOT) and neutral (IGEPAL) spherical RM cavities. Note for both the RMs the number density maintains nearly the bulk value (33.2/nm^3) at the centre and away from the interface but drops drastically within ~5Å from the interface. This sudden decrease of water density near the interface agrees well with the results from earlier simulations of aqueous AOT RM[129] and is in general agreement with the distance dependence of simulated density for water confined in RMs of various sizes.[22] This provides the necessary confidence for the present simulations to continue for the intended study.

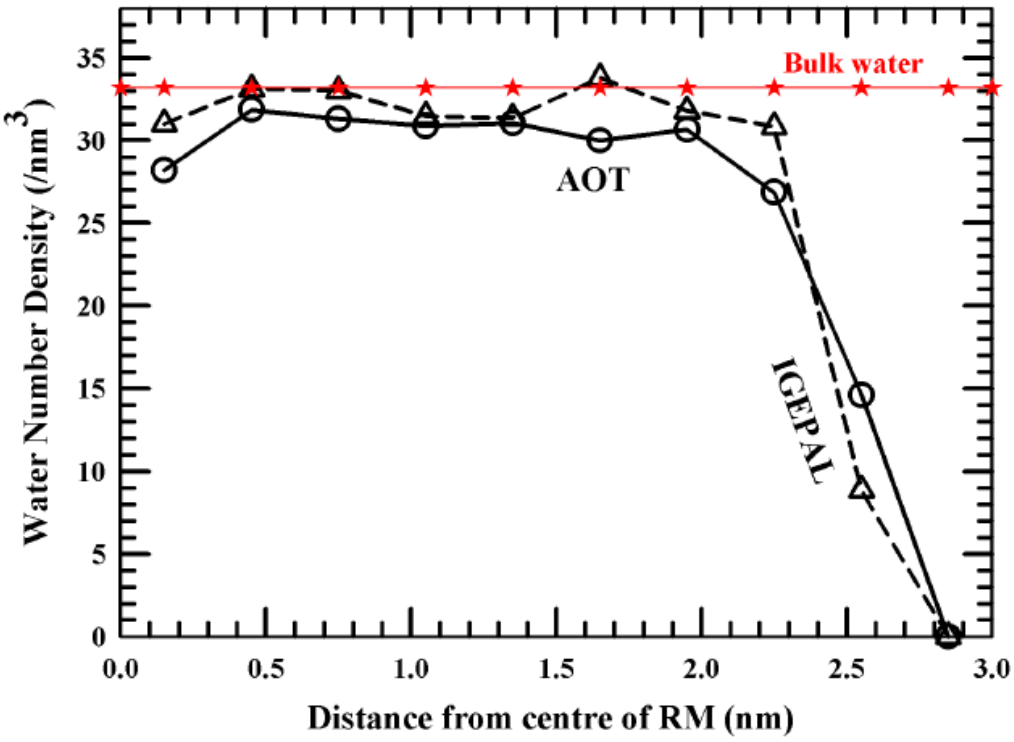

Figure 2.1: The layer-wise number density of water molecules within AOT and IGEPAL RM. The solid line represents the charged AOT RM and dashed lines the neutral one. Bulk number density is also shown for comparison.

2.2.4 Sorting out particles for exploring layer-wise and over-all motional features

It has already been mentioned that for computing layer-wise motional features, we considered only those particles which were continuously residing within a given layer over a certain period of time. In the event of re-entry after leaving a given layer, time origin for that particles was reset to zero, and motions followed. For better statistics, half of the continuous residence time for each of the layer particle was considered for computing dynamic properties in a given layer. The distributions of continuous residence times in different layers in AOT and IGEPAL RMs are shown in Figure 2.A.3 of Appendix 2.A. It is intriguing to note in these figures that residence times are not the shortest for water molecules residing in the core of both the RMs. Surprisingly, a majority of the interfacial water molecules in AOT RM possess residence times even shorter than those residing in the central core layer, although there exist water molecules that are staying for a relatively longer duration (see insets). The existence of water molecules with both relatively 'shorter' and 'longer' residence times within a given layer (with differing amplitudes) is a contrast to the simple two-state representation of confined water by dividing them into core and shell water molecules. This was already hinted at by earlier simulation studies.[16,56] Moreover, the water molecules with 'shorter' residence times might be responsible for showing faster-than-bulk dynamics reported already by a few previous studies.

For tracking the origin of "slow" dynamics, we then computed the layer-wise distributions of the longest residence times for water molecules in these RMs. This is shown in Figure 2.A.4 of Appendix 2.A, and the corresponding average times in Table 2.B.5 (Appendix 2.B). A plot of these average longest residence times, shown in Figure 2.A.5 of Appendix 2.A, suggests that water molecules become more labile as the core layer is approached for both the RMs, and that the interfacial water molecules sense the difference in the chemical nature of the confining interfaces.

2.2.5 Bulk water simulation

For the simulations of bulk water, 2060 SPC/E[48] water molecules were considered with bonds constrained using the SHAKE algorithm.[57] Equilibration was first done in the NPT ensemble employing Berendsen thermostat[58] with coupling constant 0.1ps. Velocity-Verlet algorithm[51]

with 2fs time step was used to solve the classical equations of motion. The cut-off radius for the short-range interaction was set to 15 Å. Electrostatic interactions were dealt with the smooth particle mesh Ewald algorithm using the Ewald convergence parameter 0.0036 $Å^{-1}$, and -6Å x 6 Å x 6 Å grid in momentum space. The Berendsen barostat[58] with 2ps time constant was used to maintain the pressure at 1 atm. The equilibrated structure thus obtained then transferred to the NVT ensemble for further equilibration for another 2ns. Subsequently, a production run is carried out at a temperature 300 K for 10 ns and trajectories were saved at every 0.02 ps using the Nose-Hoover thermostat with a time constant of 0.5 ps. DLPOLY MD simulation package was used[59] for the simulation results reported in this study.

2.3 Results and Discussion

2.3.1 Structural order parameters

2.3.1.1 The orientation of water dipoles

Effects of the chemical nature of the surfactant molecules on water structure under confinement have been studied via exploring the orientation of water dipoles with respect to the radial vector. Dipolar orientation (P) can be quantified as[11,20,47],

$$\Omega = \frac{\boldsymbol{r}.\boldsymbol{\mu}}{|\boldsymbol{r}|.|\boldsymbol{\mu}|} = cos\,\beta \qquad (2.1)$$

where $\boldsymbol{r}$ denotes the radial vector from the oxygen atom of water molecule to the centre of the RM and μ the dipole moment vector of a water molecule. A schematic diagram for describing this prescription for calculating dipolar orientation is given in Figure 2.A.6 of Appendix 2.A. The angle β would be zero if water dipole is pointed towards the interface, producing $\Omega = 1$. Figure 2.2 depicts the layer-wise distribution of cos β and compare between the AOT and IGEPAL RMs. The first aspect that immediately strikes is that the distribution, Ω, for 'over-all' as well as separated out water molecules in the first layer (layer#1) peaks at unity while that for IGEPAL shows a peak at ~ -0.7. These two values of cos β correspond respectively to parallel (0°) and 135° orientation of water molecules with respect to the radial vector. This is a reflection of the difference in the chemical nature of the confining interfaces (charged and neutral). In addition, Ω for water molecules in the layer#1 of AOT RM shows a secondary peak

at a $\cos\beta$ value corresponding to water dipole vector orientation at 135° which, for 'over-all' distribution, appears as a broad shoulder. These angular orientations of water molecules (with respect to the radial vector) are schematically depicted in Figure 2.A.7 of Appendix 2.A for AOT interface. We speculate that such orientations of water molecules are plausible when (i) the electrostatics between the oxygen atom of water and the counter ion Na^+at the interface of AOT RM compel the interfacial water molecules to align their molecular dipole vector parallel to the radial vector, and (ii) the H-bonding interaction between the H atom of water and the O atom of the interfaces (O atom of $-SO_3^-$ for AOT and that from $-OCH_2$ and/or $-OH$ units for IGEPAL) forcing the water dipoles to align at ~135°. Note to mimic the experimental condition we have modelled the IGEPAL molecule such that five $-OCH_2$ unit and one $-OH$ unit of each IGEPAL molecule are intruded inside the rigid surface along the periphery of RM. At this moment we cannot speculate how water molecules are residing around these intruding portions or whether some waters are getting captured within these portions is not. Our observation is that, we are getting a higher distribution of dipoles around an angle 135^o when over-all confined water is analysed, because of all these combined effects of ether and hydroxyl oxygen atoms and H atoms attached with ether groups. One might, however, like to argue here that parallel orientation of interfacial water molecules in the AOT RM could be linked to the forced random distribution of Na^+ along the inner periphery of the interface. While this could be a possibility, previous simulations[11,13,47] of AOT RMs with randomly distributed counter ions in the aqueous pool have suggested that a majority of Na^+ ions in large aqueous pools prefer to reside at the interfacial region. While stating this we would like to mention that the water molecules in the first solvation shell of Na^+have not been treated differently to separate out their contributions in the solution heterogeneity.[60] Interestingly, polarisation sensitive vibrational sum frequency generation measurements[31,61,62] of water orientation near different type of interfaces report results that corroborates with our simulation observation. A recent study of water orientation near the positively and negatively charged interfaces[31] have reported interface-sensitive orientation structures similar to our simulation predictions. These measurements have also reported orientation of water molecules at obtuse angles (~ 130^0 to 155^0) for charged interfaces. We, therefore, believe that the present model for the aqueous RM closely mimics the real reverse micellar water.

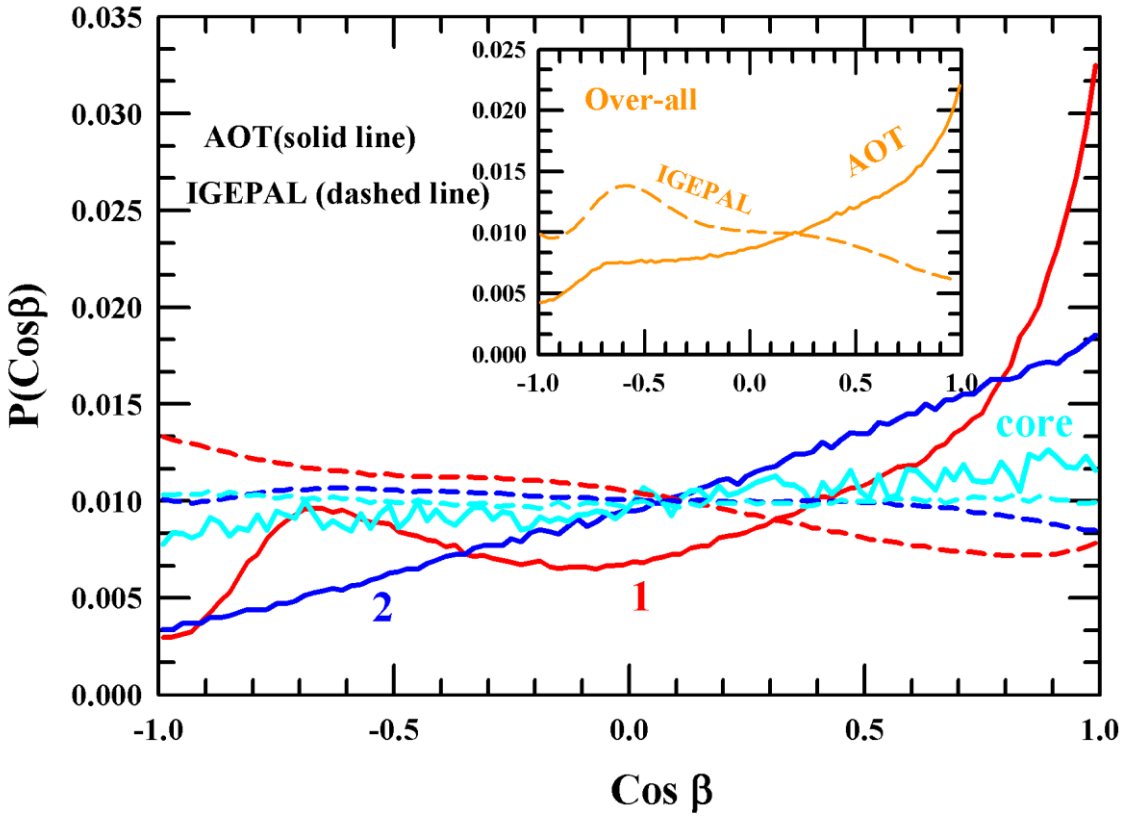

Figure 2.2: Water dipole orientation with respect to the radial vector for both types (AOT and IGEPAL) RMs. The inner panel compares the over-all water dipole orientation between the charged and the neutral RMs.

2.3.1.2 Tetrahedral order parameter (Q_i) and the distribution of the number of hydrogen bonds per water molecule ($P(N_{HB})$)

Tetrahedral structure and hydrogen-bonding pattern in the bulk water, and the effects of confinement curvature have been studied earlier.[11,20,46] The tetrahedral order parameter has been obtained by using the following expression[63]

$$Q = 1 - \frac{3}{8}\sum_{j=1}^{3}\sum_{k=j+1}^{4}(cos\theta_{ijk} + {}^{1}/_{3})^{2} \quad , \qquad (2.2)$$

where Q_i is the tetrahedral order parameter of the i^{th} water, θ_{ijk}- the angle subtended by each pair (designated by j and k) of the nearest four water molecules on the central i^{th} water molecule. For a random and uniform distribution of these angles, Q=0, whereas Q=1 reflects a perfect tetrahedral structure. A schematic diagram for the general description of the tetrahedral angle and three-dimensional tetrahedral structure of the hydrogen bonding network in the bulk water is shown in Figure 2.A.8 of Appendix 2.A.

The following prescription[5,64–67] was used for detecting hydrogen bonds between water molecules: a) the distance between the donor oxygen atom and acceptor oxygen atom is less than 3.5 Å, b) the H-O(donor)-O(acceptor) angle is less than 30°, and c) distance between O and H must be less than 2.45 Å. Figure 2.3 depicts the layer-wise probability distributions, $P(cos\,\theta)$, for the angle θ_{ijk} that each individual water molecule (i -th water molecule) forms with its two nearest neighbours, j and k. The difference between the bulk water and the confined water is quite obvious; the minor peak at $cos\,\theta$~0.5 (that is,$\theta\sim60^{\circ}$) of the two-peak structure of the bulk distribution becomes more pronounced upon confinement, and the interfacial water molecules inside both types of RMs experiences the maximum impact. In addition, the broad peak located at $\theta\sim108^{\circ}$ ($cos\,\theta$ ~ -0.3) for bulk water shifts to higher angles ($\theta\sim102^{\circ}$) upon confinement along with further broadening and loss of intensity. This modulation of peak position and intensities suggest strong impact of confinement on the orientational structure of bulk water where tetrahedrality is compromised to give rise to trigonal arrangements.

To draw a more collective and meaningful picture we have calculated the probability distribution of the tetrahedral parameter, P(Q) (Figure 2.4) and Table 2.1 summarizes layer-wise and bulk populations corresponding to peak positions of P(Q) at lower and higher Q values. These populations represent the area under the curves obtained through deconvolution of a simulated P(Q) into two fragments, as shown in Figure 2.A.9 of Appendix 2.A. Results are shown in this figure and table, therefore, clearly demonstrate that the tetrahedral arrangement for interfacial water molecules is severely affected, and the bulk tetrahedrality has not been attained even for core water molecules inside both these RMs. Notice that the average values of the order parameter, $\langle Q \rangle$, for water at the interfacial layer (layer#1) of both the RMs are quite close to that for TIP3P water confined between two parallel graphene plates held 6.5 Å apart[32]. In addition, the sudden recovery of nearly the bulk value of $\langle Q \rangle$ for a 10 Å thick TIP3P water layer reported in this work[32] is very similar to what has been observed in the present study (see Table 2.1).

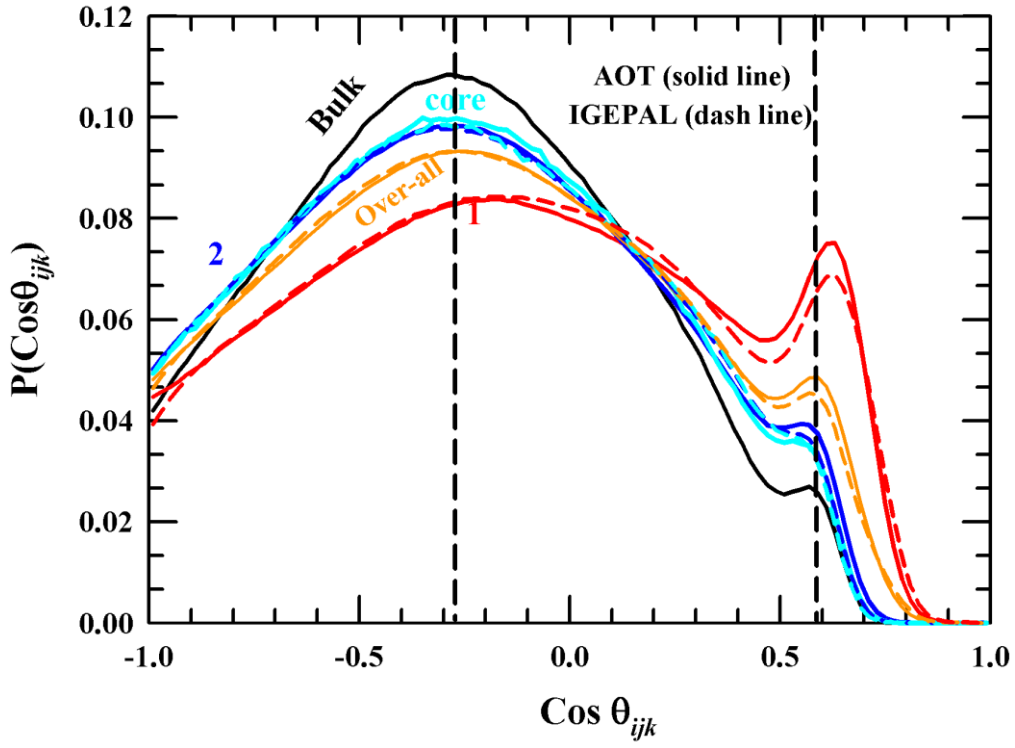

Figure 2.3: Distribution of tetrahedral angle created by the three nearest water molecules confined in these RMs. Results for water in layers 1, 2 and the core are shown here. The same for the 'over-all' and the bulk are also shown.

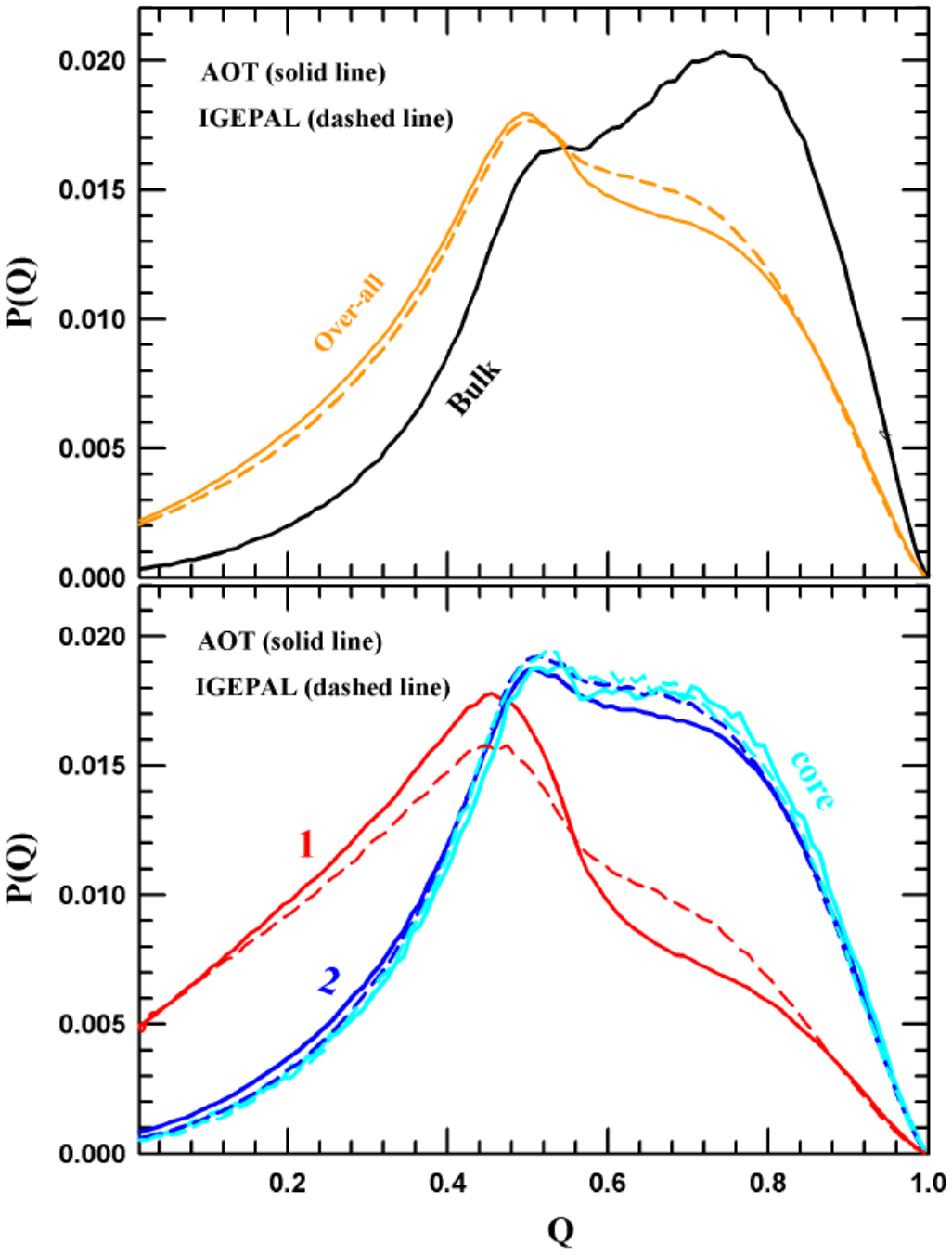

Figure 2.4: Tetrahedral order parameter distributions for water in different layers of confined aqueous pools inside the RMs under study. A comparison between the over-all and bulk is shown in the upper panel while the lower panel presents the results for layer 1, 2 and the core.

Table 2.1: Layer-wise and 'over-all' population distribution of water molecules corresponding to the peak positions at the high and the low values of the tetrahedral order parameter, *Q*. The average value of the order parameter, $\langle Q \rangle$, represents the area under the curve.

	AOT			IGEPAL		
	Centre	Area (%)	$\langle Q \rangle$	Centre	Area (%)	$\langle Q \rangle$
Layer 1	0.35	75.74	0.386	0.31	63	0.394
	0.47	13.90		0.47	17	
	0.78	**10.35**		**0.73**	**20**	
Layer 2	0.55	82	0.577	0.55	81	0.580
	0.80	**18**		**0.80**	**19**	
Layer 3	0.55	81	0.582	0.55	81	0.584
	0.80	**19**		**0.80**	**19**	
Layer 4	0.56	78	0.593	0.55	80	0.588
	0.80	**22**		**0.80**	**20**	
Core	0.56	78	0.593	0.55	80	0.590
	0.80	**22**		**0.80**	**20**	
over-all	0.35	41	0.514	0.51	33	0.522
	0.50	27		0.76	33	
	0.77	**32**		**0.33**	**33**	
Bulk water	0.58	70	0.635			
	0.81	**30**				

a) $\langle Q \rangle = \int dQ\ Q\ P(Q) / \int dQ\ \ P(Q)$

Table 2.2 summarises the average number of H-bond per water molecule (N_{HB}) in different layers of AOT and IGEPAL RMs. These average numbers, although differ between the RMs, do not clearly reflect the differences between the confined water in these RMs and the bulk water in terms of number of H-bonds per water molecule, and the variations in H-bonded structures among the layers in these two RMs. Figure 2.5 presents such a comparison where the population distributions, $P(N_{HB}/water)$ with respect to the number of H-bonds per water molecule ($N_{HB}/water$) are shown for the 'over-all', first two (layer#1 and layer#2) and core layers, and bulk water molecules. $P(N_{HB}/water)$ for other layers are presented in Figure 2.A.10 of Appendix 2.A. Notice that the population distributions depicted in these figures clearly exhibit the difference among water molecules in different layers, and between the nature of confinements. Interestingly, $P(N_{HB}/water)$ for core water molecules in both of these RMs, although differ substantially from those at the interfacial layers and bear the maximum similarity to that of the bulk, could not attain fully the bulk distribution. This difference suggests the inadequacy of the core-shell model for confined water inside RMs. It is also evident from these figures that the number of water molecules with four H-bonds are significantly less for the interfacial layers than for the bulk. We would like to point out that in an earlier study[43] it was reported that, in non-polar confinement of diameter comparable with our layer width (5 Å) the most stable hydrogen bonded structure is dimer which resembles more with gas phase structure of water. But here, in our simulated interfacial water, we find most population of water around trimmers and there also exist ample amount of dimer and tetramer, which dismiss any probability of finding the water in gas phase, like in the vicinity of hard sphere surface. In addition, this frustration in H-bonds is more severe for interfacial water molecules inside the AOT RM than inside the IGEPAL RM, reflecting the impact of the chemical nature of the confining interface. We would like to state here that a thorough and comparative study of layer-wise structural aspects of confined water and impact of the chemical nature of confining interfaces such as the present one is performed here for the first time. These results clearly demonstrate the heterogeneity in density, orientational structure, number of H-bonds, and population distribution of H-bonded water molecules relative to those for bulk water, and show the break-down of the core-shell model.

Table 2.2: Layer-wise and 'over-all' average number of hydrogen bonds per water molecule for confined water in these RMs and bulk water.

Layer #	**N_{HB}**		
	AOT RM	**IGEPAL RM**	**Bulk SPC/E water**
1	2.742	2.951	3.587
2	3.390	3.348	
3	3.414	3.398	
4	3.488	3.418	
core	3.486	3.430	
over-all	3.175	3.226	

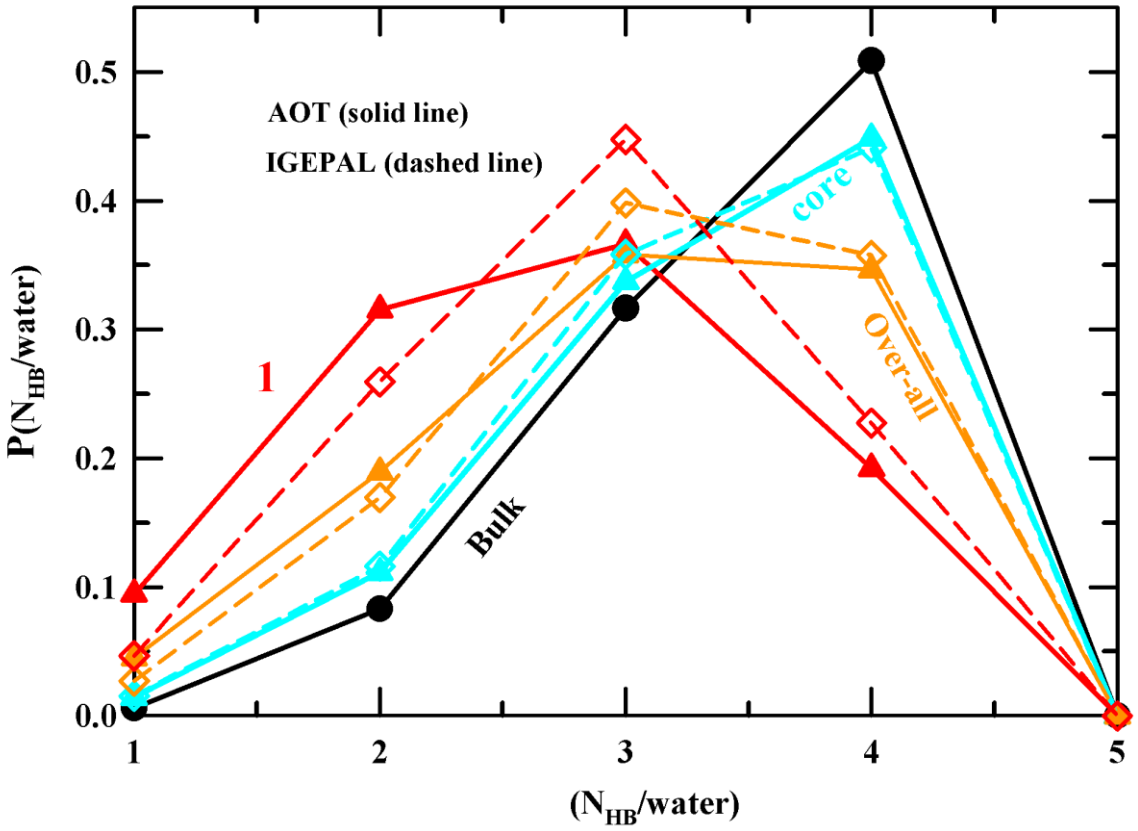

Figure 2.5: Layer-wise population distributions of confined water molecules containing a certain number of H-bonds $P(N_{HB}/water)$ are shown as a function of number of H-bonds per water molecule ($N_{HB}/water$), and compared with the corresponding results for the bulk water.

2.3.2 Dynamics

2.3.2.1 Mean-Squared Displacements (MSDs) and Translational Mobilities: 'Over-all' and Layer-wise

The 'over-all' and layer-wise (representative) centre of mass MSDs for confined water molecules in these AOT and IGEPAL RMs are presented in the upper panels of Figure 2.6. MSDs for other layers are provided in Figure 2.A.11 of Appendix 2.A. The same for bulk SPC/E water is also shown in the same figure for comparison. Note the 'over-all' MSDs in these RMs, though indicate mobilities much slower than that in bulk, are not too different from each other. As reported earlier[12,47,68] translational mobility increases gradually as one moves away from the interface toward the central layer. Water molecules residing near the interface are drastically slowed down for both types of these RMs; these interfacial water molecules move only ~ 0.5σ ($\sigma = 2.75$ Å) even after a duration of 100 ps. The near-independence of the MSDs on time for the interfacial water molecules resembles to "rattling-in-a-cage" motion[69–71] and in these RMs a strong interaction between the interface and water molecules is responsible for not allowing the stochastic Brownian (diffusive) motion to set in even long after the inertial timescale. Interestingly, water molecules in the central core region also move only ~ 1.5σ within the same time-span, and the mobility of these core water molecules are approximately an order of magnitude slower than that for the bulk water. This is contrary to what is expected[20] from the core-shell model for such large reverse micellar aqueous pools. Before exploring the motional features further, we examine how diffusive are these layer-wise centre-of-mass mobilities and whether the diffusive limit is achieved at a long time. It is known that for MSDs,[72,73]

$\langle \Delta r^2(t) \rangle = N^{-1} \left\langle \sum_{i=1}^{N} (\boldsymbol{r_i}(t) - \boldsymbol{r_i}(0))^2 \right\rangle = At^{\beta}$, at long time $\beta = 1$ corresponds to the diffusive limit while β < 1 to the sub-diffusive in the intermediate timescale and $\beta = 2$ to the free inertial motion at short times. The time profile for β could be obtained as follows,

$$\beta(t) = \frac{d}{d[ln(t)]} [ln\langle \Delta r^2(t) \rangle] \qquad (2.3)$$

The time dependence of β obtained via Eq. 2.3 from the simulated MSDs is presented in the lower panels (Figure 2.6) for the 'over-all' MSDs, and for a few selected layers. $\beta(t)$ for all layers in these RMs are shown in Figure 2.A.12 of Appendix 2.A.

These data clearly show that none of these MSDs in RMs have reached the hydrodynamic limit (β =1) at long time. Interestingly, over-all MSDs for water molecules in these RMs have not achieved the hydrodynamic limit and settle to β ~0.8 at long time. As expected, interfacial water molecules are the most affected ones, and the near constancy of the relevant MSDs with time leads to β =0 at long time. This suggests that the motional features associated with the interfacial water molecules are qualitatively different from those in other layers. In addition, the inability of the MSDs of confined water to attain the hydrodynamic behaviour at long time renders determination of translational diffusion coefficient (D_T) from Einstein's relation[73] untenable.

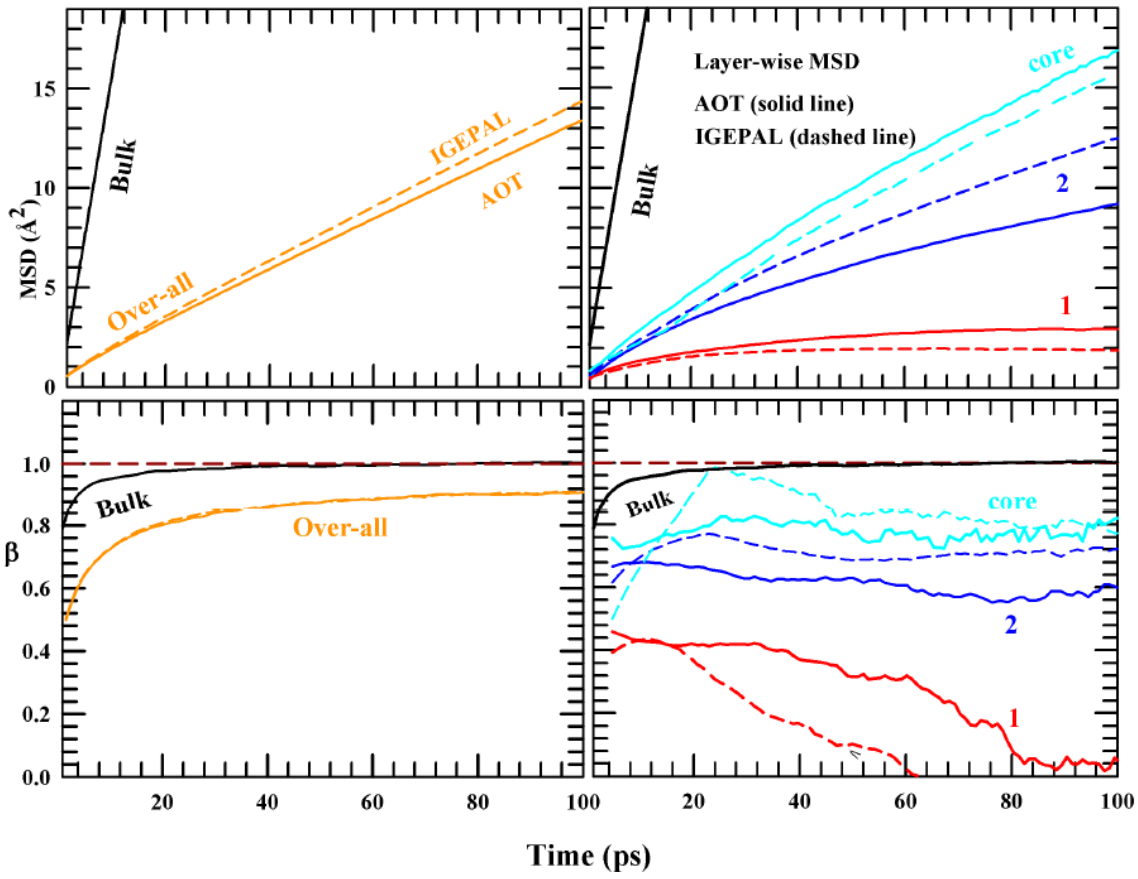

Figure 2.6: Centre-of-mass mean square displacements (MSD) for water molecules confined inside the AOT and the IGEPAL RMs, in the bulk, and in different imaginary layers are shown in the upper panels. Results for the first two layers and the core are presented here for clarity. The time dependent changes in the exponent (β) associated with these MSDs calculated from the relation, MSD$\propto t^{\beta}$ are shown in the lower panels.

2.3.2.2 Velocity autocorrelation function: Origin of difference in mobilities

We next simulate the 'over-all' and layer-wise velocity autocorrelation function (VACF) to explore the feasibility of applying the Green-Kubo relation for estimating D_T of water in these RMs. The Green-Kubo expression[73] is a macro-micro relation that connects the experimentally measurable D_T to the time-dependent velocity, $\boldsymbol{v}(t)$, of each individual moving particle of mass m:

$$D_T = \frac{k_B T}{m} \int_o^\infty dt\, C_v^N(t) \qquad (2.4)$$

where $C_v^N(t)$ denotes the normalized VACF and is given by, $C_v^N(t) = \frac{\langle \boldsymbol{v}(t).\boldsymbol{v}(0)\rangle}{\langle \boldsymbol{v}(0).\boldsymbol{v}(0)\rangle}$ and $k_B T$ is the Boltzmann constant times the absolute temperature.

Although the application of the Green-Kubo relation is not straight forward for obtaining diffusion coefficients for particles in restricted geometries[34,74], one can still use this relation to obtain a qualitative comparison of diffusivities between the bulk and confined water molecules in these RMs. Figure 2.7 presents a comparison of the simulated $C_v^N(t)$ between the bulk and confined water molecules ('over-all'), and those between water molecules in the bulk and in different layers of these RMs. The upper panel clearly demonstrates that the 'over-all' VACFs in both the RMs are quite different from that for the bulk in that the RM VACFs enters into the negative region much earlier (<100 fs) and stays longer to scan negative regions larger than that for the bulk. This difference provides a dynamical support in favour of partial disruption of H-bond network of water upon confinement and corroborates well with the simulated tetrahedral order parameter for water in these RMs presented earlier. In addition, VACF for the RMs reflects a difference (though small) between the charged and neutral interfaces. Inset of the upper panel shows this difference more clearly. The more negative region associated with the VACFs suggests[75] severely restricted mobilities for water molecules in these RMs.

Layer-wise VACFs presented in the lower panel suggest that the negative region decreases as one moves from the interfacial layer to the core, although the VACF for core water molecules remain much different from that for the bulk. Areas under these layer-wise simulated VACFs are summarized in Table 2.B.6 (Appendix 2.B) and their ratios against that for bulk provided. For water molecules in the AOT interface, the area under the VACF is negative and this

suggests more rattling than centre-of-mass translation for these interfacial water molecules. Area ratios provided in Table 2.B.6 (Appendix 2.B) indicate that the mobilities in different layers of these RMs are not only severely slowed down compared to that in the bulk but they (layer-wise mobilities) also differ considerably between the neutral and charged RMs. These layer-wise slowing down of mobilities is qualitatively similar to that found for water encapsulated inside TiO_2 nanopores[10]. Normalized VACF for waters in all the layers of the AOT and IGEPAL RMs are provided in Figure 2.A.13 of Appendix 2.A to show that the simulated layer-wise VACFs cannot be segregated into two different sets, allowing a description in terms of core and shell water molecules. More importantly, these VACFs and the area ratios clearly indicate the presence of diverse timescales and thus temporal heterogeneity in these confined systems.

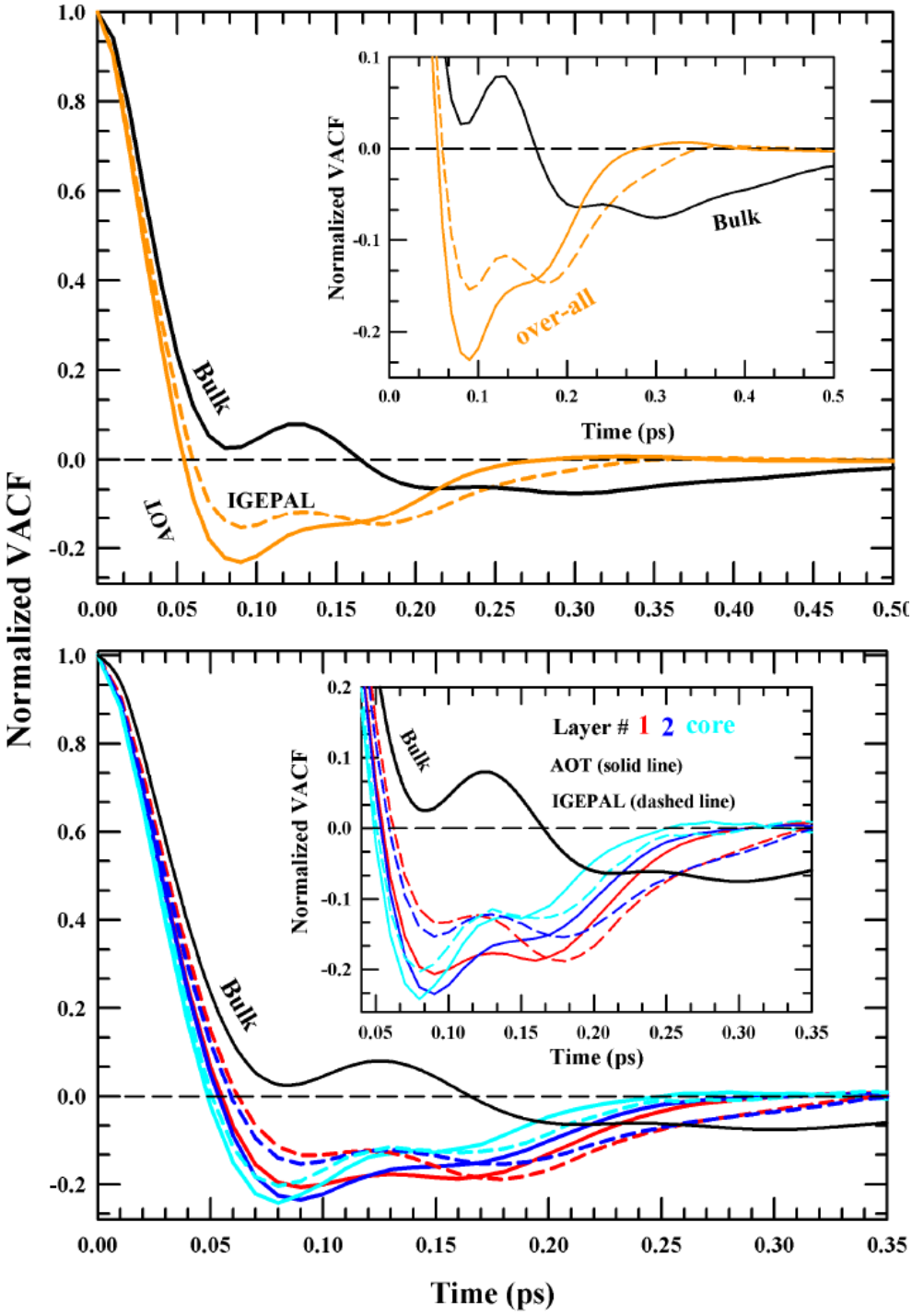

Figure 2.7: Normalized velocity autocorrelation functions (VACF) of bulk water and 'over-all' for confined water are shown in the upper panel. The lower panel provides the layer-wise VACFs and compares with that for the bulk. Both the insets present VACFs after zooming on the negative amplitudes to clearly show the impact of the chemical nature of the interfaces.

2.3.2.3 Dynamic Heterogeneity (DH): Non-Gaussian features and slow timescales

Simulated layer-wise MSDs and VACFs have clearly indicated that water molecules confined in these RMs are quite different from those in the bulk, and their motional features are associated with diverse timescales. These timescales in dynamically heterogeneous systems are connected to the deviations of particle displacement distribution from being Gaussian. This non-Gaussian (NG) feature is often monitored via the NG parameter defined as[76,77]

$$\alpha_2(t) = \frac{3\langle \Delta r^4(t)\rangle}{5\langle \Delta r^2(t)\rangle^2} - 1 \qquad (2.5)$$

where, $\langle \Delta r^4(t)\rangle = \langle [\Delta r^2(t)]^2\rangle$, $where\ \Delta r^2(t) = [\Delta \boldsymbol{r}_i(0,t).\Delta \boldsymbol{r}_i(0,t)]$,
and $\Delta \boldsymbol{r_i}(0,t) = \boldsymbol{r}_i(t) - \boldsymbol{r}_i(0)$.

Generally, $\alpha_2(t)$ shows a non-monotonic dependence on time, and a peak value greater than 0.2 for $\alpha_2(t)$ is considered as a signature of dynamic heterogeneity (DH) with peak-time as the DH timescale[78] for a given system. Note this DH peak time, denoted as τ_{NG} , originates from those particle displacements which are larger than what would have been for Gaussian distribution for a homogeneous system. Displacements smaller than those from a Gaussian distribution also contributes to the DH of a system and this is quantified by the new non-Gaussian parameter (NNG), $\gamma(t)$, as follows[76],

$$\gamma(t) = \frac{1}{3}\langle \Delta r^2(t)\rangle \left\langle \left[\frac{1}{\Delta r(t)}\right]^2 \right\rangle - 1 \qquad (2.6)$$

where, $\left\langle \left[\frac{1}{\Delta r(t)}\right]^2 \right\rangle = \left\langle \frac{1}{N}\sum_{i=1}^{N} \frac{1}{|\Delta r_i(0,t)|^2} \right\rangle$ provides the weightage to the smaller displacements to dominate $\gamma(t)$ and produce a peak timescale (τ_{NNG}) much longer than τ_{NG}. It is important to note here that, $\left\langle \left[\frac{1}{\Delta r(t)}\right]^2 \right\rangle \neq [\langle \Delta r^2(t)\rangle]^{-1}$.

Figure 2.8 (left panel) presents 'over-all' and layer-wise comparison of $\alpha_2(t)$ for water molecules confined in both type of RMs. A comparison with the bulk in the upper panel clearly indicates that, $\alpha_2(t)$ for the confined water in these RMs depict not only strong heterogeneous

dynamics but also significantly slowed down τ_{NG}. A comparison of $\alpha_2(t)$ among layers (lower panel) reveals a dramatic lengthening of τ_{NG} for the interfacial water molecules, pushing the DH timescale into the nanosecond regime. Interestingly, the core water is dynamically more heterogeneous than bulk where τ_{NG} is approximately 5 times slower than that for the latter (~4 ps versus ~0.8 ps). As expected, water molecules in the interfacial layer (layer #1) of both the charged and neutral RMs are the most heterogeneous in nature, both producing DH timescales τ_{NG} in nanoseconds. Figure 2.8 (right panel) presents a comparison of the new non-Gaussian DH parameter ($\gamma(t)$) between the water molecules confined in these RMs and bulk (right upper panel), and that between the RMs for different layers (right lower panel). The inset in the right upper panel demonstrates the striking difference in $\gamma(t)$ between the bulk and the confined water with τ_{NNG} approximately three orders of magnitude slower in these confinements than in the bulk. Note in this panel that $\gamma(t)$ senses the chemical nature of the confining interfaces (charged or neutral) with τ_{NNG} approximately twice as long for water molecules inside the charged (AOT) RM as that for those inside the neutral one. In the layer-wise comparison shown in the lower panel, the simulated $\gamma(t)$ suggests that water molecules in each layer inside the charged RM are dynamically more heterogeneous than those inside the neutral one. The peak-times (τ_{NNG}) associated with each of these layers for these RMs are summarized in Table 2.B.7 (Appendix 2.B) which reflects this DH difference quantitatively. Interestingly, τ_{NNG} for core water in the RMs are at least an order of magnitude longer than that for bulk (~10 ps *versus* ~1 ps), which suggests that the core-shell model breaks down even for larger RMs where water molecules even in the central core layer do not possess bulk-like displacement distributions.

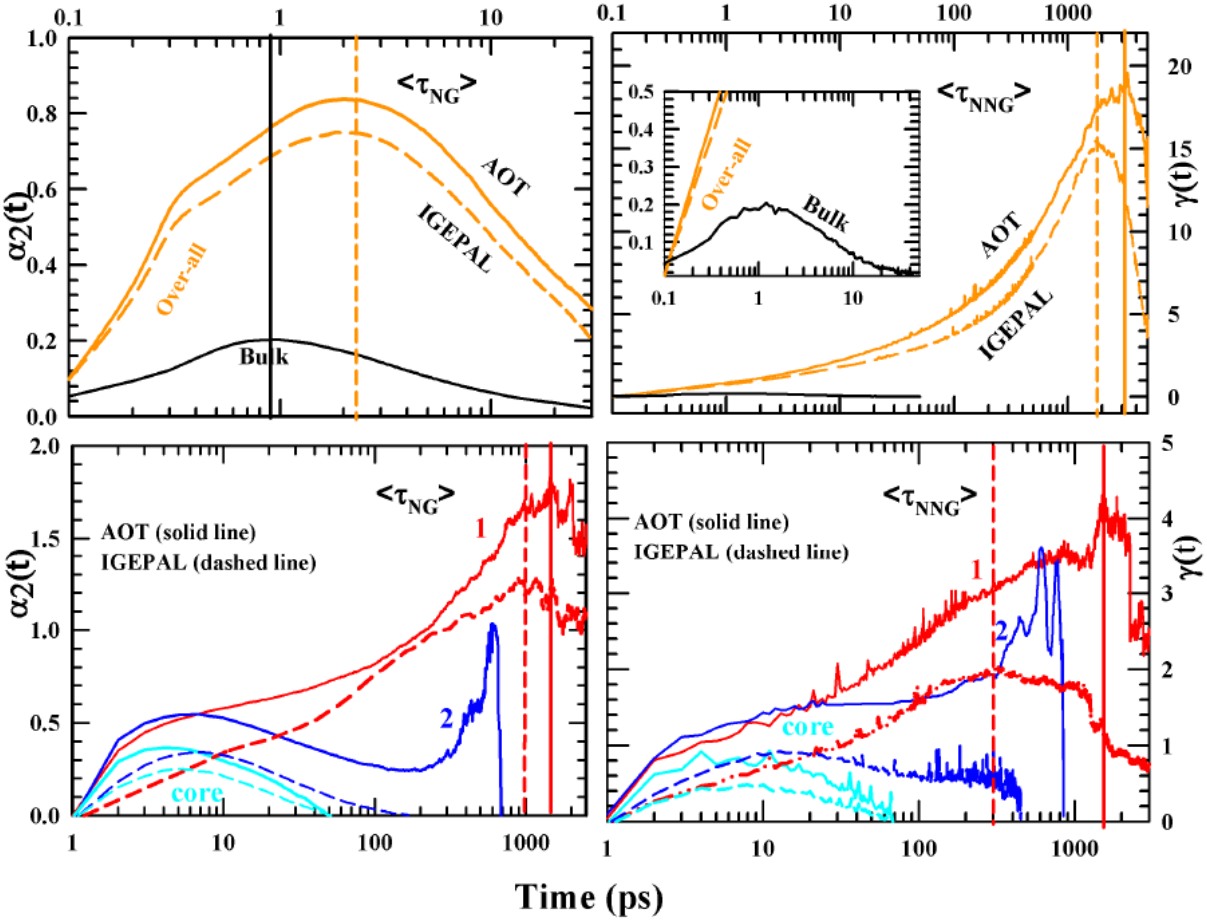

Figure 2.8: Comparison among NG parameter (left panels) and NNG parameter (right panels) for bulk water, for over-all confined water, and for water at different layers (layers 1, 2 and core) of the aqueous pool inside AOT and IGEPAL RMs. Inset shows a comparison of the NNG parameter between the bulk and over-all confined water.

2.3.2.4 Single-particle displacement distributions: Bimodality, translational jumps and common displacements across layers

The simulated time dependences of $\alpha_2(t)$ and $\gamma(t)$ have already suggested that the translational dynamics of these encapsulated water molecules are strongly temporally heterogeneous, and the origin of this heterogeneity lies in the centre-of-mass displacements that are both larger and smaller than the lengthscales covered in a Gaussian displacement distribution for a homogeneous liquid system. The distribution for the single-particle displacements, δr, can be obtained from the self-part of the van Hove correlation function, $G_s(\delta r; t)$ [76–79] as follows

$$P[log_{10}(\delta r); t] = ln(10)4\pi(\delta r)^3 G_s(\delta r; t) \quad (2.7)$$

with $\delta r(t) = N^{-1}\sum_i^N(\boldsymbol{r}_i(t) - \boldsymbol{r}_i(0))$. For $G_s(\delta r; t)$ that samples δr from a Gaussian distribution, $P[log_{10}(\delta r); t]$ becomes independent of time with a peak height ~ 2.13.[76] Deviations from this height suggest non-Gaussian displacement distribution where heterogeneity in dynamics arises from the fluctuations in local particle mobility. Figure 2.9 shows a comparison of $P[log_{10}(\delta r); t]$ between the bulk water and confined water molecules in these RMs for two DH timescales, τ_{NG} (upper panels) and τ_{NNG} (lower panels). Several interesting features are reflected from this comparison. First, the 'over-all' displacement distribution at $t = \tau_{NG}$ for confined water in these RMs lies significantly shifted toward shorter length scales than that for the bulk water, although the peak-heights are similar and ~2.13. However, the 'over-all' distributions are wider than the bulk distribution, suggesting heterogeneity in the displacement distributions for the confined water. These 'over-all' distributions peak at ~0.2σ with nearly no difference between the RMs, whereas that for the bulk crosses the 'over-all' distribution at ~0.3σ and peaks at ~0.5σ. This crossing of the 'over-all' distributions and the resultant overlap with that for the bulk provides visual proof for the conjecture that 'over-all' confined water can show not only dynamics that are different from the bulk but also those that are similar to the bulk. This provides a microscopic explanation for the observation of both bulk-like and slower-than-bulk dynamics in experiments where the measured signal is dominated by the collective response of the system.[1,18,39,80,81] The comparison of the layer-wise distributions between the AOT and IGEPAL RMs at this timescale ($t = \tau_{NG}$) is even more interesting. The core layer distributions, reflecting no difference between the RMs, represent displacements ranging between approximately one-

tenth of a water diameter to a full diameter with a peak at ~0.3σ. The distributions for the first two layers show the difference between (see also Figure 2.A.14 of Appendix 2.A for layer-distributions not shown here) the chemical nature of the interface. Interestingly, the distributions for water in these first two layers, particularly for the AOT RM, are distinctly different from other layers as they show multi-peak structures; water molecules in these layers execute displacements both shorter and longer than those accessed in the bulk. The multi-peak structure is however less prominent for water inside IGEPAL RM, and the peak at the longer displacement wing softens into an asymmetrically broadened tail for the second layer of IGEPAL RM. Strikingly, $P[log_{10}(\delta r); t]$ for the AOT second layer is dominated by the longer displacements and here the displacements are as large as $\sim 3\sigma$. We speculate that this might be linked to the additional freedom of those confined water molecules that were involved in the bound-to-free dynamic equilibrium with the charged interface and entering into the second layer immediately after getting released. This large lengthscale displacements, in fact, become a signature for confined water at longer times, for example, at $t = \tau_{NNG}$. This is demonstrated in the left lower panel of this figure where large displacements ranging between ~σ and ~ 10σ characterizes the 'over-all' distributions for RM. The origin of such large displacements can be traced to the layer-wise $P[log_{10}(\delta r); t]$ at $t = \tau_{NNG}$, shown in the right-lower panel where multi-peak structure for the distributions appear again for water molecules in the first two layers inside the AOT RM. Interestingly, $P[log_{10}(\delta r); t]$ for core water molecules suggest displacements at this timescale for both the RMs in the similar range as that for bulk water ($0.05\sigma \leq \delta r \leq 1.3\sigma$). Such a range of displacements for core water molecules further reinforces the microscopic explanation provided earlier for the observation of both bulk-like and much slower dynamics in experiments that measure the collective response of aqueous pools confined in RMs. Figure 2.9 demonstrates a significant overlap among the layer-wise displacement distributions which strongly suggests that dynamically confined water molecules cannot be divided into two different classes of water. This is another finding that signals inadequacy of the core-shell model for describing the relaxation dynamics of reverse micellar water.

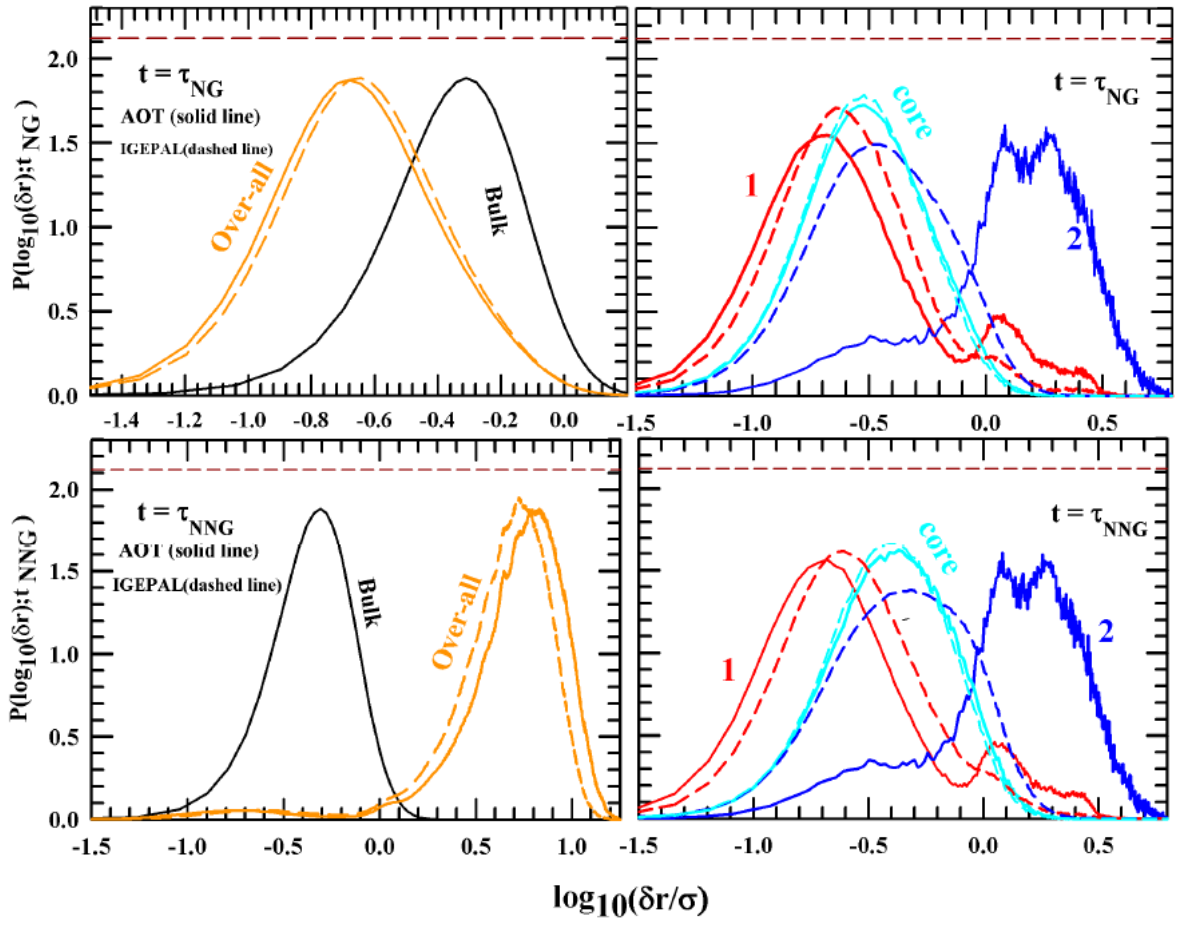

Figure 2.9: Layer-wise single-particle displacement distributions at the NG peak times (upper panels), and at the NNG peak times (lower panels). Results for bulk water are also shown for comparison.

2.3.2.5 Dynamic susceptibility of confined water in different layers: Long temporal correlations, and overlap across layers

Next, we explored the temporal correlations among water molecules in different layers of the aqueous pools inside the RMs. This was performed by simulating the dynamic susceptibility $\chi_4(k,t)$ in the limit of the nearest neighbour wave-vector, $k\sigma \rightarrow 2\pi$ via calculating the variance of the fluctuations of the self-intermediate scattering function, $F_s(k,t)$. The following expression was used for the calculations of $\chi_4(k,t)$,[82–84]

$$\chi_4(k,t) = N[\langle F_s(k,t)^2\rangle - \langle F_s(k,t)\rangle^2] \qquad (2.8)$$

where, $F_s(k,t) = N^{-1}\sum_i^N \langle cos\, k\,.\,[r_i(t) - r_i(0)]\rangle$. The timescale corresponding to the peak of $\chi_4(k,t)$ is considered as the longest time-duration (t_4^{max}) over which density fluctuations at two different space points remain correlated. A comparison between the 'over-all' dynamic susceptibilities for confined water in these RMs and bulk water Figure 2.10 (upper panel) clearly shows that the dynamical correlation for confined water is considerably stronger than that for bulk water. Notice the value of t_4^{max} is ~50 times longer for confined water (~70 ps) than that for bulk water (~1.5 ps). As expected, the layer-wise calculations of $\chi_4(k,t)$, shown in the lower panels, indicate lengthening of the t_4^{max} as one moves away from the core layer toward the interface. The timescales associated with the maximum correlation in different layers, summarized in Table 2.3, suggest correlated density fluctuations in these layers occurring over a timescale ranging from ~200 ps to ~2 ns. This means that the temporal correlations for the nearest neighbour dynamics for water molecules in these layers persist for a duration ~100-1000 times longer than that for bulk water. A close inspection of these layer-wise $\chi_4(k,t)$ also, show that the faster wing of the $\chi_4(k,t)$ of other layers overlap with that for the core layer (see Figure 2.A.15 of Appendix 2.A for $\chi_4(k,t)$ of all layers of AOT and IGEPAL RM), suggesting correlated mobility fluctuations across the layers bear some extent of commonality. This provides further support to the view that the confined water inside these RMs cannot be described in terms of bound and free water as envisaged in the core-shell model.

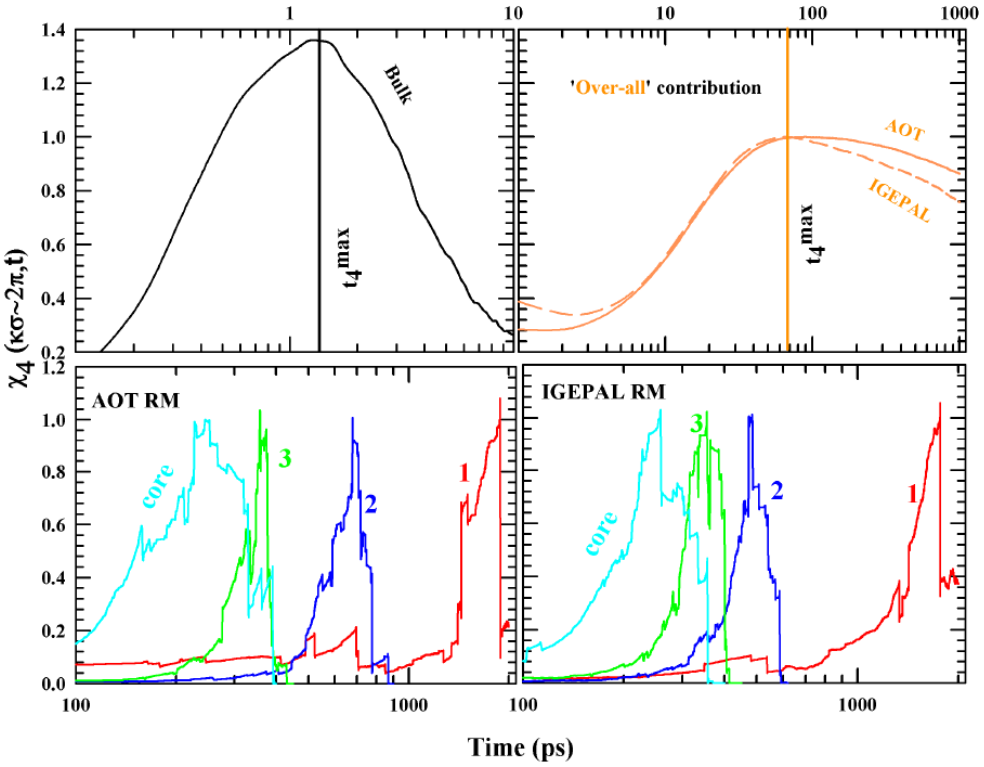

Figure 2.10: Dynamic susceptibilities for bulk water (upper left), confined water (upper right), layer-wise comparison for water confined in AOT RM (lower left) and the same for water confined in IGEPAL RM (lower right).

Table 2.3: Timescales corresponding to the maxima of the simulated layer-wise and over-all dynamic susceptibilities (t_4^{max}) for water molecules confined in these RMs. The same for the bulk water is also reported.

Layer #	**AOT RM** (t_4^{max})**/ps**	**IGEPAL RM** (t_4^{max})**/ps**	**Bulk** (t_4^{max})**/ps**
1	1885	1765	1.5
2	678	473	
3	367	354	
4	390	380	
Core	250	250	
over-all	70	70	

2.3.2.6 Collective single particle -reorientation relaxations: Agreement with experiments

Collective single particle reorientational relaxation of dipolar molecules are often monitored via the reorientational time correlation function (RTCF)[72,73].

$$C_\ell(t) = \frac{\langle P_\ell[\boldsymbol{u_i}(t).\boldsymbol{u_i}(0)]\rangle}{\langle P_\ell[\boldsymbol{u_i}(0).\boldsymbol{u_i}(0)]\rangle} \qquad (2.9)$$

where, P_ℓ denotes the Legendre polynomial of rank l and $\boldsymbol{u}_i$ a unit vector parallel to the water dipole axis.

Simulated RTCFs for $\ell = 1$, $C_1(t)$, for water molecules in both the RMs are shown in the upper panels of Figure 2.11. Simulated decays for $\ell = 2$ are shown in the lower panels. $C_1(t)$ and $C_2(t)$ decays for bulk water are also presented in these panels for comparison. The following is the general observation on these reorientational relaxations and their comparison with those for bulk water. The RTCF decays for the confined aqueous pool are considerably slower than those for the bulk. In addition, the reorientational relaxation is the slowest for water molecules in the interfacial layer for both the RMs and becomes progressively faster as the core is approached. The 'over-all' reorientational relaxations are the fastest among those simulated for the confined water, although the decay rates are much slower than their corresponding counter-parts for the bulk water. Note that these simulated $C_\ell(t)$ decays for both bulk and confined water require a sum of three exponentials for adequate description. The corresponding fit parameters are summarized in Tables 2.4 and 2.5, and the adequacy of this fit function is demonstrated via a representative figure (see Figure 2.A.16 of Appendix 2.A).

For $C_1(t)$ decays, these fits indicate relaxation timescales in the sub-picosecond, sub-10 ps and sub-100 ps regime and domination of the slowest component (~60-80% of the total amplitude). The slowest of these three relaxation time constants is ~5-20 times slower for water confined in these RMs than the corresponding one for bulk. This is expected as we have already noticed the confinement-induced slowing down of translational dynamics of water molecules and the impact of the interface. What is striking here is the presence of the faster-than-bulk timescales that characterize the initial component of all the $C_1(t)$ decays for confined water. This is demonstrated in the upper panels of Figure 2.A.17 (Appendix 2.A) where the simulated decays

for the first 0.4 ps are compared. This faster-than-bulk relaxation has been already reported in experiments[85] and model simulation[16] and attributed to the partial disruption of the tetrahedral H-bond network of bulk water upon confinement. The layer-wise and 'over-all' tetrahedral order parameter and H-bond population distribution shown earlier respectively in Figures 2.4 and 2.5 strongly support this view.

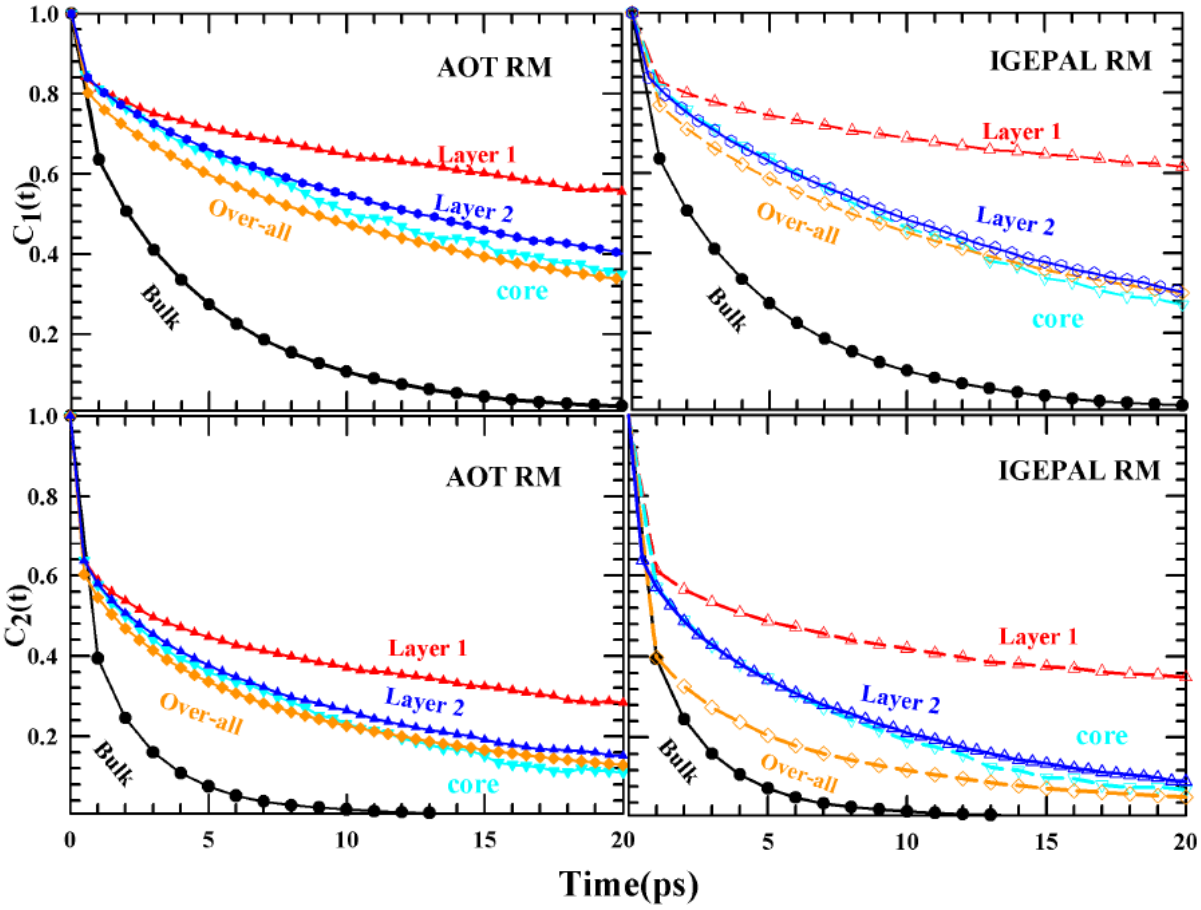

Figure 2.11: Layer-wise reorientational correlation function ($C_\ell\,(t)$) for water confined in both the AOT (left panel) and IGEPAL RMs (right panel). The same for bulk water is also shown in order to facilitate the comparison.

Table 2.4: Tri-exponential fit parameters for the simulated reorientational correlation function of rank 1, $C_1(t)$, of water molecules in different layers under the charged (AOT) and neutral (IGEPAL) confinements. Layer # 1 is the interfacial layer. Tri-exponential fit parameters for bulk water are also shown.

Layer #	**Width (Å)**	a_1	τ_1 **(ps)**	a_2	τ_2 **(ps)**	a_3	τ_3 **(ps)**	$\langle\tau\rangle_{\ell=1}$ **(ps)**
AOT RM								
1	**27.5-22.5**	0.13	0.025	0.11	1.87	0.76	61.35	48.15
2	**22.5-17.5**	0.12	0.05	0.14	3.24	0.73	32.57	24.34
3	**17.5-12.5**	0.13	0.06	0.18	4.31	0.69	25.77	18.67
4	**12.5-7.5**	0.13	0.1	0.27	7.6	0.60	27.40	18.38
core	**7.5-0**	0.14	0.1	0.31	7.77	0.55	38.61	23.70
over-all	**27.5 - 0**	0.15	0.025	0.19	3.32	0.67	29.33	19.97
Bulk water								
Tri-exponential fit		0.18	0.07	0.16	1.54	0.67	5.46	3.9
IGEPAL RM								
1	**27.5-22.5**	0.13	0.043	0.11	3.12	0.76	91.74	70.16
2	**22.5-17.5**	0.11	0.045	0.10	2.17	0.79	20.7	16.49
3	**17.5-12.5**	0.12	0.060	0.13	3.20	0.75	21.19	16.24
4	**12.5-7.5**	0.11	0.044	0.12	2.57	0.77	21.14	16.69
core	**7.5-0**	0.08	0.018	0.06	0.48	0.85	16.58	14.18
over-all	**27.5 - 0**	0.15	0.030	0.18	3.24	0.67	24.1	16.76

Table 2.5: Tri-exponential fit parameters for the simulated reorientational correlation function of rank 2, $C_2(t)$, of water molecules in different layers under the charged (AOT) and neutral (IGEPAL) confinements. Layer # 1 is the interfacial layer. Tri-exponential fit parameters for bulk water are also shown.

Layer #	Width (Å)	a_1	τ_1 (ps)	a_2	τ_2 (ps)	a_3	τ_3 (ps)	$\langle\tau\rangle_{\ell=2}$ (ps)
AOT RM								
1	**27.5-22.5**	0.3	0.024	0.19	1.7	0.5	33.45	18.22
2	**22.5-17.5**	0.3	0.034	0.23	2.07	0.48	16.64	8.4
3	**17.5-12.5**	0.3	0.037	0.22	2.11	0.47	12.27	6.3
4	**12.5-7.5**	0.29	0.036	0.22	2.088	0.49	11.6	5.95
core	**7.5-0**	0.26	0.022	0.18	0.91	0.56	11.4	6.6
over-all	**27.5 - 0**	0.33	0.020	0.26	2.22	0.41	16.61	7.43
Bulk water								
Tri-exponential fit		0.31	0.06	0.5	1.45	0.19	4.32	1.55
IGEPAL RM								
1	**27.5-22.5**	0.31	0.04	0.18	2.52	0.51	50	25.88
2	**22.5-17.5**	0.27	0.027	0.2	1.3	0.53	11.03	6.13
3	**17.5-12.5**	0.28	0.032	0.21	1.54	0.51	10.56	5.7
4	**12.5-7.5**	0.28	0.04	0.24	2.16	0.48	11.26	5.9
core	**7.5-0**	0.24	0.02	0.16	0.62	0.61	8.74	5.4
over-all	**27.5 - 0**	0.48	0.009	0.23	2.1	0.29	11.34	3.72

When the $C_2(t)$ decays are compared, similar observation appears; faster-than-bulk relaxation component, now more prominent than in $C_1(t)$ decays, appear for all of them. This is then followed by two slower components, one with the time constant of a few picoseconds and the other with a time constant of approximately ten picosecond or a few tens of picoseconds. This slowest component, as for the $C_1(t)$ decays, dominates the relaxation, and the associated timescale is ~2-12 times slower than that for the bulk. Note here that the layer-wise $C_1(t)$ and $C_2(t)$ decays are slower in each of the layers of the confined aqueous pool inside the AOT RM than those for the pool inside the IGEPAL RM, except for the interfacial layer where the reverse is observed. Slower reorientational relaxations for water inside the AOT RM than for water inside the IGEPAL RM can be understood in terms of the chemical nature of the confining interfaces. The relatively slower relaxation for the interfacial layer of IGEPAL RM is probably connected to the trapping of water inside the clefts created by the polyethylene oxide units of IGEPAL molecules that intruded inside the RM cavity (see Figures 2.A.1 and 2.A.2 of Appendix 2.A). This extra slowing down of water at the IGEPAL interface has already been observed both in experiments and simulations that followed the rotational relaxation of a large dye molecule inside these aqueous RMs[68].

We would like to mention here that the existing 2D-IR and time-resolved fluorescence measurements suggest that the timescale of reorientational relaxation of interfacial water molecules for both the charged and the neutral RMs is nearly the same (15-20 ps)[24,39]. This may appear contrasting to the present simulation observation where we find reorientation of water molecules near the charged interface is different from that for water near the neutral interface. We argue that those measurements included contributions from waters residing both at the interfacial layer and in the layer adjacent to it. This we have shown by simulating $C_2(t)$ of water for an interfacial layer of width 10 Å for both the RMs. These decays and the corresponding fits are shown in Figure 2.A.18 (Appendix 2.A), with fit parameters summarized in Table 2.B.8 (Appendix 2.B). The results are quite fascinating. We find that the longest timescale for IGEPAL interfacial layer is ~11 ps, while that for the charged interface is ~15 ps. These timescales and the dependence on the nature of the interface agree quite well to those reported by ultrafast IR and 2D-IR measurements.[24,39]

2.4 Conclusion

In summary, the core-shell model of reverse micellar water has been examined thoroughly in the present study through the simulations of a number of structural and dynamical properties for water molecules in different (but fictitious) layers, and for all encapsulated water molecules together ('over-all'). Two chemically different surfactant molecules (charged and neutral) were considered to construct model spherical RMs in which counter ions were dispersed along with the interface inside the RM cavity. The present simulation results reflect substantial structural and dynamic heterogeneities for the confined water, and severe frustration in satisfying the appropriate number of H-bonds allowed for bulk water. Structural features such as dipole orientation, tetrahedral order parameter, and H-bonded populations deviate significantly from those for the bulk, the deviation being the most pronounced for the interfacial water. Water dipole orientation within AOT RM predicted in the present study corroborates well with the polarisation sensitive vibrational sum frequency generation (VSFG) measurements of charged interfacial water.[31,61,62] Similar VSFG study with aqueous IGEPAL RMs would therefore be interesting and worth pursuing. Interestingly, the core water never resembles those of bulk, and remain different bearing the impact of confinement. Centre-of-mass mobilities are dramatically slowed down for the interfacial molecules which, on moving toward the centre of the pool, become faster but not achieving quite the bulk value. Dynamic heterogeneity signatures are the strongest for the interfacial water molecules, and even the core water molecules show significantly different DH features from those for bulk. Single-particle displacement distributions suggest a significant overlap of displacement sizes accessed by the water molecules in different layers and those in the core. The impact of this overlap is reflected in the simulated four-point correlations where dynamic susceptibilities exhibit sharing of correlated timescales across the layers.

All these results clearly demonstrate the inability of separating out the confined water properties as a weighted average of those of two distinct populations, one that is more bulk-like (free water) and the other being slower and much deviated from bulk (bound water). The applicability of this simple two-state model is also examined by varying the chemical nature of the surfactant molecules that were used to construct the reverse micelles, but the observation remained the same. However, some simulated features, particularly those for the interfacial

molecules, showed the moderate influence of the chemical nature (charged or neutral) of the surfactant employed. Simulated single particle reorientational relaxations of water dipoles showed a good agreement with measurements via time-resolved 2D-IR experiments.[39]

The present work has the following limitations. First, a non-polarizable model has been employed to represent the real water molecules. Second, the constructed RMs are forced to remain spherical during simulations by not allowing any breathing mode. Third, no geometric irregularities have been considered while constructing the inner surface of the model RMs which precluded any heterogeneity arising from the structural anomaly. The break-down of the core-shell model for RM water should, therefore, be considered as an observation for the present model, although this model has been employed earlier by many authors to address several interesting experimental findings.[13,47] It is satisfactory to note that the present model has been able to successfully predict the average anisotropy timescales of reverse micellar water measured via femtosecond 2D-IR experiments.[39] The central result of this study is, therefore, the observation of the break-down of the celebrated core-shell model for confined water even in the limit of large reverse micelles.

Appendix 2.A

AOT RM

(a)

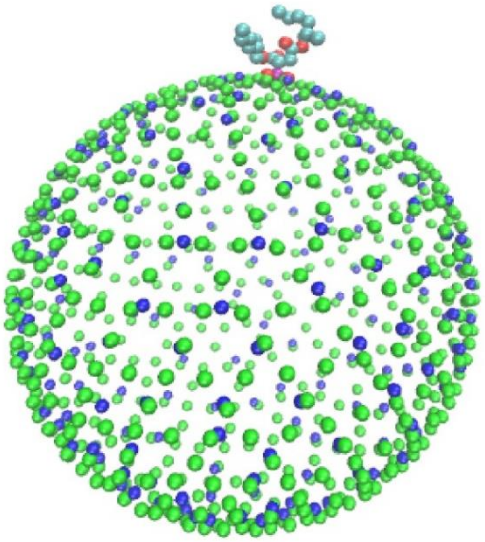

(c)

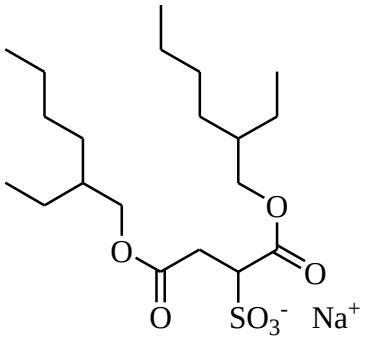

(b)

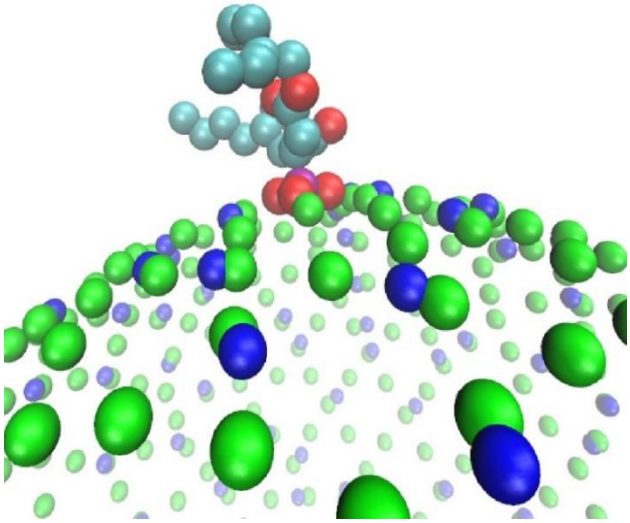

Figure 2.A.1: (a) Snapshot of an **AOT** molecule and the rigid RM interface. Green represents rigid repulsive atoms used for structural stability of RM, Blue represents **Na^+**, Red – Oxygen, Cyan- Carbon and purple – Sulphur atom of an AOT molecule.

(b) Zoomed side-view of (a). This view enables us to show that **SO_3^-** units and **Na^+** ions are on (not inside) the smooth rigid surface formed by the repulsive potential (green entity).

(c) Representative AOT molecule.

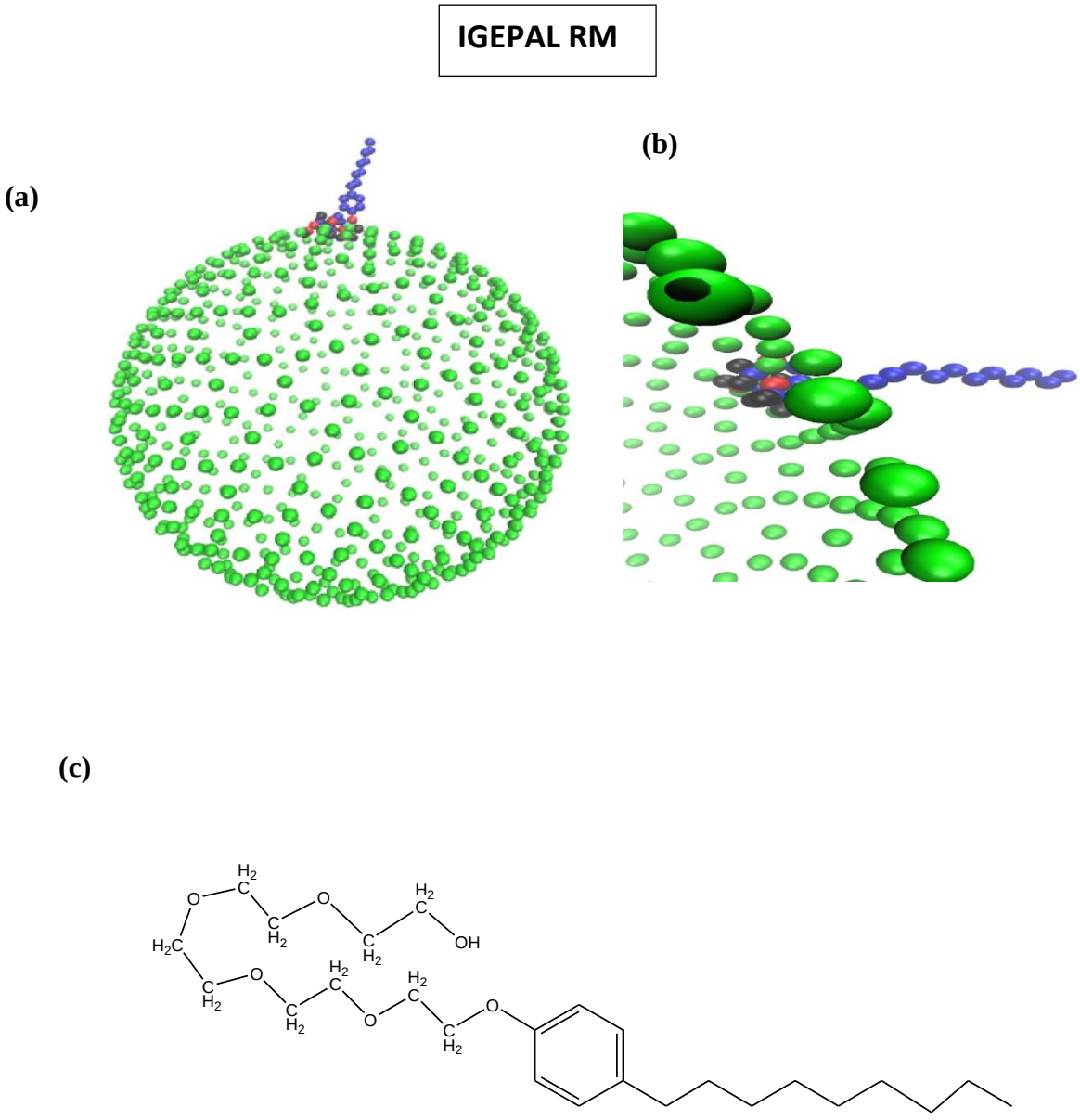

Figure 2.A.2: (a)Snapshot of one neutral IGEPAL molecule and the rigid RM interface. Green represents rigid repulsive atoms used for structural stability of RM, blue represents the carbon atom, red – oxygen, black –hydrogen atoms of IGEPAL.

(b) Zoomed side-view of (a). This view enables us to show the protruding CH_2 units (denoted by blue and black atoms) of IGEPAL surfactant inside the rigid cavity (green atomic surface).

(c) Atomic representation of IGEPAL molecule.

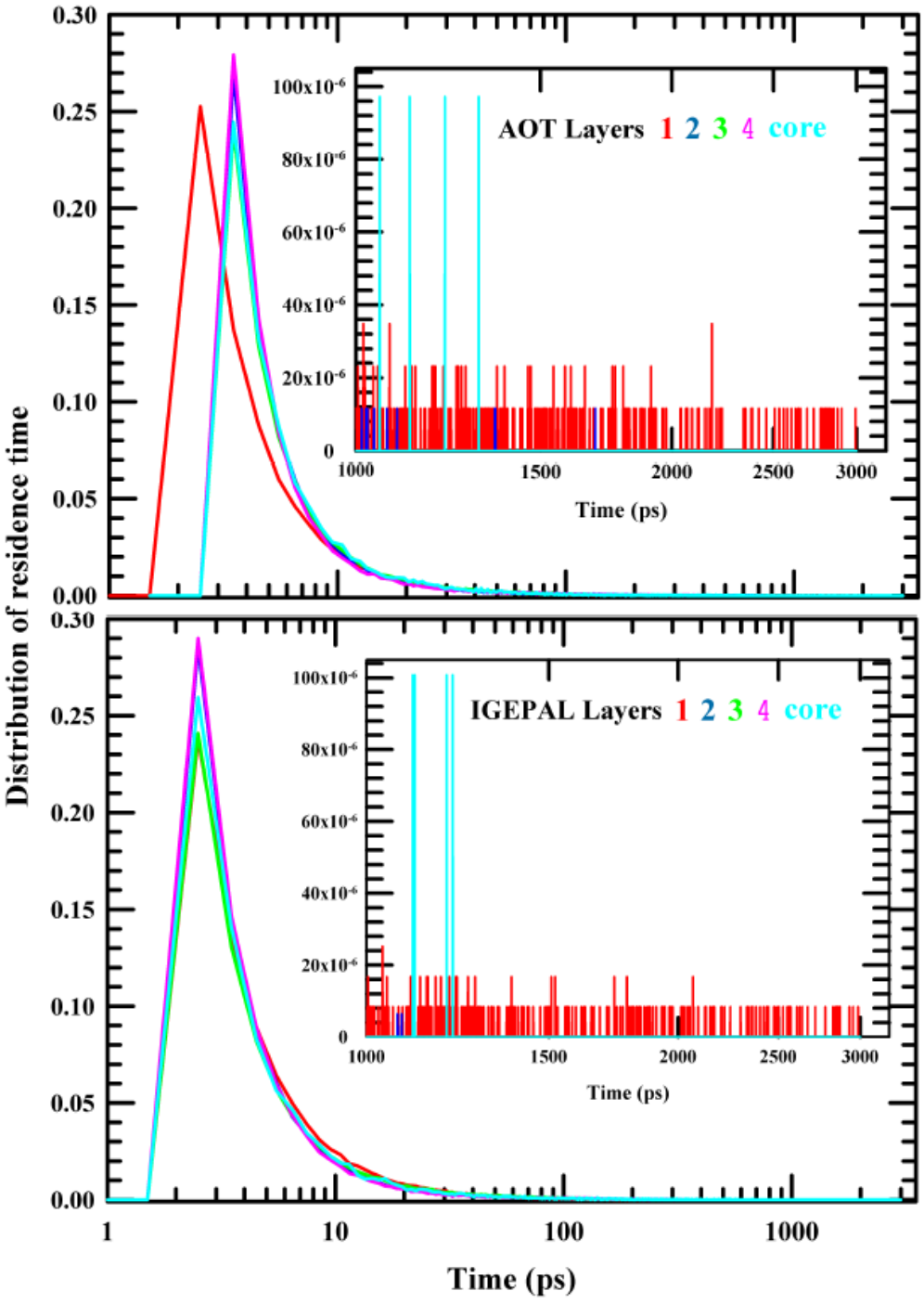

Figure 2.A.3: Distribution of residence times of water molecules in different layers of (a) AOT RM and (b) IGEPAL RM. Inset shows that even after a long duration a few water molecules reside at the interface.

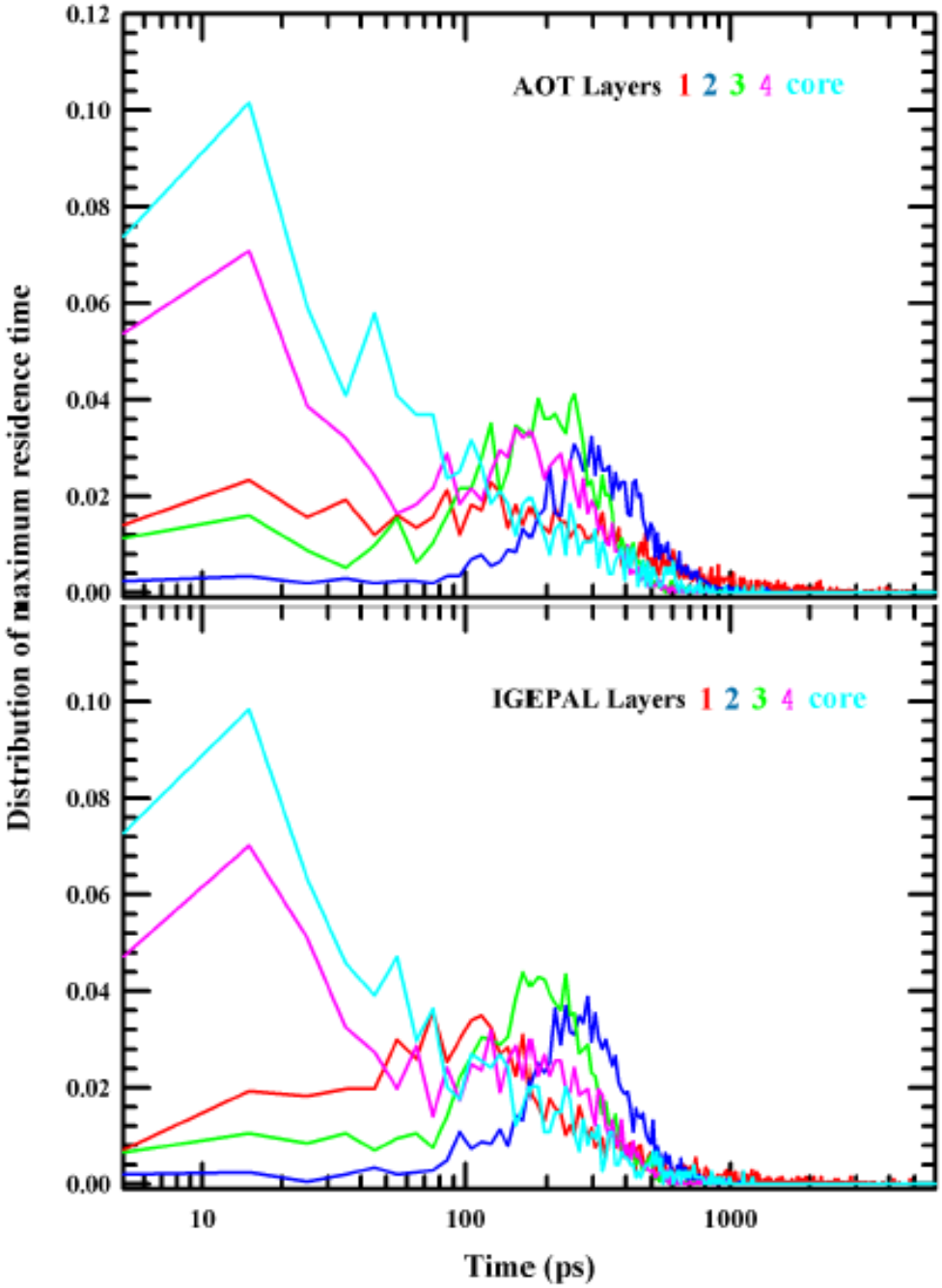

Figure 2.A.4: Distribution of the longest residence time of water molecules in different layers of (a) AOT RM and (b) IGEPAL RM. Note only those particle entries within a given layer is considered which are the longest among all entries for a particle within that given layer.

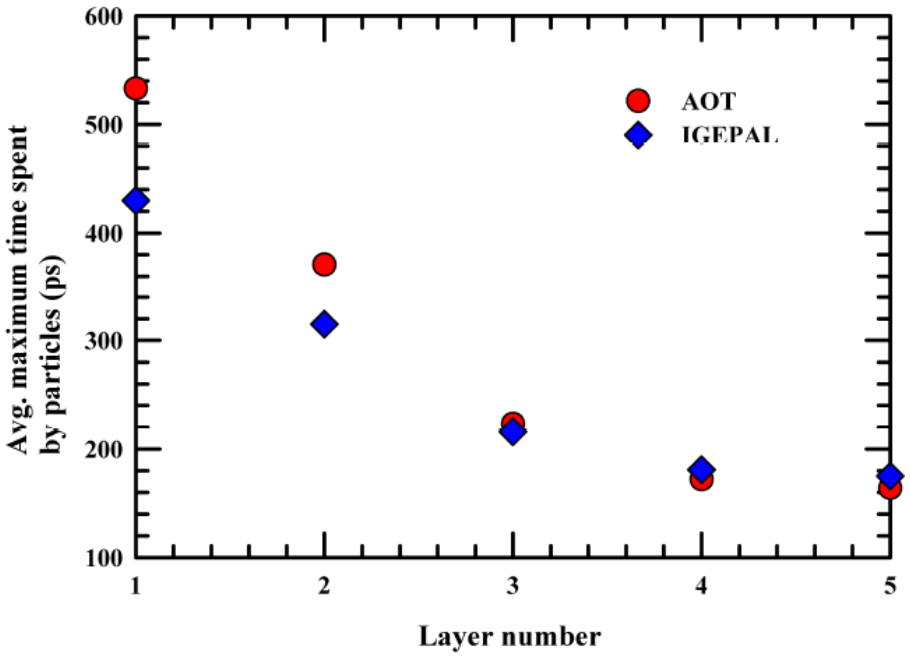

Figure 2.A.5: Graphical representation of Table S5. Layer # 5 represents the core region and layer # 1 is the interfacial layer for both RMs.

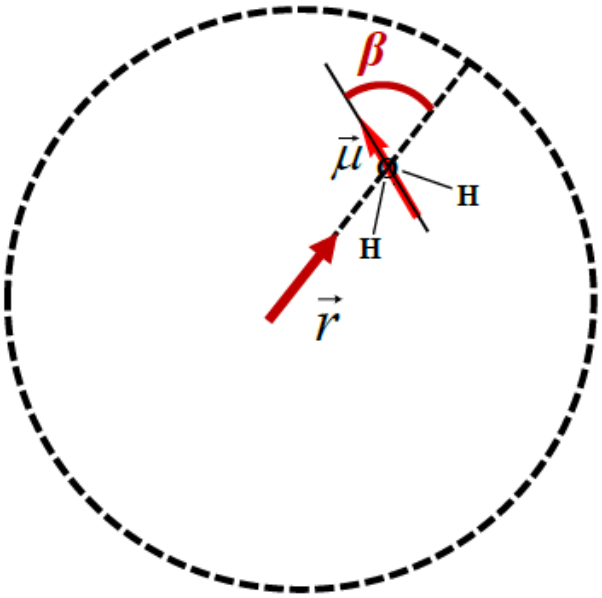

Figure 2.A.6: Schematic representation of a water dipole orientation angle within a RM cavity. $\boldsymbol{\beta}$ is the dipole orientation angle with radial vector $\vec{r}$ of the cavity.

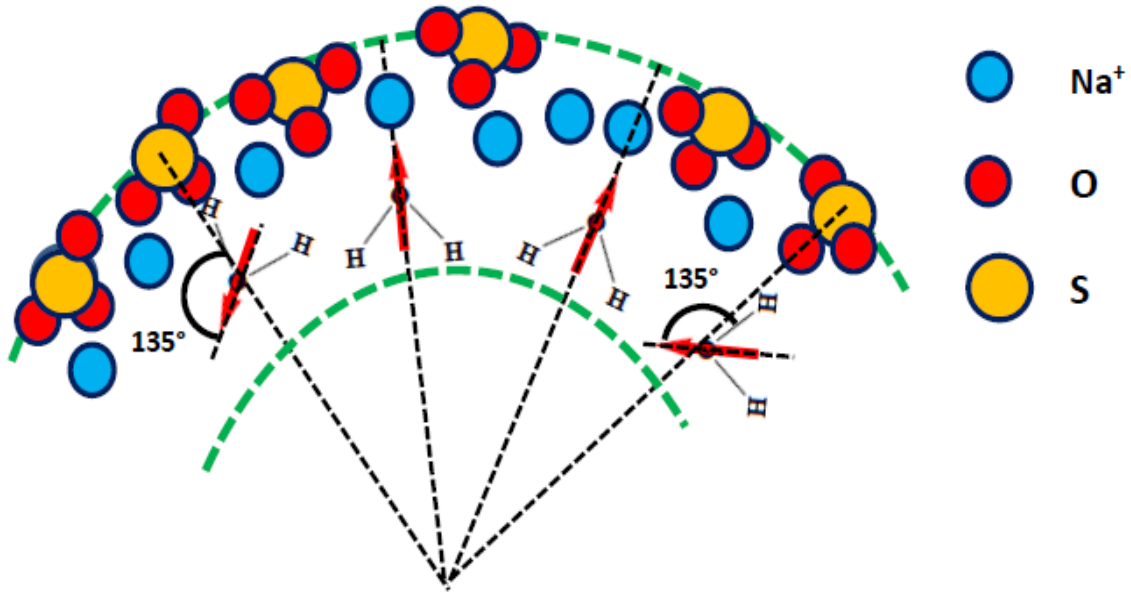

Figure 2.A.7: Probable orientations of water dipoles at the AOT interfacial layer.

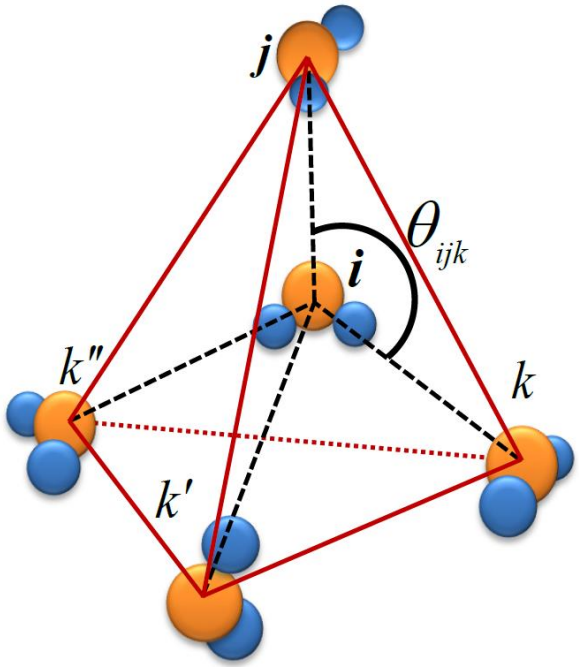

Figure 2.A.8: Schematic representations of the tetrahedral angle θ_{ijk} and the three-dimensional tetrahedral hydrogen bond network of bulk water.

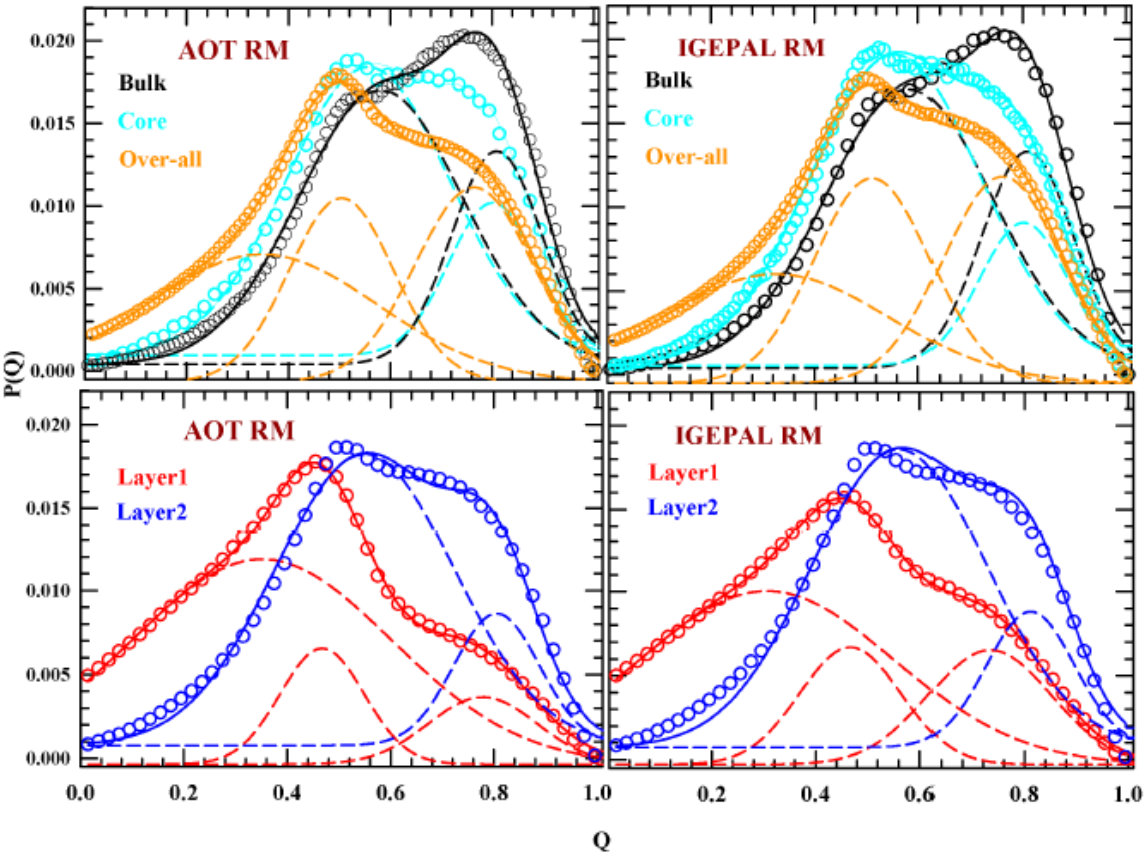

Figure 2.A.9: Deconvolution of P(Q) into several individual Gaussian components with the condition that the sum of the areas under the deconvoluted pieces should be equal to the area under the original curve taken for deconvolution.

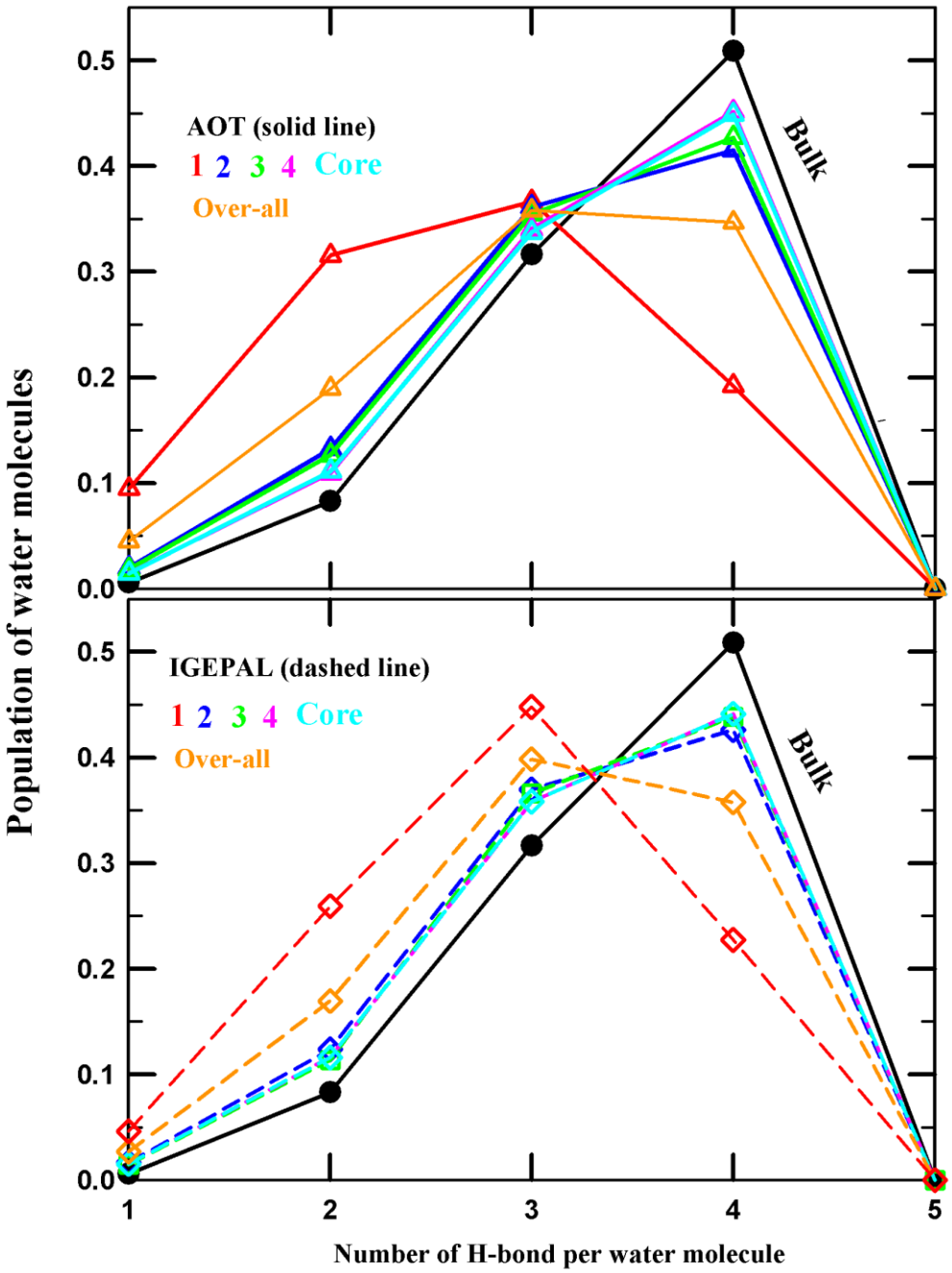

Figure 2.A.10: H-bond population distribution of bulk, over-all and layer-wise water molecules within AOT RM (upper panel) an IGEPAL RM (lower panel).

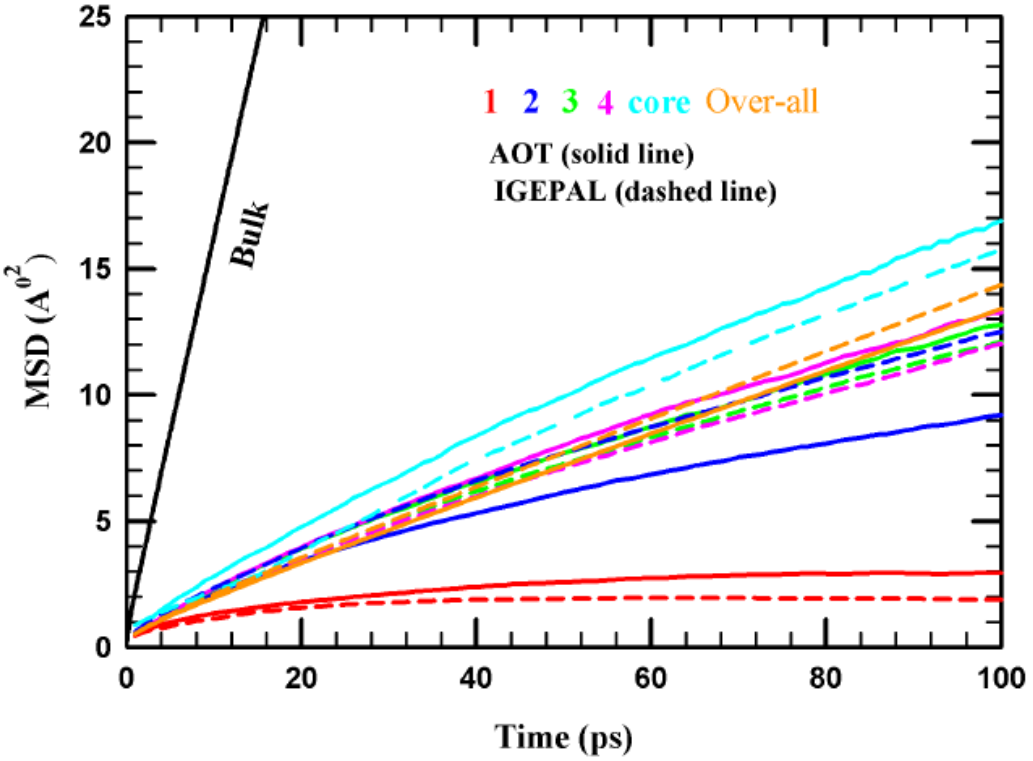

Figure 2.A.11: MSD of water residing in different layers of AOT and IGEPAL RMs. Corresponding bulk and over-all MSDs are also presented.

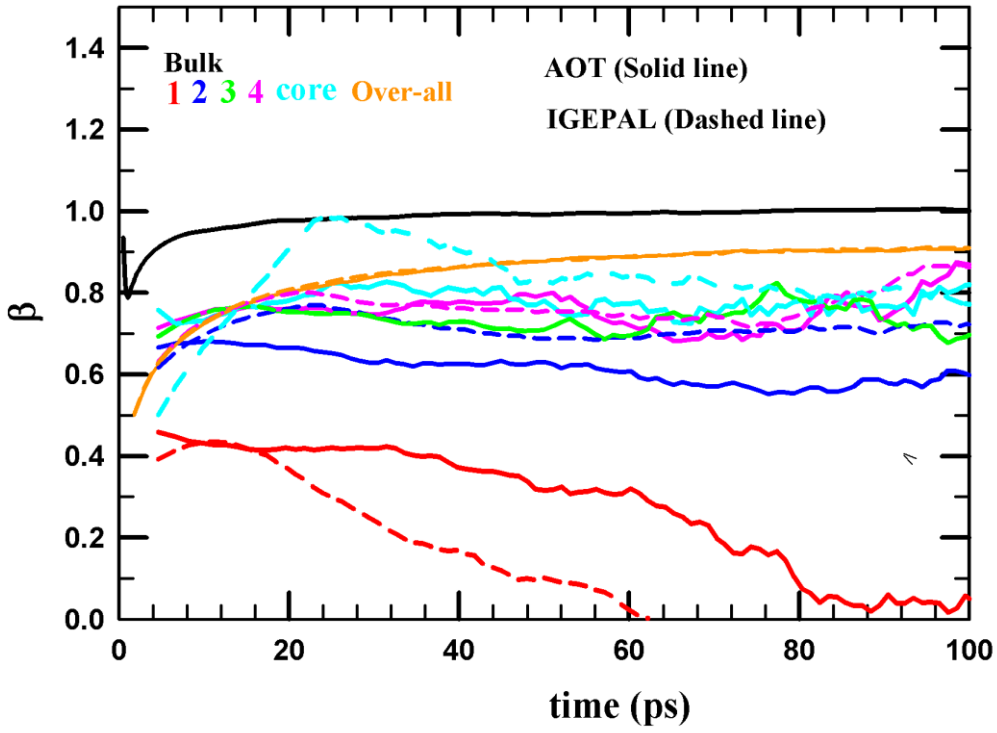

Figure 2.A.12: Time dependence of β associated with MSDs obeying the relation: MSD$\propto t^{\beta}$. Results for layers, over-all confined and bulk water are shown.

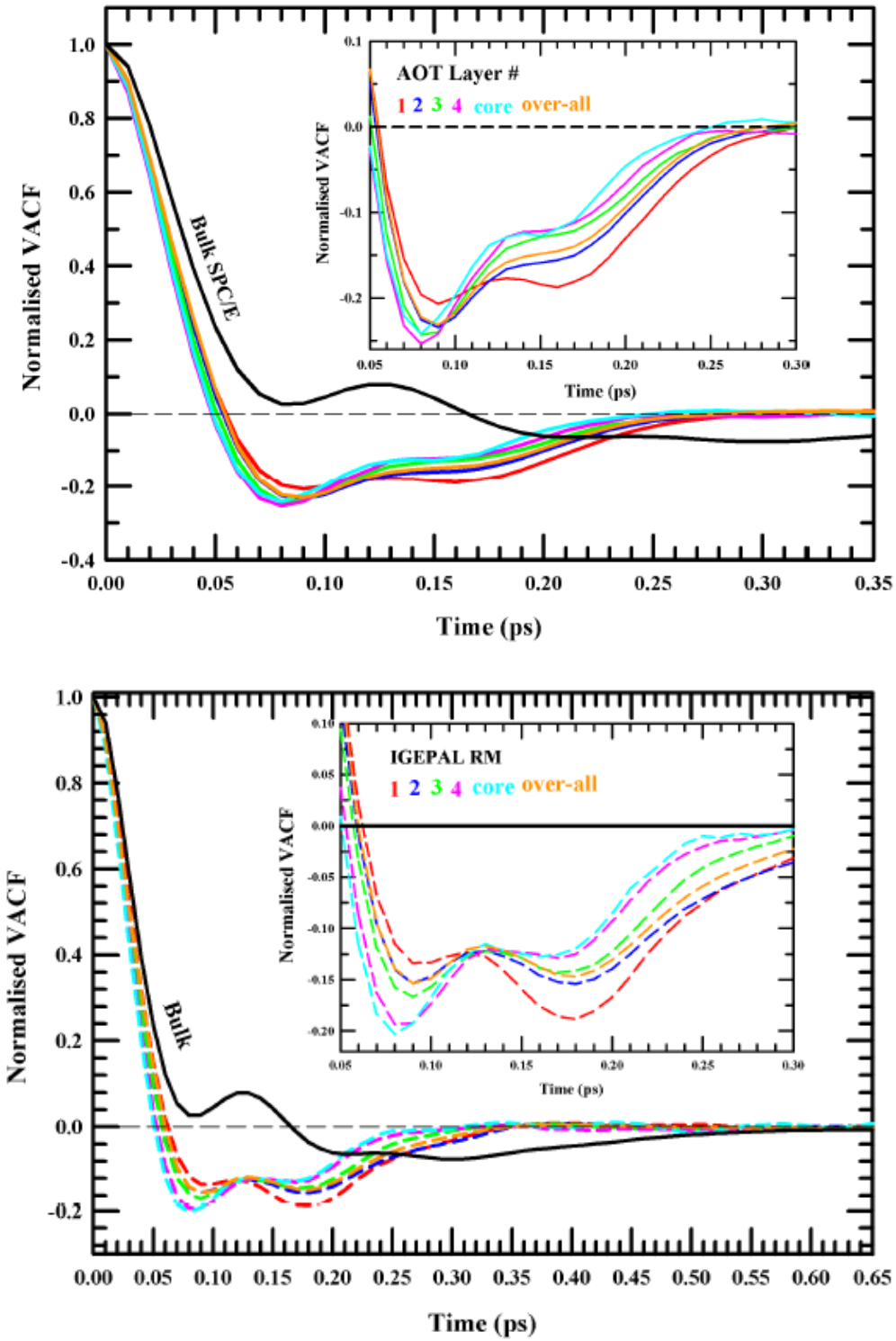

Figure 2.A.13: Normalized VACFs of confined water in different layers, over-all confined water, and bulk water.

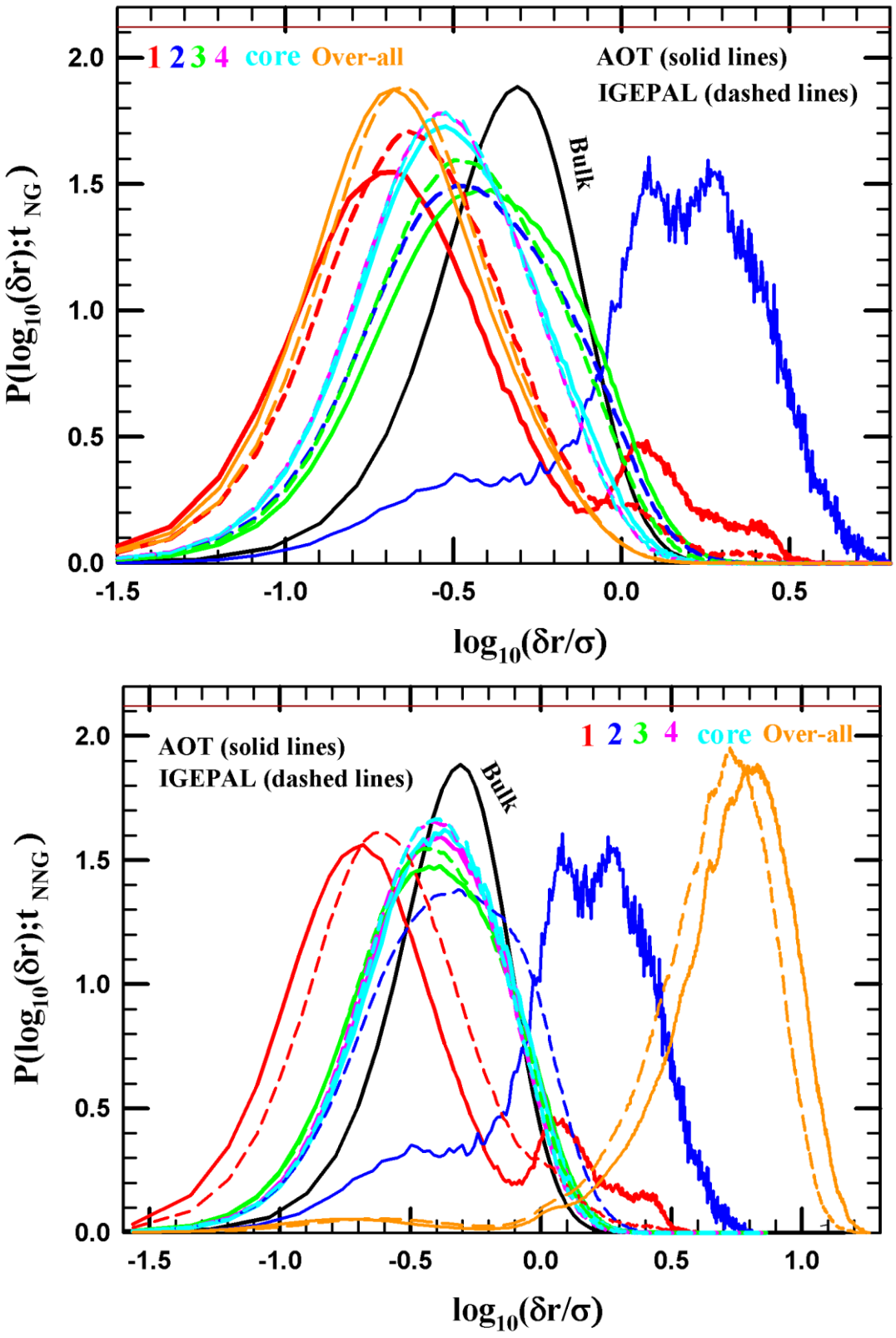

Figure 2.A.14: Single particle displacement distributions of water molecules confined within AOT and IGEPAL. Corresponding bulk results are also shown.

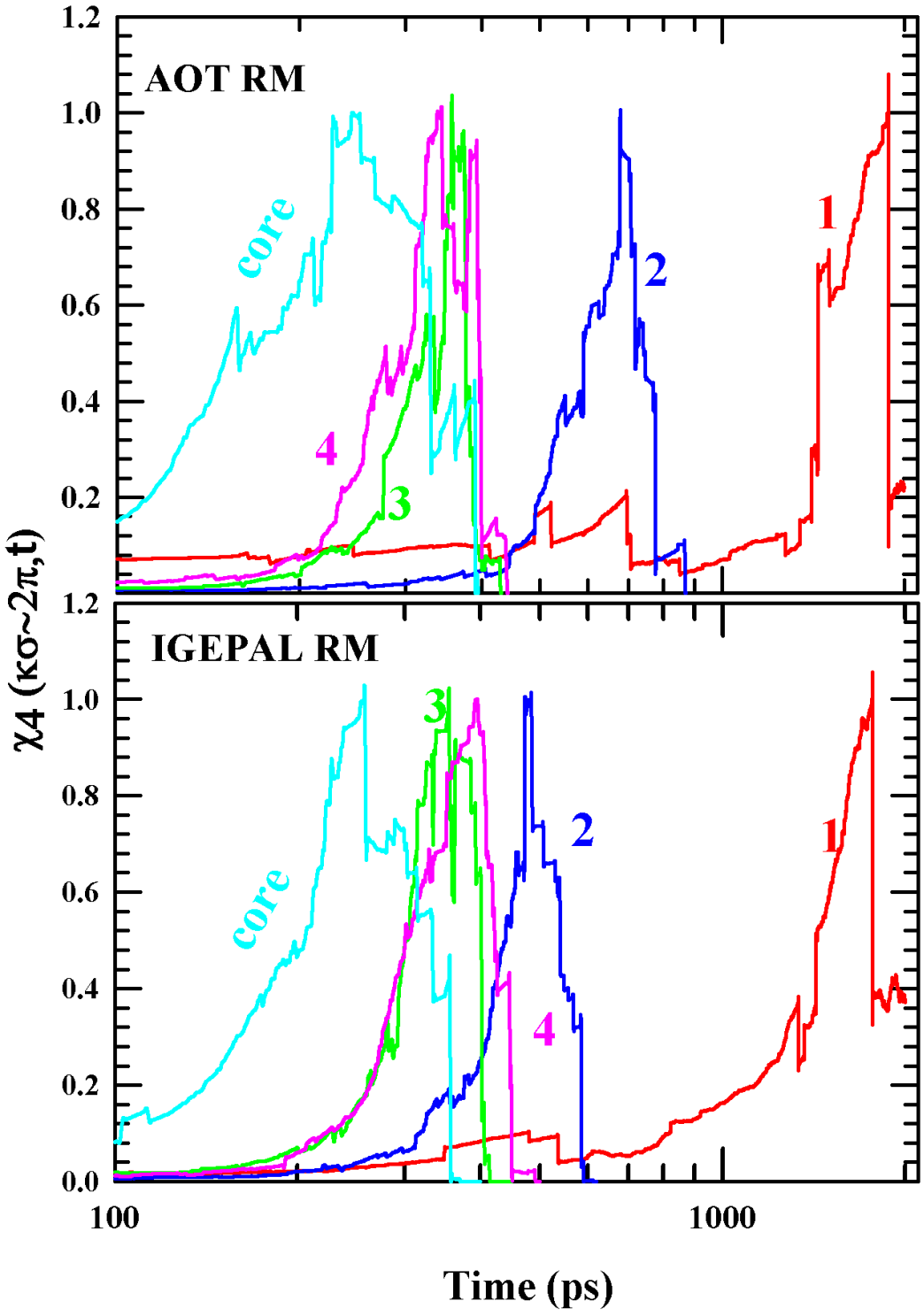

Figure 2.A.15: Dynamic susceptibilities ($\chi_4(t)$) of water molecules for confined water in different layers within AOT and IGEPAL RMs.

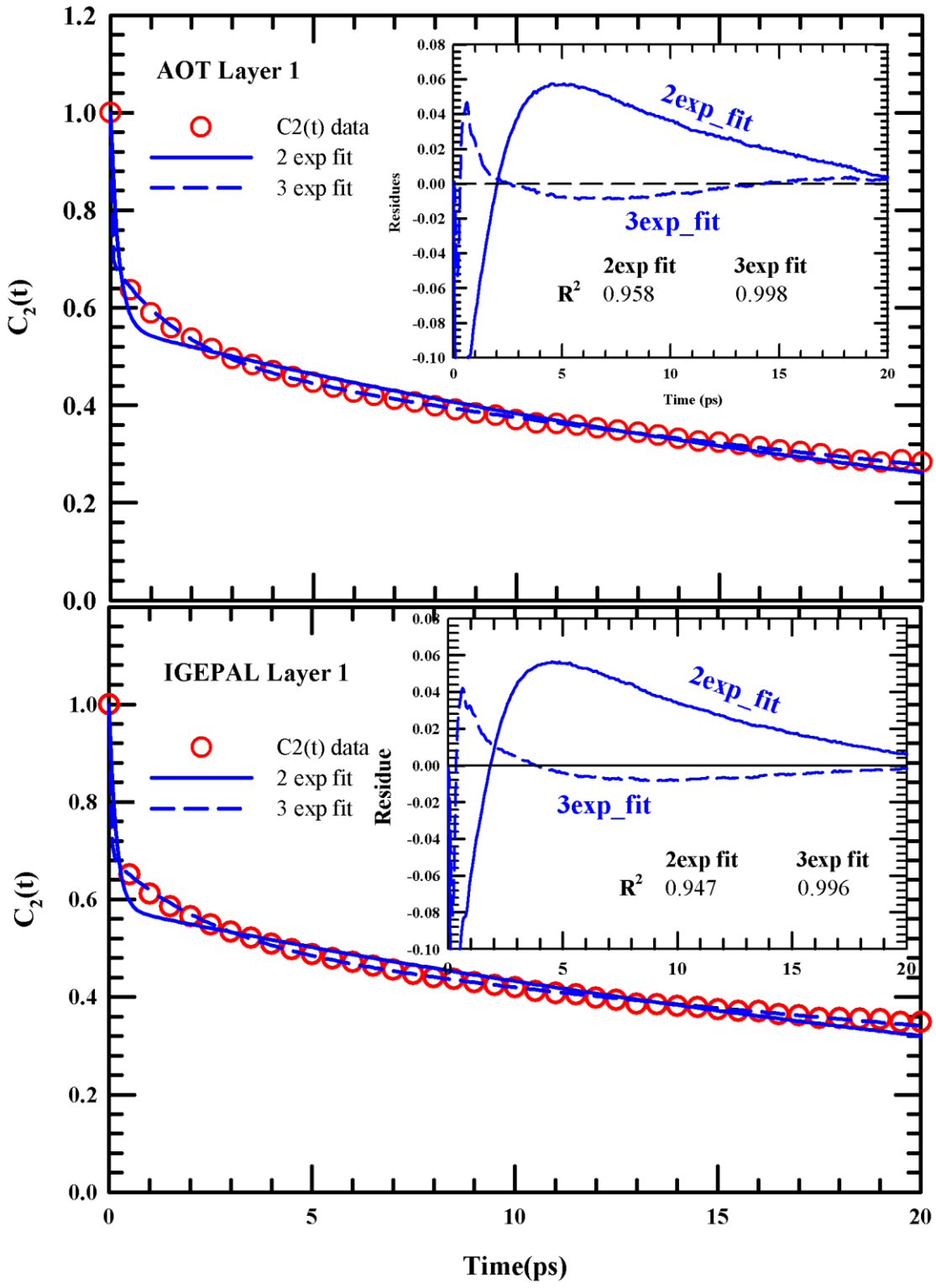

Figure 2.A.16: A comparison between 2-exponential and 3 exponential fits for $C_2(t)$ of interfacial water. Inset shows corresponding R^2 values and residues. Clearly, the 3-exp fits better describes the simulated data.

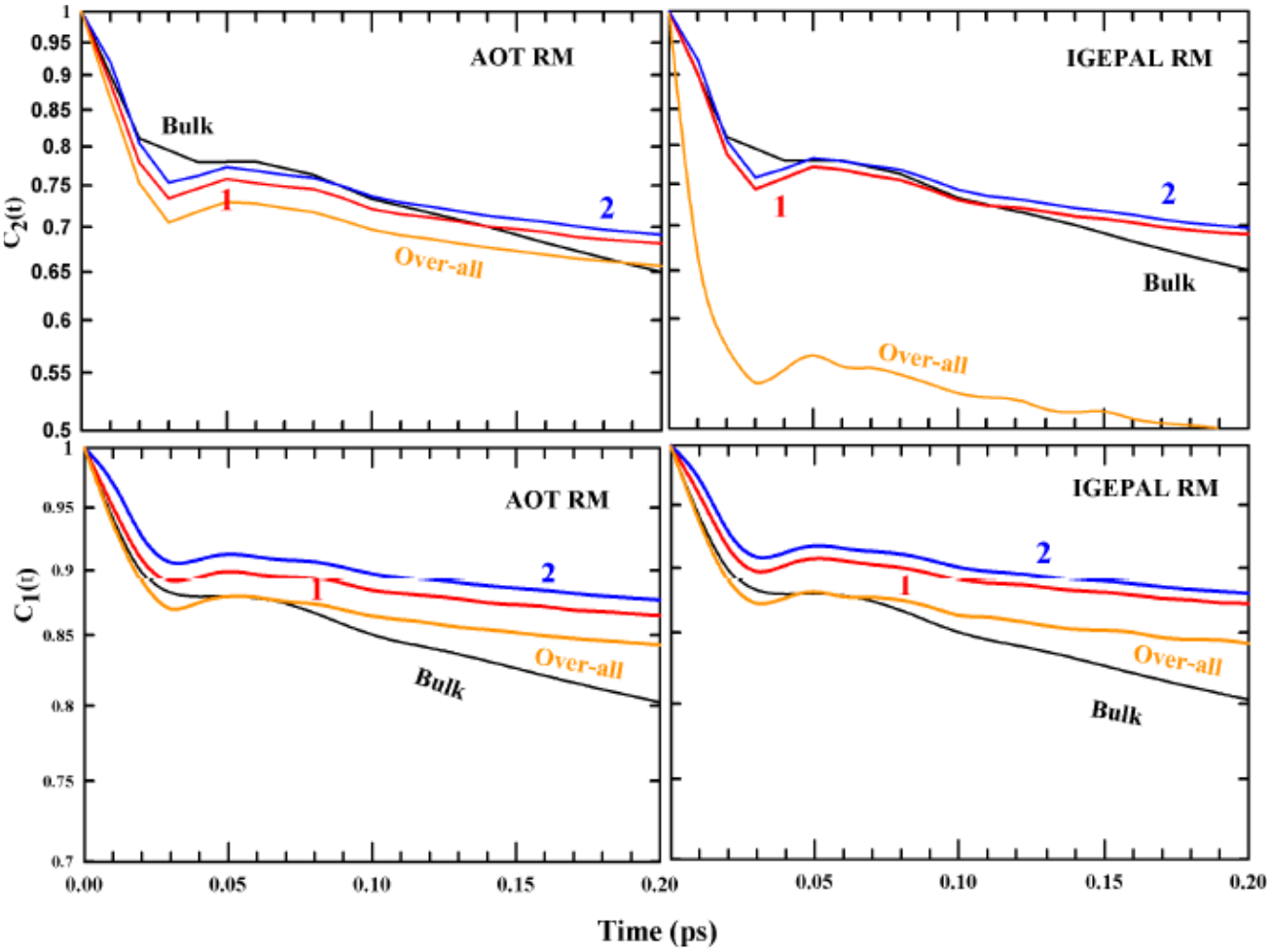

Figure 2.A.17: Representation of faster than bulk component of $C_2(t)$ (upper panel) and $C_1(t)$ (lower panel) for water residing at the first two layers and for over-all confined water.

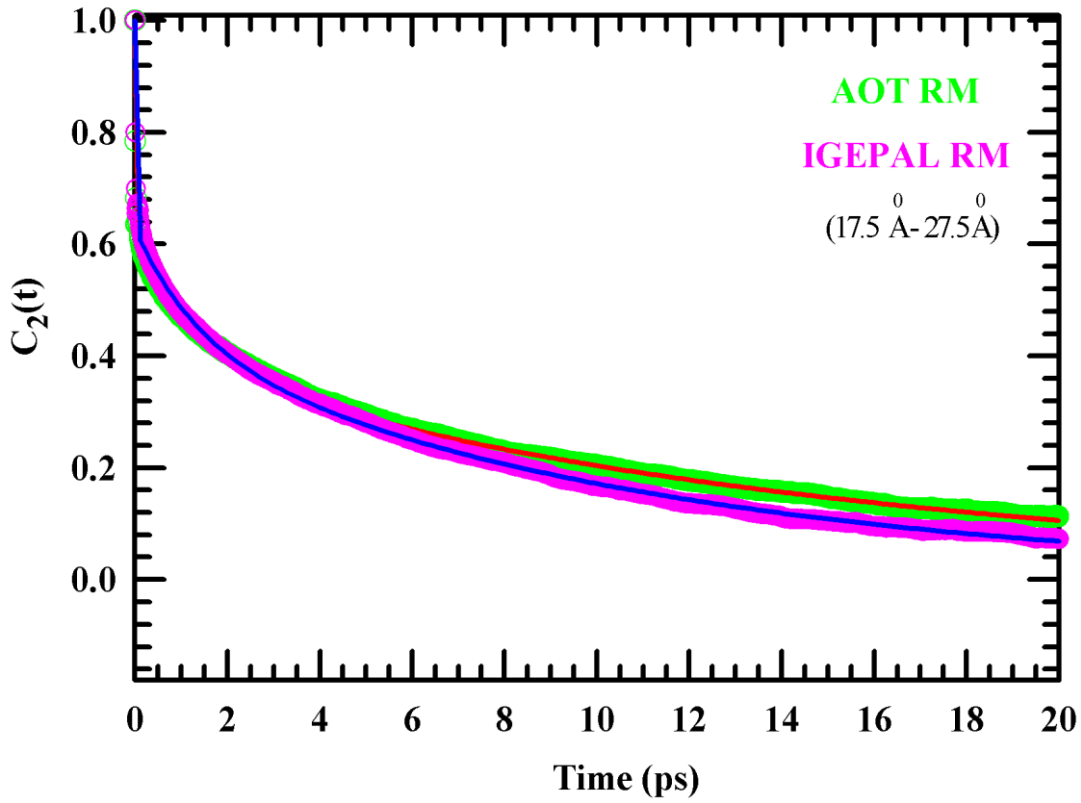

Figure. 2.A.18: Plot of $C_2(t)$ of water molecules residing within a radial distance of 17.5 Å to 27.5 Å from the centre of the pool. This essentially gives contributions from two consecutive layers starting from the interface. Green colour corresponds to AOT RM (red coloured fitting) while pink to IGEPAL RM (blue coloured fitting).

Appendix 2.B

Table 2.B.1: Partial atomic charges for AOT

Atom	q_i/(e)	
1. S_1	1.360	
2. O_3	-0.600	
3. O_3	-0.600	
4. O_3	-0.600	
5. C_31	-0.100	
6. C_1	0.630	
7. O_2	-0.340	
8. O_1	-0.520	
16. C_31	0.630	
17. O_1	-0.520	
18. O_2	-0.340	
29. Na+	1.000	**(Absent atoms are considered as charge less)**

Table 2.B.2: LJ parameters for atoms in AOT

Atoms	σ_i(Å)	ε_i(KJ/mol)
S_3	3.297	1.439
O_3	2.785	0.400
C_31	3.258	0.614
C_32	3.327	0.830
C_33	3.397	1.046
O_1	2.785	0.400
O_2	2.785	0.400
C_1	3.189	0.398
Na^+	2.276	0.482

Table 2.B.3: Partial atomic charges for IGEPAL.

Atom	q_i/(e)
1. C_R1	0.248
2. C_R1	0.016
3. C_R1	0.008
4. C_R1	- 0.037
5. C_R1	0.008
6. C_R1	0.016
7. C_32	0.008
8. C_32	0.035
9. C_32	- 0.002
10. C_32	0.006
11. C_32	- 0.002
12. C_32	0.005
13. C_32	0.007
14. C_32	- 0.019
15. C_32	0.011
16. O_1	- 0.601
17. O_1	- 0.601
18. O_1	- 0.601
19. O_1	- 0.596
20. O_1	- 0.356
21. O_1	- 0.428
22. H_1	0.415
23. C_2	- 0.122
24. C_2	- 0.125
25. H-2	0.210
26. H_2	0.210
27. C_2	- 0.112
28. H-2	0.232

29. H_2	0.232
30. C_2	- 0.115
31. H-2	0.208
32. H_2	0.208
33. C_32	0.299
34. C_32	0.304
35. H_2	0.212
36. H_2	0.212
37. C_2	- 0.107
38. H-2	0.206
39. H_2	0.206
40. C_2	- 0.124
41. H-2	0.212
42. H_2	0.212

Table 2.B.4: LJ parameters for IGEPAL**.**

Atoms	**σ_i(Å)**	**ε_i(KJ/mol)**
C_R1	3.770	0.5674
C_32	3.625	0.8302
O_1	3.034	0.4005
H_1	2.848	0.0636
C_2	3.474	0.3975
H_2	2.848	0.0636

Table 2.B.5: Average of the maximum time spent by molecules in different layers of AOT and IGEPAL RM.

Average maximum residing time by water molecules in different layers		
Layer #.	AOT RM	IGEPAL RM
1 (27.5 Å -22.5 Å)	533 ps	430 ps
2 (22.5 Å -17.5 Å)	371 ps	315 ps
3 (17.5 Å -12.5 Å)	223 ps	216 ps
4 (12.5 Å -7.5 Å)	172 ps	181 ps
5 (7.5 Å -0.0 Å) [core]	164 ps	175 ps

Table 2.B.6: Area under the curve depicting the un-normalized VACFs for bulk water as well as for water in different layers of AOT and IGEPAL RM. A comparison between the confined and bulk is also shown.

Layer #	**AOT**	**IGEPAL**	**Bulk**	**IGEPAL/ AOT**	**Bulk/AOT**	**Bulk/ IGEPAL**
1	-0.038	0.1607	0.7892	-4.28	-20.768	4.910
2	0.0314	0.1383		4.41	25.134	5.706
3	0.0341	0.2078		6.10	23.144	3.798
4	0.0316	0.1869		5.90	24.975	4.222
Core	0.1632	0.1735		1.06	4.8349	4.548
Over-all	0.1240	0.2525		2.04	6.363	3.125

Table 2.B.7: NG and NNG peak timescales for bulk water and confined water residing in different layers of AOT and IGEPAL RMs**.** These times for over-all confined water are also shown.

Layer #	**NG timescale; τ_{NG} (ps)**			**NNG timescale; τ_{NNG} (ps)**		
	AOT	**IGEPAL**	**BULK**	**AOT**	**IGEPAL**	**BULK**
1	1472	1000	1	1560	300	1
2	600	8		600	15	
3	10	8		10	10	
4	5	5		10	10	
core	5	5		10	10	
Over-all	2	2		~3500	~2000	

Table 2.B.8: Tri-exponential fit parameters for $C_2(t)$of water molecules residing within a radial distance of 17.5 Å to 27.5 Å (that is, 10 Å thickness) from the centre of the pool for both the AOT and IGEPAL RM.

	a	τ_1(ps)	b	τ_2(ps)	c	τ_3(ps)
AOT RM	0.40	0.15	0.21	1.63	0.39	15.31
IGEPAL RM	0.37	0.014	0.20	1.36	0.43	10.92

References

[1] M.D. Fayer and N.E. Levinger, Annu. Rev. Anal. Chem. **3**, 89 (2010).

[2] S. Cerveny, F. Mallamace, J. Swenson, M. Vogel, and L. Xu, Chem. Rev. **116**, 7608 (2016).

[3] R. Bergman and J. Swenson, Nature **403**, 283 (2000).

[4] H. Middendorf, Phys. B. Condens. Matter **226**, 113 (1996).

[5] S. Balasubramanian, S. Pal, and B. Bagchi, Phys. Rev. Lett. **89**, 115505 (2002).

[6] B. Bagchi, Chem. Rev. **105**, 3197 (2005).

[7] S. Pronk, E. Lindahl, and P.M. Kasson, Nat. Commun. **5**, 3034 (2014).

[8] F. Pizzitutti, M. Marchi, F. Sterpone, and P.J. Rossky, J. Phys. Chem. B **111**, 7584 (2007).

[9] N.V. Nucci, M.S. Pometun, and A.J. Wand, J. Am. Chem. Soc. **133**, 12326 (2011).

[10] E. González Solveyra, E. de la Llave, V. Molinero, G.J.A.A. Soler-Illia, and D.A. Scherlis, J. Phys. Chem. C **117**, 3330 (2013).

[11] J. Chowdhary and B.M. Ladanyi, J. Phys. Chem. B **113**, 15029 (2009).

[12] J. Chowdhary and B.M. Ladanyi, J. Phys. Chem. A **115**, 6306 (2011).

[13] J. Faeder and B.M. Ladanyi, J. Phys. Chem. B **105**, 11148 (2001).

[14] S. Romero-Vargas Castrillo′n, N. Giovambattista, I.A. Aksay, and P.G. Debenedetti, J. Phys. Chem. B **113**, 1438 (2009).

[15] A.A. Bakulin, D. Cringus, P.A. Pieniazek, J.L. Skinner, T.L. Jansen, and M.S. Pshenichnikov, J. Phys. Chem. B **117**, 15545 (2013).

[16] R. Biswas, T. Chakraborti, B. Bagchi, and K. Ayappa, J. Chem. Phys. **137**, 014515 (2012).

[17] D.E. Rosenfeld and C.A. Schmuttenmaer, J. Phys. Chem. B **115**, 1021 (2011).

[18] I.R. Piletic, D.E. Moilanen, D. Spry, N.E. Levinger, and M. Fayer, J. Phys. Chem. A **110**, 4985 (2006).

[19] E.E. Fenn, D.B. Wong, and M. Fayer, Proc. Natl. Acad. Sci. USA **106**, 15243 (2009).

[20] V.R. Hande and S. Chakrabarty, Phys. Chem. Chem. Phys. **18**, 21767 (2016).

[21] T.H. van der Loop, M.R. Panman, S. Lotze, J. Zhang, T. Vad, H.J. Bakker, W.F. Sager, and S. Woutersen, J. Chem. Phys. **137**, 044503 (2012).

[22] P.A. Pieniazek, Y.-S. Lin, J. Chowdhary, B.M. Ladanyi, and J. Skinner, J. Phys. Chem. B **113**, 15017 (2009).

[23] D.E. Moilanen, E.E. Fenn, D. Wong, and M.D. Fayer, J. Chem. Phys. **131**, 014704 (2009).

[24] D.E. Moilanen, N.E. Levinger, D. Spry, and M. Fayer, J. Am. Chem. Soc. **129**, 14311 (2007).

[25] D.E. Moilanen, E.E. Fenn, D. Wong, and M.D. Fayer, J. Am. Chem. Soc. **131**, 8318 (2009).

[26] E. Zdrali, G. Etienne, N. Smolentsev, E. Amstad, and S. Roke, J. Chem. Phys **150**, 204704 (2019).

[27] D.R. Moberg, Q. Li, S.K. Reddy, and F. Paesani, J. Chem. Phys. **150**, 034701 (2019).

[28] S. Kishinaka, A. Morita, and T. Ishiyama, J. Chem. Phys. **150**, 044707 (2019).

[29] K. -i. Inoue, M. Ahmed, S. Nihonyanagi, and T. Tahara, J. Chem. Phys. **150**, 054705 (2019).

[30] M. Heyden, J. Chem. Phys. **150**, 094701 (2019).

[31] C. Dutta, M. Mammetkuliyev, and A.V. Benderskii, J. Chem. Phys. **151**, 034703 (2019).

[32] X. Cai, W.J. Xie, Y. Yang, Z. Long, J. Zhang, Z. Qiao, L. Yang, and Y.Q. Gao, J. Chem. Phys. **150**, 124703 (2019).

[33] S.K. Mondal, S. Ghosh, K. Sahu, U. Mandal, and K. Bhattacharyya, J. Chem. Phys. **125**, 224710 (2006).

[34] P. Liu, E. Harder, and B. Berne, J. Phys. Chem. B **108**, 6595 (2004).

[35] A. Chatterjee, B. Maity, and D. Seth, Phys. Chem. Chem. Phys. **15**, 1894 (2013).

[36] B. Sengupta, J. Guharay, and P.K. Sengupta, Spectrochim Acta Part A **56**, 1433 (2000).

[37] T. Satoh, H. Okuno, K. Tominaga, and K. Bhattacharyya, Chem. Lett. **33**, 1090 (2004).

[38] D.E. Rosenfeld and C.A. Schmuttenmaer, J. Phys. Chem. B **110**, 14304 (2006).

[39] M.D. Fayer, Acc. Chem. Res. **45**, 3 (2012).

[40] F.H. Stillinger, *The Physical Chemistry of Aqueous System* (1974).

[41] A. Wallqvist and B. Berne, J. Phys. Chem. A **99**, 2893 (1995).

[42] G. Hummer and S. Garde, Phys. Rev. Lett. **80**, 4193 (1998).

[43] S. Vaitheeswaran, H. Yin, J.C. Rasaiah, and G. Hummer, Proc. Natl. Acad. Sci. USA **101**, 17002 (2004).

[44] J.C. Rasaiah, S. Garde, and G. Hummer, Annu. Rev. Phys. Chem. **59**, 713 (2008).

[45] F.N. Keutsch and R.J. Saykally, Proc. Natl. Acad. Sci. USA **98**, 10533 (2001).

[46] J. Faeder, M.V. Albert, and B.M. Ladanyi, Langmuir **19**, 2514 (2003).

[47] J. Faeder and B. Ladanyi, J. Phys. Chem. B **104**, 1033 (2000).

[48] H. Berendsen, J. Grigera, and T. Straatsma, J. Phys. Chem. B **91**, 6269 (1987).

[49] S.L. Mayo, B.D. Olafson, and W.A. Goddard, J. Phys. Chem. C **94**, 8897 (1990).

[50] S. Abel, F. Sterpone, S. Bandyopadhyay, and M. Marchi, J. Phys. Chem. B **108**, 19458 (2004).

[51] M. Allen and D. Tildesley, *Computer Simulation of Liquids* (1987).

[52] A. Amararene, M. Gindre, J.-Y. Le Huerou, C. Nicot, W. Urbach, and M. Waks, J. Phys. Chem. B **101**, 10751 (1997).

[53] A. Amararene, M. Gindre, J.-Y. Le Huérou, W. Urbach, D. Valdez, and M. Waks, Phys. Rev. E **61**, 682 (2000).

[54] S. Nosé, Mol. Phys. **52**, 255 (1984).

[55] W.G. Hoover, Phys. Rev. A **31**, 1695 (1985).

[56] R. Biswas and B. Bagchi, J. Phys. Condens. Matter **30**, 013001 (2018).

[57] J.-P. Ryckaert, G. Ciccotti, and H.J. Berendsen, J. Comput. Phys. **23**, 327 (1977).

[58] H.J. Berendsen, Jv. Postma, W.F. van Gunsteren, A. DiNola, and J.R. Haak, J. Chem. Phys. **81**, 3684 (1984).

[59] T. Forester and W. Smith, *The Dl_Poly_2 Reference Manual* (1998).

[60] M. Galib, M. Baer, L. Skinner, C. Mundy, T. Huthwelker, G. Schenter, C. Benmore, N. Govind, and J.L. Fulton, J. Chem. Phys. **146**, 084504 (2017).

[61] S. Nihonyanagi, J.A. Mondal, S. Yamaguchi, and T. Tahara, Annu. Rev. Phys. Chem. **64**, 579 (2013).

[62] S. Nihonyanagi, S. Yamaguchi, and T. Tahara, J. Chem. Phys. **130**, 204704 (2009).

[63] J.R. Errington and P.G. Debenedetti, Nature **409**, 318 (2001).

[64] A. Chandra, Phys. Rev. Lett. **85**, 768 (2000).

[65] A. Luzar, Faraday Discuss **103**, 29 (1996).

[66] T.C. Berkelbach, H.-S. Lee, and M.E. Tuckerman, Phys. Rev. Lett. **103**, 238302 (2009).

[67] A. Luzar and D. Chandler, J. Chem. Phys. **98**, 8160 (1993).

[68] B. Guchhait, R. Biswas, and P.K. Ghorai, J. Phys. Chem. B **117**, 3345 (2013).

[69] T. Pal and R. Biswas, J. Chem. Phys. **141**, 104501 (2014).

[70] D.A. Schmidt, O. zr. Birer, S. Funkner, B.P. Born, R. Gnanasekaran, G.W. Schwaab, D.M. Leitner, and M. Havenith, J. Am. Chem. Soc. **131**, 18512 (2009).

[71] T. Pal and R. Biswas, Chem. Phys. Lett. **517**, 180 (2011).

[72] T. Pal and R. Biswas, Theor. Chem. Acc. **132**, 1348 (2013).

[73] J.P. Hansen and I.R. McDonald, *Theory of Simple Liquids* (1986).

[74] S. Krishnan and K. Ayappa, J. Phys. Chem. B **109**, 23237 (2005).

[75] P. Argyrakis, A. Chumak, M. Maragakis, and N. Tsakiris, Phys. Rev. B **80**, 104203 (2009).

[76] C. Dasgupta, A. Indrani, S. Ramaswamy, and M. Phani, Eur. Lett. **15**, 307 (1991).

[77] S.C. Glotzer, J. Non-Cryst. Solids **274**, 342 (2000).

[78] D.R. Reichman, E. Rabani, and P.L. Geissler, J. Phys. Chem. B **109**, 14654 (2005).

[79] A.M. Puertas, M. Fuchs, and M.E. Cates, J. Chem. Phys. **121**, 2813 (2004).

[80] S.A. Roget, P.L. Kramer, J.E. Thomaz, and M.D. Fayer, J. Phys. Chem. B **123**, 9408 (2019).

[81] D.E. Moilanen, E.E. Fenn, D. Wong, and M. Fayer, J. Phys. Chem. B **113**, 8560 (2009).

[82] C. Toninelli, M. Wyart, L. Berthier, G. Biroli, and J.-P. Bouchaud, Phys. Rev. E. **71**, 041505 (2005).

[83] A. Rahman, Phys. Rev. **136**, A405 (1964).

[84] C. Bennemann, C. Donati, J. Baschnagel, and S.C. Glotzer, Nature **399**, 246 (1999).

[85] H.-S. Tan, I.R. Piletic, and M. Fayer, J. Chem. Phys. **122**, 174501 (2005).

Chapter 3

Does Confinement Modify Preferential Solvation and H-bond Fluctuation Dynamics? A Molecular Level Investigation Through Simulations of Bulk and Confined Three-Component Mixture

3.1 Introduction

It is well-known that the increase in entropy for mixing of alcohols (for example, methanol or ethanol) in neat water is much less than that expected for an ideal solution[1] that follows the Raoult's law[2]. Numerous studies have suggested that the three-dimensional tetrahedral H-bond network structure of water is heavily influenced by the presence of alcohol in aqueous binary mixtures. This has been reflected in the anomalous mole fraction dependence of entropy of mixing and partial molar enthalpy of water. [3,4] Interspecies H-bonding and the strong tendency of water to preserve its tetrahedral network is believed[5] to be the reason for such anomalous features of alcohol-water binary mixtures. Methanol is the first member of the homologous series of mono-hydroxy alcohols and is soluble in water at any mole fraction. The extent of non-ideal behaviour for methanol is the minimum among all other water-miscible alcohols. There also exist several studies where different views have been put forward to explain the anomalous thermodynamic properties of water-methanol mixtures[6–10]. It has been proposed in those studies that, local (neighbouring) water structure around a methanol molecule is quite similar to that of neat liquid water and this similarity persists even in the methanol-rich region of aqueous solution (methanol: water = 7:3)[7]. These conclusions, however, have been derived from the analyses of various radial distribution functions. Unfortunately, an extensive study focussing on how methanol molecules in an aqueous solution perturb the local orientational ordering and the global tetrahedral network of water in dilute solutions and severely distort them at higher alcohol mole fractions is still lacking. In the present work, our central aim is to explore, via a thorough and extensive simulation study, the impact of methanol on both the local and the global orientational order in bulk binary mixtures of methanol and water at various mixture compositions and inspect the effect of nanoscopic confinement on them. In addition, intra- and inter-species H-bond fluctuation dynamics have been followed to investigate the

influence of confinement on structural and continuous H-bond relaxation timescales. Comparison of these properties among bulk neat mixture components, bulk binary mixtures and the corresponding confined nanoscopic systems have been performed wherever possible to generate insight about the capability of water network to withstand perturbations induced by the concentration of the other mixture component and/or by nanoscopic confinement.

Relaxation dynamics of confined liquids probed by different experiments have suggested probe location dependence[11,12] of the measured relaxation timescales. The position of a solute within a solvent system and its surrounding local environment is the region, which largely dictates an experimental outcome. Experimental observation of relatively faster dynamics upon increasing the confinement radius has been attributed to enhanced mobility of solvating particles around a solute due to larger curvature of the confining surface[11]. Confinement size dependence of solute location is, therefore, a piece of critical information for proper interpretation of solute-centred dynamics. A previous simulation study with a realistic solute (coumarin 153, denoted as C153) in aqueous AOT reverse micelles (RMs) of different sizes has suggested that C153 always located itself nearer to the interface than to the centre of the confined aqueous pool[13]. This proximity to the interface was maintained even for the excited solute. This is counter to the view that an increased electrostatic interaction would drive the laser-excited C153 nearer to the centre of the pool with the increase of RM radius. Such a preferred location even for excited C153 may be understood in terms of a competition between the inherent hydrophobicity of C153 and the dipole-dipole solute-solvent interaction where ultimately the hydrophobic solute-solvent interaction wins. This interpretation then naturally raises the following questions: (i) where would C153 locate itself if the water is sequentially and then totally replaced by an amphiphilic polar solvent in a model RM? (ii) would C153 be preferentially solvated in a such a mixed environment of amphiphilic solvent and water? The second question is probably more important because it connects the celebrated preferential solvation phenomenon to confinement and alludes to the impact of confining surfaces on solute-solvent interactions. This aspect has not been investigated yet.

We address the above issues in the present work by exploring the solvation structure around C153 in binary mixtures of methanol and water at different compositions – both in the bulk, and under confinement provided by a model RM of inner diameter 55Å at 300 K. One single

solute in aqueous methanolic solutions at three different compositions have been considered. For the RM, solvent to surfactant ratio is kept fixed at w_0~10. We simulate mixture compositions corresponding to 20%, 40% and 80% water of the total population, denoting them respectively as W20, W40, W80. We represent water by the well-known SPC/E model[14]. For constructing the RM, we have considered a model interaction potential for the charged surfactant molecule, sodium bis(2-Ethylhexyl) sulfosuccinate (AOT)[15]. A united atom model of methanol (TRaPPE-UA) is used where hydrogen atoms of the methyl group are not considered explicitly[16]. We have considered a sphere of radius 7.0 Å around the centre of mass (COM) of C153 as our target sphere to explore how preferential solvation gets modulated by the confining binary mixtures. The size has been chosen as the addition of diameter of one water (2.75 Å) and one methanol molecule (4.2 Å) from the surface of the solute. Quite surprisingly, our results reveal that the preferential solvation is significantly enhanced in the confined binary mixtures via facilitating the inherent di-mixing characteristics of water and methanol.

We have performed analyses of the H-bond structural and dynamical aspects for confined binary mixtures by dividing each into two layers - an interfacial layer of 7.0 Å thickness and the inner pool of 20 Å thickness. We compared these layer-wise results with the corresponding 'overall' (considering contributions from all solvent particles of one or both components of a given confined mixture during statistical averaging) properties. Different water-water and methanol-water H-bond structural and dynamical properties have been monitored and calculated from the present simulations and the effects of confinement on average H-bond numbers and H-bond fluctuation dynamics explored. Comparing our layer-wise results for confined binary mixtures with those simulated for bulk counterparts and neat bulk systems, we have found that addition of methanol significantly affects the tetrahedrality of water H bond network structure, although confinement impact on it is small and becomes negligible as methanol concentration increases. The present simulations also find that the confinement severely affects the inter-species H-bond fluctuation dynamics while a clear trend is missing for the intra-species dynamics.

3.2 Simulation Details

3.2.1 Systems

For the three binary mixtures W20, W40 and W80 considered, the corresponding numbers of water and methanol molecules are provided in Table 3.B.1 (Appendix 3.B). We have simulated these three compositions both in the bulk and under the confinement of AOT RM with an inner radius of 27.5 Å. The modelling details of the AOT RM, force field parameters of AOT surfactant and Na^+ ions are taken from an earlier work[15,17,18]. The force field parameters and ground-state charge distribution of C153 atoms have been taken from an already published work[19].

3.2.2 Bulk system simulations

All the three compositions were equilibrated in NPT ensemble employing a Berendsen thermostat[20] with a coupling constant of 0.1 ps for 2ns at a temperature 298 K to reach desired experimental density. One C153 molecule was dissolved in each of these three mixtures. The pressure was maintained constant at 1 atm. by using the Berendsen barostat[20] with 0.2 ps time constant. Periodic boundary condition[21] was employed throughout the simulation of cubic simulation boxes. Simulated and experimental densities[22] of these systems are compared in Table 3.B.2 (Appendix 3.B) and Figure 3.A.1 (Appendix 3.A). A good agreement between them provides the necessary confidence about the basic correctness of the simulation protocols employed. Time evolution of bulk densities during NPT simulations are presented in Figure 3.A.2 (Appendix 3.A) for the sake of reproducibility. Classical equation of motions was integrated by using velocity Verlet algorithm[21] with 1fs time-step. Electrostatic interactions were dealt with the Ewald sum technique[21,23] with a precession of 10^{-7}. The cut-off radius for short-range interaction was set at 11 Å. Then a production run of 5 ns was carried out with pre-equilibrated structure in NVT ensemble at 298 K using the Nose-Hoover thermostat[24,25] with a time constant of 0.5 ps. During this production, run trajectories were saved after every 0.1ps for analysis of structural properties, whereas for hydrogen-bond dynamics separate trajectories were generated for every 0.01 ps.

3.2.3 Confined system simulations

Coordinate trajectories were generated by using the velocity Verlet algorithm[21] with a time step of 2 fs. The temperature was set at 298 K using the Nose- Hoover thermostat[24,25] with 0.5 ps time step. Trajectories were collected after equilibration of 40 ns in NVT ensemble following the literature procedure[26–28]. A total of 20 ns trajectories were collected at every 0.1 ps time gap while a production run in NVT ensemble was carried out. The cut-off radius for short-range interaction was set to 11 Å. A separate trajectory for 1 ns was generated for hydrogen bond lifetime calculations where trajectories were saved at every 0.01 ps. For carrying out all the simulations reported here, we had used the DL-POLY[29] MD simulation software.

3.2.4 Fidelity check of force field

Table 3.B.2 (Appendix 3.B) compares the previously reported experimental densities of all the bulk binary mixtures with those from our present simulation study. The error is within the tolerance limit. The radial mass densities of the confined mixtures (inside AOT RM) have been calculated and then normalized with the corresponding bulk simulated densities. Both radial distance dependent mass densities and corresponding normalized densities are depicted in Figure 3.A.3(a) and 3.A.3(b) (Appendix 3.A) respectively. These normalized densities are nearer to 1 when the systems approach the corresponding bulk densities. This figure shows the usual trend of density[17,30] drop near the interface for confined aqueous systems. For W20 and W40 confined systems, the densities near the centre are less than the corresponding bulk counterpart. As a consequence, the layer adjacent to the interface acquires higher densities than bulk before showing a drastic decrease near the interface. All these observations provide the necessary confidence to perform the intended simulations using the force fields and models employed.

For analysis, the confined solvent pool inside the RM is divided into two imaginary radial layers, namely, the ‘interfacial’ region and the ‘core’ or ‘inner’ region. The interfacial region has been assumed to be of 7.00 Å width, considering a layer created by one water and one methanol molecules (σ_{water} [31]+ $\sigma_{methanol}$[32] = (2.75 + 4.2) Å)The radius of the inner region is 20 Å. We have analysed data for the interfacial and the inner regions for each of the systems and

also for the 'overall' properties where contributions from all confined solvent molecules have been taken into account.

3.3 Results and Discussion

3.3.1 Environment around C153 in the bulk and confined binary mixtures

Because one of the aims of the present study is to explore how preferential solvation around a dissolved solute is influenced by nano-confinement of binary solvent mixtures, the immediate environment around C153 is the most important region. Our simulations suggest that the solute, C153 resides approximately in the same region inside these RM confined mixtures. This is shown in Figure 3.1 where probability distribution for the C153 location is shown as a function of distance from the centre of the confined fluid. Snapshots of the interior of these RMs, shown in Figure 3.A.4 of Appendix 3.A, reflect that C153 locates itself away from the centre of the aqueous pool and relatively closer to the interface (but not sticking to the charged interface).

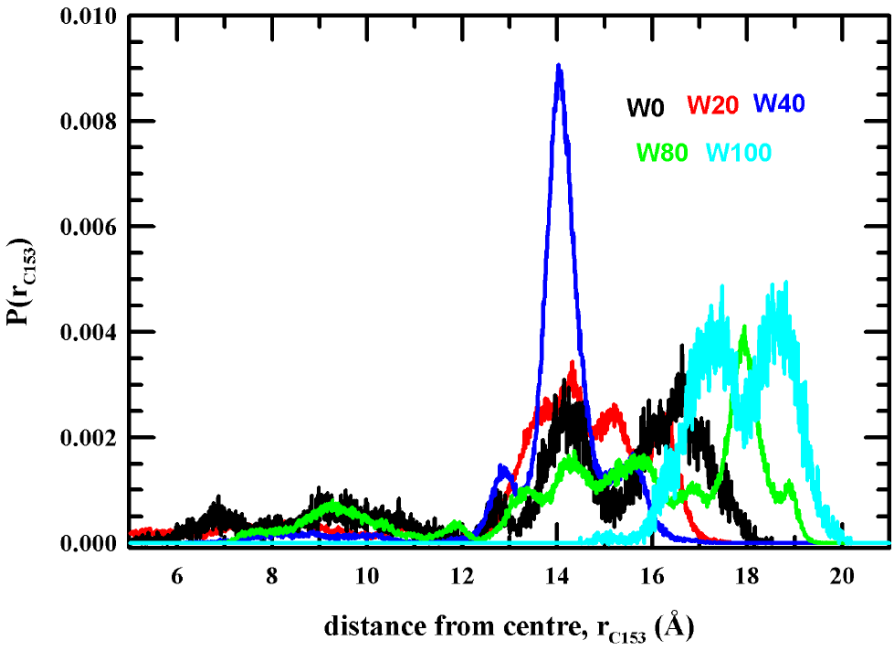

Figure 3.1: Probability distribution of the position of C153 center-of-mass (COM), $P(r_{C153})$ from the centre of the RM in these three confined binary mixtures. $P(r_{C153})$ in pure water RM (W100) and pure methanol RM (W0) are also provided for comparison.

3.3.1.1 Effects of confinement on preferential solvation

The preferential solvation phenomenon for C153 in these aqueous solutions of methanol is examined in Figure 3.2 where the populations of methanol and water in the immediate environment of the solute is monitored as a function of mixture composition. Note the upper panels of Figure 3.2 depict the simulated number of different types of solvating particles for C153 in these bulk and confined binary mixtures, while the lower panels present the corresponding fractions. As expected, the number of water molecules in the immediate environment of C153 increases as water concentration is increased in both the bulk and the confined binary mixtures. A closer inspection of the upper panels, however, clearly reveals that (i) the increase in the number of water molecules in the immediate environment of C153 with water concentration is not as sharp in the confinement as in the bulk (~10 times in the RM versus ~17 times in the bulk) and (ii) the decrease of the number of methanol molecules in the immediate environment of C153 upon increasing water concentration in the mixture is not as strong in the confinement as found for the bulk (~2.5 in the bulk versus 1.3 in the RM). This becomes more obvious in the lower panels where the change of population in number fraction is compared between the confined and bulk binary mixtures for the compositions studied. This indicates that confinement is capable of influencing the preferential solvation phenomenon through modulation of the solute-solvent interactions at the molecular lengthscale. This is important because this suggests that the curvature of a nanoscopic geometric boundary can participate in solvent sorting and assist a dissolved solute to better execute its preference of a particular component over the other in a mixture. In the context of a cellular environment where multi-component fluid exists, this observation may have a bearing on designing drugs where optimization of the ratio of the hydrophilic-to-hydrophobic interaction is critical for appropriate solubility, transportation and release in multi-component aqueous media.

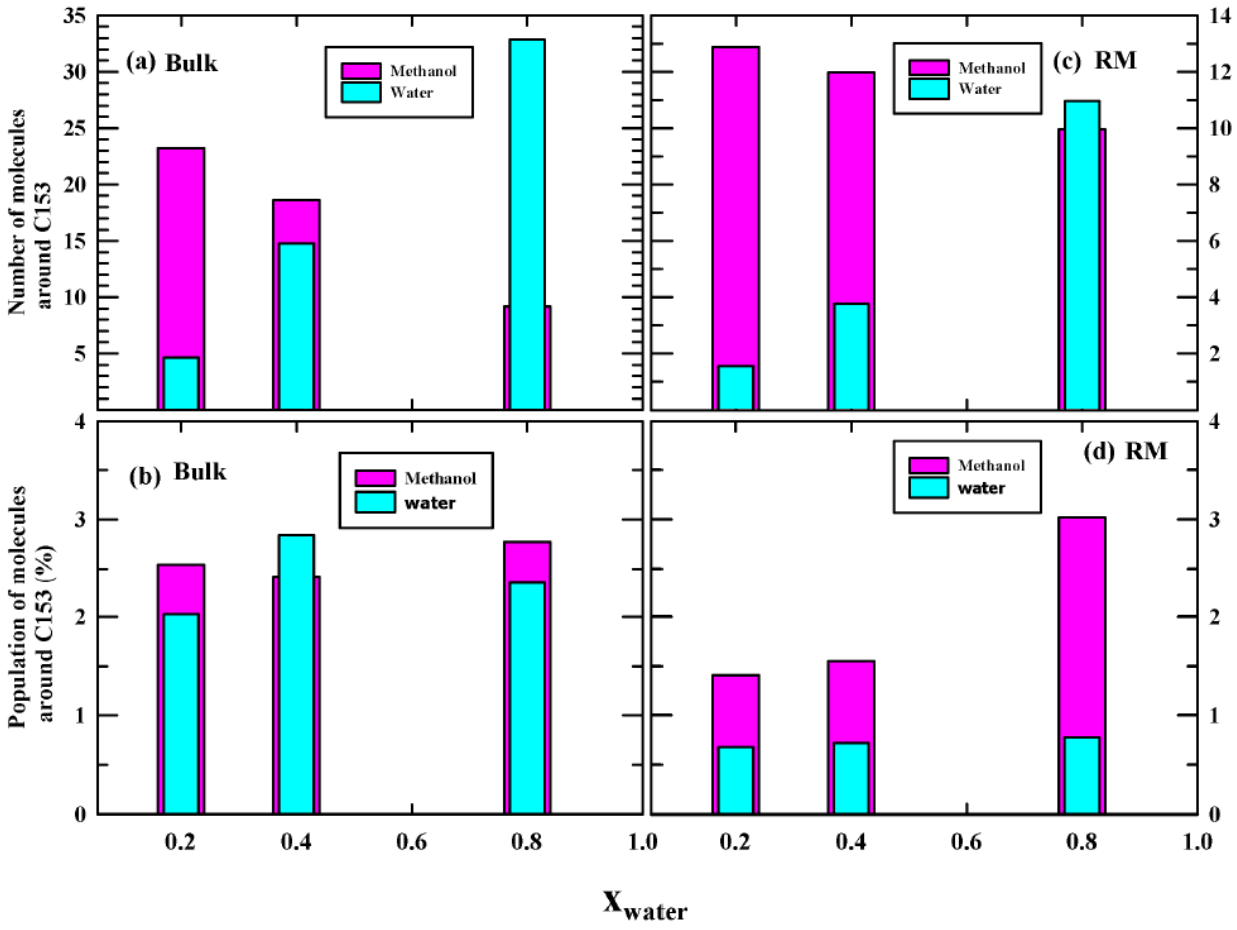

Figure 3.2: Number of mixture component molecules around the dissolved solute C153 in these *bulk* binary mixtures (left panels) and in the corresponding *confined* binary mixtures (right panels). Note the number of molecules is shown in the upper panels while the corresponding fractions are presented in the lower panels.

Figure 3.A.5 (Appendix 3.A) compares the distance-dependent fractional population distribution in these bulk and confined binary mixtures. This radial population distributions show that the methanol populations in the immediate environment of C153 in all these confined mixtures are larger than that of water. For the corresponding bulk binary mixtures, however, this trend is not followed, and the population of water in the immediate environment of C153 in W40 becomes larger than that of methanol. What is even more intriguing is that the methanol population around C153 in W80 becomes greater in the RM confinement than that in the bulk binary mixture. This is an interesting scenario for preferential solvation of C153 in aqueous binary mixture of methanol under confinement. Can this difference in the relative population distributions of methanol be considered as an indication of confinement-enhanced preferential solvation of C153? Keeping in mind the coarse-grained nature of the interaction potentials employed and thus the inherent inadequacy of reproducing the real solution structure in simulations, these results should be interpreted with care. This caveat notwithstanding, distance-dependent population distributions shown in this figure corroborates well with the results presented in Figure 3.2. These results also reveal that water and methanol molecules are not participating in the formation of large clusters, leading to alcohol-rich and alcohol-depleted domains.

Next, we show in Figure 3.3 the ratio of methanol and water populations ($R = P(MeOH)/P(H_2O)$) in the immediate environment of C153 in these bulk and RM-confined binary mixtures. Clearly, the methanol population in the immediate environment of the dissolved C153 is much higher than the water population. This figure therefore strongly suggests that the preferential solvation of C153 in aqueous methanol solution becomes more pronounced under nanoscopic confinement, and this enhancement is further augmented at low methanol concentration.

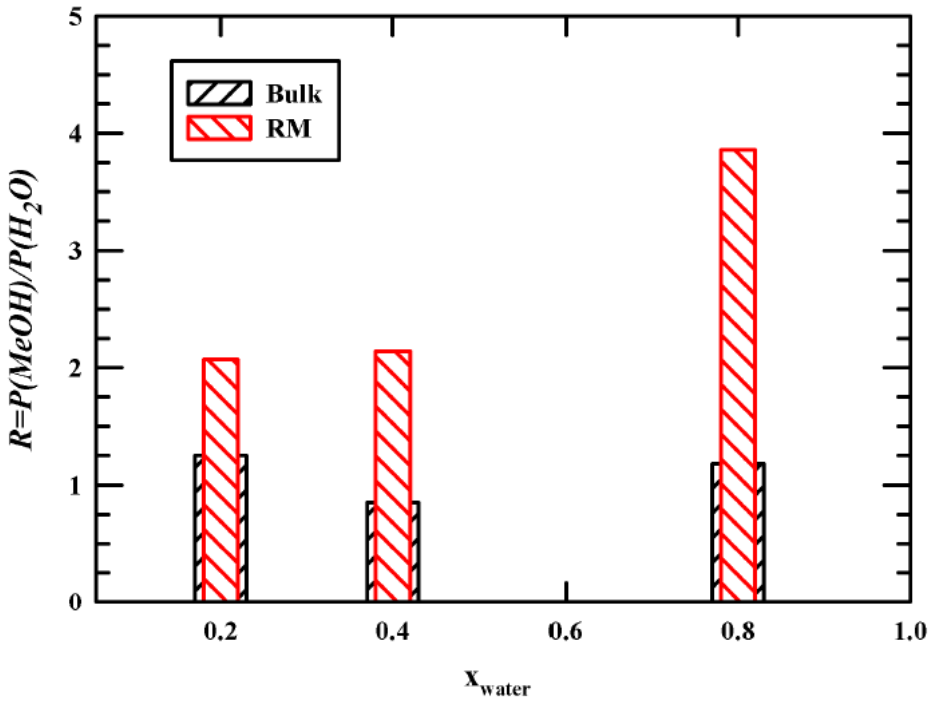

Figure 3.3: Ratio of methanol and water populations ($R = P(MeOH)/P(H_2O)$) within a spherical region of radius 7.0 Å around C153 COM. Results for both the bulk and confined binary mixtures are presented.

3.3.2 Hydrogen bond structure and dynamics of the system

3.3.2.1 Effects of confinement on the H-bond structure of aqueous methanol solutions

For exploring the effects of confinement on the H-bond structure and dynamics of methanol-water binary mixtures, we have calculated both the inter- and the intra-species average number of H-bonds per acceptor molecule, namely, n_{ww} (water-water H-bond per water molecule), n_{mm} (methanol-methanol H-bond per methanol molecule), and n_{mw} (methanol-water H-bond per methanol molecule). While obtaining the average number of H-bonds, we have also calculated the average population of molecules which are participating in forming the H-bonds. This allows us to explain the underlying molecular picture in detail. This is because the calculated n_{xy} (x and y denote the species) will describe the actual number of inter-species or intra-species H bonds, excluding the contributions from the non-participating molecules.

The following protocol[33–37] has been followed for detecting the H-bonds between water molecules (n_{ww}):

a) the distance between the donor oxygen atom and acceptor oxygen atom is less than 0.35 nm, b) the $O-H$(donor)-O (acceptor) angle is less than 30°, and c) distance between O and H must be less than 0.245 nm.

For methanol-methanol hydrogen bonds (n_{mm}), the following geometric criteria[38] have been considered:

a) the distance between the donor oxygen atom and the acceptor oxygen atom is less than 0.35 nm, b) the $O-H$ (acceptor)- O (donor) angle is less than 30°, and c) distance between O (donor) and H (acceptor) must be less than 0.26 nm.

The above criteria have also been followed for calculating the number of H-bonds between methanol and water, n_{mw}.

The effects of confinement on the tetrahedral structure of water in these binary mixtures have been investigated via the calculations of the distribution of tetrahedral order parameter (Q_i)[39],

$$Q_i = 1 - \frac{3}{8}\sum_{j=1}^{3}\sum_{k=j+1}^{4}(cos\theta_{ijk} + {}^{1}/_{3})^2 \qquad (3.1)$$

where Q_i represents the tetrahedral order parameter of the i^{th} water, θ_{ijk} the angle subtended by each pair (designated by j and k) of the nearest four water molecules on the central i^{th} water molecule. For a random and uniform distribution of these angles, $Q = 0$; for a perfect tetrahedral structure, $Q = 1$. Note that the distribution, $P(Q)$, rather than the ensemble averaged value of Q itself, is what is more relevant here. This is because for compositions like W20, W40 the average Q values for the bulk binary mixtures are nearly zero although there exist a considerable number of water molecules for which $Q > 0$. The ensemble-averaged Q values for bulk and confined systems are provided in Table 3.B.3 (Appendix 3.B). Although for W80, the average Q value is not such deviated from neat water $< Q >$, we find the $P(Q)$ is very much different from neat water $P(Q)$. For these bulk systems, overall tetrahedrality is compromised upon addition of methanol. The impact of confinement on $P(Q)$ for water in these three binary mixtures have been explored via a systematic comparison among the simulated distributions for these bulk and confined mixtures, confined neat water and bulk neat

water. In this way, we attempt to study and qualitatively understand the influence on the tetrahedrality of bulk neat water under spherical confinement, the addition of a small molecular hydroxylic solvent that is soluble in water at any proportion and subsequently confining these binary aqueous mixtures under the spherical confinement of the same size.

3.3.2.1.1 Tetrahedral order parameter distribution $P(Q)$

The effects of the addition of methanol and confinement upon the tetrahedral network structure of water are illustrated in Figure 3.4. Simulated $P(Q)$ for water in W20, W40 and W80 are shown for both bulk and under confinement. Note that for confined binary mixtures, the average 'over-all' distributions are presented along with the separated distributions for the RM 'interfacial' and the 'core' water molecules. The corresponding distributions for bulk and confined neat water[17] are also shown in each of the panels for facilitating the comparison. One general observation is that the tetrahedral order parameter distributions for water in all these binary mixtures in bulk and under confinement are wider than those for neat water in bulk and under confinement. The width (full width at the half maximum) of these distributions increases with the increase of methanol concentration in the aqueous mixture. Moreover, $P(Q)$ samples population with negative Q values for binary mixtures more than that for neat RM water and this population with negative order parameter values becomes nearly equal to that with positive Q values in the methanol-dominated binary mixtures. This is very interesting and immediately suggests that the long-range orientational order of water is perturbed more upon addition of alcohol than confining neat water in a nanoscopic RM cage. Confinement does assist in further distorting the tetrahedrality of the bulk binary mixtures at all these compositions but the impact remains always minimal. The separated-out distributions for the interfacial water (7.00 Å thickness) and core water (~20 Å radius) molecules of the confined mixtures resemble each other in both shape and width and are very similar to the 'over-all' distributions in each of these mixtures. All these results, therefore, demonstrate that presence of the alcohol imparts a more debilitating impact on the orientational order of water than induced by nanoscopic confinement.

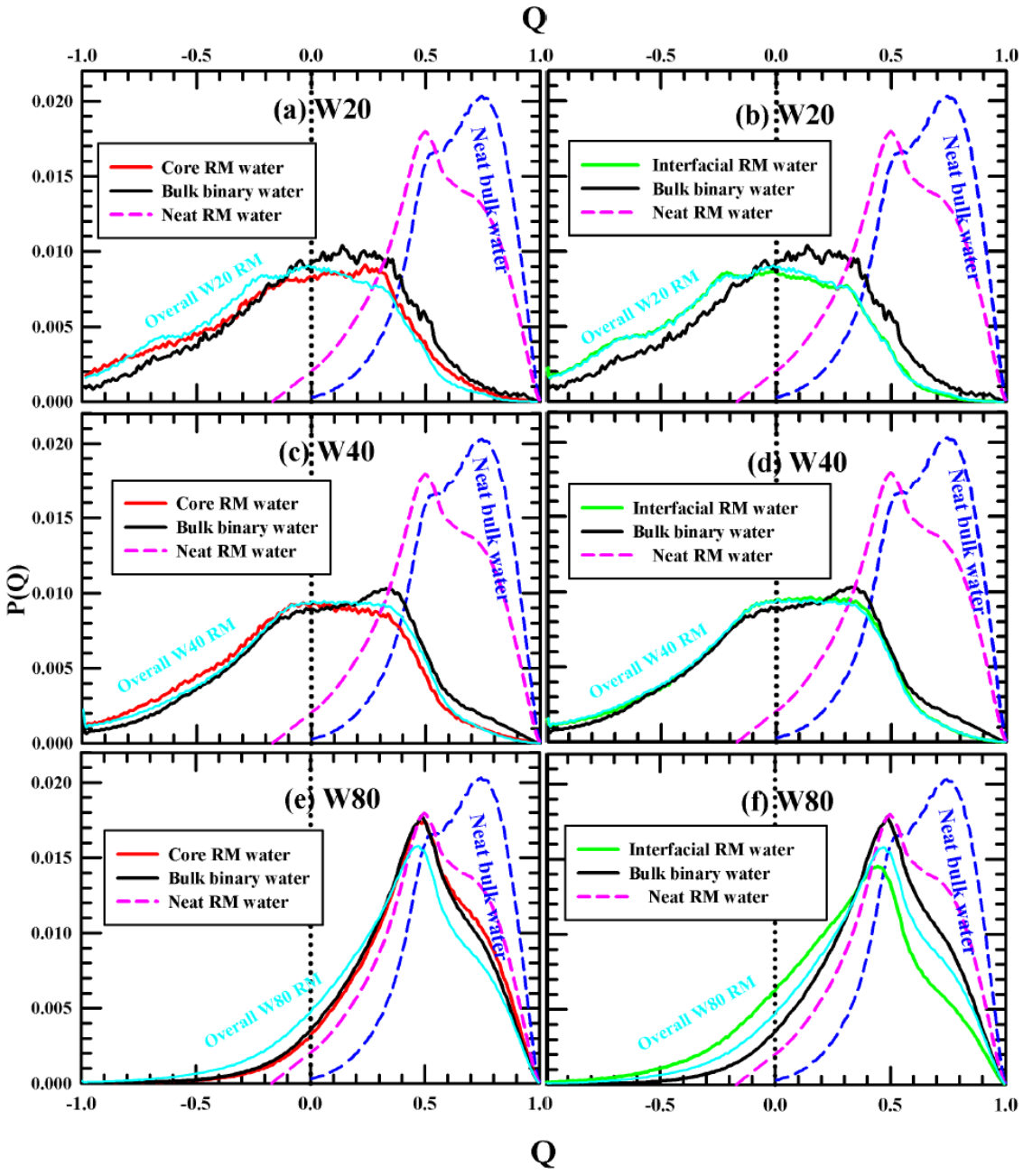

Figure 3.4: Tetrahedral order parameter (Q) distribution P(Q) for water molecules in these three binary mixtures ((a), (b) W20, (c), (d) W40, (e), (f) W80). Left column represents P(Q) of water in the core of the RM (a sphere of radius of 20 Å from the centre of the confined pool) and bulk mixtures. The right column represents the same for interfacial water molecules and, water molecules in those bulk binary mixtures. For comparison P(Q) of neat bulk water is shown in each of these panels.

It has already been pointed out that for binary mixtures a significant population is characterized by $Q < 0$ values. For neat bulk water, the main peak of the distribution of $cos\theta_{ijk}$, $P(cos\theta)$ is broad and appears at ~107º, a value quite close to the tetrahedral angle (109.5º). A weak shoulder at ~50º also accompanies the angle distribution. Here θ_{ijk} is the angle subtended by each pair (designated by *j* and *k*) of the nearest four water molecules on the central i^{th} water molecule. Figure 3.5 presents the simulated $P(cos\theta_{ijk})$ for water in these three binary mixtures in bulk and under confinement. The dramatic impact of methanol on water tetrahedrality at the local level is quite obvious for the W20 bulk binary mixture (upper panel) where the typical broad peak at ~107º for both bulk and RM-confined neat water has disappeared nearly completely; instead, the shoulder at ~50º for neat water has acquired significant population, shifted to further lower angles and broadened significantly providing a peak at ~25º. This is a new and novel observation which demonstrates the devastating impact of methanol on water tetrahedrality in aqueous solutions at very high alcohol concentrations. Nanoscopic confinement of this binary mixture (W20) further flattens the peak at ~107º via shifting more populations to lower angles, resulting in significant growth of the peak at ~25º. This feature is observed for both the interfacial and core water molecules under confinement at this composition. Gradual increase of water concentration leads to regaining of the local tetrahedrality slowly (see the middle panel for W40) and pushing the low angle peak back toward relatively higher angles. This peak is finally restored at the angle (~50º) where the shoulder for neat bulk water appears but with increased populations (see the lower panel for W80). For W80 binary mixture, the population densities around these peak positions (~107º and ~50º) for water molecules inside the RM core and in the bulk are very similar. However, the population distributions for interfacial water molecules at this composition reflect a different behaviour where the low angle population (~50º) is increased by ~2-3 fold over that for the corresponding core water but this increase occurs at the cost of reducing the population that possess near tetrahedrality. Water molecules with near-tetrahedral orientations (~107º) may be linked to water molecules that possess 'strong hydrogen bonds' revealed in the Raman spectroscopic measurements of liquid water[40,41] via the observation of a peak at ~3250 cm^{-1}. Water molecules with orientation angle ~50º, on the other hand, maybe termed as those with 'weak hydrogen bonds' and are responsible for the peak ~3440 cm^{-1} in the relevant Raman spectra of liquid water[40,41] Interestingly, results reported by a very recent Raman spectroscopic study[42] corroborates well with our simulation findings.

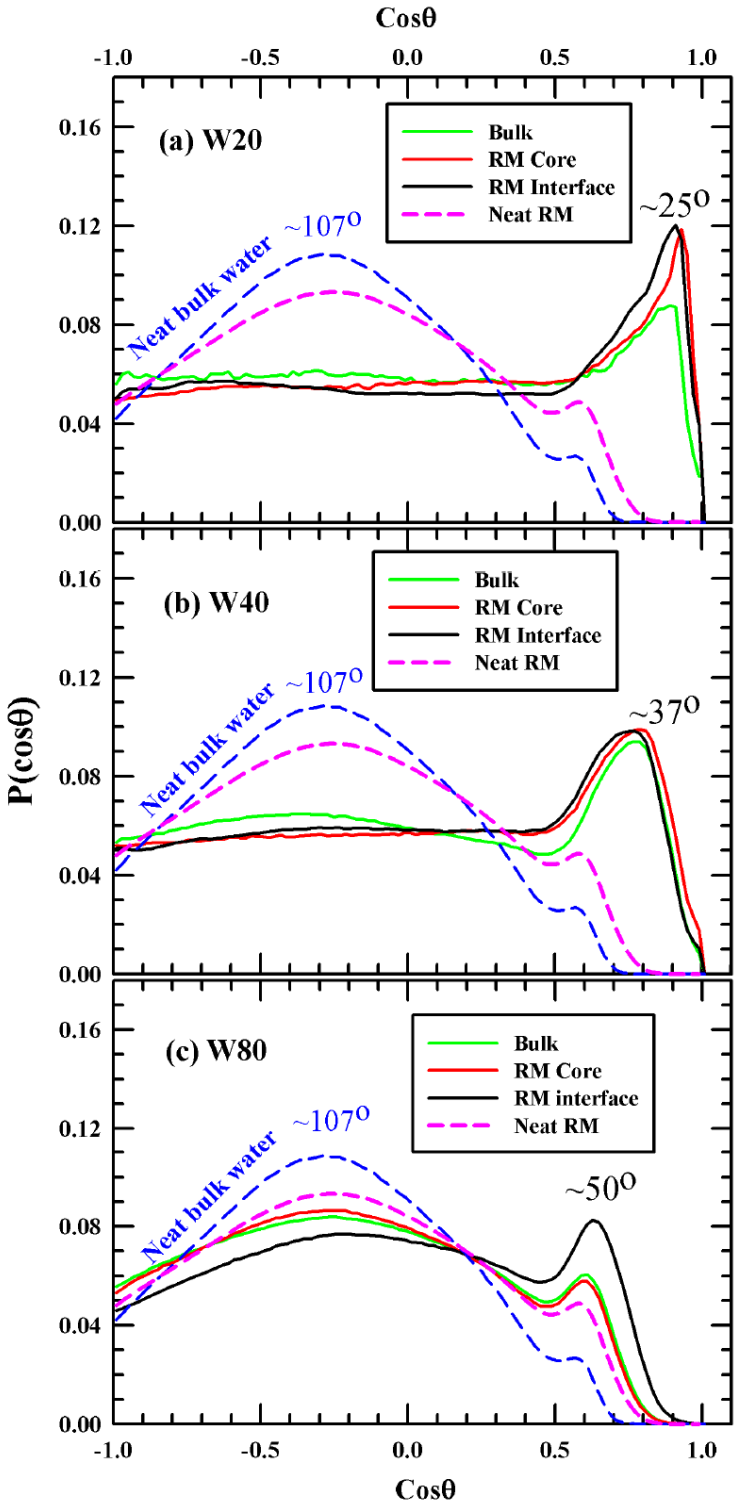

Figure 3.5: Distribution of orientation angle of one water COM with two other nearest neighbours water COM, $P(cos\theta)$, in these binary mixtures ((a) W20, (b) W40, (c)W80). $P(cos\theta)$ for water molecules residing in the inner core of the RM, at the interface and for water in the corresponding bulk mixtures are shown. $P(cos\theta)$ for neat bulk water is provided in each of these panels.

This detailed analysis of tetrahedral order parameter for water in aqueous methanol solutions provides an opportunity to discuss two different propositions regarding water structure in these binary mixtures that were put forward by neutron diffraction[7] and a widely held view[43]. Relevant neutron diffraction measurements[7] of methanol-water mixture suggests that bulk water-like tetrahedral network structure exists even for solutions at high methanol concentrations. While the other view[6,43] is that, the water-structure around methanol becomes 'enhanced' in aqueous solutions up to a certain methanol concentration and then softens up and gets distorted upon further addition of methanol. Our results, shown in Figure 3.4, reflects overlap of the tetrahedral order parameter distributions for neat bulk water with the bulk binary mixtures at all the three methanol concentrations. This overlap of $P(Q)$ suggests that a non-negligible bulk-like water population exists in aqueous solutions even at a very high methanol concentration (see, for example, the results for W20). The extent of overlap increases as methanol is diluted via successive addition of water in the binary mixture. This may be construed as 'regaining' or 'enhancement' of the tetrahedral network structure of water at a very low concentration of methanol. Note that the neutron scattering measurements probes structure at the molecular lengthscale, whereas the Raman scattering probes the collective part of the polarizability fluctuations. This inherent difference in lengthscales that are probed by the neutron scattering (nearest-neighbour density fluctuations) and the Raman scattering (collective polarizability fluctuations measurements[44,45]) has been reflected in the respective conclusions on solution water structure based on results from these two different measurements. However, simulations can avoid this lacuna and probe both the local and collective structures semi-accurately. The present simulation study is therefore rightly suited for uniformly and cogently explaining the water structure in these binary mixtures revealed by experiments that probe different lengthscales.

3.3.2.1.2 Number of Hydrogen bonds per molecule

We have calculated, for these bulk and confined binary mixtures, the average number of inter-species and intra-species hydrogen bonds (N_{xy}^{H}) and the corresponding participating fraction populations (f_{xy}) of the relevant species. Simulated results are shown in Figure 3.6 where the average number of H-bonds are shown in the upper panels and the participating fraction population in the lower panels. H-bond numbers corresponding to confined RM systems are

provided in Table 3.B.4 (Appendix 3.B) and that of bulk systems are given in Table 3.B.5 (Appendix 3.B). Results for bulk and confined binary mixtures have been compared to explore the confinement effects. In addition, N_{xy}^{H} and f_{xy} for molecules in the interfacial and the inner (core) regions have been separately calculated to examine the impact of the interface on these quantities, and the difference (if any) among the corresponding interfacial, core and overall quantities. Number of water-water hydrogen bonds (N_{ww}^{H}) per water molecules in W20, W40 and W80 binary mixtures and the fraction of water molecules (f_{ww}) participating in the water-water H-bonds in them are shown respectively in Figure 3.6(a) and **3.**6(b). As the methanol concentration is diluted by successive addition of water in the binary mixture, N_{ww}^{H} increases from ~1.3 to ~2.8 for both the bulk and the confined systems. Considering N_{ww}^{H} ~ 3.58 for neat bulk water[17], it is clear that addition of methanol in water hinders the formation of direct water-water H-bonds, and the impact of confinement on this hindrance appears to be weak across the mixture composition when the overall N_{ww}^{H} for RM confined mixture is compared with the bulk counterpart. However, the simulated N_{ww}^{H} for the interfacial water molecules in W20 and W40 is slightly larger than that for the core water molecules but the reverse is seen for W80. Noticing that these numbers are small and the associated error could be as large as the difference between them, one is tempted to ignore this mixture composition-dependent difference. However, if we recognize that a substantial portion of the total water population in these binary mixtures would be utilised to solvate the charged AOT interface and the associated counterions, then the number of water molecules available for the core region would be much less for mixtures with low water concentrations. If this is indeed the scenario for confined mixtures, then the participating fractional water population for water-water H-bond should reflect a corroborative mixture composition dependence. This behaviour is clearly reflected in Figure 3.6(b) where the simulated f_{ww} in the core is less than that in the interface for W20 and W40 mixtures but nearly the same for W80. The same logic explains the reverse mixture composition dependence of the methanol-methanol counter-parts, N_{mm}^{H} and f_{mm}, shown in Figure 3.6(c) and Figure 3.6(d). For methanol-water H-bonds and fraction population, N_{mw}^{H} and f_{mw}, the composition dependence is shown in Figure 3.6(e) and 3.6(f). What is striking here is the large difference in N_{mw}^{H} and f_{mw} between the bulk and confined binary mixtures. This can be understood by considering the hydration of the charged interface and counterions, and recognizing that these inter-species quantities would be regulated by the availability of either of the mixture components.

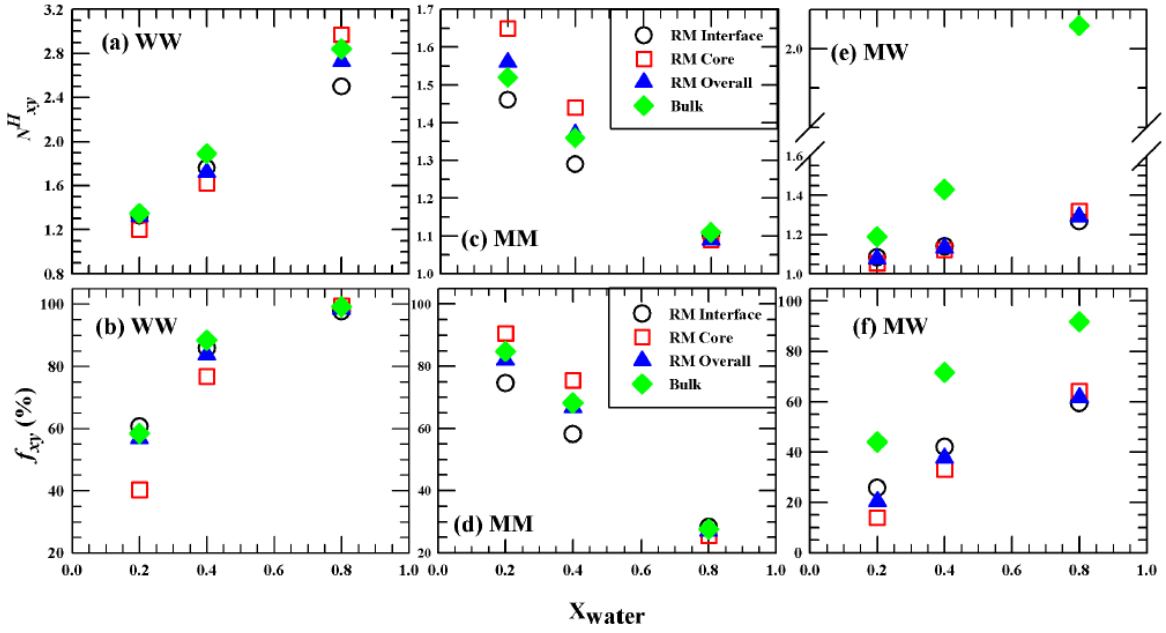

Figure 3.6: The average number of H-bonds per donor molecule (N_{xy}^{H}) (upper panel) and population of donor molecules (f_{xy}) participating in the formation of H-bonds (lower panel) for these three binary mixtures. Parameters corresponding to core water in the RM, interfacial water and the overall RM water are shown and compared against the corresponding bulk values. Legends shown in the middle panel uniformly represent data shown in all the six panels.

3.3.2.2 Intra- and Inter-species H-bond fluctuation dynamics: Structural and Continuous

Structural H-bond relaxation dynamics has been followed via the dynamic correlation function, $C_{HB}(t)$ [33,34,36],

$$C_{HB}(t) = \frac{<h(0)h(t)>}{<h>} \qquad (3.2)$$

Here the reformation of H-bond with another neighbouring molecule, after the rupture of a hydrogen bond with an initial partner, is allowed and accounted for. As a result, a connection to the centre-of-mass motion of the participating molecules is established. This means that faster translational motion of the participant molecules will shorten the structural H-bond lifetime[46,47]. The average structural H-bond lifetimes $< \tau_C^{HB} >_{avg}$ are then obtained by time

integrating the multi-exponential fit functions that adequately describe the simulated decays of the correlation function[48–50]:

$$< \tau_c^{HB} >_{avg} = \int_0^\infty dt\,[C_{HB}(t)] = \int dt\ [\sum_{i=1}^{n} a_i \exp(-t/\tau_i)] = \sum_i^n a_i\,\tau_i \ \text{ with } \sum_i a_i = 1.$$

The continuous hydrogen bond lifetime is calculated from the time-correlation function, $S_{HB}(t)$[33,34,36],

$$S_{HB}(t) = \frac{<h(0)H(t)>}{<h>} \qquad (3.3)$$

Note in the above equation that $H(t)$ becomes unity if the tagged pair of molecules, for which $h(0)$ is calculated, remains continuously H-bonded for a time *t* or else $H(t) = 0$. $S_{HB}(t)$ describes the probability that a tagged pair of molecules remain continuously H-bonded for a duration of *t* and becomes zero when this continuity of the H-bond between the same partners breaks down. The average continuous H-bond lifetime $< \tau_S^{HB} >_{avg}$, has been obtained, as before, via time integration: $< \tau_S^{HB} >_{avg} = \int_0^\infty dt\,[S_{HB}(t)]$.

Table 3.B.6 (Appendix 3.B) summarizes the simulated structural and continuous H-bond lifetimes for water-water, methanol-water and methanol-methanol species in these three bulk and confined binary mixtures. These average times are calculated only for the overall and inner core H-bonded species. Figure 3.7 depicts the mole fraction dependencies of the average structural and the continuous H-bond lifetimes for water-water (left panels), water-methanol (middle panels) and methanol-methanol (right panel) species. Representative multi-exponential fits to $S_{HB}(t)$ and $C_{HB}(t)$ and corresponding fit qualities are shown in Figure 3.A.6 (Appendix 3.A). Fit parameters for each of the simulated $S_{HB}(t)$ and $C_{HB}(t)$ are shown in Tables 3.B.7- 3.B.14 (Appendix 3.B). Note all the calculated average times in these panels show non-monotonic composition dependence to varying degrees. This is not surprising as several earlier time-resolved fluorescence measurements have already reported non-linear composition dependence of various relaxation rates in bulk aqueous solutions of alcohols and other amphiphilic molecules[51–54]. The interesting aspect of this general observation is, however, the emergence of this non-monotonicity in simulations of composition-dependent H-bond fluctuation dynamics, where coarse-grained classical interaction potentials have been employed. This reflects that these model interaction potentials are capable of qualitatively

capturing the solution structure of these binary mixtures although the composition at which the abrupt change in the slope of the average relaxation times occurred differs between simulations and dynamic fluorescence measurements.

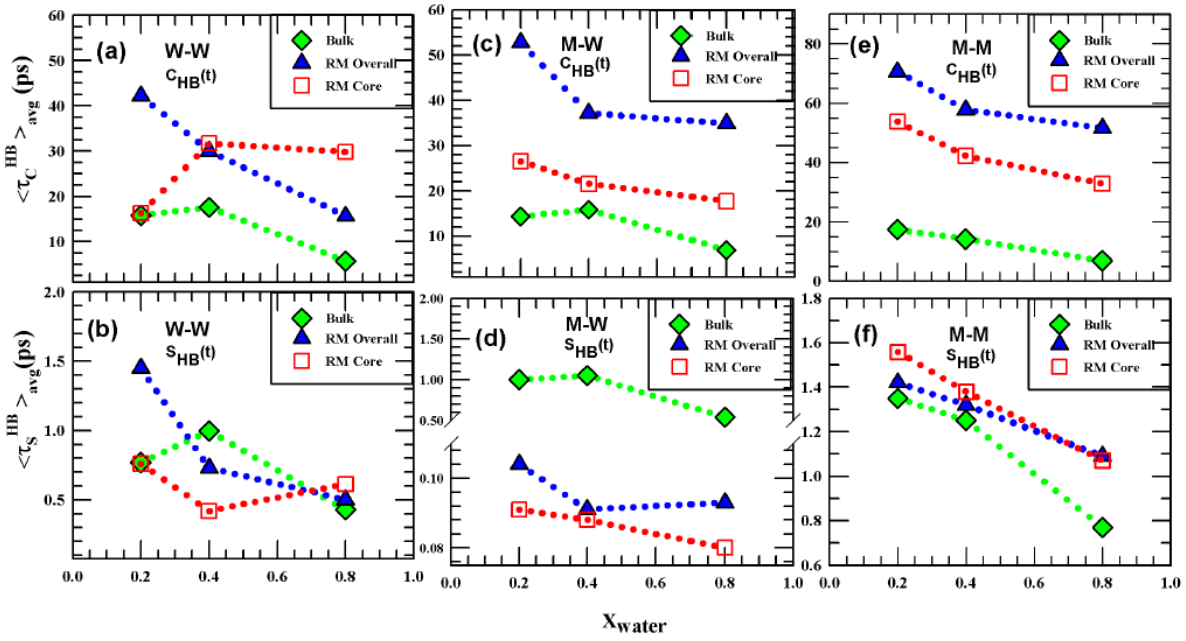

Figure 3.7: Average structural H-bond relaxation times, τ_C^{HB},(upper panel) and the continuous hydrogen bond relaxation times, τ_S^{HB}, (lower panel) for water-water (WW) (left column), methanol-water (MW) (middle column) and methanol-methanol (MM) (right column) are shown. Corresponding average lifetimes for these three bulk binary mixtures are also presented for comparison.

The composition-dependent structural H-bond lifetimes shown in the upper panels indicate that the overall $< \tau_c^{HB} >_{avg}$ slows down substantially upon confining these binary mixtures and the confinement impact is stronger for methanol-methanol (M-M) and methanol-water (M-W) than water-water (W-W) structural H-bond lifetimes. Dilution of methanol upon addition of water increases the number of more mobile water molecules (relative to those engaged in solvation of the AOT interface and the counterions) which, in turn, shortens $< \tau_c^{HB} >_{avg}$ at higher water content. Simulated mean squared displacements (MSDs) at these three compositions, shown in Figure 3.A.7 (Appendix 3.A), supports this view. Interestingly, the overall $< \tau_c^{HB} >_{avg}$ for water-water becomes faster upon increasing the water mole fraction

in the RM whereas it levels off for water-methanol species. The reason for such a behaviour can be found in the composition dependence of structural lifetimes for core water molecules, shown also in all these panels along with the average lifetimes for both bulk and confined binary mixtures. The overall water-water $< \tau_c^{HB} >_{avg}$ plateaus because the addition of water molecules beyond those necessary for solvating the charged interface and counter ions does not increase any further the average centre-of-mass mobility of core water molecules. At higher water mole fraction, however, the number of water molecules with relatively higher mobilities increases in the interfacial region (~7Å thick) because water molecules beyond a certain number are not required for fully solvating the charged interface and the counterions. The shortened Debye screening length due to an effective screening[2] allows a greater number of water molecules in the interfacial region in accessing relatively higher mobilities at higher water concentration. Consequently, the overall water-water $< \tau_c^{HB} >_{avg}$ for the confined mixture becomes shorter upon increasing the water mole fraction. Unfortunately, $< \tau_c^{HB} >_{avg}$ for the interfacial water molecules could not be estimated in the present simulations because of technical reasons. These reasons include the non-availability of sufficient number of water molecules within the interfacial region that supports reformation of H-bond after the breakage of the H-bond with the initial partner, followed by centre-of-mass diffusion and subsequently allowing the generation of statistically meaningful data for the relevant $C_{HB}(t)$.

The mixture composition dependence of methanol-water overall $< \tau_c^{HB} >_{avg}$ can be understood from the concentration-dependent water mobilities in these confined binary mixtures. Methanol-methanol (MM) structural H-bond relaxation times follow a similar trend shown by the corresponding methanol-water average relaxation timescale ($< \tau_c^{HB} >_{avg}$). For bulk binary mixtures, the mole fraction dependence of $< \tau_c^{HB} >_{avg}$ reflects the change in the solution structure upon changing the mixture composition.

The non-monotonicity in composition dependence is observed also for the continuous H-bond lifetimes, $< \tau_S^{HB} >_{avg}$, shown in the lower panels of Figure 3.7. The non-monotonic mole fraction dependence of $< \tau_S^{HB} >_{avg}$ in bulk, aqueous solutions of alcohol is a new finding and connected probably to the alcohol-induced modifications of the water structure in solutions. Note that methanol-methanol continuous H-bond lifetimes becomes longer upon confinement

but become shorter upon successive addition of water in the mixture. The similarity in water-water $< \tau_S^{HB} >_{avg}$ values among bulk binary mixture, overall and core water molecules for W80 is understandable. The difference between the overall and core $< \tau_S^{HB} >_{avg}$ values for W20 and W40 mixtures suggests that the water-water H-bonds for interfacial water molecules are longer-lived than those for core water in these binary mixtures. The same conclusion may be drawn for the methanol-water H-bonds in all these binary mixtures. The striking difference between the bulk and overall water-water $< \tau_S^{HB} >_{avg}$ values for W20 mixture clearly indicates that the water-water H-bonds for interfacial water molecules are strongly influenced by the charged interface. Motional restriction of interfacial water molecules and the consequent reduction in the configurational entropy in this water-depleted mixture may be a reason for increasing the water-water $< \tau_S^{HB} >_{avg}$ value by more than a factor of two over that in the corresponding bulk mixture. Because methanol is not preferred near the interface, this consideration does not apply to methanol-water H-bonds and, as a result, the $< \tau_S^{HB} >_{avg}$ values in these bulk binary mixtures remain larger than the corresponding overall values for confined mixtures.

The preference of the mixture components for respective locations inside the RM confinement has been investigated to support the explanations provided above for composition dependence of the H-bond lifetimes. Figure 3.8 depicts the simulated fractional population of water and methanol at the interfacial and the inner core regions of RM for these three mixtures. Note here that for W20 mixture, water molecules locate predominantly near to the interfacial region (upper panel). This is because the majority of water molecules at this composition is being utilized to solvate the charged interface and the counterions in this region. Water, being more polar than methanol, therefore overwhelmingly populates this interfacial region for all the confined mixtures. Interestingly for W80, methanol population near the interfacial region appears to be larger than water. Note this fraction percentage has been calculated with respect to the individual number of component particles present in this mixture This picture, therefore, suggests that the more polar water molecules in the core region expel a dominant portion of methanol away and the expunged methanol particles are compelled to populate the interfacial region because of confinement. Data in the lower panel further support the view where methanol molecules in W20 and W40 mixtures prefer to locate themselves in the core region as water predominantly resides at the interface. For W80, water overwhelmingly populates the

core region, forcing some of the methanol molecules to leave this region. This relative preference of locations shown by water and methanol in these confined binary mixtures subtly brings out the demixing feature inherent to aqueous solutions of alcohol although methanol is miscible in water at all proportions without any solubility gap.

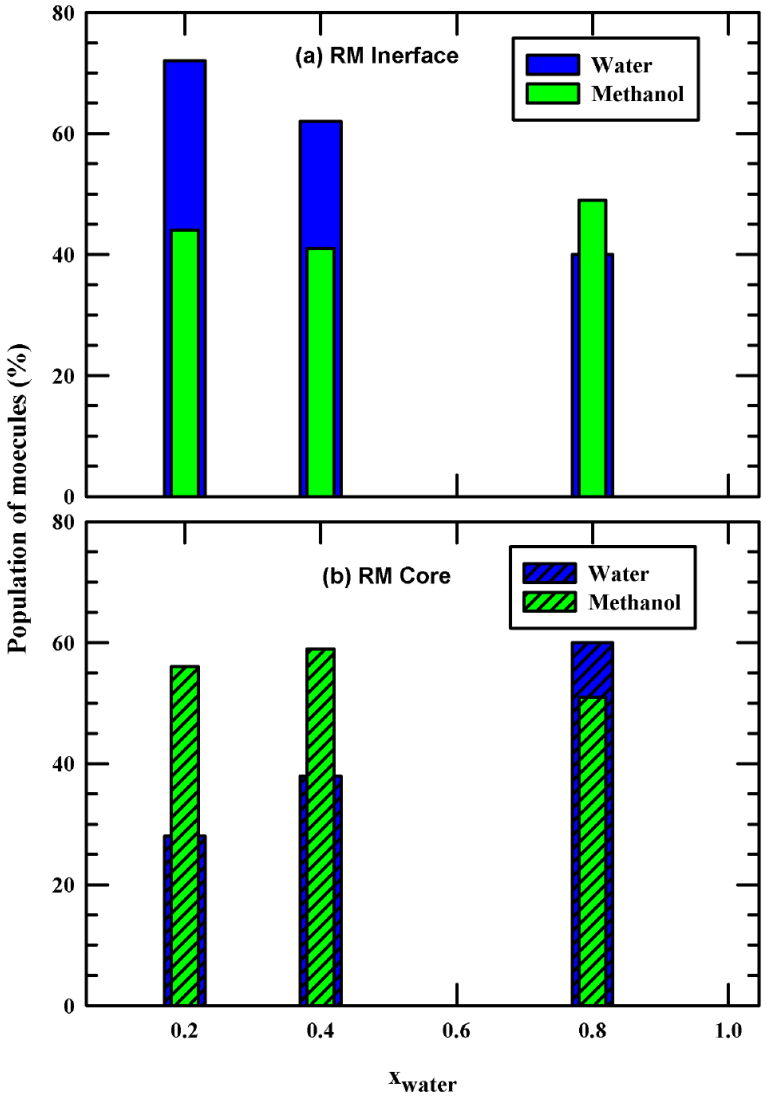

Figure 3.8: Fractional population of water and methanol at the interfacial region (a), and in the core region (b) of the RM for these three binary mixtures.

3.4 Conclusion

In summary, the phenomenon of preferential solvation of a neutral dipolar solute dissolved in binary mixtures of water and methanol and its mixture composition dependence have been thoroughly investigated via molecular dynamics simulations. The effects of confinement of these aqueous alcohol solutions by a nanoscopic spherical AOT reverse micellar cavity have been explored. Three representative binary mixtures covering methanol-rich to water-rich compositions have been considered. We have observed confinement-induced enhancement of preferential solvation in each of the binary mixtures studied. In these confined mixtures the dissolved neutral dipolar solute, C153, has been found to locate itself away from the centre of the aqueous pool and relatively closer to the interface (but not sticking to the charged interface).

When scrutinizing the H-bonding network structure of these methanol-water binary mixtures, the tetrahedral network has been found to be strongly affected by the presence of the alcohol itself; confinement plays a mere secondary role in distorting the already strongly influenced global tetrahedral order parameter and local tetrahedrality. Nanoscopic RM confinement has been found to significantly slow down the water-water, methanol-water and methanol-methanol structural H-bond fluctuation dynamics over those in the bulk binary mixtures. The continuous H-bond fluctuation dynamics, on the hand, becomes faster upon confinement of these mixtures except for the methanol-dominated mixture (W20) where most of the water molecules engage themselves in solvating the charged AOT interface. In W20 mixture, the interfacial water slows down considerably the continuous H-bond dynamics possibly because of their restricted motions. Finally, we would like to end by noting that the elementary knowledge gained here about the confinement-induced enhancement of preferential solvation may have a strong bearing on drug dissolution in a cellular environment and their transportation. Further detailed studies on confined systems with the confinement of cylindrical shapes resembling blood vessels may be interesting and are thus worth exploring.

Appendix 3.A

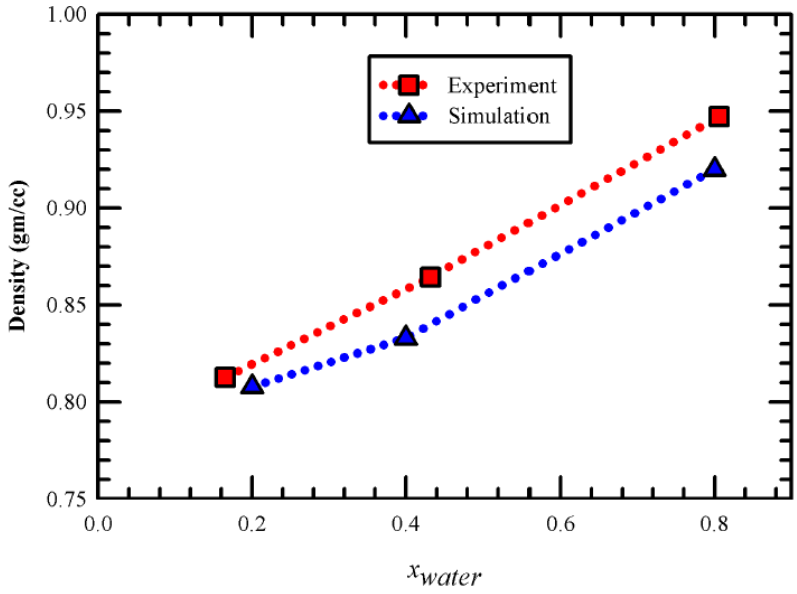

Figure 3.A.1: Comparison of our simulated density with available experimental density.

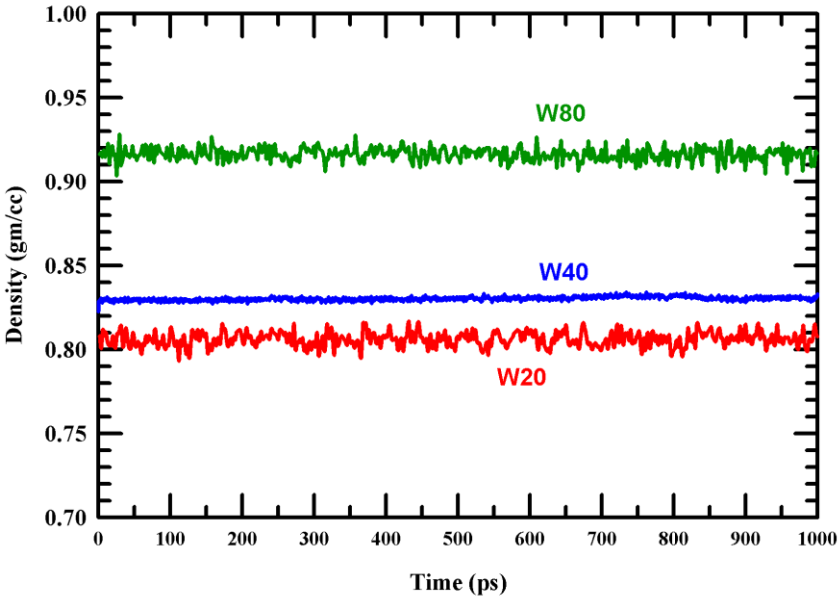

Figure 3.A.2: Time evolution of densities duping 1ns NPT run with pre-equilibrated system. This figure ensures our systems have reached equilibration before our production run.

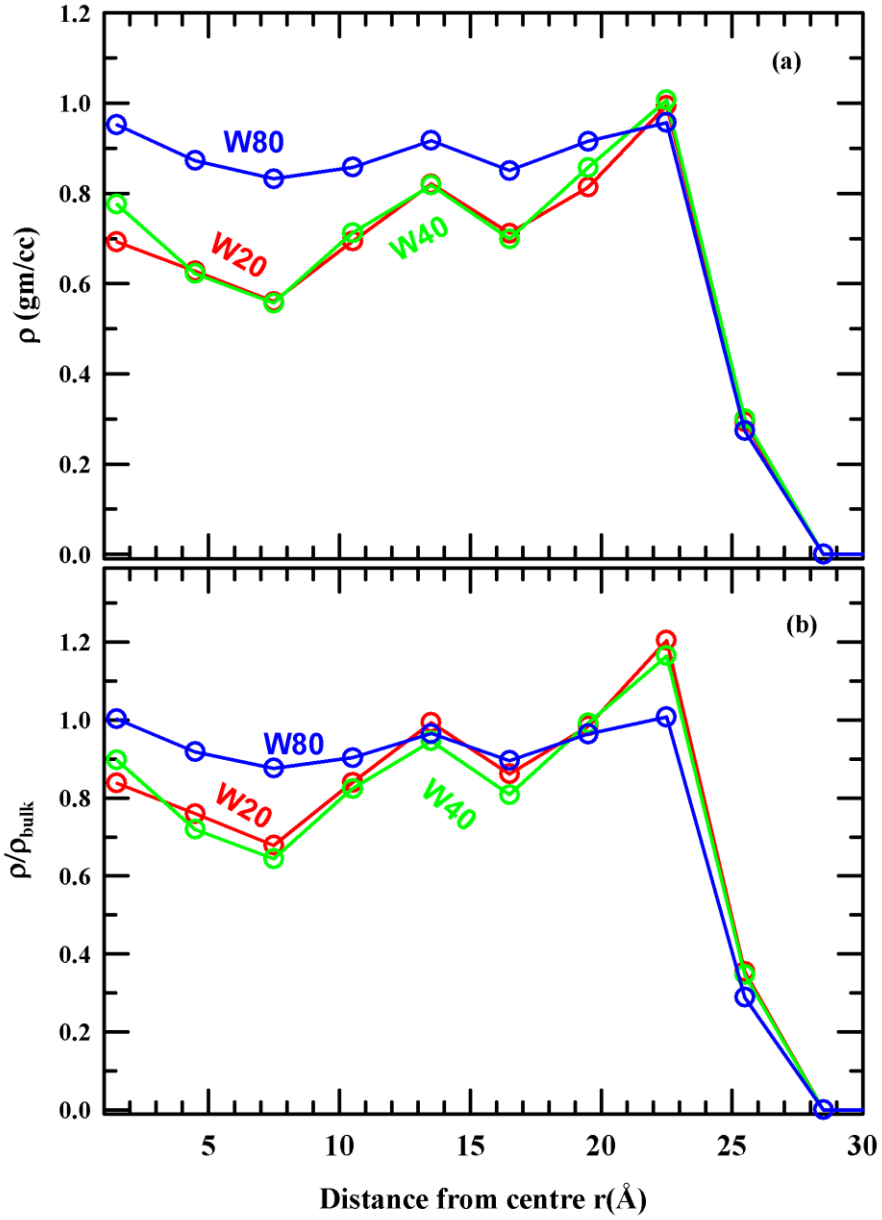

Figure 3.A.3: Distance dependent density of three alcohol-water binary mixtures inside the AOT RM having 27.5 Å cavity radius. The distance is measured from the cavity centre. The mass density (ρ) is shown in the upper panel while the normalized density with respect to that of its bulk (ρ/ρ_{bulk}) is shown in the lower panel.

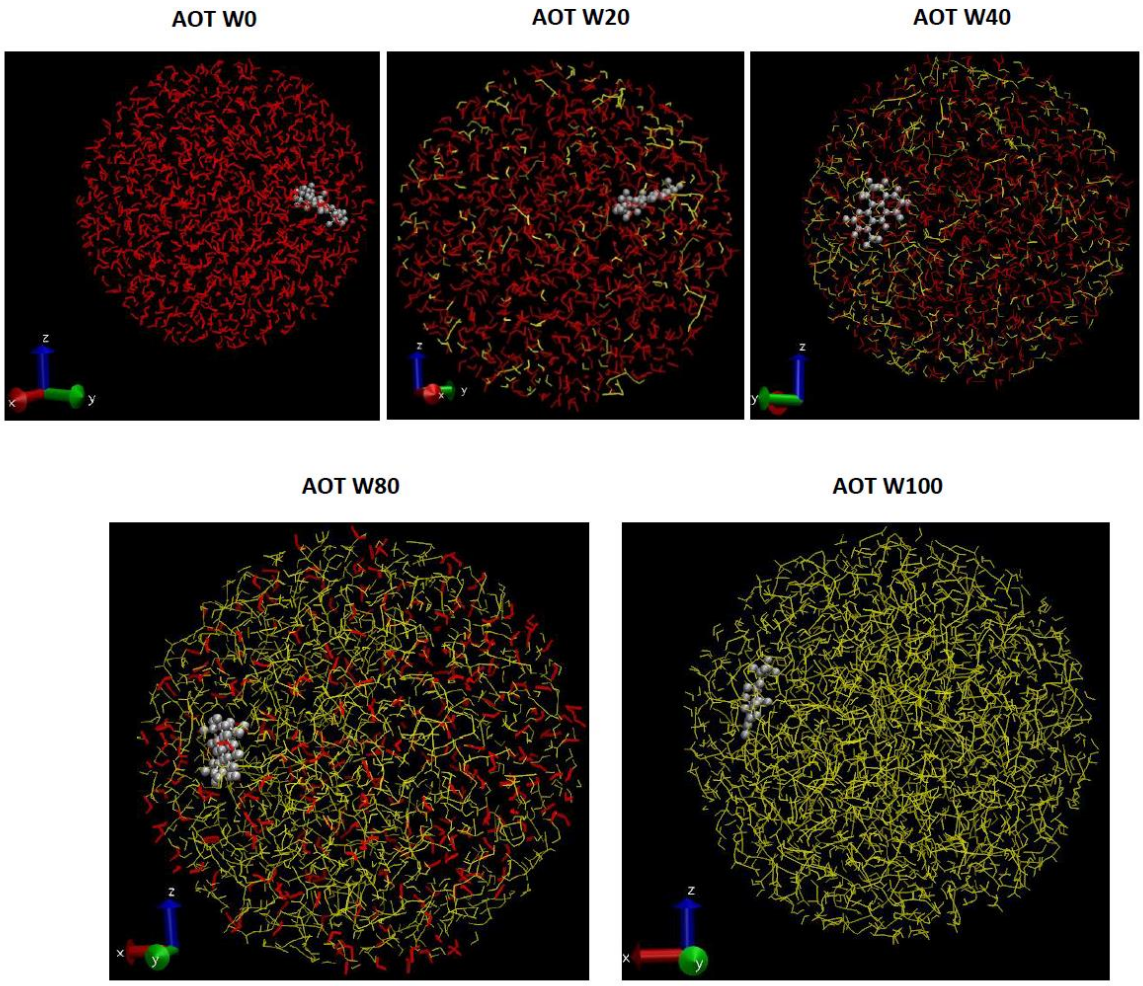

Figure 3.A.4: Snapshots of five simulated RMs to visualise position of C153. Only the inside of the RM is presented. Red lines are methanol, yellow lines are water and C153 is represented by white ball and stick.

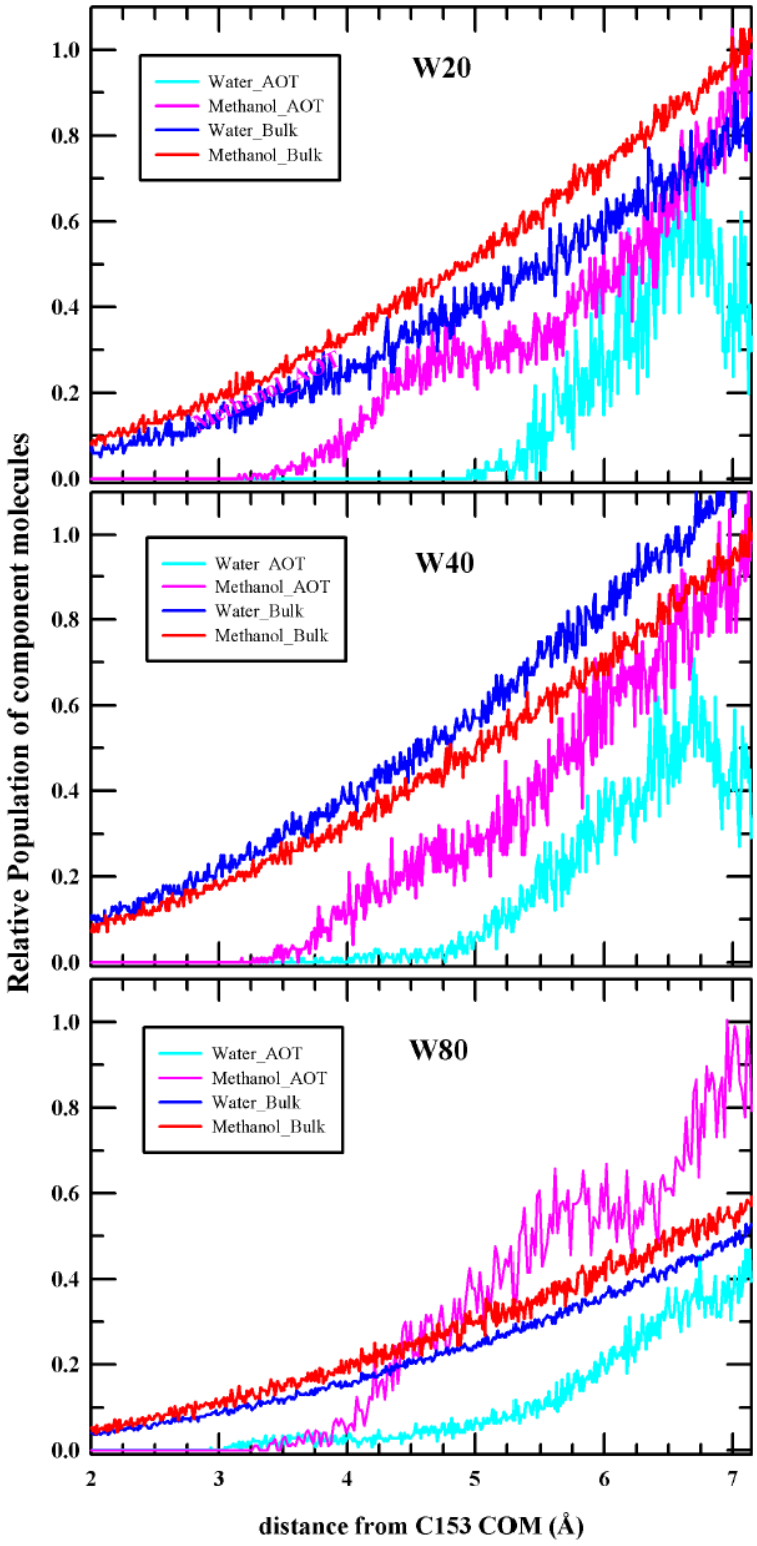

Figure 3.A.5: The relative population of water and methanol molecules of these three binary mixtures ((a) W20, (b) W40, (c) W80) both in the bulk and under confinement, shown as a function of distance from the COM of C153.

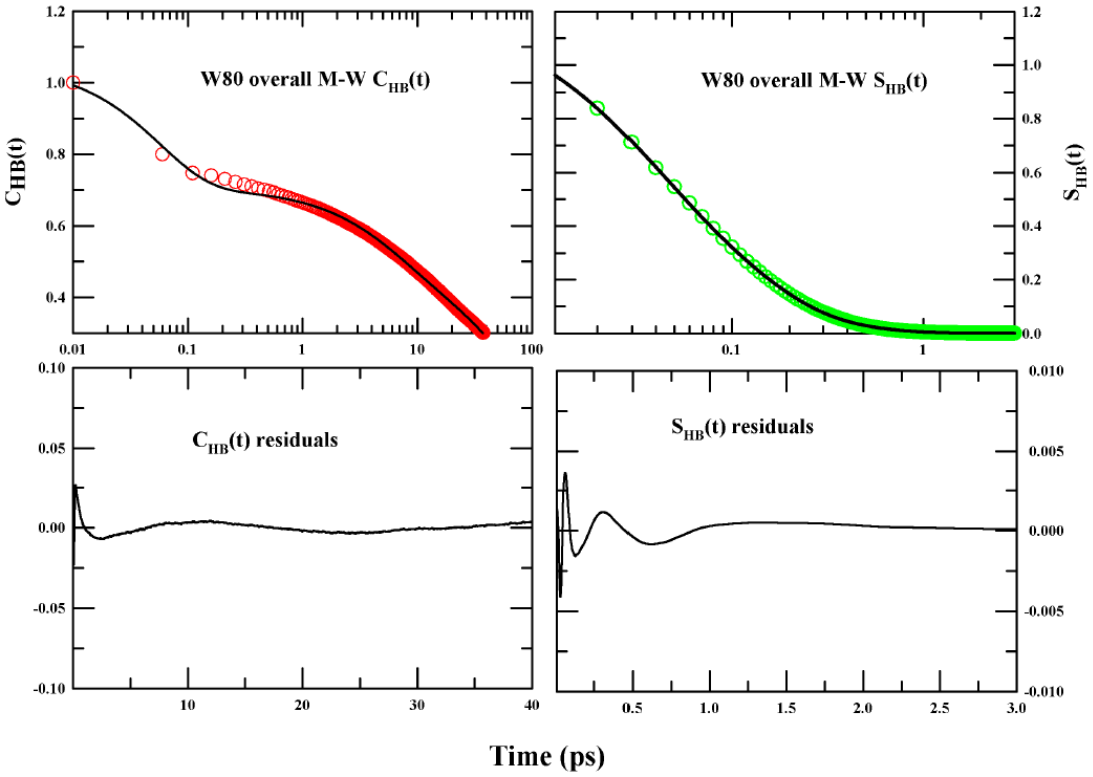

Figure 3.A.6: Representative three exponential fits to $C_{HB}(t)$ and $S_{HB}(t)$ and the corresponding residuals. The behaviour of residual indicates that the multi-exponential fits adequately describe these simulated decays.

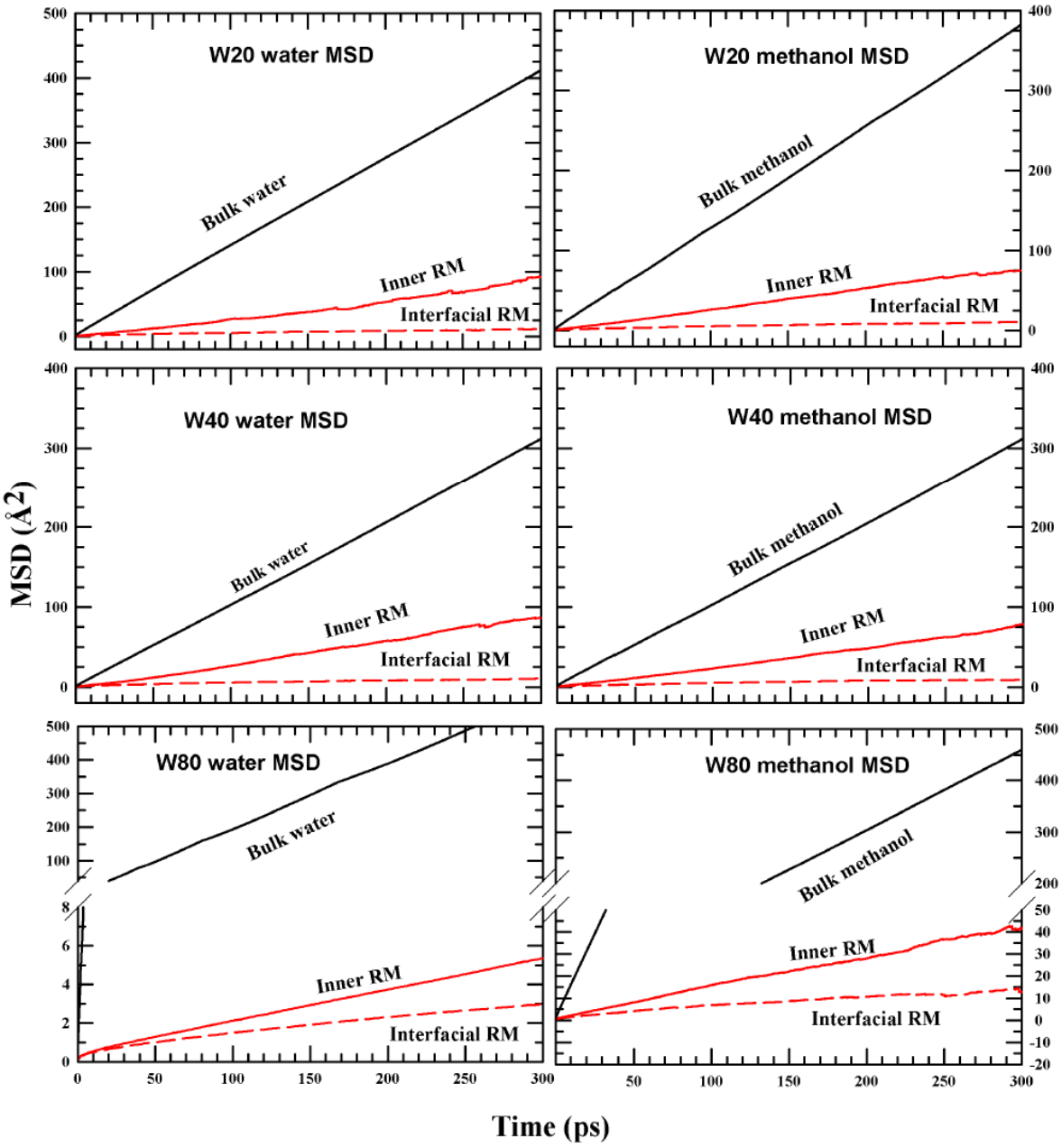

Figure 3.A.7: Mean squared displacement of water (left column) and methanol (right column) within RM system for three binary mixtures.

Appendix 3.B

Table 3.B.1: Number of water and methanol molecules simulated at different compositions.

Mixture	Water mole fraction	N_{water}	N_{meth}
W20	0.2	230	915
W40	0.4	520	770
W80	0.8	1400	330

Table 3.B.2: The simulated mass density of three compositions and comparison with available experimental density. Note exact mole-fraction dependent comparison is not possible because of unavailable data. We carried out error analysis with nearest available mole-fraction density (given in the parenthesis).

Mixture	Density (gm/cc)		Error (relative to experiments) (%)
	Simulations	Experiments	
W20	0.808	0.8127 (x_w~0.1650)	0.6
W40	0.833	0.8644 (x_w~0.4320)	3.63
W80	0.92	0.9472 (x_w~0.8060)	1.35

Table 3.B.3: Ensemble averaged tetrahedral order parameter of three binary mixtures both in bulk and confined systems.

	AOT RM			Bulk
	Interface	**Inside**	**Overall**	
W20	-0.206	-0.178	-0.19	-0.035
W40	-0.039	-0.090	-0.053	0.020
W80	0.294	0.456	0.374	0.437

Table 3.B.4: The average number of hydrogen bonds per donor molecule and population of donor molecules participating in the corresponding hydrogen bonding in the three binary mixtures *confined* in AOT RM. The average number of H-bonds per donor molecule at the interface, at the inner core and averaged over all RM water ('over-all') are also shown.

Confined Hydrogen bond									
	W20			W40			W80		
	Interface	***Inner***	***Overall***	***Interface***	***Inner***	***Overall***	***Interface***	***Inner***	***Overall***
MM	1.46	1.65	1.56	1.29	1.44	1.37	1.10	1.09	1.09
population(%)	74.6	90.60	81.95	58.21	75.49	66.68	28.31	25.54	27.10
WW	1.33	1.20	1.32	1.76	1.62	1.72	2.50	2.97	2.73
population(%)	60.66	40.26	56.77	85.82	76.72	83.64	97.61	99.4	98.5
MW	1.08	1.06	1.08	1.14	1.12	1.13	1.27	1.32	1.29
population(%)	25.67	13.98	20.38	42.03	33.16	37.72	59.40	64.27	61.65

Table 3.B.5: The average number of H-bonds per donor molecule and population of donor molecules participating in the corresponding H-bonding in the three *bulk* binary mixtures.

Bulk H-bond			
Species	**W20**	**W40**	**W80**
Methanol-Methanol (MM)	1.52	1.36	1.11
Part (%)	84.82	68.21	27.68
Water-Water (WW)	1.35	1.89	2.84
Part (%)	58.40	88.37	99.14
Methanol-Water (MW)	1.19	1.43	2.03
Part (%)	44	71.73	91.80

Table 3.B.6: Average Structural and continuous H-bond lifetimes for water-water (WW), methanol-water (MW) and methanol-methanol (MM) H-bonds in these three bulk and confined binary mixtures.

		WW		**MW**		**MM**	
		$< \tau_c^{HB} >_{avg}$	$< \tau_S^{HB} >_{avg}$	$< \tau_c^{HB} >_{avg}$	$< \tau_S^{HB} >_{avg}$	$< \tau_c^{HB} >_{avg}$	$< \tau_S^{HB} >_{avg}$
W20	**RM core**	16.30	0.76	26.49	0.09	53.76	1.56
	RM Overall	42.19	1.45	52.50	0.10	70.59	1.42
	Bulk	15.78	0.77	14.36	1.00	17.43	1.35
W40	**RM Core**	31.70	0.42	21.51	0.09	42.25	2.03
	RM Overall	30.0	0.73	37.16	0.09	57.75	2.26
	Bulk	17.60	0.10	15.82	1.05	14.22	1.25
W80	**RM Core**	29.85	0.61	17.69	0.08	32.84	1.07
	RM Overall	15.70	0.50	34.86	0.09	51.65	1.09
	Bulk	5.75	0.43	6.89	0.54	6.95	0.77

Table 3.B.7: Fit parameter for water-water, methanol-methanol and methanol-water structural H-bond dynamics ($C_{HB}(t)$) in ***bulk*** mixtures. Average timescales are calculated using $< \tau_{C/S}^{HB} >_{avg} = \frac{(\sum_{i=1}^{n} a_i \tau_i)}{(\sum_{i=1}^{n} a_i)}$.

		a_1	τ_1 (ps)	a_2	τ_2 (ps)	a_3	τ_3 (ps)	$< \tau_C^{HB} >_{avg}$(ps)
WW	W20	0.15	0.34	0.35	6.33	0.50	27.03	15.78
	W40	0.10	0.27	0.27	5.24	0.63	25.64	17.60
	W80	0.18	0.22	0.52	2.95	0.31	13.70	5.75
MM	W20	0.11	0.30	0.22	6.85	0.67	23.81	17.43
	W40	0.13	0.31	0.33	6.71	0.54	22.22	14.22
	W80	0.14	0.23	0.60	4.22	0.27	16.40	6.95
MW	W20	0.14	0.30	0.30	5.99	0.56	22.22	14.36
	W40	0.12	0.32	0.34	6.14	0.53	25.64	15.82
	W80	0.25	0.39	0.58	4.29	0.17	19.23	6.89

Table 3.B.8: Fit parameter for water-water, methanol-methanol and methanol-water continuous H-bond relaxation ($S_{HB}(t)$) dynamics in ***bulk*** mixtures.

		a_1	τ_1 (ps)	a_2	τ_2 (ps)	a_3	τ_3 (ps)	$< \tau_S^{HB} >_{avg}$ (ps)
WW	**W20**	0.168	0.126	0.54	0.58	0.3	1.47	0.770
	W40	0.156	0.154	0.503	0.75	0.34	1.745	0.996
	W80	0.172	0.101	0.353	0.32	0.476	0.626	0.428
MM	**W20**	0.131	0.172	0.303	0.675	0.566	1.984	1.35
	W40	0.152	0.183	0.353	0.734	0.495	1.95	1.25
	W80	0.110	0.128	0.468	0.528	0.422	1.20	0.77
MW	**W20**	0.196	0.177	0.526	0.768	0.2755	2.04	1.00
	W40	0.103	0.136	0.358	0.525	0.540	1.57	1.05
	W80	0.173	0.109	0.506	0.400	0.322	0.987	0.539

Table 3.B.9: Fit parameters for methanol-water (MW) structural H-bond relaxation ($C_{HB}(t)$) dynamics in ***confined*** mixtures.

	a_1	τ_1 (ps)	a_2	τ_2 (ps)	a_3	τ_3 (ps)	$< \tau_C^{HB} >_{avg}$ (ps)
W20 overall	0.31	0.05	0.14	5.56	0.6	90.9	52.70
W40 overall	0.33	0.06	0.19	5.99	0.53	71.43	37.16
W80 overall	0.34	0.06	0.21	5.88	0.49	71.43	34.86
W20 inside	0.35	0.06	0.19	6.37	0.50	52.63	26.49
W40 inside	0.35	0.06	0.23	6.25	0.46	45.46	21.51
W80 inside	0.37	0.05	0.23	4.54	0.46	38.46	17.69

Table 3.B.10: Fit parameters for methanol-water (MW) continuous H-bond relaxation ($S_{HB}(t)$) dynamics in ***confined*** mixtures.

	a_1	τ_1 (ps)	a_2	τ_2 (ps)	a_3	τ_3 (ps)	$< \tau_s^{HB} >_{avg}$(ps)
W20 overall	0.48	0.03	0.56	0.11	0.14	0.34	0.10
W40 overall	0.50	0.03	0.58	0.10	0.12	0.31	0.09
W80 overall	0.50	0.03	0.58	0.10	0.13	0.31	0.09
W20 inside	0.43	0.03	0.58	0.09	0.19	0.24	0.09
W40 inside	0.41	0.03	0.57	0.08	0.23	0.22	0.09
W80 inside	0.35	0.02	0.6	0.06	0.29	0.18	0.08

Table 3.B.11: Fit parameters for water-water (WW) structural H bond relaxation ($C_{HB}(t)$) dynamics in ***confined*** mixtures.

	a_1	τ_1 (ps)	a_2	τ_2 (ps)	a_3	τ_3 (ps)	$< \tau_C^{HB} >_{avg}$(ps)
W20 overall	0.15	0.14	0.49	13.16	0.37	97.1	42.19
W40 overall	0.18	0.19	0.32	6.89	0.50	55.55	30.0
W80 overall	0.17	0.09	0.16	2.86	0.67	22.73	15.70
W20 inside	0.07	0.16	0.58	16.13	0.34	20	16.30
W40 inside	0.11	0.39	0.23	6.45	0.65	45.45	31.70
W80 inside	0.13	0.13	0.20	3.53	0.67	43.48	29.85

Table 3.B.12: Fit parameters for water-water (WW) continuous H-bond relaxation dynamics ($S_{HB}(t)$) in ***confined*** mixtures.

	a_1	τ_1 (ps)	a_2	τ_2 (ps)	a_3	τ_3 (ps)	$< \tau_S^{HB} >_{avg}$(ps)
W20 overall	1	1.45	**	**	**	**	1.45
W40 overall	0.26	0.12	0.61	0.57	0.12	2.86	0.73
W80 overall	0.44	0.15	0.57	0.77	**	**	0.50
W20 inside	1.03	0.76	**	**	**	**	0.76
W40 inside	0.32	0.07	0.77	0.57	**	**	0.42
W80 inside	0.39	0.23	0.65	0.84	**	**	0.61

Table 3.B.13: Fit parameters for methanol-methanol (MM) structural H bond relaxation ($C_{HB}(t)$) dynamics in ***confined*** mixtures.

	a_1	τ_1 (ps)	a_2	τ_2 (ps)	a_3	τ_3 (ps)	$< \tau_C^{HB} >_{avg}$(ps)
W20 overall	0.08	0.23	0.14	7.48	0.79	88.50	70.59
W40 overall	0.09	0.22	0.16	7.08	0.75	75.19	57.75
W80 overall	0.106	0.21	0.20	8.16	0.69	72.46	51.65
W20 inside	0.04	0.90	0.19	12.56	0.77	66.67	53.76
W40 inside	0.05	0.70	0.17	9.44	0.77	52.36	42.25
W80 inside	0.08	0.31	0.17	7.29	0.75	42.02	32.84

Table 3.B.14: Fit parameters for methanol-methanol (MM) continuous H-bond relaxation dynamics ($S_{HB}(t)$) in ***confined*** mixtures.

	a_1	τ_1 (ps)	a_2	τ_2 (ps)	a_3	τ_3 (ps)	$< \tau_S^{HB} >_{avg}$(ps)
W20 overall	0.06	0.067	0.30	0.45	0.64	2.01	1.42
W40 overall	0.12	0.11	0.43	0.66	0.45	2.26	1.32
W80 overall	0.14	0.11	0.48	0.61	0.38	2.08	1.09
W20 inside	0.03	0.06	0.33	0.60	0.64	2.12	1.56
W40 inside	0.04	0.07	0.40	0.61	0.56	2.03	1.38
W80 inside	0.09	0.10	0.44	0.55	0.47	1.76	1.07

References

[1] E. Boucher and J. MURRELL, *Properties of Liquids and Solutions* (Wiley, 1982).

[2] P. Atkins and J. De Paula, *Elements of Physical Chemistry* (Oxford University Press, USA, 2013).

[3] K. Liltorp, P. Westh, and Y. Koga, Can. J. Chem. **83**, 420 (2005).

[4] Y. Koga, Can. J. Chem. **77**, 2039 (1999).

[5] H. Frank and M. Evans, J. Chem. Phys. **13**, 507 (1945).

[6] F. t Franks and D. Ives, Q. Rev. Chem. Soc. **20**, 1 (1966).

[7] S. Dixit, J. Crain, W. Poon, J.L. Finney, and A.K. Soper, Nature **416**, 829 (2002).

[8] H.S. Frank and M.W. Evans, J. Chem. Phys. **13**, 507 (1945).

[9] M. D'angelo, G. Onori, and A. Santucci, J. Chem. Phys. **100**, 3107 (1994).

[10] A. Soper and J. Finney, Phys. Rev. Lett. **71**, 4346 (1993).

[11] B. Guchhait, R. Biswas, and P.K. Ghorai, J. Phys. Chem. B **117**, 3345 (2013).

[12] D. Mandal, A. Datta, S.K. Pal, and K. Bhattacharyya, J. Phys. Chem. B **102**, 9070 (1998).

[13] B. Guchhait, R. Biswas, and P.K. Ghorai, J. Phys. Chem. B **117**, 3345 (2013).

[14] H. Berendsen, J. Grigera, and T. Straatsma, J. Phys. Chem. B **91**, 6269 (1987).

[15] S.L. Mayo, B.D. Olafson, and W.A. Goddard, J. Phys. Chem. **94**, 8897 (1990).

[16] B. Chen, J.J. Potoff, and J.I. Siepmann, J. Phys. Chem. B **105**, 3093 (2001).

[17] A. Baksi, P.Kr. Ghorai, and R. Biswas, J. Phys. Chem. B **124**, 2848 (2020).

[18] S. Abel, F. Sterpone, S. Bandyopadhyay, and M. Marchi, J. Phys. Chem. B **108**, 19458 (2004).

[19] P. Kumar and M. Maroncelli, J. Chem. Phys. **103**, 3038 (1995).

[20] H.J. Berendsen, Jv. Postma, W.F. van Gunsteren, A. DiNola, and J.R. Haak, J. Chem. Phys. **81**, 3684 (1984).

[21] M.P. Allen and D.J. Tildesley, *Computer Simulation of Liquids* (Oxford university press, 2017).

[22] E.J. Wensink, A.C. Hoffmann, P.J. van Maaren, and D. van der Spoel, J. Chem. Phys. **119**, 7308 (2003).

[23] A. Aguado and P.A. Madden, J. Chem. Phys. **119**, 7471 (2003).

[24] S. Nosé, Mol. Phys. **52**, 255 (1984).

[25] W.G. Hoover, Phys. Rev. A **31**, 1695 (1985).

[26] J. Faeder and B.M. Ladanyi, J. Phys. Chem. B **105**, 11148 (2001).

[27] J. Faeder, M.V. Albert, and B.M. Ladanyi, Langmuir **19**, 2514 (2003).

[28] J. Faeder and B. Ladanyi, J. Phys. Chem. B **104**, 1033 (2000).

[29] T. Forester and W. Smith, *The Dl_Poly_2 Reference Manual* (1998).

[30] V.R. Hande and S. Chakrabarty, Phys. Chem. Chem. Phys. **18**, 21767 (2016).

[31] Y. Zhang and Z. Xu, Am. Mineral. **80**, 670 (1995).

[32] A. Perera, F. Sokolić, and L. Zoranić, Phys. Rev. E **75**, 060502 (2007).

[33] A. Luzar, Faraday Discuss. **103**, 29 (1996).

[34] A. Chandra, Phys. Rev. Lett. **85**, 768 (2000).

[35] T.C. Berkelbach, H.-S. Lee, and M.E. Tuckerman, Phys. Rev. Lett. **103**, 238302 (2009).

[36] S. Balasubramanian, S. Pal, and B. Bagchi, Phys. Rev. Lett. **89**, 115505 (2002).

[37] A. Luzar and D. Chandler, J. Chem. Phys. **98**, 8160 (1993).

[38] M. Ferrario, M. Haughney, I.R. McDonald, and M.L. Klein, J. Chem. Phys. **93**, 5156 (1990).

[39] J.R. Errington and P.G. Debenedetti, Nature **409**, 318 (2001).

[40] H. Yui, K. Kanoh, H. Fujiwara, and T. Sawada, J. Phys. Chem. A **106**, 12041 (2002).

[41] F. Li, Z. Li, S. Li, W. Fang, C. Sun, and Z. Men, Spectrochim. Acta. A. Mol. Biomol. Spectrosc. **199**, 462 (2018).

[42] F. Li, Y. Wang, Z. Men, and C. Sun, Phys. Chem. Chem. Phys. **22**, 26000 (2020).

[43] Water, A. Comprehensive Treatise, Edited by F. Franks; Plenum: N. Y. (1972).

[44] B. Bagchi, *Statistical Mechanics for Chemistry and Materials Science* (CRC Press, 2018).

[45] B. Bagchi, *Molecular Relaxation in Liquids* (OUP USA, 2012).

[46] S. Das, R. Biswas, and B. Mukherjee, J. Phys. Chem. B **119**, 274 (2015).

[47] S. Das, R. Biswas, and B. Mukherjee, J. Phys. Chem. B **119**, 11157 (2015).

[48] A. Biswas, A. Priyadarsini, and B.S. Mallik, J. Phys. Chem. B **123**, 8753 (2019).

[49] B.S. Mallik, A. Semparithi, and A. Chandra, J. Phys. Chem. A **112**, 5104 (2008).

[50] A. Bankura, A. Karmakar, V. Carnevale, A. Chandra, and M.L. Klein, J. Phys. Chem. C **118**, 29401 (2014).

[51] N. Sarma, J.M. Borah, S. Mahiuddin, H.A.R. Gazi, B. Guchhait, and R. Biswas, J. Phys. Chem. B **115**, 9040 (2011).

[52] S. Indra and R. Biswas, J. Chem. Sci. **128**, 1943 (2016).

[53] T. Pradhan, P. Ghoshal, and R. Biswas, J. Phys. Chem. A **112**, 915 (2008).

[54] T. Pradhan, P. Ghoshal, and R. Biswas, J. Chem. Sci. **120**, 275 (2008).

Chapter 4

Dynamical Anomaly of Aqueous Amphiphilic Solutions: Connection to Solution H-bond Fluctuation Dynamics?

4.1 Introduction

Numerous measurements on aqueous binary mixtures of different amphiphilic molecules have repeatedly revealed anomalous changes in thermodynamic properties[1–7] that cannot be explained employing the concept of random mixing[8]. This means that the Boltzmann's equation would be insufficient for estimating the entropy of mixing for these systems because the enthalpy of mixing is not zero or negligible. This, in turn, indicates that the presence of one species is strongly influencing the interaction among molecules of the other species (same species interaction), rendering statistical mechanical calculations based on the random mixing theory untenable for such solutions. Binary mixture of triethylamine (TEA) and water is a classic example[9] where water-TEA H-bonding interactions contribute significantly to the enthalpy of mixing. Another important factor that critically regulates the mixing is the hydrophobic interaction arising from the ethyl groups. Hydrophobic interaction coupled with hydrophobic hydration and the interspecies H-bonding interactions therefore jointly governs the physical chemistry of aqueous amphiphilic solutions. Naturally, solution structure and dynamics reflect mixture composition dependence that is commensurate with the internal balance between the H-bonding and hydrophobic interactions in such macroscopically homogeneous binary systems.

The structural aspects of aqueous amphiphilic solutions have been explored via neutron diffraction measurements[10–13] by employing tertiary butanol (TBA) as a model amphiphile. The water rich-region has been specially investigated in these measurements to understand how hydrophobic interaction of tertiary butyl (-CMe_3, Me=CH_3) groups among TBA molecules and the corresponding hydrophobic hydration modifies the three-dimensional tetrahedral H-bonded network structure of water. These studies then proceeded further to connect the anomalous

mixture composition dependence of different thermodynamic quantities, particularly those measured at very low TBA concentrations, to the modifications in water structure in such solutions. Several simulation and computational studies have examined the hydrophobic hydration induced modification in solution structure and the role of inter-species H-bonding in binary aqueous mixtures of TBA[14–18] and other alcohols.[19–23] Interestingly, studies employing TBA as an amphiphile is relatively more in number although investigations employing other amphiphiles also focused on solute-induced distortion of water structure, solution heterogeneity and dynamics[24–26]. The reason for employing TBA emerges from the fact that TBA possesses the largest aliphatic group among monohydroxy alcohols that are miscible with water at any proportion. Because of the presence of both the hydrophobic tertiary butyl group and the hydrophilic hydroxyl (-OH) moiety, TBA molecules can simultaneously participate in hydrophobic and hydrophilic interactions with water. This leads to segregation of aqueous solution into microscopic polar and nonpolar domains.[27]

Steady state UV-VIS absorption measurements[28–31] of aqueous solutions of different amphiphiles employing fluorescent probe molecules in the last several years have repeatedly shown not only unexpected spectral shifts (of probe absorption spectrum) upon successive addition of amphiphilic molecules in water but also demonstrated an abrupt change in the direction of the spectral shift (first downward and then upward) at a particular amphiphile concentration. This has been depicted in Figure 4.1. This 'passing through a minimum' for absorption spectral shifts occurs at a very low concentration of amphiphile, and is specific to the amphiphilic hydrophobicity. This is shown in Table 4.1 where $x_{Cosolvent}^{min}$ represents this concentration in mole fraction for a variety of amphiphiles that include 2-butoxyethanol (2-BE)[29], TBA[28,30–32], tetrahydrofuran (THF)[33], 1,4-dioxane (dioxane)[33], tetramethylurea (TMU)[34] and ethanol[28]. Notice that for TBA in water, $x_{Cosolvent}^{min}$ is quite close to the mole fraction of TBA at which the maximum anomaly in the measured thermodynamic quantities has been detected;[2,35–40] subsequent neutron diffraction and neutron scattering studies[10,13,41,42] have indicated the dominance of hydrophobic hydration and hydrophobic interaction induced solute association at that low mole fraction. Mixture composition dependent water structure probed later[14] via simulations of the tetrahedral order parameter, reveals a linear decrease of tetrahedrally coordinated water with x_{TBA} in the concentration range studied. One may extend this idea and assume that similar mechanism of mixing and solvation could be responsible for

hosting the other amphiphiles shown in Table 4.1 at very low concentrations in their respective aqueous solutions.

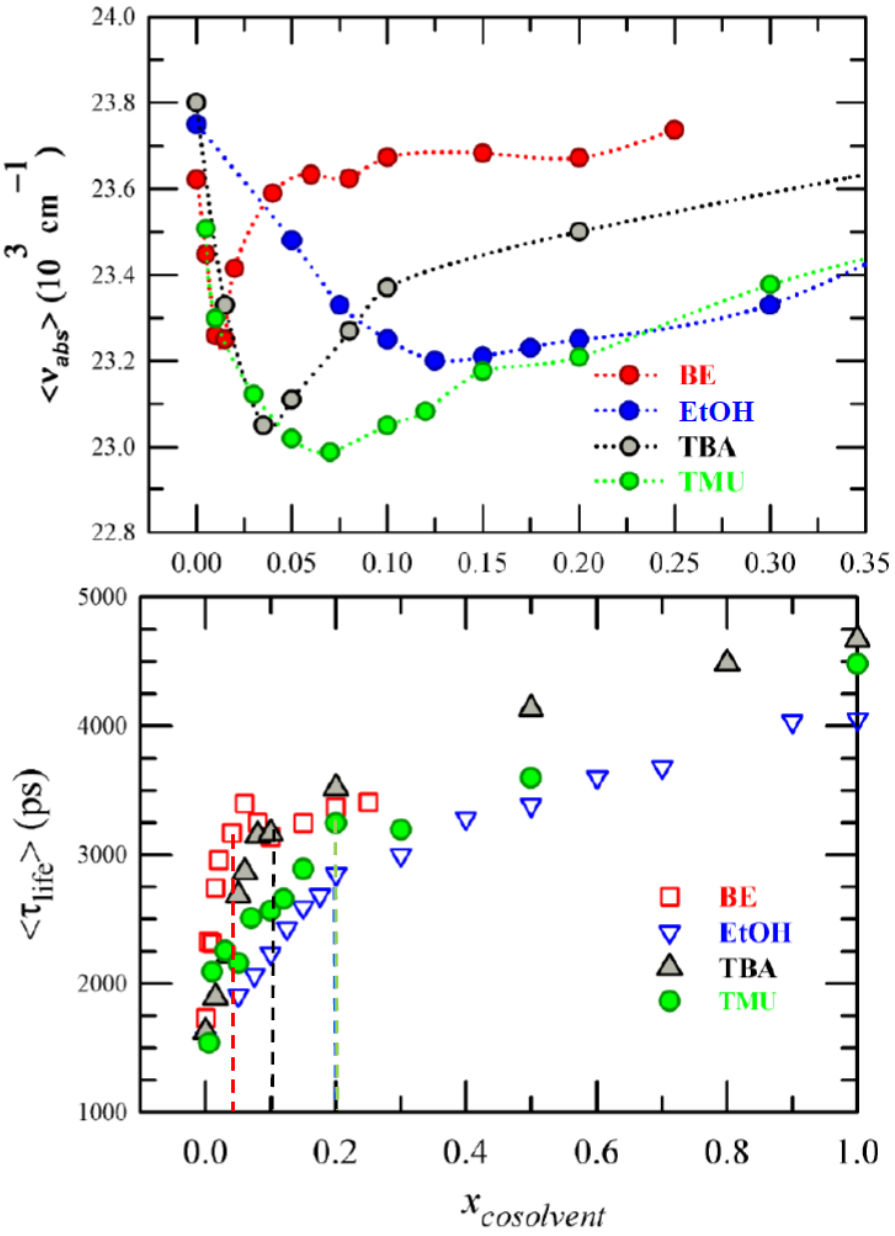

Figure 4.1: Amphiphile mole fraction dependence of UV-VIS absorption spectral frequencies of a neutral dipolar fluorescent solute, coumarin153 (C153), in aqueous solutions of BE, EtOH, TBA, and TMU (upper panel), and the average excited state fluorescence lifetimes ($\langle\tau_{life}\rangle$) of the same solute in those aqueous solutions (lower panel). Dotted lines in the upper panel guide the eyes to connect the data for a particular aqueous solution. Vertical broken lines in the lower panel indicate the amphiphile mole fractions at which the abrupt changes in the slopes occur. All data are color coded.

However, another intriguing observation appears when one carefully examines the corresponding time-resolved fluorescence data reported for these aqueous amphiphilic solutions. These data include mixture composition dependent average excited state fluorescence lifetimes ($\langle\tau_f\rangle$) and average rotational correlation times ($\langle\tau_r\rangle$) of a non-reactive probe solute, coumarin 153 (C153), dissolved at micromolar concentrations and have been accessed via monitoring the excited state population relaxations and dynamic fluorescence anisotropies of the dissolved probe solutes.[28–30,32] A simple survey of these composition dependent average relaxation times ($\langle\tau_f\rangle$ and $\langle\tau_r\rangle$) immediately reveals that these dynamical quantities exhibits a sharp change in their respective slopes when plotted as a function of amphiphile concentration. The mole fractions at which this sharp change for $\langle\tau_f\rangle$ and $\langle\tau_r\rangle$ occur are denoted by $x_{Cosolvent}^{dyn}$ in Table 4.1 and the corresponding experimental values[28,29] for aqueous binary mixtures of 2-BE, TBA, THF, dioxane, TMU and ethanol are summarized.

Table 4.1: Amphiphile mole fractions in binary aqueous mixtures where abrupt changes occur in the steady state UV-VIS absorption spectral properties and dynamical quantities (average rate of population and/or rotational relaxations) from time-resolved fluorescence measurements employing neutral dipolar fluorophores.

Cosolvent	$X_{Cosolvent}^{min}$ (UV-VIS Absorption)	$X_{Cosolvent}^{dyn}$ (Abrupt change in dynamics)
2- butoxyethanol[29] (2-BE)	0.02	0.04
Tertiary butanol (TBA)[28,30-32]	0.04	0.1
Tetrahydrofuran (THF)[33]	0.05	0.1
Dioxane[33]	0.07	0.15
Tetramethylurea (TMU)[34]	0.08	0.2
Ethanol[28]	0.1	0.2

Notice that $x_{Cosolvent}^{dyn}$ values are different for different amphiphiles and uniformly greater by approximately a factor of two than the corresponding $x_{Cosolvent}^{min}$ values. Studies with other non-reactive probe solutes[43,44] and solutes that undergo excited state intramolecular charge transfer reaction[30–32] have also reported similar amphiphile concentration dependence. This is intriguing and might very well represent a generic feature for aqueous macroscopically homogeneous amphiphilic solutions. This general observation also suggests that sharp changes is possibly accompanying the solution dynamics at or around these amphiphile mole fractions ($x_{Cosolvent}^{dyn}$).

The probable reasons that lead to connect the above anomalous composition dependence of $\langle\tau_f\rangle$ and $\langle\tau_r\rangle$ to the fluctuations in solution dynamics are as follows. First, the available neutron scattering studies for aqueous alcoholic solutions[10–12] do not indicate any anomaly in the solution structural aspect around $x_{Cosolvent}^{dyn}$. Second, the simulated amphiphile-water clusters can persist only for a few to several picoseconds,[17,19] and therefore they cannot probably generate the anomaly in the measured $\langle\tau_f\rangle$ and $\langle\tau_r\rangle$ values that are in the sub-nanosecond to a few nanosecond regime .[28,29] Third, no anomalous composition dependence of radiative (k_r) and non-radiative (k_{nr}) population relaxation rates of C153 in binary aqueous mixtures of TBA and ethanol have been found in earlier measurements.[28] Fourth, the composition dependent viscosities[45–48] of these solutions cannot be the source for this anomalous mole fraction dependence as the composition dependent viscosities, shown in Figure 4.A.1 (Appendix 4.A), do not indicate any extrema around $x_{Cosolvent}^{dyn}$. The origin of this 'dynamical anomaly' may therefore originate from a more fundamental solution aspect than the inter-layer momentum transfer[49] of component particles. In such a scenario and in the absence any other studies probing local solution dynamics, it is natural to speculate that fluctuations in the intra- and inter-species H-bond dynamics in these aqueous amphiphilic solutions may bear a connection to this experimental observation that has been termed here as 'dynamical anomaly'.

In this work, we have followed the intra- and inter-species H-bond dynamics and solution structural aspects of an amphiphile-water system at various amphiphile concentrations by employing TBA as a model amphiphile. We have monitored the composition dependence of fluctuations in terms of standard deviation by performing computer simulations at twelve TBA

mole fractions including the neat systems. These mole fractions are x_{TBA} =0, 0.01, 0.02, 0.03, 0.04, 0.06, 0.1, 0.13, 0.15, 0.17, 0.2 and 1. Such a closely-spaced x_{TBA} has been employed to track the structural and dynamical fluctuations in a fine concentration grid so that the simulation findings can provide microscopic insight to the experimental spectroscopic data already discussed. Note that such a thorough composition dependent simulation study probing the H-bond fluctuation dynamics and inter-species interactions has not been performed before for any amphiphile-water systems. The choice of TBA as a model amphiphile is motivated by the availability of neutron scattering studies for aqueous solutions of TBA for very low to low TBA mole fractions which could be used as benchmark to verify the predictions on structural aspects by the present simulations. In addition, existing simulation results of TBA-water system employing different model potentials for TBA can provide an idea about the 'degree of correctness' of the present simulations. In order to make the study internally consistent and self-contained, we have monitored the composition dependent spatial and radial distribution functions, the tetrahedral order parameter and the relative populations of water and TBA that are participating in the intra- and the inter-species H-bonding in these solutions. All these together provide a cogent and molecular level explanations for the structural and dynamical anomalies exhibited respectively by the steady state UV-VIS absorption and the time dependent fluorescence measurements[28–32] discussed above.

4.2 Simulation Details

All atom model potential for TBA reported in earlier simulations[16] has been employed in the present study. In this potential, the anharmonicity in the O-H bond stretching has been incorporated via a Morse-type potential. This model potential has been found to successfully reproduce the aggregation behaviour of TBA in aqueous solutions.[17,50]

Four site TIP4P/2005 model[51] of water is employed here, as this rigid four site model best represents the tetrahedral hydrogen bond structure of water[52]. A total of 10,000 molecules, comprising of water and TBA were used in all the ten binary mixtures studied. Simulations of neat water were also carried out by using 10,000 TIP4P/2005 model water molecules. For neat TBA, simulations employing 128 molecules were carried out. Number of participant water and TBA molecules simulated in different compositions are given in Table 4.B.1 (Appendix 4.B)

All force field parameters and the number of water and TBA molecules at different compositions used in this work are summarized in Tables 4.B.2- 4.B.4 (Appendix 4.B).

The simulations were performed at 298 K, employing the periodic boundary conditions[53] and the Nosé–Hoover thermostat[54,55] (with a time constant of 2 ps). The equation of motions was integrated using the velocity-Verlet algorithm[53] with a timestep of 1 fs. Electrostatic interactions were calculated using the particle mesh Ewald method of order 4 and with the Fourier spacing of 0.1 nm^{-1}. The nearest neighbour cut off for calculations of both the van der Waals and the electrostatic interactions was considered as 0.9 nm. All systems were equilibrated for 1 ns in the NPT ensemble. The pressure was kept constant at 1 bar and compressibility was maintained at 5e-5 bar^{-1} using the Parrinello-Rahman barostat[56] with time-constant 2 ps. Trajectories were saved at every 0.1 ps time gap throughout the production run of 10 ns, after equilibration of 2 ns in the NVT ensemble. For the calculations of H-bond fluctuation dynamics, separate trajectories were generated using the NVT ensemble with the pre-equilibrated trajectories. This time the trajectories were saved at a regular time interval of 0.01 ps in order to better track the faster relaxation dynamics. We performed block averaging over ten blocks with different time-origins while calculating the variance of hydrogen bond timescales.

A table showing the equilibrated density of all the simulated systems along with experimentally available densities and earlier simulated density of neat TBA are provided in Table 4.B.5 (Appendix 4.B). The agreement the simulations and experimental data is satisfactory. The GROMACS 4.5.6 simulation package[57–61] was used for simulation studies reported here. For calculations and visualization of the surface distribution functions (SDFs), TRAVIS[62] and VMD[63] software packages were used.

4.3 Results and Discussion

As we have already stated that the main focus of this work is to thoroughly investigate the microscopic reasons behind the abrupt changes in the mole fraction dependent average relaxation times reported in measurements employing a fluorescent solute in aqueous amphiphilic solutions, we followed the H-bond relaxation dynamics in detail. However, structural details have also been carefully examined to explain the mole fraction dependence of the steady state absorption spectral shifts which are connected to the structural anomaly. This is done in order to make the study uniform and internally consistent.

4.3.1 Radial Distribution Function (RDF) and Coordination Number (CN)

The composition dependence of the centre-of-mass (COM) RDFs for TBA-TBA, TBA-water and water-water have been monitored for this aqueous amphiphilic solution. The simulated RDF peak values, representing the RDF value at contact, ($g(\sigma)$, σ being the distance of the closest approach between the central molecule and another molecule as the nearest neighbour) are shown as a function of TBA mole fraction (x_{TBA}) in the upper panel of Figure 4.2. Numbers corresponding to Figure 4.2 is provided in Table 4.B.6 (Appendix 4.B). The *inset* of this panel shows the composition dependent ratio between the $g(\sigma)$ at a given x_{TBA} and that for neat TBA, $R^{peak} = [g(\sigma)]_{x_{TBA}}/[g(\sigma)]_{x_{TBA=1}}$. The $g(\sigma)$ values for neat TBA and neat water are summarized in Table 4.B.7 (Appendix 4.B). The non-monotonic dependence of RDF peak indicates aggregation of TBA molecules in dilute aqueous solutions, the extent of aggregation being the maximum at $x_{TBA}\sim0.04$. This is the mole fraction where the UV-VIS absorption spectra of reactive and non-reactive fluorescent probes showed minima before reversing the direction of the composition dependence upon further addition of TBA in water.[28,31,32] This non-monotonicity has been found in earlier simulation studies[14,15,18,64–67] and explained in terms of TBA aggregation following observations from the relevant neutron scattering measurements.[10,42,68] The interesting aspect here, however, is the simulation predictions of appreciable TBA aggregation even at extremely low concentrations, $x_{TBA} < 0.04$, a mole fraction range not accessible to neutron scattering measurement because of poor signal-to-noise ratio.[10] Data in the inset suggests a sharp increase of $g(\sigma)$, from ~1.5 times with respect to that for neat TBA ($g(\sigma)$ = 2.03 for neat TBA) to ~2.5 times for changing x_{TBA} from 0.01 to 0.03 in the aqueous solution. In this mole fraction regime, the TBA-water $g(\sigma)$ decreases sharply (middle panel), indicating hydrophobic hydration of the aggregated TBA cluster. This

is reinforced by the concomitant increase in the water-water $g(\sigma)$ (lower panel), although the *inset* shows the increase is limited to within ~20% over the value for neat water. This increase in TBA-TBA and water-water $g(\sigma)$ with simultaneous decrease in TBA-water $g(\sigma)$ upon successive addition of TBA in aqueous solution in the very low TBA mole fraction regime indicates hydrophobicity driven aggregation of TBA followed by hydrophobic solvation, a conclusion in agreement with the general observation of several existing simulation[14,15,64–66] and experimental[10,42,68,69] studies.

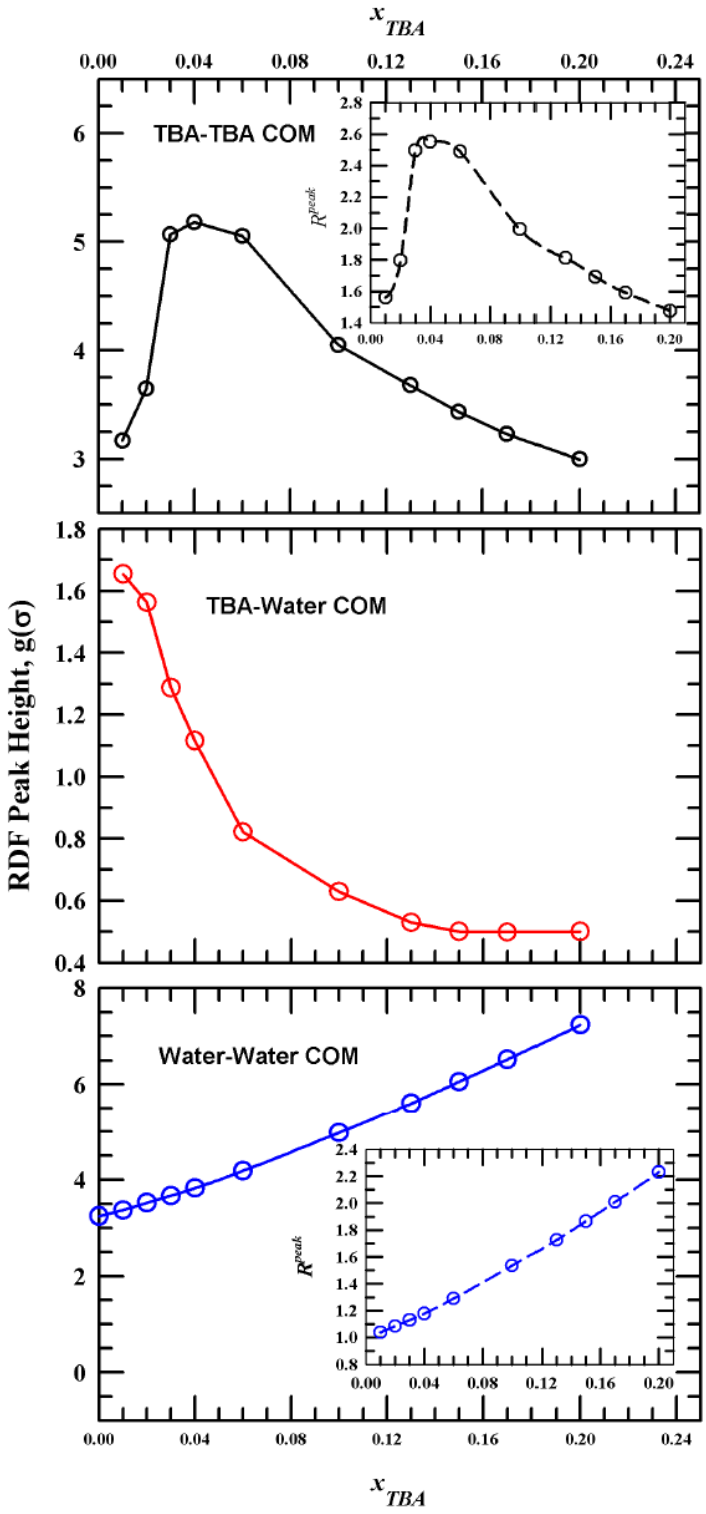

Figure 4.2: The composition dependent peak-heights (first peaks) of TBA-TBA (upper panel), TBA-water (middle panel) and water-water RDFs. Insets represent the ratios between the RDF peak heights at finite TBA mole fractions and that in the neat solvent.

The next question we investigate is what happens to this hydrophobicity-driven TBA aggregation at x_{TBA} >0.04? The TBA-TBA $g(\sigma)$ clearly decreases as x_{TBA} is further increased. Interestingly, this aggregation is not completely diminished even at x_{TBA}=0.2, a TBA concentration where one expected the solution structure would be governed by alcohol-alcohol interactions.[10] The value of TBA-TBA $g(\sigma)$ at x_{TBA}=0.2 being 1.5 times larger than that in neat TBA suggest that hydrophobic interaction among alcohol molecules is still operative and the subsequent hydrophobic hydration leads to a continuous increase of water-water $g(\sigma)$ (lower panel) and the consequent decrease of TBA-water $g(\sigma)$. The water-water $g(\sigma)$ being ~2.4 times larger at x_{TBA}=0.2 than that for neat water reflects the inherent de-mixing at the microscopic level between these two mixture components. The extent of de-mixing is different for different model potentials and this is the reason, for example, behind predicting uniformly lower TBA-TBA $g(\sigma)$ values in this x_{TBA} range employing Lee-Vegt potential in simulation studies reported earlier[64].

Next, we investigate the x_{TBA} dependences of intra- and inter-species coordination numbers, and the intra-species percentages of populations in the nearest neighbor. This is done to closely examine whether the first solvation shells and thus the local solution structures themselves carry the imprint of structural anomalies which are then reflected in the steady state and time-resolved spectroscopic studies. The numbers of TBA molecules around a central TBA molecule (CN_{t_t}), water molecules around a central TBA molecule (CN_{t_w}) and water molecules around a central water molecule (CN_{w_w}) have been estimated as a function of x_{TBA} via the following formula where we have used the first minima distances of RDFs as shell radii for the relevant calculations:

$$CN = 4\pi\rho \int_0^{r_{shell}} dr\, r^2\ g_{ij(r)}, \qquad (4.1)$$

where $g_{ij\,(r)}$ denotes intra- and inter-species RDFs at various solution mole fractions studied. Note that the CN calculated in this way represent the number of j^{th} particle in the first solvation shell of i^{th} particle in a binary mixture and is different from total coordination number which accounts for molecules of both the components that together constitute the full solvation shell. The simulated coordination numbers and fraction populations at different x_{TBA} are summarized in Figure 4.3. Table 4.B.7 (Appendix 4.B) shows the corresponding quantities for neat water and neat TBA. All CN and corresponding participation population plotted in Figure 4.3 are

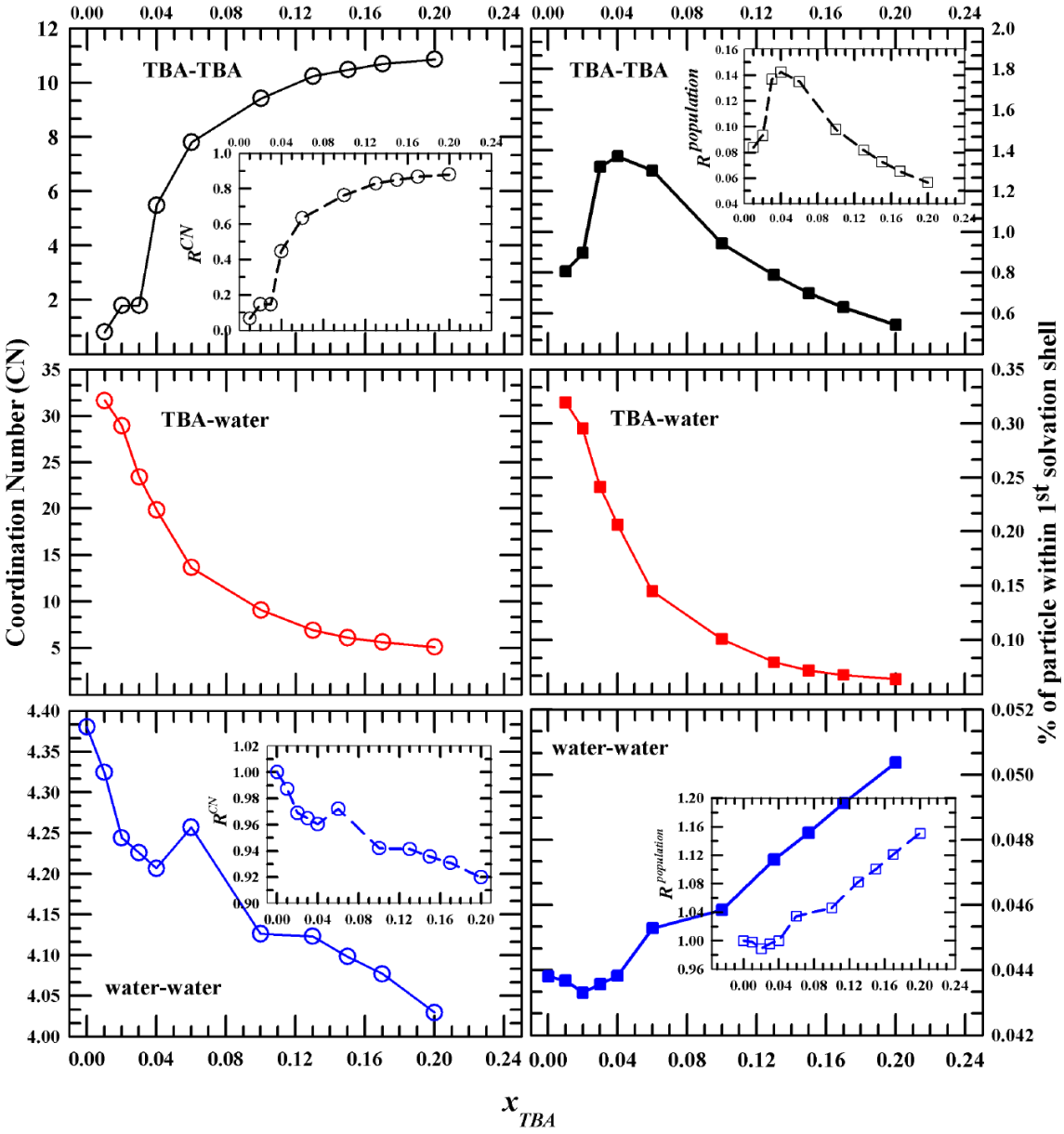

Figure 4.3: Composition dependent coordination numbers (left column) and the corresponding

fraction of particles within the first solvation shell (right column). Upper panel presents simulated data for TBA-TBA, middle panel TBA-water and lower panel water-water. Insets show the data ratioed against the values in the respective neat solvents.

given in Table 4.B.8 (Appendix 4.B) It is quite interesting to note that the TBA-TBA coordination number (left upper panel) shows a mild hump at x_{TBA}~ 0.04, which becomes a distinct peak in the curve showing the x_{TBA} dependence of percentage population in the first solvation shell (right upper panel). This relative increase of percentage population in the first solvation shell for mixtures up to $x_{TBA} \leq 0.04$, followed by an exponential-like decrease upon further increase of TBA concentration reflects hydrophobicity-induced TBA aggregation in very dilute aqueous TBA solutions. Such a non-monotonic x_{TBA} dependence is absent for the simulated population percentage of water molecules in the first solvation shell of TBA, and a gradual decrease with TBA concentration is noticed for both the coordination number and the population (middle panels). The water-water coordination number, on the other hand, shows a sharp change in the direction of alcohol concentration dependence at x_{TBA} ~0.04 (lower left panel); this sharp change becomes a flat minimum around this mole fraction for the simulated water-water percentage population (lower right panel).

4.3.2 Number of H-bonds and Participation Papulation

The solution structure is further investigated by probing the intra-and inter-species H-bonding interactions and the percentage of respective populations participating in such interactions. A variety of H-bonded molecular complexes can coexist in these binary mixtures because of the presence of -OH group in both TBA and water which can simultaneously act as a H-bond donor and an H-bond acceptor. This gives rise to the possible existence of both exclusively intra-species H-bonded complexes (for example, via TBA-TBA and water-water interactions) and mixed inter-species H-bonded complexes (via TBA interactions both with water and TBA molecules) in these aqueous amphiphilic solutions. Our aim here is to clarify whether at extremely low TBA concentrations there exist any direct TBA-TBA contacts or it is the neighboring water molecules that host each of the TBA molecule separately in clathrate-type environments. In addition, one would like to know what happens to water-water direct contacts and its tetrahedral network structure as x_{TBA} is successively increased in solutions. More importantly, one would like to know whether average H-bond properties of any of the H-

bonded complexes exhibit anomalous TBA concentration dependence that can explain in microscopic terms the steady state and time-resolved spectroscopic data discussed here.

The following condition[70,71] has been followed to detect H-bonds between water molecules: a) the distance between the donor oxygen atom and the acceptor oxygen atom is less than 0.35 nm, b) the O-H (donor) -O (acceptor) angle is less than 30°, and c) the distance between the oxygen (O) and hydrogen (H) atoms must be less than 0.245 nm.

For monitoring alcohol-alcohol hydrogen bonding, the geometrical criteria[72] that have been considered are as follows: a) the distance between the donor and acceptor oxygen atoms is less than 0.35 nm, b) the O-H (acceptor)-O (donor) angle is less than 30°, and c) the distance between O (donor) and H (acceptor) is less than 0.28 nm.

The above criteria for detecting H-bonding between TBA molecules have also been employed for monitoring TBA-water H-bonding. The fractions of TBA and water molecules participated to intra- and inter-species H-bonding have been calculated in order to find non-participation of any of the species at any mixture composition. Results obtained in this analysis is expected to compliment the results on x_{TBA} dependence of average number of H-bonds per TBA or water. While calculating average number of hydrogen bonds per molecule we have considered only the participant molecules, not all the molecules of a given species that are present in a solution at a particular TBA mole fraction.

Figure 4.4 depicts composition dependent number of hydrogen bonds per molecule, N_{i-j}^{HB} (left panel) and fractions of the populations (in percentage) that are participating and not participating in forming inter-molecular H-bonds (right panel). The average number of inter-molecular H-bonds between TBA-TBA in neat TBA ($N_{TBA-TBA}^{HB}$) and water-water in neat water (N_{W-W}^{HB}), and the corresponding population percentages have been simulated and summarized in Table 4.B.9 (Appendix 4.B). Notice $N_{TBA-TBA}^{HB}$ increases with x_{TBA} and approaches toward the value for neat TBA (upper panel). Interestingly again, the increase in $N_{TBA-TBA}^{HB}$ with x_{TBA} is much sharper for solutions with $x_{TBA} \leq 0.04$ than those at higher mole fractions. The TBA

population that participate in the TBA-TBA H-bonding (upper right panel, 'P') is gradually approaching with x_{TBA} toward the neat value (54%) but not before showing a different slope of increase for solutions with $x_{TBA} \leq 0.04$. The non-participating population ('NP') depicts, as expected, the mirror image of the x_{TBA} dependence found for participating population. At extremely dilute solutions ($x_{TBA} \leq 0.03$), the TBA-TBA direct H-bonding is very rare and in this regime the H-bonding requirement is satisfied via interacting exclusively with water (middle panel). The overwhelming domination of TBA-water interaction via ~100% participation of water at these mixture compositions provides further support to the view of

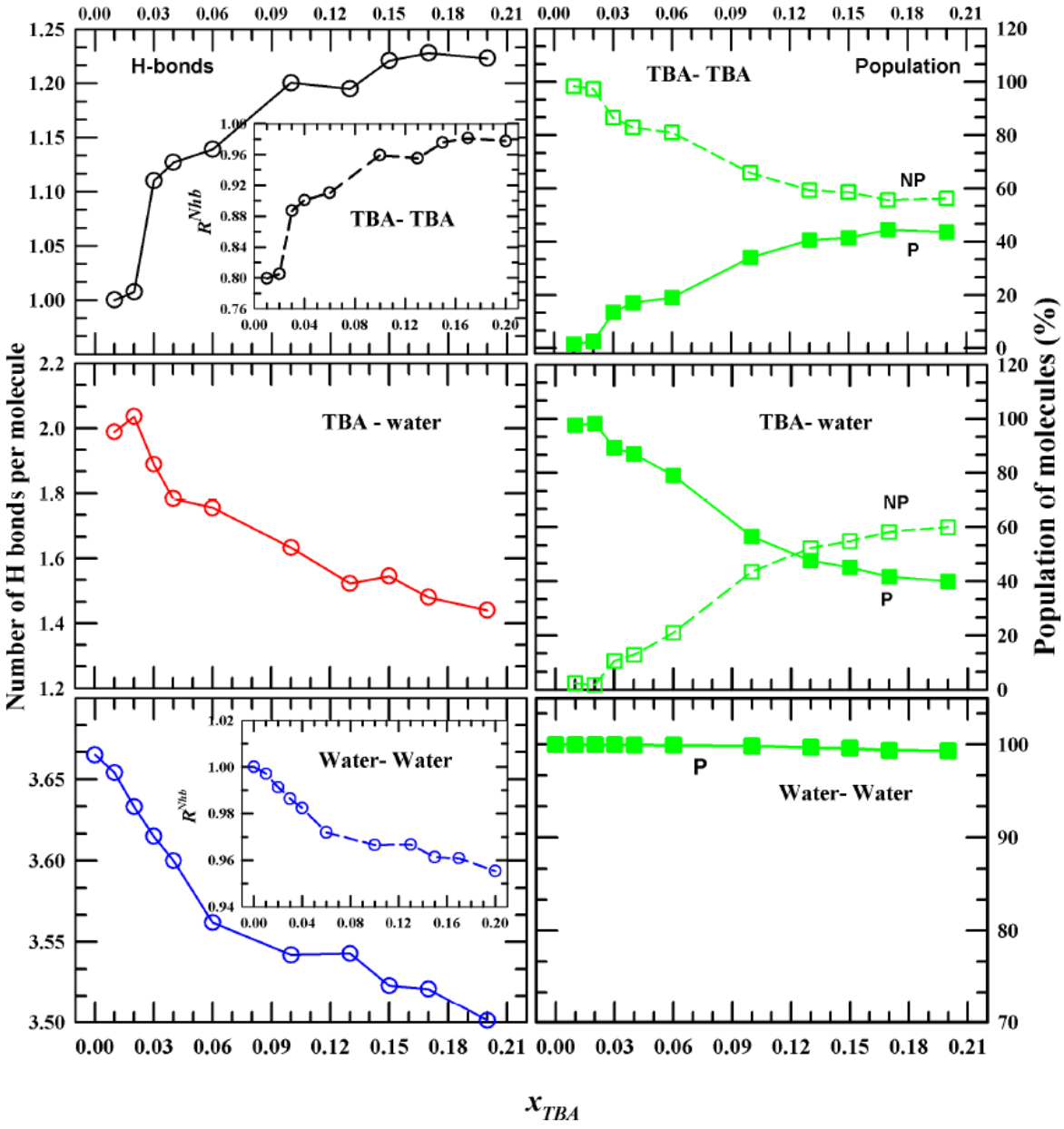

Figure 4.4: Composition dependent number of H-bonds per molecule (left column) and fractional participating ('P') and non-participating ('NP') populations in the formation of H-bonds (right column). Insets represent data ratioed against the corresponding values for the neat solvents.

clathrate-type structure formation in aqueous solution at extremely dilute amphiphile concentrations. The x_{TBA} dependent number of water-water H-bonds, N_{W-W}^{HB}, on the other hand, shows a mild kink at x_{TBA} ~ 0.12 (lower left panel), whose signature can also be found for number of H-bonds between TBA and water per TBA molecule, $N_{TBA-water}^{HB}$ (middle panel). Participation of each of the water molecules in forming H-bond with another water molecule across the x_{TBA} studied (lower right panel) only confirms the irresistible tendency of water molecule in forming H-bonds with its neighbors and preserving its three-dimensional tetrahedral network structure.

TBA possesses the hydroxyl (-OH) group and therefore, like water, can act as both a donor and an acceptor for H-bonding. This gives rise to the possibility of TBA forming (i) H-bonds only with water, (ii) only with TBA, (iii) simultaneously both with water and TBA, and (iv) remaining free (not H-bonded) in these binary mixtures. Since the anomalous mole fraction dependent thermodynamic properties of these amphiphilic aqueous solutions have been believed to reflect the underlying microscopic solution structure, a close examination of these H-bonded complexes may provide a clue to explain the composition dependent steady state and time-resolved spectroscopic properties. We present in Figure 4.5 the simulated populations of TBA molecules that have participated in the intra- and the inter-molecular H-bonding, and those not interacting via H-bonding in solutions at different mole fractions. Numbers depicted in Figure 4.5 are summarized in Table 4.B.10 (Appendix 4.B) Composition dependent respective populations shown in the upper panel of Figure 4.5 indicate that the TBA population H-bonded exclusively with water (water-TBA-water) dominates the solution up to $x_{TBA} \leq 0.15$, while the population of TBA interacting simultaneously with both water and TBA (water-TBA-TBA) remains the least across the mole fraction studied. The population denoting the exclusive interaction of TBA with water (water-TBA-water) decreases with x_{TBA}, whereas TBA-TBA-TBA, water-TBA-TBA, and non-H-bonded TBA populations increase, with varying extent, upon successive addition of TBA in the aqueous solution. Interestingly, the composition dependence of these populations in solutions with $x_{TBA} \leq 0.04$ is rather irregular and somewhat different from that at higher mole fractions. We note here that the mixed H-bonded population, TBA-TBA-water, remains within ~5% of the total population and appears to be nearly-insensitive to x_{TBA} . When this rather weak dependence is magnified in the lower panel, two peaks, one well-formed and the other somewhat diffused, are clearly visible at x_{TBA} ~0.04 and ~0.10, respectively. This double-peak behaviour of the composition

dependence becomes more prominent in the inset where the rate of change of population with TBA mole fraction, $\frac{d[P_{TBA-TBA-water}]}{dx_{TBA}}$, is shown as a function of x_{TBA}.

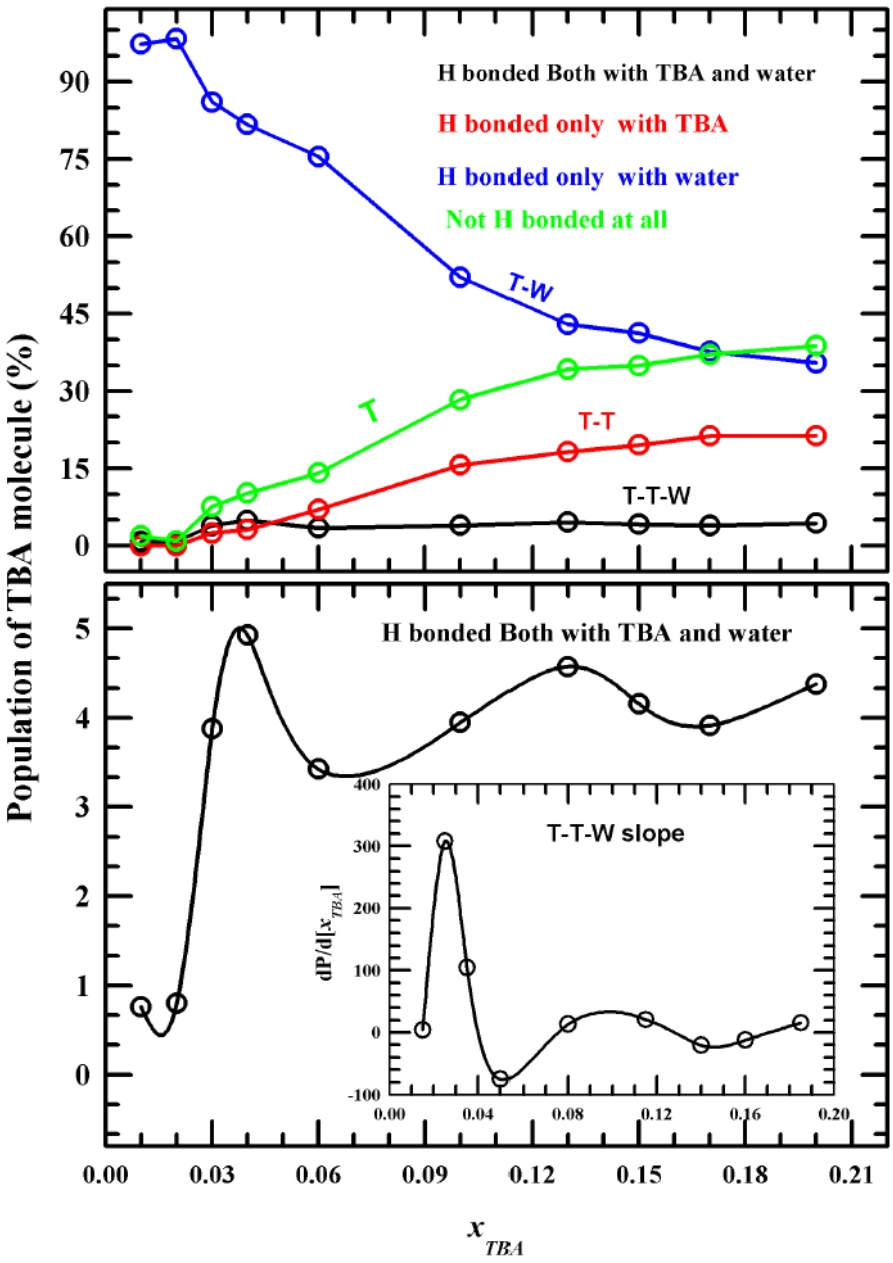

Figure 4.5: Upper panel: Composition dependent fraction of TBA molecules (in %) H-bonded only to TBA (T-T), only to water (T-W), both to TBA and water (T-T-W), and not H-bonded to any one of them (T). Lower panel: TBA population H-bonded to both TBA and water molecules (T-T-W) are shown in an expanded scale. Inset depicts the composition dependent slope of the T-T-W population.

4.3.3 Tetrahedral order parameter

Next, we explore the impact of TBA on the tetrahedral network structure of water across the mole fractions for detecting abrupt changes, if any, in the composition dependence of tetrahedrality of water. Our earlier works have already revealed substantial disruption of water tetrahedrality in the presence of simple alcohol like methanol in bulk aqueous binary mixtures and for confined water molecules near a charged interface[73,74].

The effects of TBA and its concentration on the tetrahedral H-bond network of water have been studied via the tetrahedral order parameter (Q) defined as follows[75]:

$$Q_i = 1 - \frac{3}{8}\sum_{j=1}^{3}\sum_{k=j+1}^{4}(cos\theta_{ijk} + {}^{1}/_{3})^2 \text{ and } \langle Q \rangle = \frac{1}{n_{water}}\sum_i Q_i, \quad (4.2)$$

where Q_i is the tetrahedral order parameter of the i^{th} water, θ_{ijk}- the angle subtended by each pair (designated by j and k) of the nearest four water molecules on the central i^{th} water molecule. For a random and uniform distribution of these angles, $Q = 0$; for a perfect tetrahedral structure, on the other hand, $Q = 1$. A schematic diagram for the general description of the tetrahedral angle and three-dimensional tetrahedral structure of the H-bond network in the bulk water is shown in Figure 4.A.3 (Appendix 4.A). The x_{TBA} dependent distribution of the tetrahedral order parameter, $P(Q)$, shown in Figure 4.A.4 (Appendix 4.A) reveals that the tetrahedral water population (molecules that are tetrahedrally H-bonded) molecules are increasingly transferred toward the less coordinated population upon successive addition of TBA. This is also reflected in the distribution of angles among the central water and its neighbouring water molecules, $P(cos\theta)$, shown in Figure 4.A.5 (Appendix 4.A). Figure 4.6 depicts composition dependent ensemble-averaged tetrahedral order parameter for water in aqueous TBA solutions. Ensemble averaged Q values are summarized in Table 4.B.11 (Appendix 4.B). For neat water[74], $Q \approx 0.67$. As TBA concentration increases, Q decreases, suggesting amphiphile-induced partial disruption of water tetrahedrality. This has been reported already in a number of simulation studies that involve aqueous binary mixtures of alcohols.[14,73] What has not been examined in those studies, however, is the rate of change of water tetrahedrality as a function of alcohol mole fraction. This composition dependent slope, $\frac{d[\langle Q \rangle]}{dx_{TBA}}$, is shown in the inset of Figure 4.6, which clearly indicates appreciable changes in the water tetrahedrality at two TBA mole fractions; one is around 0.04 and the other ~0.12. More

importantly, $\frac{d[\langle Q \rangle]}{dx_{TBA}}$ makes a better visual representation of the deformation that the tetrahedral H-bond network of water suffers while accommodating TBA without allowing macroscopic de-mixing. The weak irregularity in the x_{TBA} dependence of Q becomes more evident in the composition dependent slope, and correlates well with the x_{TBA} dependence observed in the relevant steady state and time-resolved spectroscopic measurements.

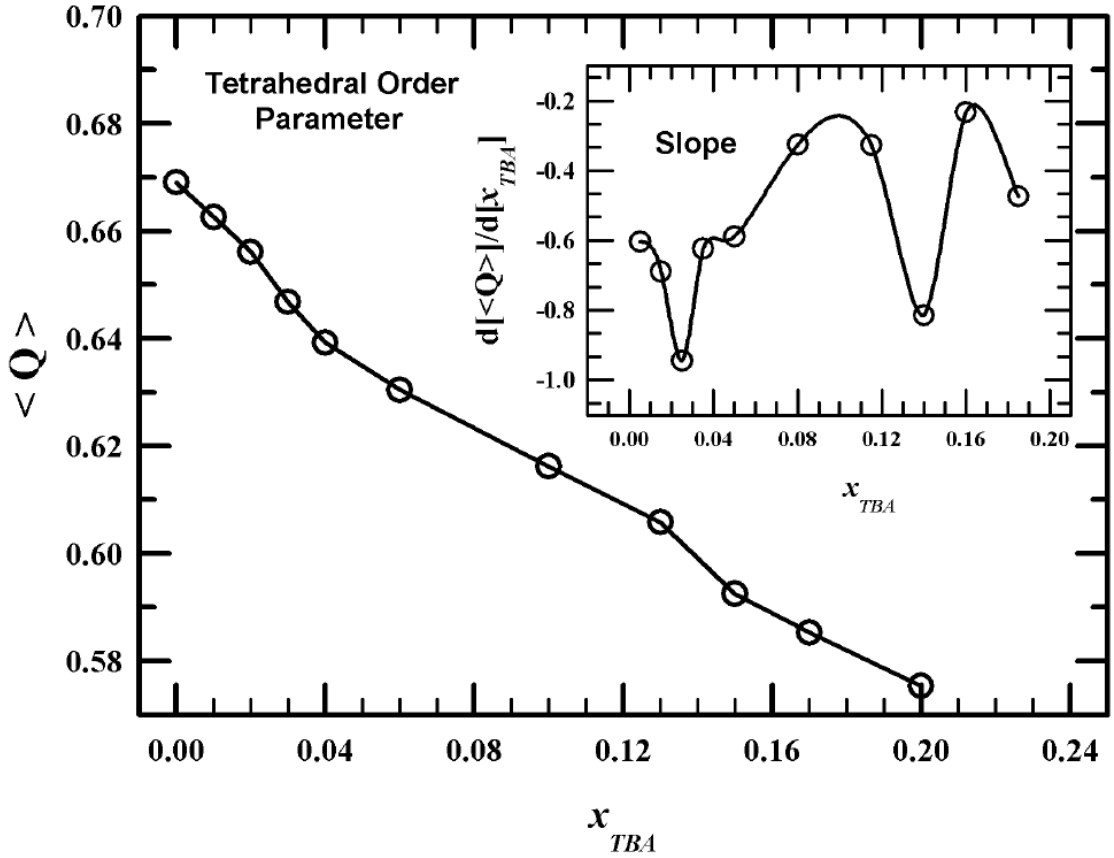

Figure 4.6: Composition dependent ensemble-averaged tetrahedral order parameter of water molecules in the aqueous TBA solutions studied. He tetrahedral order parameter for neat water is also shown. Inset depicts the slope of composition dependent tetrahedral order parameter values.

4.3.4 Spatial Distribution Function (SDF)

We have already gained a qualitative idea about the relative spatial arrangements of TBA and water in these aqueous binary mixtures via the simulated RDFs. However, RDF being two dimensional and thus far removed from the real solution scenarios, it cannot depict the solvation structure around a central molecule in an actual solution condition. A better description of solvation structure in solutions can be obtained via accessing the surface distribution functions (SDFs).[67,76] This has been performed by using the TRAVIS software[62]. Composition dependent SDFs related to the spatial arrangements of water and TBA molecules around a central TBA molecule is shown in Figure 4.7. The isosurfaces are mapped corresponding to those isovalues (local number densities) which suggest the completion of the first solvation shell of the TBA molecule under focus. Isovalues corresponding to TBA and water isosurfaces are summarized in Table 4.B.12 (Appendix 4.B). Figure 4.A.6 (left panel) shows the x_{TBA} dependence of isovalues for TBA- TBA SDFs. Interestingly, these isovalues qualitatively follow the trend of the composition dependent intensities of the first minima of TBA-TBA shown in Figure 4.A.6 (right panel, Appendix 4.A). Note these isovalues corresponds to the first minima found in $g(r,\theta,\phi)$ [76,77]. As the present analysis involves only the centre-of-mass of the concerned molecules, SDFs shown here would be less anisotropic than those constructed after considering atomistic distribution functions.

In Figure 4.7 blue surface corresponds to water and red surface to TBA molecules. Notice that water molecules completely encapsulate the reference TBA molecule symmetrically in aqueous mixtures up to $x_{TBA} \leq 0.04$. Remaining TBA molecules are then found to surround the water layer that had encapsulated the central TBA molecule. This suggests that TBA-TBA direct contact at these low TBA concentrations is rare. However, this could not be verified in neutron scattering measurements because of low signal-to-noise ratio. The number of H-bonds per water molecule and the water tetrahedral network structure have been found to be slightly affected in this concentration regime (see Figure 4.4 and Figure 4.6). For solutions with $x_{TBA} \geq 0.06$, water isosurface surrounding the reference TBA becomes asymmetric. This suggests hydrophobic hydration of the tertiary butyl groups of the TBA molecules. Note two TBA isosurfaces exist near the reference TBA molecules at all compositions studied. This is because of the similar depths in the first and the second minima of the composition dependent TBA-TBA RDFs (see Figure 4.A.2 (Appendix 4.A)). For solutions with $x_{TBA} > 0.06$, TBA

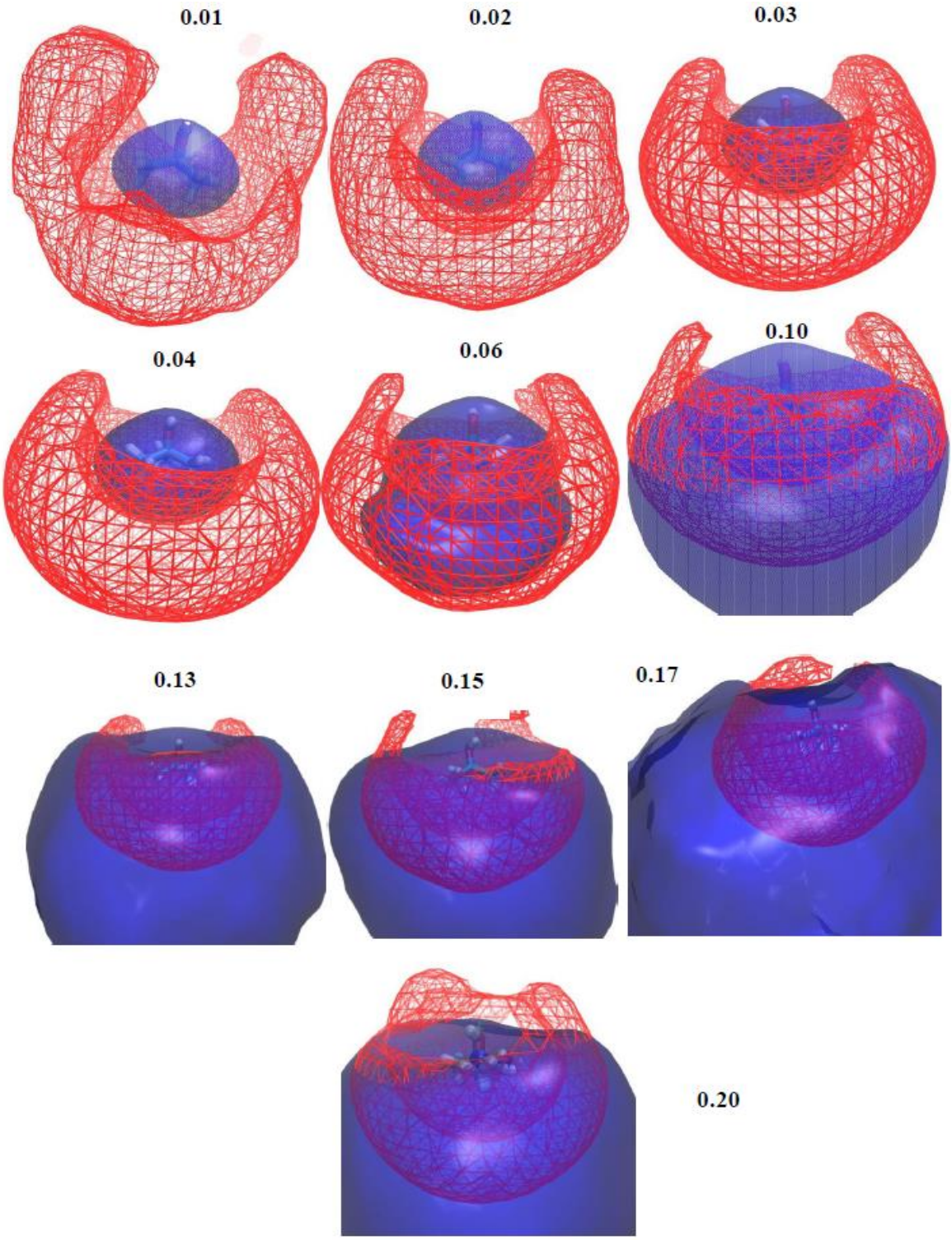

Figure 4.7: Composition dependent spatial distribution functions (SDF) for water and TBA molecules around a reference TBA molecule. Blue color denotes water surface and red TBA surface.

molecules allow very little interstitial space for water molecules, and as a result, the water surface smears out. This corroborates with the composition dependent population of TBA molecules that are not participating in H-bond formation with either water or TBA molecules (see Figure 4.5).

4.3.5 Hydrogen Bond Relaxation Dynamics

To characterize TBA-water and water-water H-bond dynamics, we have monitored two H-bond autocorrelation functions. The lifetime of a continuous H-bond has been calculated from the time-correlation function, $S_{HB}(t)$[70,78,79],

$$S_{HB}(t) = \frac{<h(0)H(t)>}{<h>}, \qquad (4.3)$$

h(t), a hydrogen bond population operator, is unity when the particular tagged pair of molecules are hydrogen bonded and zero otherwise. $H(t)$ takes a value 1 if the tagged pair of molecules, for which *h(0)* is calculated, remains continuously H-bonded for a time t or else $H(t) = 0$. $S_{HB}(t)$ describes the probability that a tagged pair of molecules remain H-bonded for a timespan t and it approaches zero when continuity of the H-bond between them breaks down. The average continuous H-bond lifetime is then obtained via the time integration of $S_{HB}(t)$, $\langle \tau_s^{HB} \rangle = \int_0^\infty dt\, S_{HB}\,(t)$.

The fluctuations (or variance) in these average timescales are calculated as follows

$$\sigma^{\,2}_{\tau_x} = \frac{\sum_i^N (\tau_{xi} - \langle \tau_x \rangle)^2}{N-1}, \qquad (4.4)$$

The simulated x_{TBA} dependent $\langle \tau_s^{HB} \rangle$ and the corresponding fluctuations are summarized respectively in Table 4.B.13 (Appendix 4.B). Figure 4.8 shows the composition dependent lifetime ($\langle \tau_s^{HB} \rangle$) and variance ($\sigma^{\,2}_{\tau_x}$) for the continuous water-water, TBA-water and TBA-TBA H-bond relaxation dynamics. The choice of these intra- and inter-species H-bond relaxations arises from the simulated composition dependence of the population of the TBA molecules that

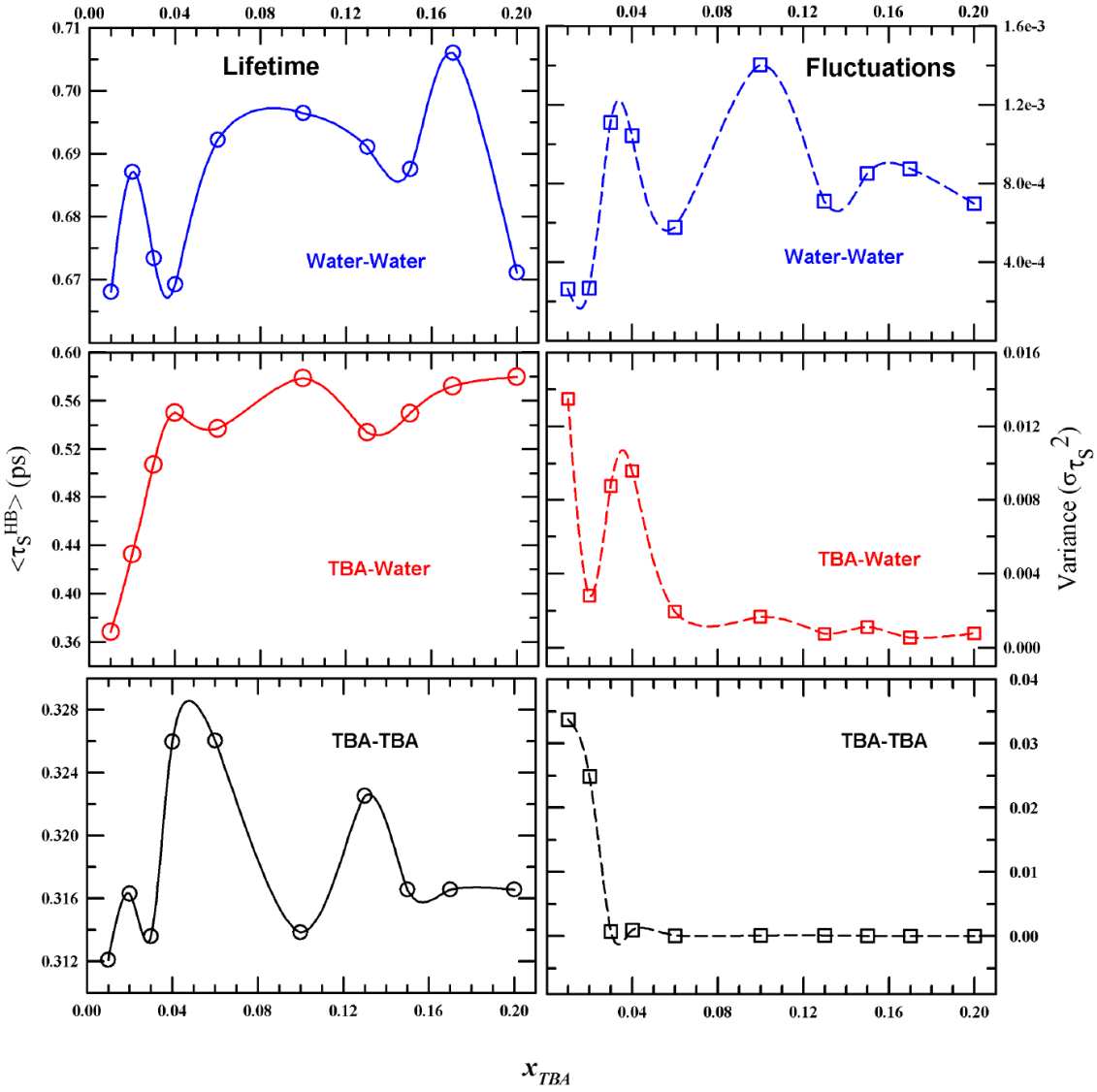

Figure 4.8: Composition dependent average continuous H-bond relaxation times ($< \tau_S^{HB} >$) (left column) and the corresponding fluctuations (right panel) of TBA-TBA, TBA-water and Water-Water H-bonded molecules.

are H-bonded simultaneously both with neighboring water and TBA molecules. It is interesting to note that water-water H-bond relaxation time ($\langle\tau_s^{HB}\rangle$) shows appreciable fluctuations around x_{TBA} ~ 0.1, whereas such fluctuations around this mole fraction are absent for TBA-water and TBA-TBA continuous H-bond lifetimes (right panels). The individual intra-species lifetimes, however, are larger by ~15-25% than their respective neat values and this is shown in Figure 4.A.7 (Appendix 4.A). The TBA-water H-bond lifetimes, on the other hand, are larger by ~40-120% than the TBA-TBA neat value ($\langle\tau_s^{HB}\rangle$ = 0.26 ps for neat TBA) and reaches the water-water neat value (($\langle\tau_s^{HB}\rangle$ = 0.57 ps for neat water) at x_{TBA} ~ 0.1. This, when juxtaposed against the x_{TBA} dependenceies of the measured average fluorescence lifetimes and/or rotational correlation times, appears quite intriguing and suggests a novel interplay between the amphiphile concentration dependent H-bond fluctuation dynamics and the excited state population or rotational relaxations of a fluorescent solute probe dissolved in such a medium. This is indeed a new observation which demands further experimental and simulation study.

4.4 Conclusion

In summary, the present simulations find significant fluctuations in the water-water continuous H-bond lifetime in the binary aqueous mixtures of TBA around the alcohol mole fraction where time-resolved fluorescence measurements have repeatedly reported abrupt changes in the mixture composition dependent average fluorescence lifetimes and rotational correlation times of dissolved foreign solutes. Such a finding is new and probably signals an interconnection between the solution H-bond dynamics and fluorescence dynamics of a dissolved solute probe. Previous works have established that the three-dimensional H-bond network structure of water distorts to accommodate small amphiphilic molecules. However, no study was conducted to probe the impact of such distortion on the H-bond relaxation dynamics and the average lifetime. This study makes an attempt to address that concern and opens up a possibility for examining this interconnection between the H-bond relaxation dynamics of aqueous mixtures and the reactive and non-reactive dynamics of dissolved fluorescent solutes in them.

Appendix 4.A

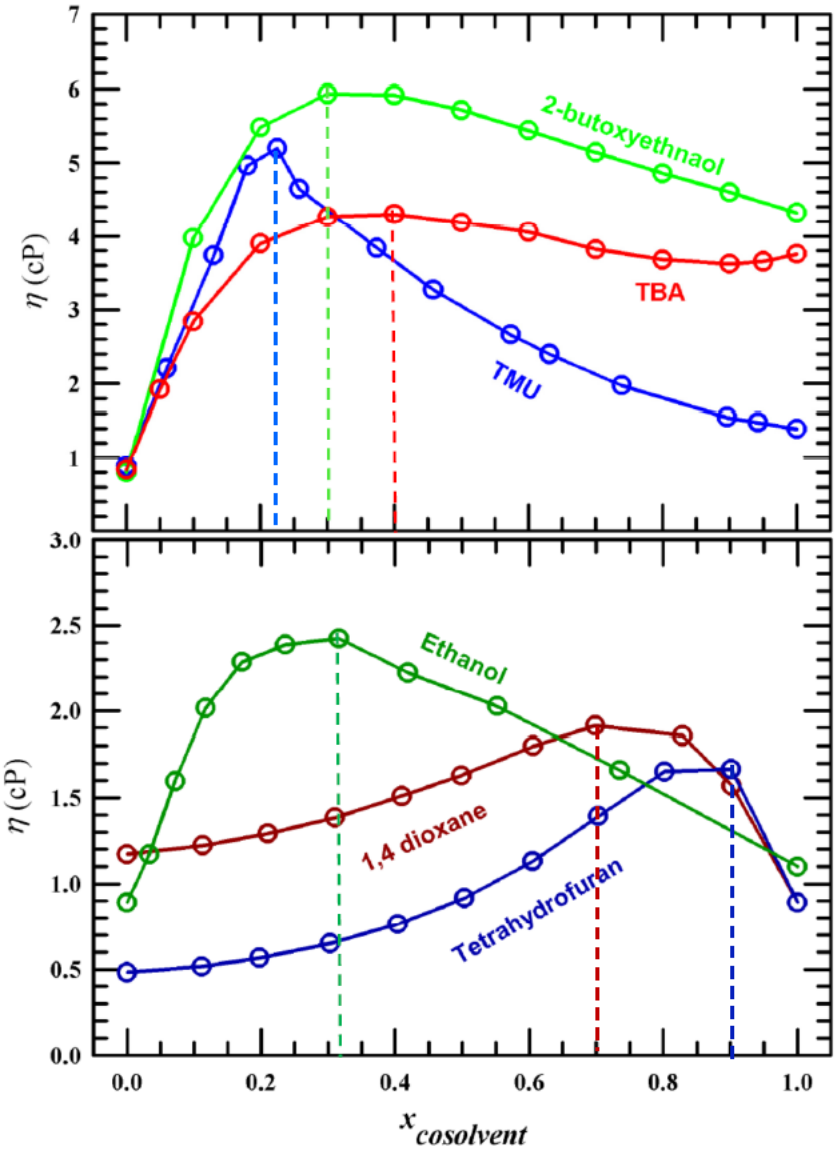

Figure 4.A.1: Experimental amphiphile mole fraction dependent viscosities of aqueous solutions. Vertical lines indicate the approximate peak positions on the mole fraction axis.

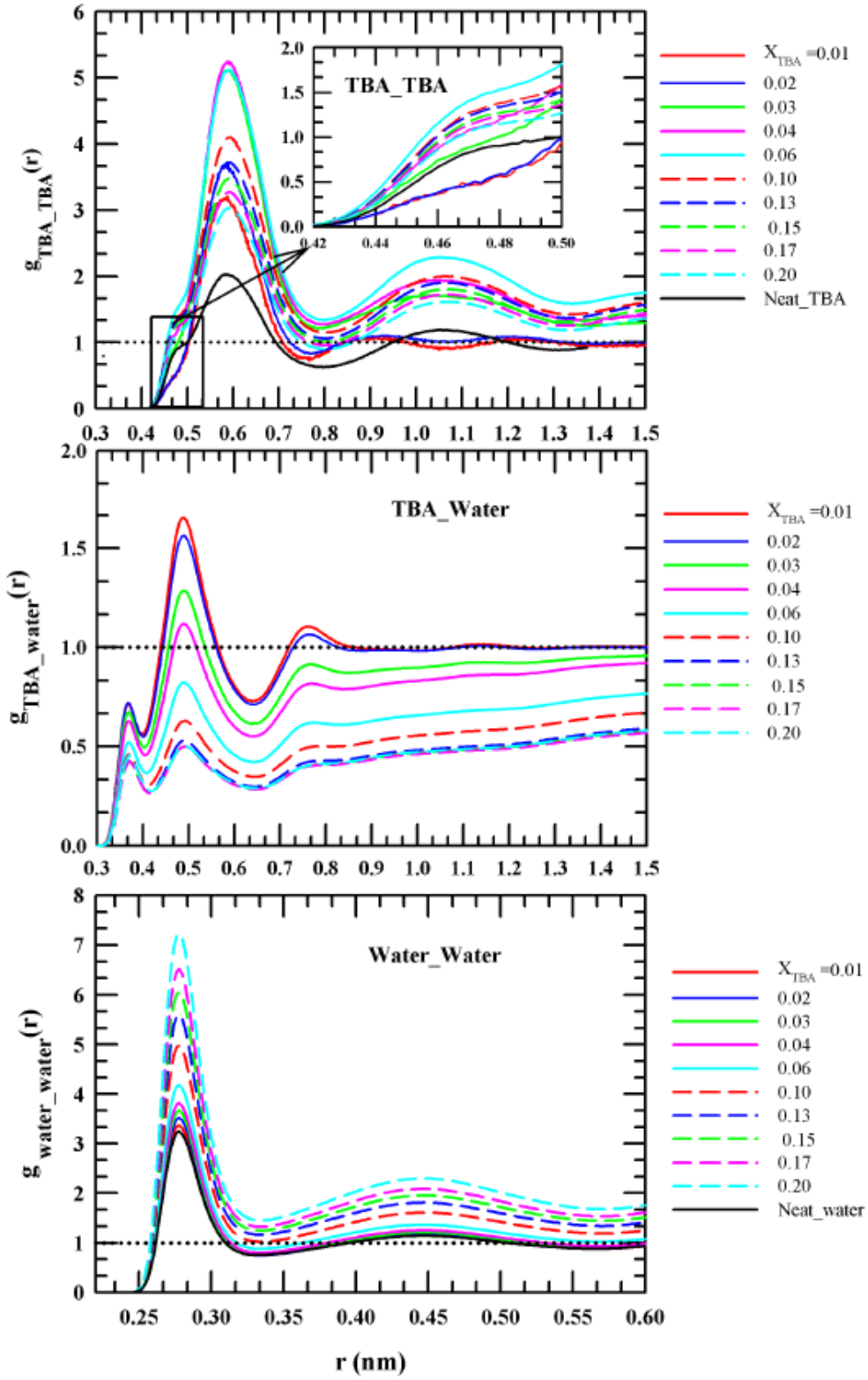

Figure 4.A.2: Radial distribution functions for TBA-TBA, TBA-water, Water -water.

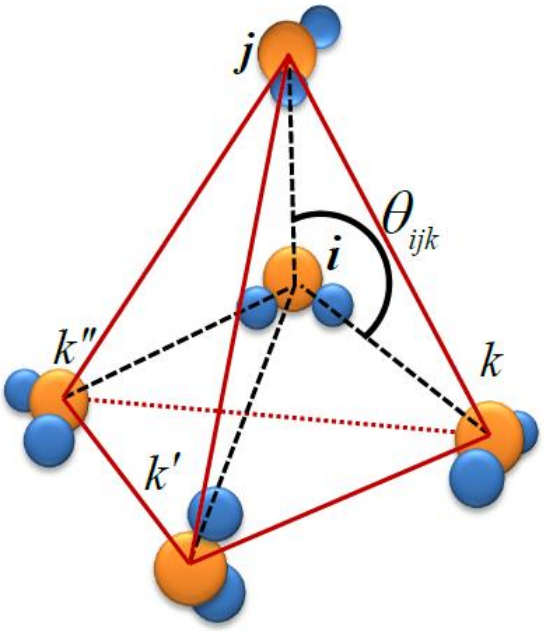

Figure 4.A.3: Schematic diagram of tetrahedral H-bond network for water.

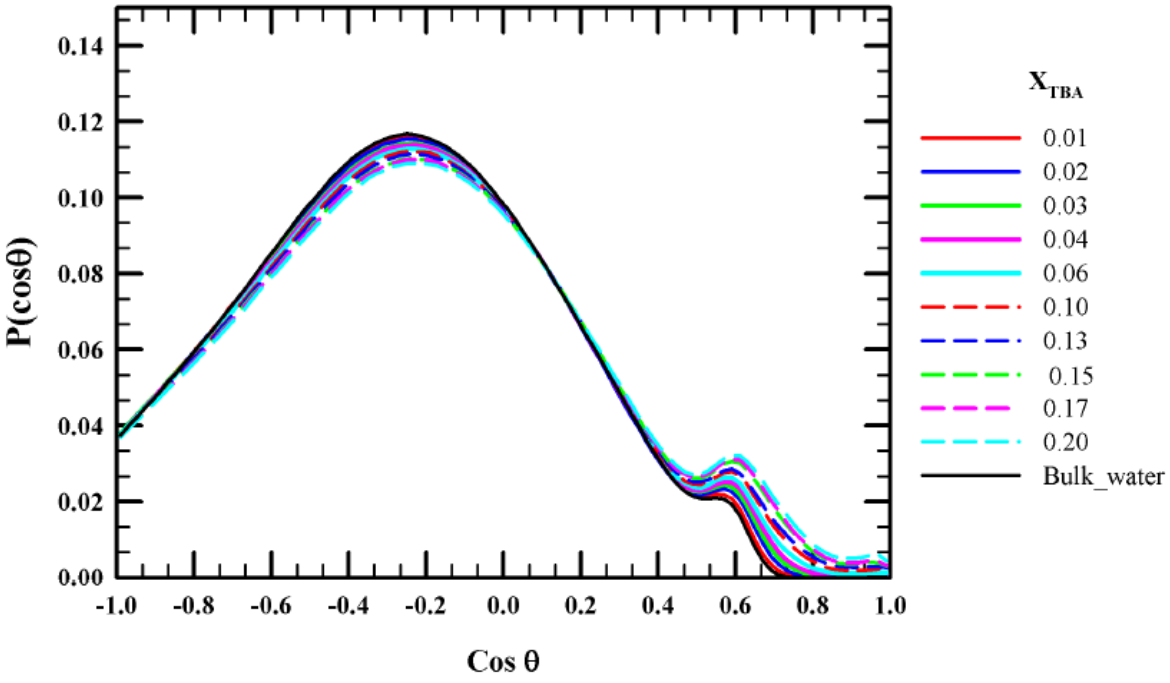

Figure 4.A.4: Composition dependent distribution of tetrahedral order parameter $P(Q)$.

(Different compositions are color coded).

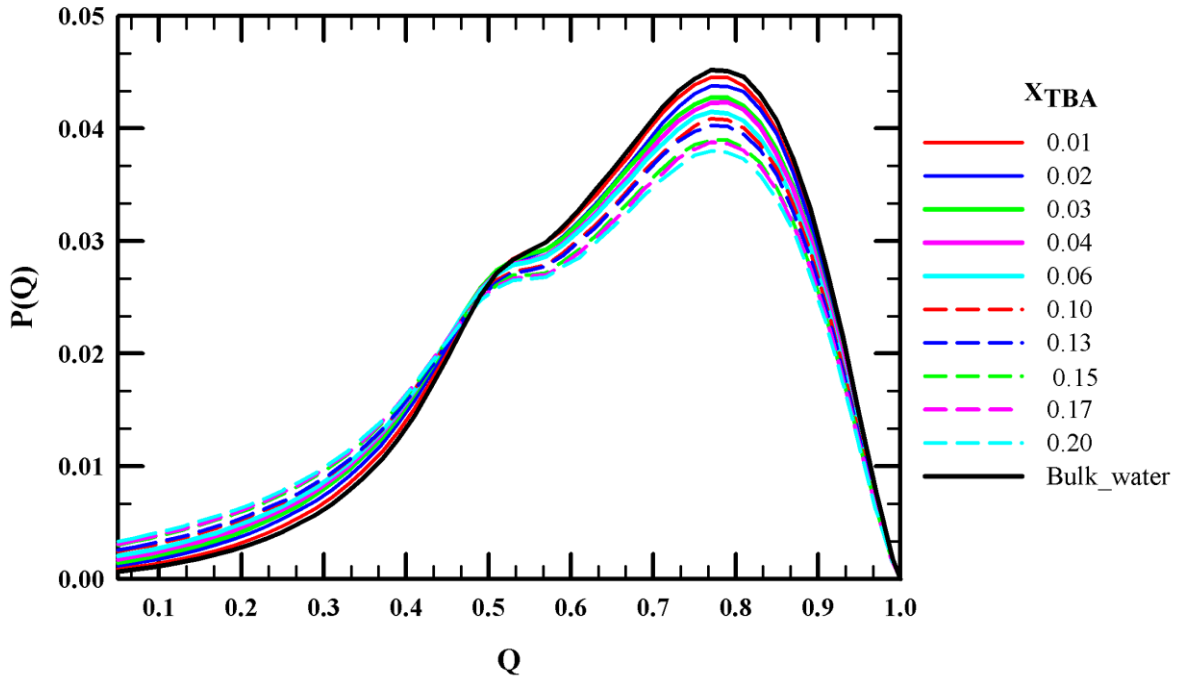

Figure 4.A.5: Composition dependent distribution of angles $P(\cos\theta_{ijk})$ subtended by two neighboring molecules at the central water molecule (shown in Figure 4.A.3). (Different compositions are color coded)

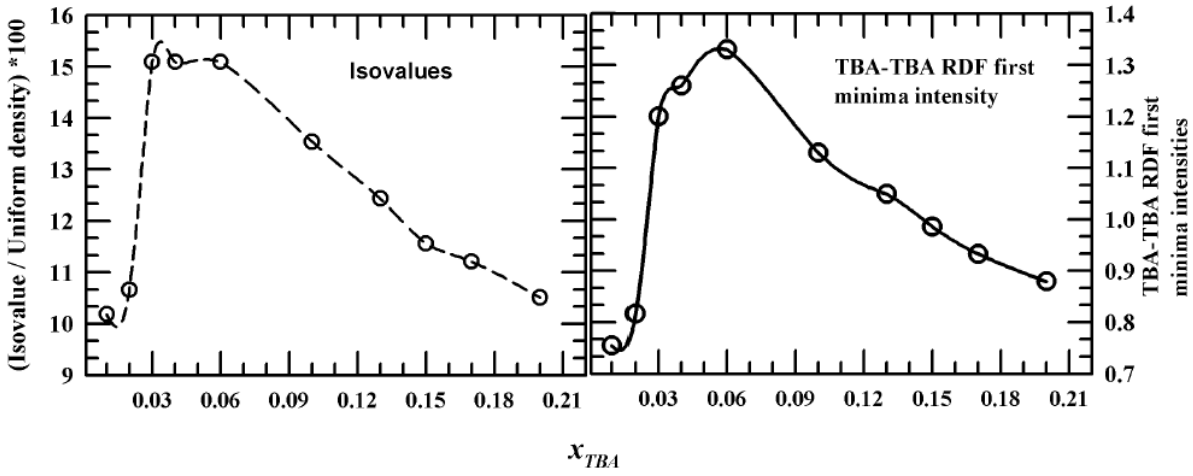

Figure 4.A.6: Composition dependent TBA-TBA isovalues and its comparison with the composition dependent first minimum intensities of TBA-TBA RDFs.

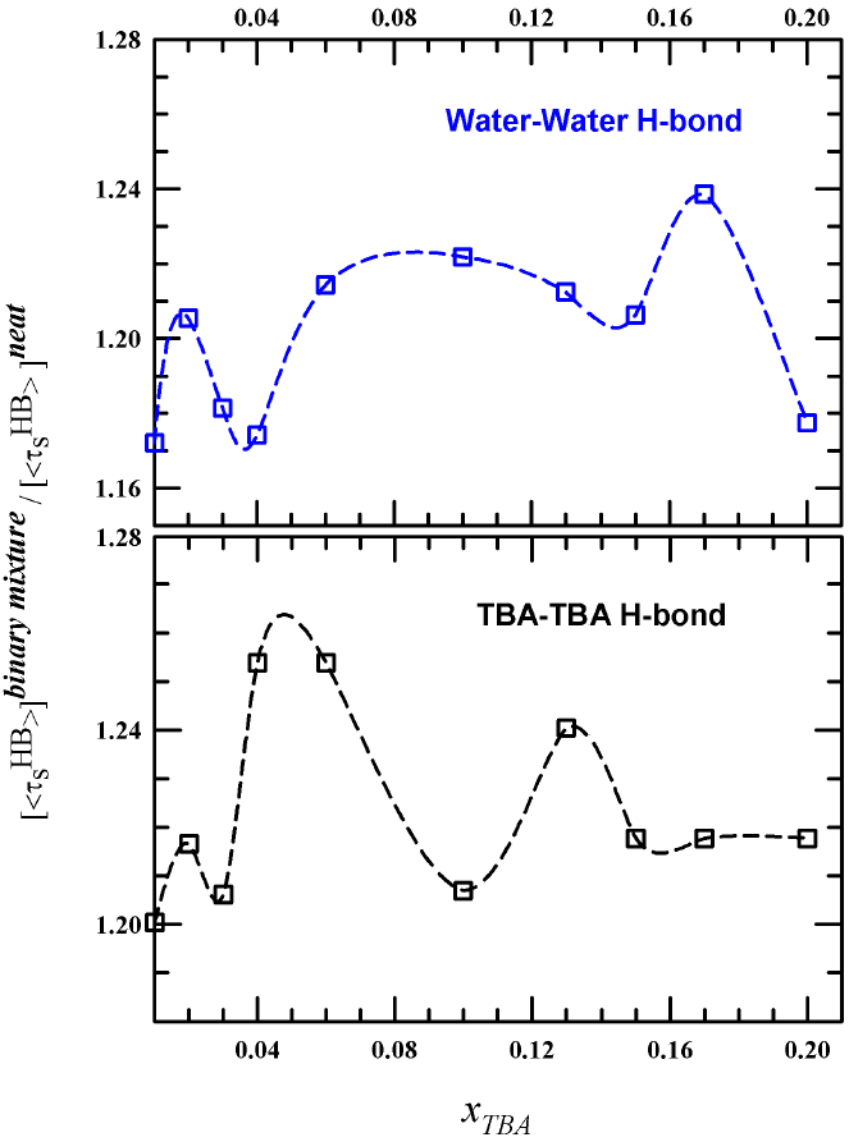

Figure 4.A.7: Composition dependent TBA-TBA and water-water average continuous H-bond relaxation times ratioed against the respective values for the neat systems. Note, water-water $< \tau_S^{HB} >$ is divided by neat water $< \tau_S^{HB} >$ (0.57 ps) and TBA-TBA values divided by neat TBA $< \tau_S^{HB} >$ (0.26 ps).

Appendix 4.B

Table 4.B.1: Number of TBA and water molecules employed in the present simulation study.

x_{TBA}	**0.01**	**0.02**	**0.03**	**0.04**	**0.06**	**0.10**	**0.13**	**0.15**	**0.17**	**0.20**
N_{TBA}	100	200	300	400	600	1000	1300	1500	1700	2000
N_{water}	9900	9800	9700	9600	9400	9000	8700	8500	8300	8000

Table 4.B.2: Non-bonded force field parameters for all atom representation of TBA-TBA interaction.

atoms	$\varepsilon_i(kJ/mol)$	σ_i(Å)	q_i
O	0.67	3.00	-0.5723
C(*tert*-butyl)	0.1674	3.80	0.3885
C(methyl)	0.1674	3.80	-0.3510
H(methyl)	0.1674	2.40	0.1010
H(hydroxyl)	0.0	0.0	0.3278

Table 4.B.3: Bonded (bonds and angle) force field parameters for TBA-TBA interaction.

Bonds			Angles		
	$K_R(kJ/mol/\text{Å}^2)$	$R_{eq}(\text{Å})$		$K_\theta(kJ/mol/deg^2)$	$\theta_{eq}(deg)$
$O-H$	2284	0.9292	$H-O-C_{tb}$	195.4	111.28
$O-C_{tb}$	1580	1.4164	$O-C_{tb}-C_m$	314.0	111.28
C_m-C_{tb}	923	1.5240	$C_m-C_{tb}-C_m$	222.3	108.745
C_m-H_m	1294	1.111	$C_{tb}-C_m-H_m$	143.1	111.445
			$H_m-C_m-H_m$	147.3	108.754

Table 4.B.4: Torsional force field parameters for TBA-TBA interaction.

dihedral angle	phase angle (deg)	K_{DIH} (kJ/mol)	multiplicity
$H-O-C_{tb}-C_m$	0	0.58	3
$O-C_{tb}-C_m-H_m$	0	0.83	3
$C_m-C_{tb}-C_m-H_m$	0	0.83	3

Table 4.B.5: Comparison between the experimental and simulated densities. Relative errors (with respect to experiment) are also shown.

x_{TBA}	Present simulations	Experiments	Relative Error (%)
0.01	996.56	990.41	0.049
0.02	994.30	984.98	0.394
0.03	983.48	980.15	0.152
0.04	978.44	975.61	0.174
0.06	971.20	965.05	0.45
0.10	913.86	942.10	2.99
0.13	897.70	--------	-------
0.15	883.00	917.47	3.75
0.17	883.07	--------	-------
0.20	858.08	896.99	4.33
1.00	754.40	780.43	3.34

Table 4.B.6: First peak heights ($g(\sigma)$) of the TBA-TBA, TBA-water and water-water RDFs.

x_{TBA}	TT	TW	WW
0.0	------	-------	3.24
0.01	3.17	1.65	3.37
0.02	3.64	1.56	3.52
0.03	5.07	1.29	3.67
0.04	5.18	1.12	3.82
0.06	5.06	0.82	4.18
0.10	4.05	0.63	4.99
0.13	3.68	0.53	5.60
0.15	3.43	0.50	6.06
0.17	3.23	0.50	6.52
0.20	3.00	0.50	7.23
1.0	2.03	-------	-------

Table 4.B.7: Structural and dynamical parameters for neat TBA and neat water.

	g(σ)	CN_{ij} / population P_{ij}^{CN}(%)	N_{i-j}^{HB}/ Population P_{ij}^{HB} (%)	τ_{hb}^{S}(ps)	$< Q >$
Neat TBA	2.03	12.35 / (9.65 %)	1.25 / (54%)	0.26	------
Neat water	3.24	4.38 / (4.38%)	3.67 / (100%)	0.57	0.67

Table 4.B.8: Coordination Numbers (CN_{xy}) of species *y* around species *x* within a distance corresponding to the first minima of RDF ($g_{xy}(r)$) and corresponding fraction of species molecules within the same distance (P_{xy}^{CN}). TT represents TBA-TBA, TW TBA-water and WW water-water.

x_{TBA}	CN_{TT}	P_{TT}^{CN} (%)	CN_{TW}	P_{TW}^{CN}(%)	CN_{WW}	P_{WW}^{CN}(%)
0.0	------	------	-------	------	4.38	0.04
0.01	0.81	0.81	31.66	0.32	4.32	0.04
0.02	1.79	0.90	28.98	0.30	4.24	0.04
0.03	1.79	1.32	23.46	0.24	4.22	0.04
0.04	5.48	1.37	19.81	0.21	4.20	0.04
0.06	7.81	1.30	13.65	0.14	4.25	0.05
0.10	9.42	0.94	9.09	0.10	4.12	0.05
0.13	10.24	0.79	6.91	0.08	4.12	0.05
0.15	10.48	0.70	6.10	0.07	4.10	0.05
0.17	10.69	0.62	5.62	0.07	4.08	0.045
0.20	10.86	0.54	5.12	0.06	4.03	0.05
1.0	12.35	9.65	-------	-------	-------	-------

Table 4.B.9: Composition dependent average number of H-bonds between species *i* and *j* (N_{i-j}^{HB}) and population of participant (*i*) molecules (P_{i-j}^{HB}) in percentage.

x_{TBA}	N_{T-T}^{HB}	P_{T-T}^{HB} (%)	N_{T-W}^{HB}	P_{T-W}^{HB}(%)	N_{W-W}^{HB}	P_{W-W}^{HB}(%)
0.0	------	------	-------	------	3.66	100.0
0.01	1.00	1.62	1.99	97.65	3.65	99.99
0.02	1.00	2.66	2.03	98.22	3.63	99.98
0.03	1.11	13.47	1.89	89.38	3.61	99.98
0.04	1.13	17.06	1.78	87.13	3.60	99.95
0.06	1.14	19.04	1.75	79.05	3.56	99.94
0.10	1.20	34.14	1.63	56.50	3.54	99.85
0.13	1.19	40.69	1.52	47.68	3.54	99.70
0.15	1.22	41.47	1.54	45.16	3.52	99.59
0.17	1.23	44.40	1.48	41.72	3.52	99.37
0.20	1.22	43.70	1.44	39.99	3.50	99.31
1.0	1.25	39.99	-------	-------	-------	---------

Table 4.B.10: Population of TBA molecules participating in H-bonding with only TBA, only water, both with TBA and water molecules. Population of TBA molecules not participating in H-bond formation.

x_{TBA}	**Only TBA (%)** $[P_{TBA-TBA}]$	**Only water (%)** $[P_{TBA-water}]$	**Both TBA water (%)** $[P_{TBA-TBA-water}]$	**Not H bonded at all (%)**
0.0	-------	-----	-------	------
0.01	0.00	97.32	0.76	1.92
0.02	0.00	98.28	0.80	0.92
0.03	2.45	86.05	3.88	7.61
0.04	3.12	81.72	4.92	10.22
0.06	7.01	75.48	3.42	14.09
0.10	15.66	52.08	3.95	28.31
0.13	18.17	42.98	4.57	34.27
0.15	19.57	41.28	4.16	34.99
0.17	21.29	37.65	3.91	37.14
0.20	21.32	35.51	4.38	38.79
1.0	----	-----	-----	-----

Table 4.B.11: Composition dependent ensemble averaged tetrahedral order parameter $< Q >$ for water in aqueous TBA solutions.

x_{TBA}	$< Q >$
0.0	0.6690
0.01	0.6626
0.02	0.6561
0.03	0.6468
0.04	0.6393
0.06	0.6304
0.10	0.6162
0.13	0.6058
0.15	0.5924
0.17	0.5853
0.20	0.5753
1.0	----

Table 4.B.12: Composition dependent isovalues used for plotting spatial distribution functions (SDFs) for TBA-TBA and TBA-water surfaces.

x_{TBA}	Relative TBA-TBA isovalues * 100	Relative TBA- water isovalues
0.01	10.1838	31.925
0.02	10.6585	30.342
0.03	15.0900	29.027
0.04	15.0900	27.725
0.06	15.0900	25.256
0.10	13.5400	20.972
0.13	12.4339	18.589
0.15	11.5585	17.107
0.17	11.2086	15.847
0.20	10.5090	14.144

Table 4.B.13: Block averaged continuous hydrogen bond relaxation ($S_{HB}(t)$) times $< \tau_{S\,(i\_j)}^{HB} >$ and the corresponding variances.

x_{TBA}	$< \tau_{S\,(T\_T)}^{HB} >$ **(ps)**	$\sigma_{\tau_S}^2$	$< \tau_{S\,(T\_W)}^{HB} >$ **(ps)**	$\sigma_{\tau_S}^2$	$< \tau_{S\,(W\_W)}^{HB} >$ **(ps)**	$\sigma_{\tau_S}^2$
0.01	0.2995	0.0337	0.4440	0.0135	0.6755	2.6395e-4
0.02	0.2873	0.0249	0.4600	2.8191e-3	0.7012	2.6823e-4
0.03	0.3163	7.4014e-4	0.5171	8.7367e-3	0.6814	1.1092e-3
0.04	0.3142	9.7095e-4	0.5180	9.5908e-3	0.6836	1.0434e-3
0.06	0.3256	9.3178e-5	0.5247	1.9547e-3	0.7108	5.7744e-4
0.10	0.3149	1.1143e-4	0.5684	1.6763e-3	0.7141	1.4026e-3
0.13	0.3216	1.3529e-4	0.5890	7.4551e-4	0.7005	7.0926e-4
0.15	0.3170	4.0624e-5	0.5240	1.1220e-3	0.6992	8.5090e-4
0.17	0.3171	2.6439e-5	0.6231	5.4704e-4	0.7162	8.7406e-4
0.20	0.3129	3.0964e-5	0.5977	7.7133e-4	0.6821	6.9798e-4
1.0	0.2582	--------	-------	-------	-------	-------

References

[1] G. Roux, D. Roberts, G. Perron, and J.E. Desnoyers, J. Solut. Chem. **9**, 629 (1980).

[2] K. Nakanishi, Bull. Chem. Soc. Jpn. **33**, 793 (1960).

[3] P. Jones, A.K. Covington, Symposium on Equilibria and Reaction Kinetics in Hydrogen-bonded Solvent Systems (1968: University of Newcastle upon Tyne), University of Newcastle upon Tyne, and W.F.K. Wynne-Jones, *Hydrogen-Bonded Solvent Systems: Proceedings* (Routledge, 1968).

[4] F. Franks, F. DS Reid in Water: A Comprehensive Treatise, Edited by F. Franks. (**1973)**.

[5] Y. Koga, *Solution Thermodynamics and Its Application to Aqueous Solutions: A Differential Approach* (Elsevier, 2017).

[6] Y. Koga, J. Phys. Chem. **100**, 5172 (1996).

[7] G.I. Egorov and D.M. Makarov, J. Chem. Thermodyn. **43**, 430 (2011).

[8] E. Boucher and J. MURRELL, *Properties of Liquids and Solutions* (Wiley, 1982).

[9] P. Atkins and J. De Paula, *Elements of Physical Chemistry* (Oxford University Press, USA, 2013).

[10] D. Bowron, J. Finney, and A. Soper, J. Phys. Chem. B **102**, 3551 (1998).

[11] D. Bowron and S.D. Moreno, J. Chem. Phys. **117**, 3753 (2002).

[12] D. Bowron and S. Díaz Moreno, J. Phys. Chem. B **109**, 16210 (2005).

[13] S. Dixit, J. Crain, W. Poon, J.L. Finney, and A.K. Soper, Nature **416**, 829 (2002).

[14] S. Banerjee, J. Furtado, and B. Bagchi, J. Chem. Phys. **140**, 194502 (2014).

[15] R. Gupta and G.N. Patey, J. Chem. Phys. **137**, 034509 (2012).

[16] P.G. Kusalik, A.P. Lyubartsev, D.L. Bergman, and A. Laaksonen, J. Phys. Chem. B **104**, 9526 (2000).

[17] P.G. Kusalik, A.P. Lyubartsev, D.L. Bergman, and A. Laaksonen, J. Phys. Chem. B **104**, 9533 (2000).

[18] S. Paul and G. Patey, J. Phys. Chem. B **110**, 10514 (2006).

[19] S. Banerjee, R. Ghosh, and B. Bagchi, J. Phys. Chem. B **116**, 3713 (2012).

[20] A.R. Abdel Hamid, R. Mhanna, R. Lefort, A. Ghoufi, C. Alba-Simionesco, B. Frick, and D. Morineau, J. Phys. Chem. C **120**, 9245 (2016).

[21] M. Požar, B. Lovrinčević, L. Zoranić, T. Primorać, F. Sokolić, and A. Perera, Phys. Chem. Chem. Phys. **18**, 23971 (2016).

[22] A. Perera, Pure Appl. Chem. **88**, 189 (2016).

[23] A. Perera, F. Sokolić, and L. Zoranić, Phys. Rev. E **75**, 060502 (2007).

[24] H. Laurent, D.L. Baker, A.K. Soper, M.E. Ries, and L. Dougan, J. Phys. Chem. B **124**, 10983 (2020).

[25] S. Zhang, B. Andrews, R. Schweitzer-Stenner, and B. Urbanc, J. Phys. Chem. B **124**, 11600 (2020).

[26] A. Ghoufi, J. Phys. Chem. B **124**, 11501 (2020).

[27] F. Franks and J. Desnoyers, Water Sci. Rev. **1**, 171 (1985).

[28] T. Pradhan, P. Ghoshal, and R. Biswas, J. Chem. Sci. **120**, 275 (2008).

[29] S. Indra and R. Biswas, J. Chem. Phys. **142**, 204501 (2015).

[30] H.A.R. Gazi and R. Biswas, J. Phys. Chem. A **115**, 2447 (2011).

[31] T. Pradhan, H.A.R. Gazi, and R. Biswas, J. Chem. Phys. **131**, 054507 (2009).

[32] T. Pradhan, P. Ghoshal, and R. Biswas, J. Phys. Chem. A **112**, 915 (2008).

[33] S. Indra, B. Guchhait, and R. Biswas, J. Chem. Phys. **144**, 124506 (2016).

[34] S. Indra and R. Biswas, J. Chem. Sci. **128**, 753 (2016).

[35] C. de Visser, G. Perron, and J.E. Desnoyers, Can. J. Chem. **55**, 856 (1977).

[36] K. Iwasaki and T. Fujiyama, J. Phys. Chem. **83**, 463 (1979).

[37] T.M. Bender and R. Pecora, J. Phys. Chem. **90**, 1700 (1986).

[38] G. Euliss and C. Sorensen, J. Chem. Phys. **80**, 4767 (1984).

[39] G. Roux, D. Roberts, G. Perron, and J.E. Desnoyers, J. Solut. Chem. **9**, 629 (1980).

[40] M. Brai and U. Kaatze, J. Phys. Chem. **96**, 8946 (1992).

[41] G. D'Arrigo and J. Teixeira, J. Chem. Soc. Faraday Trans. **86**, 1503 (1990).

[42] J.L. Finney, D. Bowron, R.M. Daniel, P. Timmins, and M.A. Roberts, Biophys. Chem. **105**, 391 (2003).

[43] D. Banik, S. Bhattacharya, P.K. Datta, and N. Sarkar, ACS Omega **3**, 383 (2018).

[44] S. Chakraborty, E. Sehanobish, and M. Sarkar, Chem. Phys. Lett. **501**, 118 (2010).

[45] C. Okpala, A. Guiseppi-Elie, and D.M. Maharajh, J. Chem. Eng. Data **25**, 384 (1980).

[46] P.K. Kipkemboi and A.J. Easteal, Can. J. Chem. **72**, 1937 (1994).

[47] I.S. Khattab, F. Bandarkar, M.A.A. Fakhree, and A. Jouyban, Korean J. Chem. Eng. **29**, 812 (2012).

[48] D.-R. Chiou, S.-Y. Chen, and L.-J. Chen, J. Chem. Eng. Data **55**, 1012 (2010).

[49] J.P. Hansen and I.R. McDonald, *Theory of Simple Liquids* (1986).

[50] S. Paul and G. Patey, J. Phys. Chem. B **116**, 4991 (2012).

[51] J.L. Abascal and C. Vega, J. Chem. Phys. **123**, 234505 (2005).

[52] E. Duboué-Dijon and D. Laage, J. Phys. Chem. B **119**, 8406 (2015).

[53] M.P. Allen and D.J. Tildesley, *Computer Simulation of Liquids* (Oxford university press, 2017).

[54] S. Nosé, Mol. Phys. **52**, 255 (1984).

[55] W.G. Hoover, Phys. Rev. A **31**, 1695 (1985).

[56] M. Parrinello and A. Rahman, J. Appl. Phys. **52**, 7182 (1981).

[57] D. Hess and E. Lindahl, Univ. Gron. **2010**, 1991 (2001).

[58] D. Van Der Spoel, E. Lindahl, B. Hess, G. Groenhof, A.E. Mark, and H.J. Berendsen, J. Comput. Chem. **26**, 1701 (2005).

[59] E. Lindahl, B. Hess, and D. Van Der Spoel, Mol. Model. Annu. **7**, 306 (2001).

[60] H.J. Berendsen, D. van der Spoel, and R. van Drunen, Comput. Phys. Commun. **91**, 43 (1995).

[61] H. Bekker, H. Berendsen, E. Dijkstra, S. Achterop, R. Van Drunen, D. Van der Spoel, A. Sijbers, H. Keegstra, B. Reitsma, and M. Renardus, in (World Scientific Singapore, 1993), pp. 252–256.

[62] M. Brehm and B. Kirchner, J. Cheminformatics **4**, F1 (2012).

[63] W. Humphrey, A. Dalke, and K. Schulten, J. Mol. Graph. **14**, 33 (1996).

[64] M.E. Lee and N.F. van der Vegt, J. Chem. Phys. **122**, 114509 (2005).

[65] M. Kiselev, D. Ivlev, Y. Puhovski, and T. Kerdcharoen, Chem. Phys. Lett. **379**, 581 (2003).

[66] A. Fornili, M. Civera, M. Sironi, and S.L. Fornili, Phys. Chem. Chem. Phys. **5**, 4905 (2003).

[67] S. Kaur and H.K. Kashyap, J. Chem. Sci. **129**, 103 (2017).

[68] D. Bowron, A. Soper, and J. Finney, J. Chem. Phys. **114**, 6203 (2001).

[69] G. D'Arrigo, J. Teixeira, R. Giordano, and F. Mallamace, J. Chem. Phys. **95**, 2732 (1991).

[70] A. Luzar, Faraday Discuss. **103**, 29 (1996).

[71] A. Luzar and D. Chandler, J. Chem. Phys. **98**, 8160 (1993).

[72] M. Ferrario, M. Haughney, I.R. McDonald, and M.L. Klein, J. Chem. Phys. **93**, 5156 (1990).

[73] A. Baksi and R. Biswas, J. Phys. Chem. B **124**, 11718 (2020).

[74] A. Baksi, P.Kr. Ghorai, and R. Biswas, J. Phys. Chem. B **124**, 2848 (2020).

[75] J.R. Errington and P.G. Debenedetti, Nature **409**, 318 (2001).

[76] I. Svishchev and P. Kusalik, J. Chem. Phys. **99**, 3049 (1993).

[77] P.G. Kusalik and I.M. Svishchev, Science **265**, 1219 (1994).

[78] A. Chandra, Phys. Rev. Lett. **85**, 768 (2000).

[79] S. Balasubramanian, S. Pal, and B. Bagchi, Phys. Rev. Lett. **89**, 115505 (2002).

Chapter 5

Why Some Reactions Occurring in Widely Different Viscous Media Possess Similar Reaction Rate? An Analytical Investigation Employing Experimental Dielectric Relaxation Data

5.1 Introduction

This chapter explores the interconnection between solvent friction and reaction rate. This is one of the ways that a solvent can exert control on a reaction occurring in it. Solvent polarity is the other factor which can tune a reaction via modifying the reaction barrier.[1,2] In a two-dimensional picture of a reaction barrier separating the reactant and the product surfaces, a reactant molecule experiences solvent friction while crossing the barrier top. The downward curvature of the barrier then decides the extent of coupling between the reaction rate and solvent friction. In a non-Markovian rate theory,[3,4] the friction experienced by the reactant is not that exerted by the zero-frequency shear viscosity of the medium. The frictional resistance, in contrast, depends on the frequency with which the reactive mode vibrates and/or oscillates. This, in other words, sets a timescale for the reactant to reside on the barrier top. If the barrier is high and the curvature is sharp, the medium friction becomes the friction that involves the faster collective modes of the solvent motion. For a low barrier reaction, relatively broadened curvature allows the reactant to spend more time on barrier top, probing solvent friction for a longer duration. Reactions involving low barrier are therefore amenable to frictional resistance proportional to medium viscosity and the solvent impact on these reactions can be understood via the Smoluchowski description[5,6] of the reaction in the overdamped limit. For barrier-less reactions, on the other hand, solvent control may arise from the stabilization of the intermediate or the newly germinated product molecule where underdamped solvent modes such as collective intermolecular modes and librations assume significant importance.

For ultrafast reactions, such as, electron transfer reactions (ETRs), collective solvent modes can indeed be critically important. This is probably reflected in the repeated observation of ETRs and charge transfer reactions (CTRs) being nearly insensitive to or strongly decoupled from solvent viscosity.[7–9] This can be qualitatively explained by either assuming that solvents play minimal role for ETRs or only the ultrafast solvent polarization modes couple to the ETRs. ETRs involve appreciable charge transfer (for example, $Fe^{+2} \rightarrow Fe^{+3}$) and it is difficult to believe that solvent polarization can remain non-responsive to such charge transfer and the subsequent stabilization via solvent reorganization. One approach then would be to explore that part of the solvent friction which involves inertial and collective solvent modes. This, in turn, means the calculations of the frequency dependent solvent friction, incorporating both the collective and diffusive solvent modes in a consistent manner. Fortunately, such a prescription is already available.[10,11] In this scheme, the generalized rate of solvent polarization contains the wavenumber (k) and frequency (z) dependent solvent rotational ($\Gamma_R(k,z)$) and translational ($\Gamma_T(k,z)$) frictional kernels. The $k \rightarrow 0$ and $z \rightarrow \infty$ limits of these kernels then describe the frictional response arising from the collective and inertial solvent modes. In the collective wavenumber limit ($k \rightarrow 0$), $\Gamma_R(k \rightarrow 0, z)$ has been connected to the frequency dependent dielectric function, $\varepsilon(z)$, of a medium which can be accessed via dielectric relaxation (DR) measurements. Note here that in this wavenumber limit, extremely fast underdamped solvent motions fall in the high frequency regime and have been incorporated via the intermolecular vibrations and librations that contribute to the dielectric dispersion from the infinite frequency dielectric constant to square of the refractive index, $\varepsilon_\infty - n^2$. In DR experiments, this belongs to the tera-Hertz regime of $\varepsilon(z)$.

Three differently viscous media spanning a viscosity variation of three orders of magnitude have been considered for representative calculations. They are an ionic liquid ([BMIM][PF_6], $\eta \sim 310$ cP)[12], a common dipolar solvent (ethanol, $\eta \sim 1.08$ cP)[13] and an ionic deep eutectic solvent (Acetamide+ LiBr, $\eta \sim 1950$ cP).[14] experimental viscosities and dielectric constants of these systems are summarized in Table 5.1. Rotational frictional kernel ($\Gamma_R(k,z)$) has been calculated, as already mentioned, by using the analytical expression that connects solvent medium friction to the experimental dielectric relaxation (DR) data.

5.2 Theoretical Formalism and Method of Calculation

The relation that connects the wavenumber and frequency dependent rotational frictional kernel, $\Gamma_R(k,z)$, to the frequency dependent dielectric function, $\varepsilon(z)$, is the following:[15–17]

$$\frac{2k_BT}{I[z+\Gamma_R(k,z)]} = \frac{z\varepsilon_0[\varepsilon(z)-\varepsilon_\infty]}{f(110;k\to0)\varepsilon_\infty[\varepsilon_0-\varepsilon_\infty]} \qquad (5.1)$$

Where, $\varepsilon_\infty$is the dielectric constant in the high-frequency limit and I the moment of inertia. $f(110,k)$ is related to the orientational direct correlation function, $c(100,k)$, through the relation[18,19] $f(110,k) = 1 - (\rho_d^0/_{4\pi})c(110,k)$.

The necessary inputs for the calculations of $\Gamma_R(k,z)$ are therefore as follows: (i) the wavenumber dependent orientational static structure factor, $c(110,k)$ and (ii) the experimental dielectric relaxation data of these liquids. The orientational static structure factor for these liquids is obtained from the mean spherical approximation (MSA) model[20,21] with proper correction at $k \to 0$, using the experimental static dielectric constant after approximating the dipolar species as dipolar hard spheres.

The dielectric relaxation data used in the present calculations have been taken from various measurements employing different frequency windows: $(0.1 \le \nu/GHz \le 3000)$ for [BMIM][PF_6][22], $(0.2 \le \nu/GHz \le 50)$ for the ionic DES[14], $(0.2 \le \nu/GHz \le 89)$ for ethanol[23]. In those DR experiments, measured $\varepsilon(z)$ data were found to fit to the following forms,

$$\varepsilon(\nu) = \varepsilon_\infty + \frac{\Delta\varepsilon_1}{(1+(i2\pi\nu\tau_1)^{1-\alpha_1})^{\beta_1}} + \frac{\Delta\varepsilon_2}{(1+i2\pi\nu\tau_2)} + \frac{\Delta\varepsilon_3}{(1+i2\pi\nu\tau_3)} + \frac{\Delta\varepsilon_4}{{\nu_4}^2-\nu^2+i\gamma_4\nu},$$

for [BMIM][PF_6],

$\varepsilon(\nu) = \varepsilon_\infty + \sum_{j=1}^{j=4} \frac{\Delta\varepsilon_j}{(1+i2\pi\nu\tau_j)}$, for (acetamide + LiBr) DES,

$\varepsilon(\nu) = \varepsilon_\infty + \sum_{j=1}^{j=3} \frac{\Delta\varepsilon_j}{(1+i2\pi\nu\tau_j)}$, for ethanol.

Here τ_j denotes the relaxation time associated with the $\Delta\varepsilon_j$ dispersion. α_1 and β_1 determine the shape of a relaxation mode. In addition, $z = 2\pi i\nu$. The experimental dielectric relaxation data for these three systems are provided in Table 5.2.

The orientational dynamics is calculated through the following prescription[12,16–19,24–26]. We have calculated the reorientation time correlation function (RTCF) of rank ℓ by Laplace transformation ($\mathcal{L}^{-1}$) of a frequency dependent term which is dependent on rotational kernel found from Eq. 1. Laplace transform is then numerically obtained via the Stehfest algorithm.

$$C_\ell(t) = \mathcal{L}^{-1}[z + \frac{\ell(\ell+1)k_BT}{I[z+\Gamma_R(z)]}]^{-1} \quad (5.2)$$

RTCFs for $\ell = 1$ and $\ell = 2$ have been calculated from Eq.2. Multi-exponential fits to the simulated RTCFs then lead to the analytical estimation of the average reorientational correlation times through time integration: $\tau_{avg}^{\ell} = \int_0^\infty dt\ C_\ell(t) = \frac{\sum a_i\tau_i}{\sum a_i}$.

It is evident from Table 5.3 that a considerable part of the high frequency dispersion, $\varepsilon_\infty - {n_D}^2$, have remained undetected in the present measurements for (Acetamide +LiBr) DES. This means that the relevant calculations have completely missed the frictional contributions from the ultrafast solvent modes.

In order to account for the missing high frequency dielectric dispersion in our calculations, we have attributed this dispersion, $\varepsilon_\infty - {n_D}^2$, to one or a couple of damped collective intermolecular modes of the solvent as follows:[10–12,22,27]

$$\varepsilon(z) = \varepsilon_\infty + \sum_i \frac{\Delta S_i}{[1+(z\tau_i)^{1-\alpha_i}]^{\beta_i}} + [\Delta S_{CIM}\Omega^2/(\Omega^2 + z^2 + z\Gamma)] \quad (5.3)$$

where Γ, the damping constant, being approximately twice as large as the resonating frequency Ω, and $\Delta S_{CIM} = \varepsilon_\infty - {n_D}^2$. We expect a little variation in Ω will not affect the qualitative understanding regarding the role of this collective mode in the high frequency frictional response of the medium. This assignment is similar in spirit to what was done before while calculating ionic conductivities and dynamic solvation response in water.[26]

Measurements[22] of $\varepsilon(z)$ in the frequency range of $0.1 \leq z/GHz \leq 3000$ have indicated contributions from the IL collective modes around ~70-120 cm^{-1} for several imidazolium ILs. This has been assigned to cation CIM (restricted rotation or oscillatory motion). Terahertz time-domain spectroscopic measurements[28] involving metalocenium ILs have suggested that inter-ion vibrations between the cations and anions and cation CIM are responsible for the observed dynamics in the THz region. These studies also have revealed that the bands appearing in the frequency range ~ 20-50 cm^{-1} show the maximum amplitude. Optical heterodyne-detected Raman-induced Kerr-effect spectroscopic (OHD-RIKES) study[29–34] of several imidazolium ILs have attributed the collective IL dynamics in this region to the collective intermolecular modes of imidazolium ring at frequencies at 30, 65 and 100 cm^{-1} corresponding to different anionic configuration around cations. Interestingly, simulation studies[35–37] with finite number of cations and anions (within ILs) have also suggested the collective dynamics in the THz region (~30 cm^{-1}).

In the low frequency Kerr spectra[38] for DESs obtained via Fourier transforming the collected Kerr transients, a characteristic band clearly appears for $[0.78\ CH_3CONH_2 + 0.22\ LiBr]$ DES. Because of less depolarized Raman activities of intermolecular/interionic vibrational motions for spherical ions (which are mostly collision induced or interaction induced translational motions), this band can only be attributed to the collective solvent mode involving the H-bonded molecules. This has motivated us to assign the resonating frequency at around $100\ cm^{-1} (\sim 3\ THz)$ for this DES for carrying out the dispersion, $\varepsilon_\infty - {n_D}^2$, unaccounted for in the available DR data.

Table 5.1 Viscosity values and dielectric constants for the DES, [BMIM][PF_6] and ethanol.

System	**Acetamide + LiBr (DES)**	**[BMIM][PF6] (IL)**	**Ethanol (Dipolar Liquid)**
Viscosity (cP)	1950 (293 K)	310 (298 K)	1.095 (298 K)
$\boldsymbol{\varepsilon_0}$	23.6 (293 K)	11.8 (298 K)	24.35 (298 K)

Table 5.2 Experimental DR data for [BMIM][PF_6], DES, and ethanol.

System	ε_0	τ_1	α_1 β_1	$\Delta\varepsilon_1$	τ_2	$\Delta\varepsilon_2$	τ_3	$\Delta\varepsilon_3$	τ_4	$\Delta\varepsilon_4$	ε_∞
[BMIM][PF_6]	11.8	1406	0.0 0.37	7.04	38.8	0.45	1.26	0.81	ν_4=2.77 THz γ_4=7.77 THz	1.38	2.10
Acetamide +LiBr	23.6	715		13.3	131	3.0	30	1.4	4.0	0.4	5.6
Ethanol	24.3	161		20.2	3.3	1.43	1.43	0.22			1.93

Table 5.3 Missing dispersion and frequency coverage of different experiments

System	ε_0	ε_∞	$n_D{}^2$	$\varepsilon_\infty - n_D{}^2$	Frequency window (employed in experiments)
[BMIM][PF_6]	11.8	2.10	1.9850	0.115 (1.18%)	0.1GHz-3 THz
(Acetamide+LiBr)	23.6	5.6	1.9796	3.62 (20.11%)	0.2GHz-50 GHz
Ethanol	24.35	1.93	1.85	0.09 (0.4%)	0.1GHz-1.5THz

5.3 Numerical Results and Discussion

5.3.1 Frequency dependent Rotational kernel, $\Gamma_R(k \to 0, z)$ employing experimental DR data

Frequency dependent rotational frictional kernel, $\Gamma_R(k, z)$, calculated via Eq. 1 in the limit of zero wavenumber, is presented in Figure 5.1 for the three representative solvents. Available experimental DR data[14,22,23] from Table 5.2 has been used in these calculations as inputs. Note the available frequency coverage of all the three systems is not the same. The frequency (horizontal axis) has been scaled with the highest frequency coverage of DR data of each individual systems. For example, for DES, frequency has been scaled with 50 GHz – the highest frequency of the measurement window. We find that at high frequency region rotational kernel of three different system approaches three different values, the difference being huge between the DES and the other two solvents.

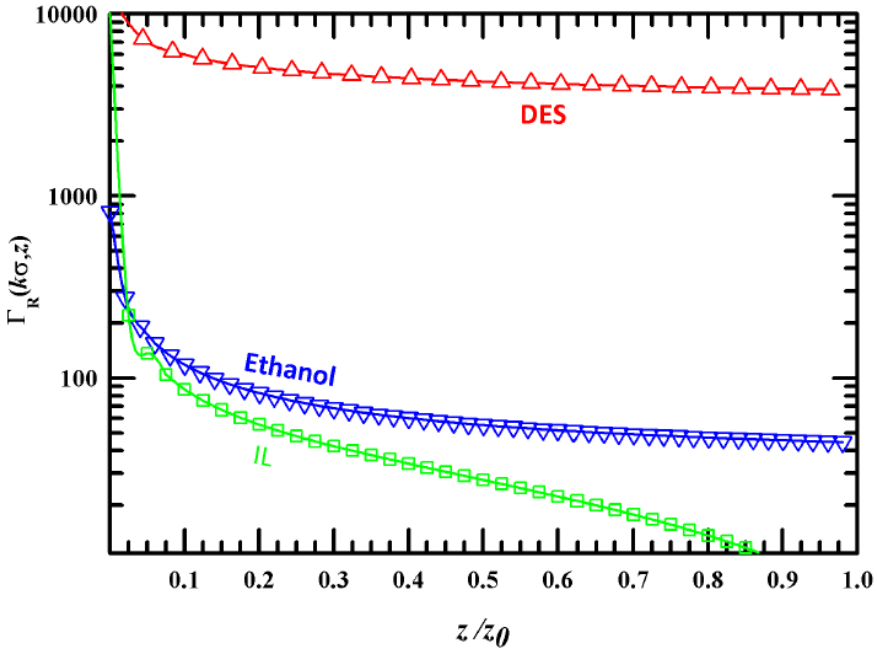

Figure 5.1: Frequency dependent rotational frictional kernel, $\Gamma_R(k \to 0, z)$, for the three different systems obtained via using the experimentally available dielectric relaxation (DR) data. Note the frequency axis has been scaled with the highest frequencies accessible to three different DR experiments.

It is now important to note that a significant amount of dispersion is missing in the DR data summarized in Table 5.3. The most pronounced missing dispersion (~20% of the total available dispersion) is for the DES studied here where the frequency window employed in the measurements was $0.2 \leq \nu/GHz \leq 50$. For IL and Ethanol, the missing components are relatively smaller - ~1.2 % and ~0.4 %., respectively. This is the reason for the dramatic difference in $\Gamma_R(k \to 0, z)$ between the DES and the other two solvents.

In order to address this issue, we have attributed the missing dispersion, as discussed earlier in Section 2, to a CIM centered at $100\ cm^{-1}$ for all these three systems, and calculated $\Gamma_R(k \to 0, z)$. Numerical results after incorporating the missing high frequency dispersion are shown in Figure 5.2. The inseparability of the calculated frictional kernels, particularly at higher frequencies, is quite insightful. The near independence and/or strong decoupling of ETR on solvent viscosity can now be explained in terms of nearly the same high frequency rotational frictional response in these three solvents of widely different viscosities. It is also interesting to note that, although the zero-frequency rotational friction ($\Gamma_R(0)$) for these three systems are drastically different from each other (because it probes the zero-frequency dielectric constant, ε_0), the high frequency rotational response ($\Gamma_R(\infty)$) is quite small compared to the zero-frequency value and comparable to each other (see Table 5.4).

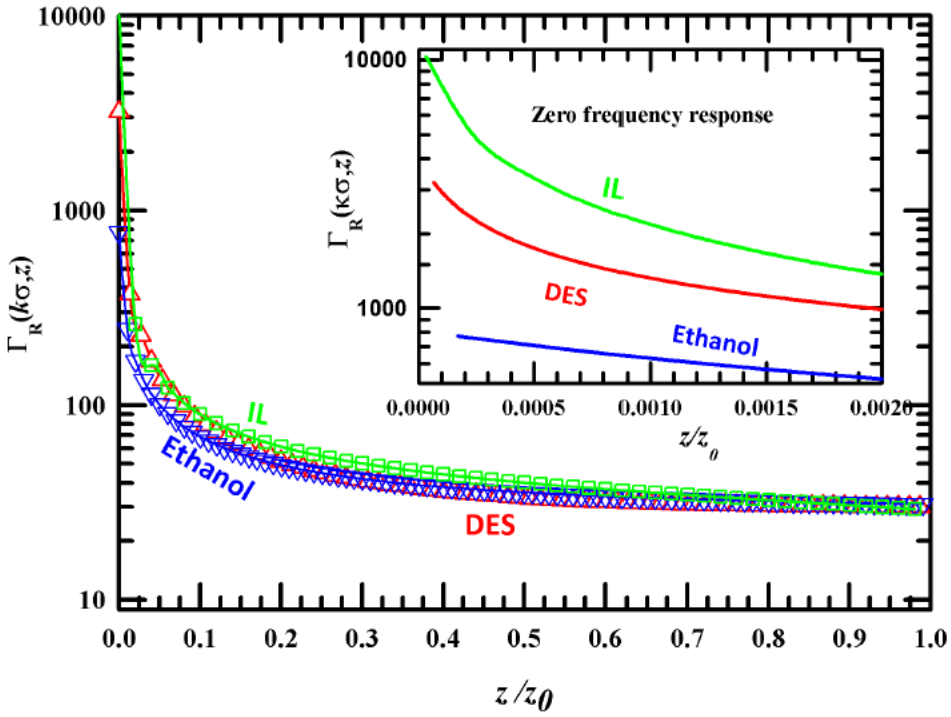

Figure 5.2: Frequency dependent rotational Kernel for three different systems obtained after addition of ultrafast component to experimentally available dielectric relaxation (DR) data. X axis has been scaled with 3 THz for all the systems.

Table 5.4: Zero frequency and high frequency rotational Kernel values for three systems [BMIM][PF_6], DES, and Ethanol.

System	$\boldsymbol{\Gamma_R(0)}$	$\boldsymbol{\Gamma_R(\infty)}$
IL ([BMIM][PF_6])	10000	29
DES (Acetamide + LiBr)	3206	30
Ethanol	169	30

5.3.2 Reorientational time correlation Function of rank $\ell = 1$, $C_1(t)$

Next, we examine how addition of collective intermolecular modes influences analytically evaluated reorientational timescales of these three systems. Reorientational time correlation function RTCF of rank ℓ , $C_\ell(t)$ has been calculated via equation 5.2. First, we employed experimentally available DR data as input to equation 5.2 and calculated $C_1(t)$. We present the numerical results in Figure 5.3. These $C_1(t)$ decays have been found to fit to multi-exponential functions of time.

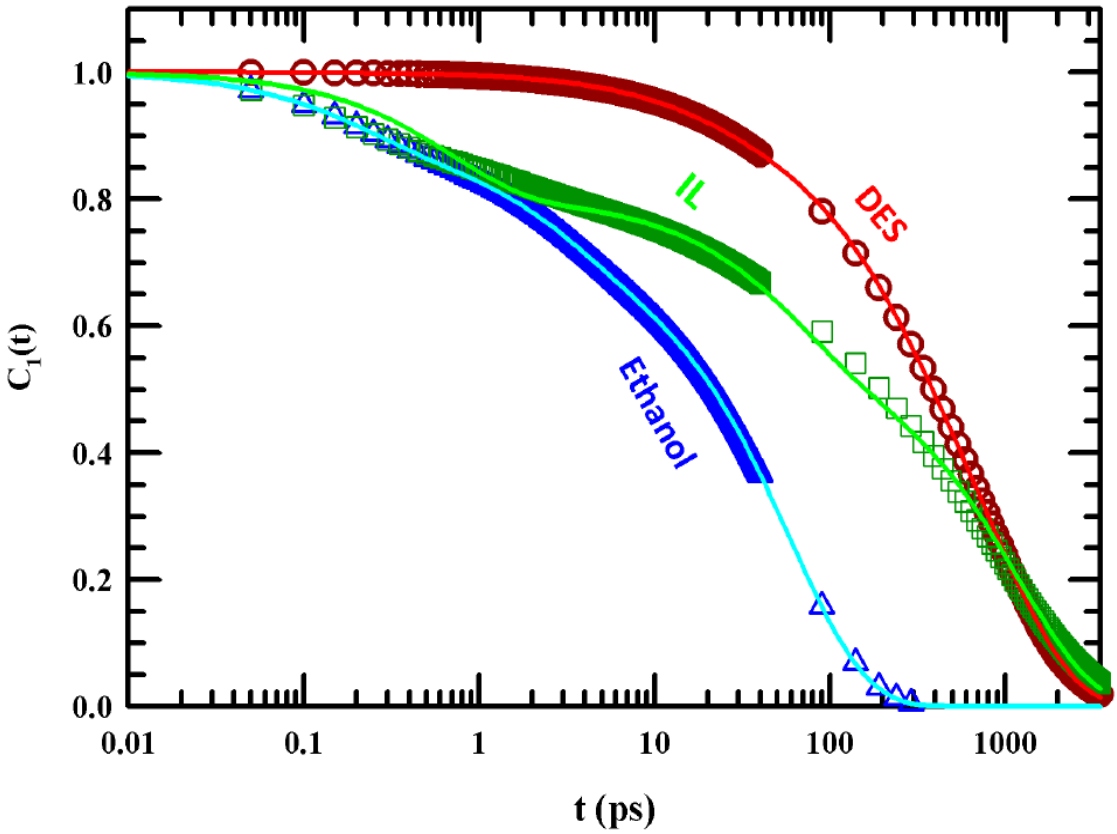

Figure 5.3: Normalized reorientational time correlation function (RTCF) of rank $\ell = 1$ for the three systems [BMIM][PF_6], DES, and ethanol obtained via equation 5.2 using the experimentally available dielectric relaxation (DR) data as input parameters.

Next, following our earlier approach we have incorporated collective intermolecular mode at a resonating frequency of 100 cm^{-1} for the missing dielectric dispersion at high frequency. With these modified DR data for these three solvents $C_1(t)$ decays have been calculated. Results are shown in Figure 5.4.

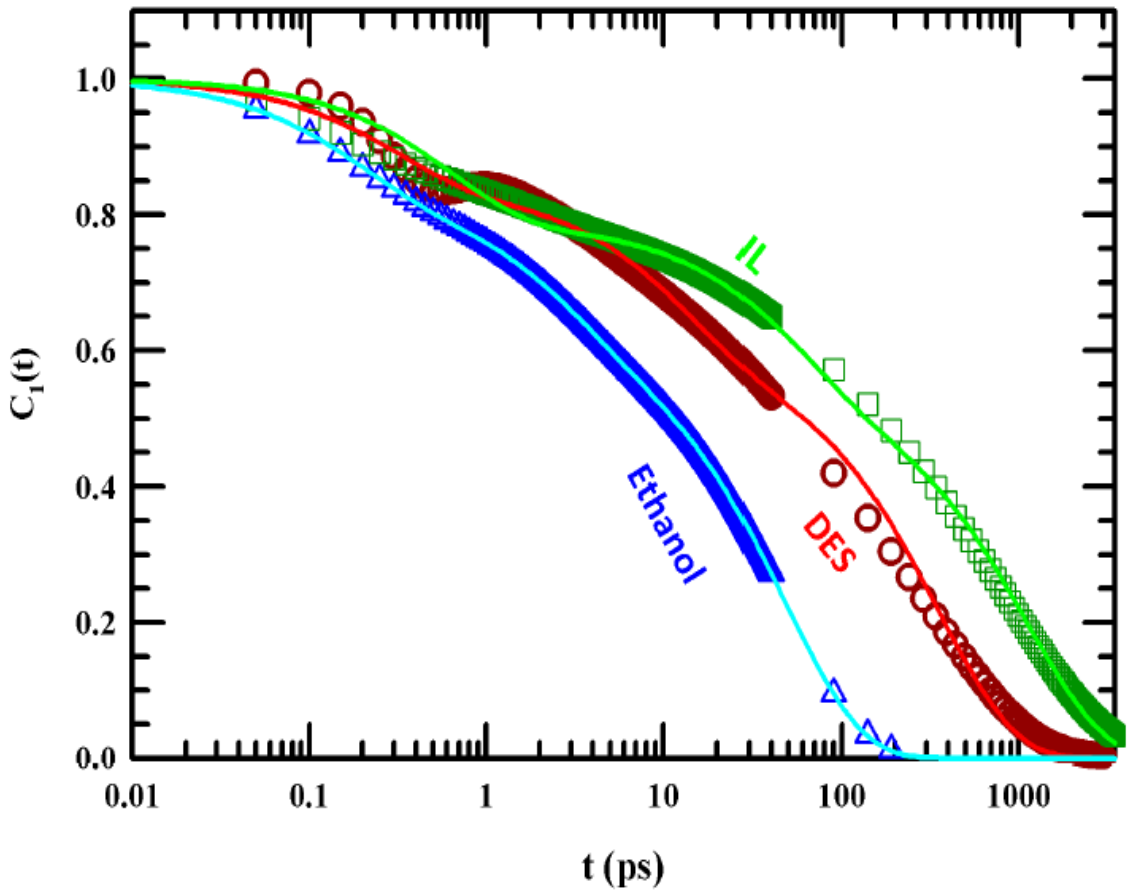

Figure 5.4: RTCF of rank $\ell = 1$ for [BMIM][PF_6], DES, and ethanol obtained via equation 5.2 after addition of CIM at 100 cm^{-1} to the experimentally available DR data as input.

The multi-exponential fit parameters corresponding to $C_1(t)$ with and without ultrafast component along with available simulated parameters are presented in Table 5.5, Table 5.6 and Table 5.7 for these three systems.

Table 5.5: Comparison of multi-exponential fit parameters of analytically calculated and simulated $C_1(t)$ for deep eutectic system (DES).

DES $C_1(t)$	**without CIM**	**with CIM**	**Available Simulation Results**[39]
a	0.022	0.1689	0.11
τ_1 (ps)	93.545	0.1126	0.6
b	0.7420	0.1453	0.35
τ_2 (ps)	732.60	4.8239	15.4
c	0.1549	0.2889	0.49
τ_3 (ps)	73.74	50	52.9
d	0.0798	0.4385	0.05
τ_4 (ps)	1904.30	476.19	588.2
τ_{avg} (ps)	708.93 ps	225	60.8

Data in Table 5.5 suggest that reorientation time predicted from our analytical study after addition of CIM for the ionic DES agrees better with the available simulation prediction.

Table 5.6 reports the multi-exponential fit parameter for [BMIM][PF_6] where missing dispersion was comparatively smaller (~1.2%). The analytically predicted timescales with and

without the CIM contribution to experimental DR data are similar because of the small missing dispersion. The prediction of a nanosecond component (~2ns) in simulations can also be seen in our analytical calculations (~1ns). However, the 40 ns component found in simulations is completely absent. This inconsistency between theory and simulations may arise because of the following reasons: (i) 40 ns timescale corresponds to a peak frequency in the mega-Hertz (MHz) regime which has not been covered in the relevant DR measurements. Slow rotation of a composite body may account for this relaxation timescale; and (ii) the interaction potential employed for simulations of the IL may not be appropriate and therefore, this timescale might be spurious.

Table 5.6: Comparison of multi-exponential fit parameters of analytically calculated and simulated $C_1(t)$ for [BMIM][PF_6].

Ionic Liquid $C_1(t)$	**without CIM**	**with CIM**	**Simulation Result**[40]
a	0.14	0.14	0.04
τ_1 **(ps)**	1.38	1.22	107.5
b	0.25	0.22	0.06
τ_2 **(ps)**	68	54	2000
c	0.54	0.57	0.85
τ_3 **(ps)**	1203	1002	38782
τ_{avg} **(ps)**	667	583	34830

Table 5.7 summarizes the calculated and simulated timescales associated with $C_1(t)$ decay for ethanol. The analytically predicted timescales with and without the addition of the CIM contribution are also found not to be very different because of the small missing dispersion. Note that a better agreement appears between theory and simulations when the CIM contribution is incorporated in the calculations.

Table 5.7: Comparison of multi-exponential fit parameters of analytically calculated and simulated $C_1(t)$ for Ethanol.

Ethanol $C_1(t)$	**Our Result without UF**	**Our Result with UF**	**Simulation Result**[41]
a	0.11	0.1635	
τ_1 (ps)	0.20	0.1725	
b	0.17	0.0471	
τ_2 (ps)	2.84	1.82	
c	0.025	0.1576	
τ_3 (ps)	30.39	2.96	
d	0.69	0.6312	
τ_4 (ps)	60.60	47.62	
τ_{avg} (ps)	43.45	30.30	27

5.4 Conclusion

In this analytical study, we have investigated the origin behind the near-independence of rates of electron transfer reaction (ETR) in solvents of widely different viscosities. Three differently viscous media - an ionic liquid ([BMIM][PF_6], $\eta \sim 310$ cP), a dipolar solvent (ethanol, $\eta \sim 1.09$ cP) and a high viscous deep eutectic solvent (acetamide+ LiBr, $\eta \sim 1950$ cP) have been chosen for the representative calculations. Rotational part of the solvent friction was calculated employing the available experimental DR data. Missing dispersion ($\varepsilon_\infty - n^2$) in the available experimental DR data have been incorporated in our calculations via a CIM centered at 100 cm^{-1}. Subsequent calculations of $\Gamma_R(\kappa \to 0, z)$ reveal that the high frequency values of this frictional kernel are nearly identical, although their zero frequency values are very different. This insensitivity of $\Gamma_R(\kappa \to 0, z)$ in the limit of high frequency to medium viscosity can explain the near-independence and/or strong decoupling of ETR rate from medium viscosity. Calculated reorientational correlation functions for $\ell = 1$ have been found to agree better with simulation predictions after incorporating the CIM contribution to the available experimental DR data.

References

[1] J.T. Hynes, J. Stat. Phys. **42**, 149 (1986).

[2] B. Bagchi, *Molecular Relaxation in Liquids* (OUP USA, 2012).

[3] J.E. Straub, M. Borkovec, and B.J. Berne, J. Chem. Phys. **84**, 1788 (1986).

[4] B. Carmeli and A. Nitzan, J. Chem. Phys. **79**, 393 (1983).

[5] P.-H. Chavanis, Entropy **21**, (2019).

[6] M.V. Smoluchowski, Ann. Phys. **353**, 1103 (1916).

[7] X. Li, M. Liang, A. Chakraborty, M. Kondo, and M. Maroncelli, J. Phys. Chem. B **115**, 6592 (2011).

[8] R. Lynden-Bell, Electrochem. Commun. **9**, 1857 (2007).

[9] Y. Shim and H.J. Kim, J. Phys. Chem. B **111**, 4510 (2007).

[10] S. Daschakraborty and R. Biswas, J. Chem. Phys. **137**, 114501 (2012).

[11] S. Daschakraborty, T. Pal, and R. Biswas, J. Chem. Phys. **139**, 164503 (2013).

[12] H.K. Kashyap and R. Biswas, J. Phys. Chem. B **112**, 12431 (2008).

[13] B. González, N. Calvar, E. Gómez, and Á. Domínguez, J. Chem. Thermodyn. **39**, 1578 (2007).

[14] K. Mukherjee, A. Das, S. Choudhury, A. Barman, and R. Biswas, J. Phys. Chem. B **119**, 8063 (2015).

[15] S. Roy and B. Bagchi, Chem. Phys. **183**, 207 (1994).

[16] S. Roy and B. Bagchi, J. Chem. Phys. **99**, 9938 (1993).

[17] S. Roy and B. Bagchi, J. Chem. Phys. **99**, 1310 (1993).

[18] B. Bagchi, Annu. Rev. Phys. Chem. **40**, 115 (1989).

[19] B. Bagchi and A. Chandra, in *Adv. Chem. Phys.* (John Wiley & Sons, Ltd, 1991), pp. 1–126.

[20] E. Waisman and J.L. Lebowitz, J. Chem. Phys. **56**, 3093 (1972).

[21] E. Waisman and J.L. Lebowitz, J. Chem. Phys. **56**, 3086 (1972).

[22] A. Stoppa, J. Hunger, R. Buchner, G. Hefter, A. Thoman, and H. Helm, J. Phys. Chem. B **112**, 4854 (2008).

[23] J.T. Kindt and C.A. Schmuttenmaer, J. Phys. Chem. **100**, 10373 (1996).

[24] R. Biswas and B. Bagchi, J. Phys. Chem. **100**, 1238 (1996).

[25] N. Nandi, S. Roy, and B. Bagchi, J. Chem. Phys. **102**, 1390 (1995).

[26] B. Bagchi and R. Biswas, in *Adv. Chem. Phys.* (John Wiley & Sons, Ltd, 1999), pp. 207–433.

[27] H.K. Kashyap and R. Biswas, J. Phys. Chem. B **114**, 16811 (2010).

[28] A. Chakraborty, T. Inagaki, M. Banno, T. Mochida, and K. Tominaga, J. Phys. Chem. A **115**, 1313 (2011).

[29] G. Giraud, C.M. Gordon, I.R. Dunkin, and K. Wynne, J. Chem. Phys. **119**, 464 (2003).

[30] H. Shirota and E.W. Castner, J. Phys. Chem. A **109**, 9388 (2005).

[31] H. Shirota and E.W. Castner, J. Phys. Chem. B **109**, 21576 (2005).

[32] H. Shirota, K. Nishikawa, and T. Ishida, J. Phys. Chem. B **113**, 9831 (2009).

[33] T. Fujisawa, K. Nishikawa, and H. Shirota, J. Chem. Phys. **131**, 244519 (2009).

[34] D.A. Turton, J. Hunger, A. Stoppa, G. Hefter, A. Thoman, M. Walther, R. Buchner, and K. Wynne, J. Am. Chem. Soc. **131**, 11140 (2009).

[35] Y. Shim and H.J. Kim, J. Phys. Chem. B **112**, 11028 (2008).

[36] C. Schröder and O. Steinhauser, J. Chem. Phys. **131**, 114504 (2009).

[37] C. Schröder, J. Hunger, A. Stoppa, R. Buchner, and O. Steinhauser, J. Chem. Phys. **129**, 184501 (2008).

[38] R. Biswas, A. Das, and H. Shirota, J. Chem. Phys. **141**, 134506 (2014).

[39] S. Das, R. Biswas, and B. Mukherjee, J. Chem. Phys (under revision).

[40] T. Pal and R. Biswas, Theor. Chem. Acc. **132**, 1348 (2013).

[41] L. Saiz, J.A. Padró, and E. Guàrdia, J. Phys. Chem. B **101**, 78 (1997).

Chapter 6

Concluding Remarks and Future Problems

6.1 Concluding Remarks

The present Thesis summarizes a detailed investigation on hydrogen bonding structure and dynamics of different aqueous amphiphilic solutions both in bulk and confined state via molecular dynamics simulation studies. We also examined the near-independence of reaction rates on viscosity for electron transfer reaction with an analytical approach. Aqueous amphiphilic solutions like aqueous methanol, aqueous tertiary butyl alcohol (TBA) have been studied in simulations. Moderate sized (diameter ~ 55 Å) reverse micelle (RM) has been considered while exploring the effect of confining geometry on neat water and aqueous methanol solution structure and dynamics. Effect of confining geometry on solution hydrogen-bonded structure and dynamics has been investigated extensively via global and local order of orientation of water molecules and inter- and intra-species hydrogen bond lifetimes. Besides all these, different spatio-temporal heterogeneity parameters also have been studied to explore the effects of confinement geometry and chemical nature of surfactant (charged or neutral) molecules. It has been found that the two-state model, namely 'core-shell' model, for describing confined water in aqueous RM is inadequate. Preferential solvation has been found to be facilitated in aqueous alcohol solutions in presence of spherical confinement. Finally, we analyzed the inter- and intra-species hydrogen bond times and corresponding fluctuation in aqueous TBA solutions at very low to low alcohol concentrations. Interestingly, H-bond lifetime fluctuations are found to be correlated with solute-centered reactive and non-reactive relaxation dynamics. An analytical study also reveals how solvent friction which is coupled only to high frequency collective solvent modes, can dictate reaction rates for the electron transfer process. This study also explains near-independence of electron transfer rate in solvents of widely different viscosities.

Since conclusions have been provided at the end of each of the chapters in this Thesis, we refrain ourselves from providing conclusion separately. Instead, we discuss here a few relevant and interesting problems which can be studied in the near future.

6.2 Future Problems

6.2.1 Effects of confinement on structural and temporal heterogeneity of aqueous methanol solutions: A Molecular Dynamics Simulation Study.

It has been explored[1] how preferential solvation gets facilitated and microscopic di-mixing feature in methanol-water binary mixture become accentuated upon confinement in the relevant simulation study. Although aqueous methanol system is not a macroscopically heterogeneous system, they are microscopically heterogeneous. Till now no study has been performed to explore composition dependent spatial and temporal heterogeneity of aqueous methanol solutions. The effects of confinement on spatial and temporal heterogeneity of aqueous methanol should be explored via all-atom molecular dynamic simulations in order to understand the additional motional anomaly appearing from the confining surfaces. This separation of individual impact on motional features would require simulations of neat and binary mixtures – both in the bulk and under confinement. A composition dependence study, ranging from extremely dilute to highly concentrated methanolic aqueous solutions, should provide a detailed understanding.

6.2.2 How hydrogen Bond Lifetime distribution and corresponding fluctuations behave around 'dynamically' anomalous composition of aqueous amphiphilic solutions: A simulation study employing aqueous TMU solution as a model system.

Experimental time resolved fluorescence spectroscopic studies[2–6] have repeatedly reported an abrupt change in composition dependent probe lifetime in aqueous amphiphilic solutions. The origin is yet to be explored. To explore the origin behind this phenomenon, no simulation studies have been reported till now. We have presented simulation results of aqueous TBA solution in chapter 5, where we found unusual fluctuation in continuous water-water hydrogen bonds lifetime at a composition where experimental studies predicted the abrupt change in mole fraction dependent probe lifetimes. But it is still not clear how the continuous hydrogen bond fluctuations (continuous water-water hydrogen bond timescale) can be correlated with such long probe lifetimes which are of the order of hundreds of picoseconds. It will be

interesting to explore different time correlation functions via molecular dynamic simulation studies of aqueous tetramethylurea (TMU) solution at different TMU mole fractions. Investigation of structural H-bond lifetimes and the associated fluctuations may provide an important clue to this phenomenon.

6.2.3 Effect of cylindrical nanoconfinement on preferential solvation and microscopic di-mixing in aqueous alcohol solutions: A simulation study for understanding basics of targeted drug activation.

In chapter 2 of this thesis, we have presented simulated results[7] on how preferential solvation in aqueous methanol solution gets facilitated under spherical confinement (Reverse micelle). In the living world, this knowledge is really useful in the research of targeted drug delivery as nearly every drug molecule has both hydrophobic and hydrophilic parts. These drugs get activated depending on the chemical nature (pH) of the targeted regions. So, exploring how this preferential solvation phenomenon gets affected due to cylindrical confinement (resembling blood carrying nano-sized veins) will be an interesting topic. This can be done by carrying out molecular dynamic simulations of aqueous methanol solutions within a cylindrical nanopore.

6.2.4 Effect of size of alcohols on water tetrahedral Hydrogen bond structure: A Molecular Dynamic Study exploring water structure at a very local level.

How the addition of alcohol perturbs water tetrahedral hydrogen bond structure is a longstanding question. Numerous simulations and experimental studies[8–12] have been performed to explore this interesting aspect. Two schools of thoughts have been proposed: one that predicts[13] water hydrogen bond structure gets enhanced upon addition of alcohol up to certain concentration and another proposes water hydrogen bond structure remains pure water like around alcohol molecules even at composition methanol: water (wt %) =7:3.[14] This debate is yet to be solved. It will be interesting to explore how the effects of the addition of alcohol on water tetrahedral structure depend on alcohol hydrophobic chain length. Composition dependent aqueous alcohol (which are miscible with water at all proportion) systems can be

studied via all atom molecular dynamic simulations. The composition range for aqueous alcohol solutions is an important choice. After choosing the composition range, simulations can be run for different alcohols. It will be really interesting to see how tetrahedrality and hydrogen bond dynamics changes for different alcohols. This study will also explore by how miscibility feature and hydrogen bonding are interconnected, and how heterogeneity aspect depends on the alkyl chain length – both in bulk and in binary aqueous mixtures. A similar study can be extended for non-water mixtures, such as acetonitrile-alcohol and acetonitrile-dioxane/tetrahydrofuran mixtures. One may also like to explore the difference between the heterogeneity features on water structure and dynamics induced by a hydroxylic solvent (such as alcohol) and a non-hydroxylic solvent (such as acetonitrile).

References

[1] A. Baksi and R. Biswas, J. Phys. Chem. B **124**, 11718 (2020).

[2] S. Indra, B. Guchhait, and R. Biswas, J. Chem. Phys. **144**, 124506 (2016).

[3] T. Pradhan, H.A.R. Gazi, and R. Biswas, J. Chem. Phys. **131**, 054507 (2009).

[4] T. Pradhan, P. Ghoshal, and R. Biswas, J. Chem. Sci. **120**, 275 (2008).

[5] T. Pradhan, P. Ghoshal, and R. Biswas, J. Phys. Chem. A **112**, 915 (2008).

[6] H.A.R. Gazi and R. Biswas, J. Phys. Chem. A **115**, 2447 (2011).

[7] A. Baksi, P.Kr. Ghorai, and R. Biswas, J. Phys. Chem. B **124**, 2848 (2020).

[8] S. Dixit, J. Crain, W. Poon, J.L. Finney, and A.K. Soper, Nature **416**, 829 (2002).

[9] T.C. Berkelbach, H. S. Lee, and M.E. Tuckerman, Phys. Rev. Lett. **103**, 238302 (2009).

[10] A. Luzar and D. Chandler, J. Chem. Phys. **98**, 8160 (1993).

[11] S. Banerjee, J. Furtado, and B. Bagchi, J. Chem. Phys. **140**, 194502 (2014).

[12] H. Laurent, D.L. Baker, A.K. Soper, M.E. Ries, and L. Dougan, J. Phys. Chem. B **124**, 10983 (2020).

[13] F. Li, Y. Wang, Z. Men, and C. Sun, Phys. Chem. Chem. Phys **22**, 26000 (2020).

[14] S. Dixit, J. Crain, W. Poon, J.L. Finney, and A.K. Soper, Nature **416**, 829 (2002).

Addendum I

Glucose-Water-Urea Deep Eutectics: How Water Structure and Dynamics Alters in a Crowded Environment

Ad.1.1 Introduction

Search for environmentally less harmful solvent has led to the advent of new classes of solvents such as room temperature ionic liquids[1], gas-expanded liquids[2], room-temperature supercritical fluids[3], and their aqueous binary mixtures and deep eutectic solvents (DESs)[4–6]. It has been found that the DESs are most efficient if aspects like biodegradability, flexibility in transportation, ease of handling and less toxicity are considered. DESs are multicomponent molten mixtures with a significantly lower liquidus temperature than the melting temperature of each of the individual components. Deep depression of the freezing point of DESs is a combined result of extensive inter-constituent H-bonding and the gain in entropy for being in the liquid phase. Recently, naturally abundant DES (NADESs) have received wide attention because of the inherent greenness and eco-sustainability. These NADESs[5,7,8] are based on natural compounds like amino acids, organic acids, urea and sugars. There are numerous experimental studies[5,8–10] which report various applications of different NADESs but study on detailed interactions and dynamics of these NADES is still very few and at the nascent stage.

In this simulation study we considered an earlier reported[11] glucose based NADES which was prepared by mixing glucose ($C_6H_{12}O_6$), urea (NH_2CONH_2), and water at the 6:4:1 weight ratio. This system is very complex and highly hydrogen bonded. Different structural aspects probing inter-and intra-species interactions have been studied. We explore the heterogeneity inherent to this complex ‘metastable’ system. This study aims at close inspection of how water hydrogen bonding structure and dynamics get affected in such a crowded environment where water is present as a minor component. Here we present some of the initial results which will provide a glimpse about the microstructure and dynamics of water in glucose based NADES.

Ad. 1.2. Simulation Details

The DES system (Glucose: Urea: water = 6:4:1 wt %) was treated via the standard equilibrium molecular dynamics simulation technique. Periodic boundary conditions[12] were employed to eliminate size effects. The leap-frog algorithm[12] with a time-step of 2 fs was used to integrate Newton's equation of motions maintaining fixed bond lengths. β-D glucose molecules were modelled atall-atom level, keeping the bond lengths fixed but bond angles and dihedrals flexible. Chair form of the β-D glucose molecule was used during simulations as this form is mostly available in nature. SPC/E[13] model of water and all atom urea interaction potential were used. OPLS-AA force field was used to define interaction parameters for glucose[14–16] and urea[17] during simulations.

The functional form of the glucose and Urea FF is given by,

$$V(r) = \sum_{bonds} K_r\left(r - r_{eq}\right)^2 + \sum_{angles} K_\theta\left(\theta - \theta_{eq}\right)^2 + \left\{\frac{V_1}{2}[1 + \cos(\phi + f_1)] + \frac{V_2}{2}[1 - \cos(2\phi + f_2)] + \frac{V_3}{2}[1 + \cos(3\phi + f_3)]\right\} + \sum_{i<j}\left(q_i q_j e^2/r_{ij} + A_{ij}/r_{ij}^2 - C_{ij}/r_{ij}^6\right)$$

66 number of glucose molecules, 111 water and 133 urea molecules were considered according to the weight percentage of experimentally prepared[11] DES. Packmol[18] software was used to build the initial cubic box with mentioned number of solvents uniformly. Starting configuration was subjected to energy minimization with steepest-descent algorithm.[12] Then the energy minimised structure was subjected to number of NVT equilibration steps, starting at a higher temp 500 K and then cooled down to 328 K in 50 K temperature step. Each of these runs were 500ps long. This cooling down process before NPT run was followed for better equilibration of this highly viscous (255 cP)[11] liquid at 328 K. Then a final NPT equilibration for 10ns was carried out to find the equilibrated density of the simulated DES. A well converged density was found in our simulation and it matches well with experimental density. During the NPT equilibration temperature was maintained at 328 K using the v-rescale thermostat[19] with 0.5 ps

time-constant. Pressure was maintained at 1 bar using the Berendsen barostat[20] with a time-constant of 2 ps. A cut-off of 1.4 nm was applied for non-bonded interactions. Electrostatic interactions were handled with highly efficient particle mess Ewald (PME) method[12].

Using the densities obtained from NPT run an additional NVT equilibration at 328 K was carried out for better statistics before the final production run of 100 ns with NVT ensemble in the same temperature. During the final NVT production run the trajectories were saved with a time-gap of 0.1 ps. An additional NVT production run of 10 ns was considered with the pre-equilibrated structure for H-bond dynamics analysis when we saved the trajectories and velocities at every 0.01 ps time gap. All the bonds were kept constrained during the whole simulation procedure using LINCS algorithm.[12] For performing all the simulations reported here, GROMACS 4.6.5 MD simulation package[21–24] was used. The simulated density (1.28 gm/cc) was found to be within 6% of error relative to the experimental density[11] (1.3639 gm/cc). Glucose, water and Urea atomic representations are shown in scheme Ad.1.

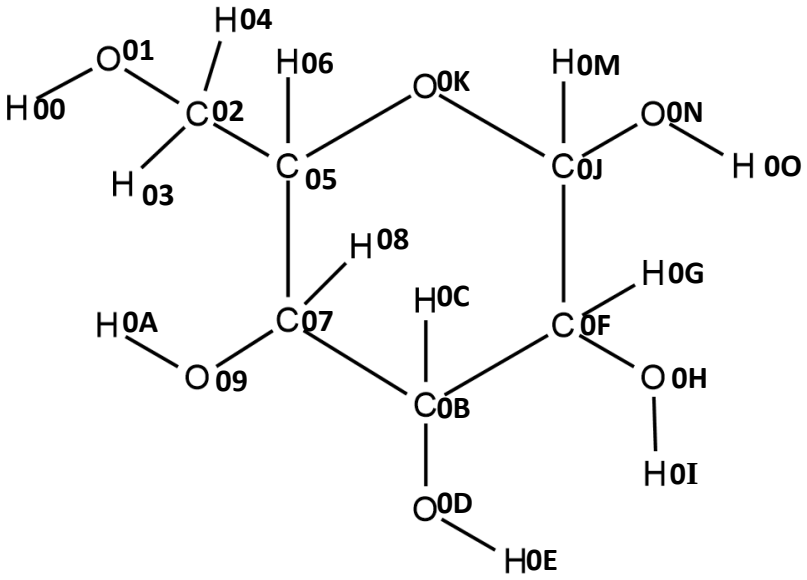

Glucose

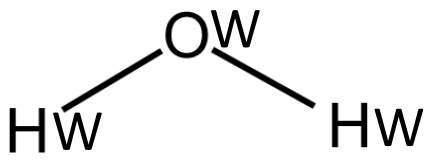

Water

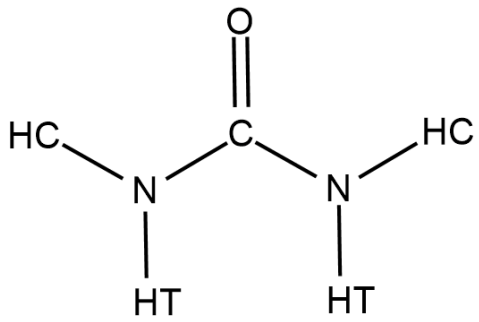

Urea

Scheme Ad.1: Atomic representations of glucose, urea and water molecules.

Ad.1.3 Simulation Results

Ad.1.3.1 Structural Properties

Ad.1.3.1.1 Radial Distribution Functions (RDFs)

Figure Ad.1.1 shows interactions between different species within this DES. Upper panel depicts oxygen-oxygen (OW-OW) interaction between the water molecules. For comparison, oxygen-oxygen RDF for pure water is presented. A very high and more intense (~5 times) first peak is found for OW-OW RDF, suggesting water clustering in this DES system. Middle panel depicts the RDF between different atoms of water and urea. It is found that interaction between water oxygen and urea hydrogen is negligible whereas interactions between water oxygen and urea carbon, nitrogen and oxygen are quite similar.

Lower panel shows RDFs between water oxygen and glucose oxygen atoms. These results suggest water oxygen and glucose ring oxygen (O0K). Oxygen atoms O0N shows slightly increased interaction than the ring oxygen whereas all other oxygen atoms are shows similar interactions with water. These results suggest that the interaction between water oxygen and glucose may be asymmetric.

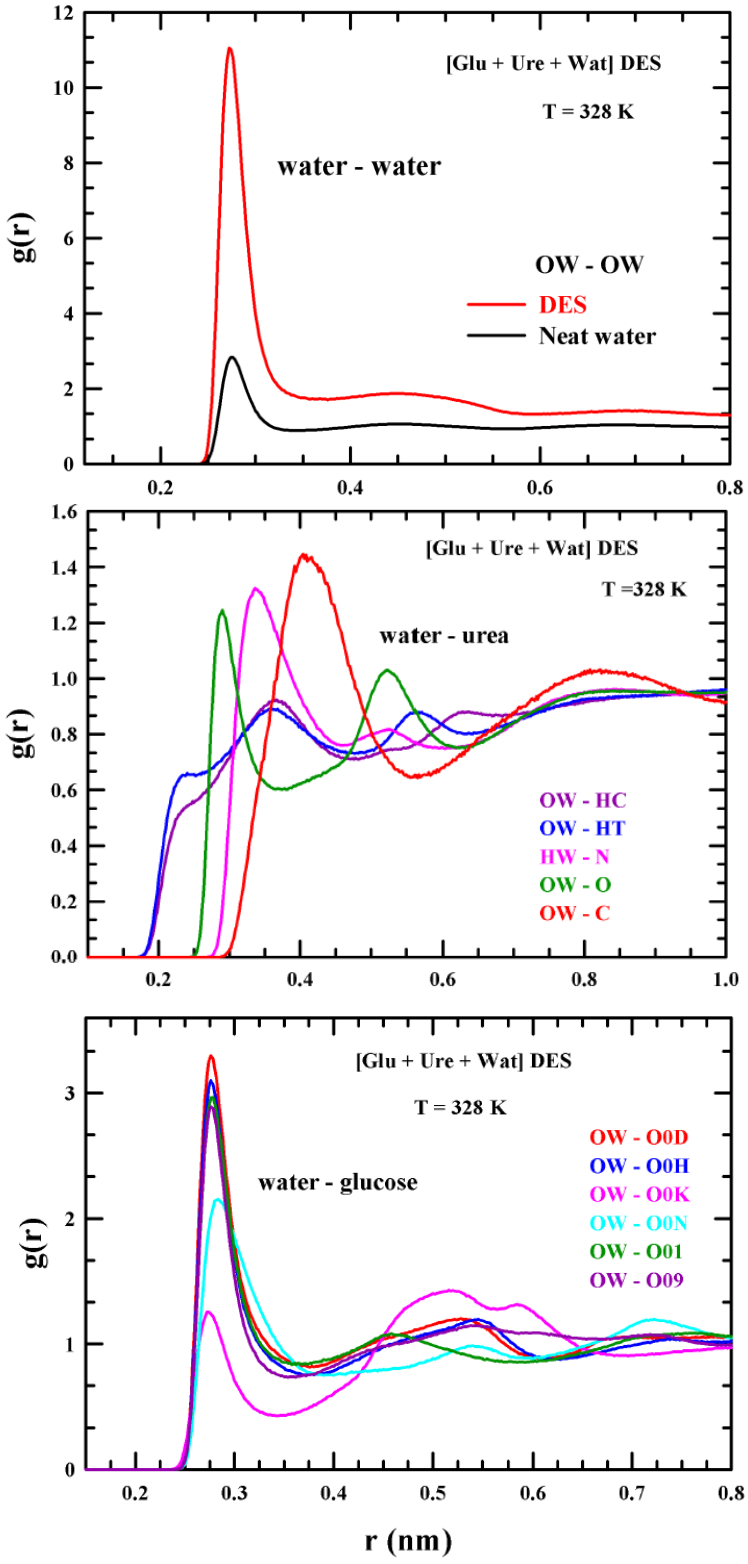

Figure Ad.1.1: Radial distribution function between different atoms of (a) water-water (b) water -urea (c) water-glucose. For comparison, OW-OW RDF of neat water is presented in (a).

Ad.1.3.1.2 Average number of hydrogen bonds between water molecules

Next, we calculate the average number of water-water hydrogen bonds per water molecule and corresponding participation population of water in DES at 328 K. Analysis for neat water also done at the same temperature for better comparison. The following prescription was used for detecting hydrogen bonds between water molecules: a) the distance between the donor oxygen atom and acceptor oxygen atom is less than 0.35 nm, b) the H-O (donor)-O (acceptor) angle is less than 30^{o}, and **c)** distance between O and H must be less than 0.28 nm. It is found that, while in neat water system average water-water H bonds per water molecule is nearly 3.5, it decreases to 1.62 in this DES. Interestingly, population of participant water molecules in water-water H-bonding is found to be ~78 % (shown in figure Ad.1.2). Note that in neat water, participation is ~100% for water molecules for water-water hydrogen bond formation.[25] We can therefore speculate that 78% water molecules are participating in water-water H-bond formation in addition to interacting with urea and glucose via H-bond interaction. The remaining 22 % is solely forming H-bonds with glucose and/or urea. Detailed H-bonding analysis results are still awaited.

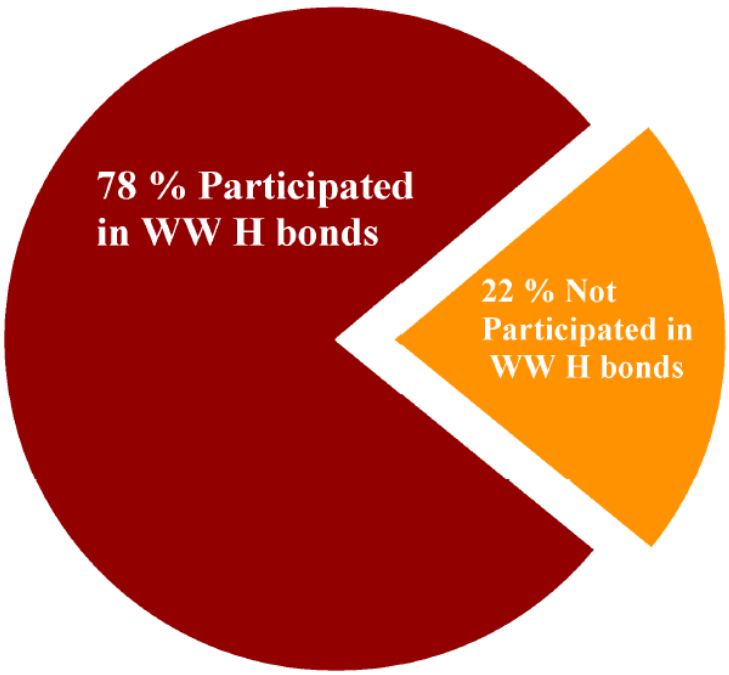

Figure Ad.1.2: Representation of participant and non-participant water population in the formation of direct water-water H-bonds in glucose-urea-water DES under study.

Ad.1.3.2 Dynamic Properties

Ad.1.3.2.1 Mean Squared Displacements (MSDs): Rattling-in-cage

Simulated center-of-mass mean square displacements (MSDs) for glucose, urea and water molecules in [Glu+Ure+Wat] DES at 328 K are presented in Figure Ad.1.3 (upper panel). MSDs exhibit t^{β} dependence, and it is associated with three different regimes: (i) $\beta = 2$ at initial times corresponds to inertial regime, (ii) $\beta < 1$ at intermediate time describes the sub-diffusive regime and finally (iii) $\beta = 1$ at long time, confirming the diffusive regime. The upper panel of Figure Ad.1.3 reveals the presence of sub-diffusive regime at the intermediate time for component particles in this DES suggesting rattling in a cage motion. Presence of rattling-in-cage motion suggests the presence of heterogeneous relaxation time scales in this DES. This behaviour of simulated MSDs correlates well with the experimental observation[11] of fractional viscosity dependence of solute rotation times, $\langle \tau_r \rangle \propto (\eta/T)^p$ with $p \approx 0.3 - 0.5$. The simulated dynamic heterogeneity presented in the next section will provide further support to this view.

Table Ad.1.1: Diffusion co-efficient values obtained from linear fitting the MSDs for glucose, urea and water molecules in [Glu+Urea+Water] DES

	D_{Glu} ($\times 10^{-9} m^2/sec^{-1}$)	D_{Ure} ($\times 10^{-9} m^2/sec^{-1}$)	D_{Wat} ($\times 10^{-9} m^2/sec^{-1}$)
[Glu+Ure+Wat] DES	1.197	0.727	0.133
Pure water (SPC/E) at T=328 K	-	-	3.255

The power, $\beta(t)$, in $\langle |\Delta r(t)|^2 \rangle \propto t^{\beta(t)}$, are presented in the lower panel of Figure Ad.1.3 after accessing the targeted time dependence via the following relation,

$$\beta(t) = \frac{d}{d[\ln(t)]} [ln\langle \Delta r^2(t) \rangle] \qquad \text{(Ad 1.1)}$$

Here, the MSDs will reach the diffusive limit (hydrodynamic limit), when $\beta = 1$. This Figure clearly shows that the MSDs reach the diffusive regime (β ~1) after a timescale of ~2 ns. We have calculated the diffusion coefficients of glucose, urea and water by considering MSDs in the diffusive limit through the Einstein relation[26] and these values are summarized in Table Ad.1.1. This result clearly shows that water diffusion in this DES is ~30 times slower than that in neat bulk water.

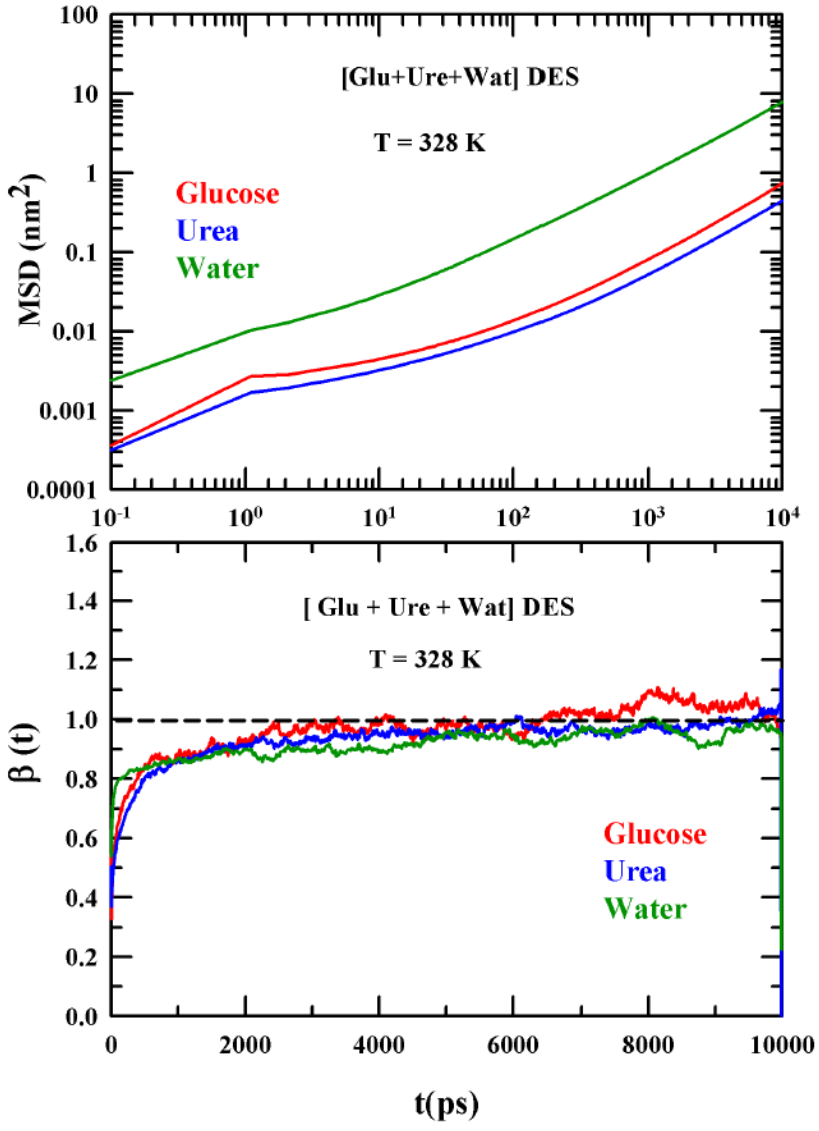

Figure Ad.1.3: MSDs of centre of mass of glucose, water and urea molecules in glucose-urea-water DES at 328 K (upper panel). Time dependence of exponent (β) is shown in the lower panel.

Ad. 1.3.2.2 Non-Gaussian and new Non-Gaussian parameters

Next, we have calculated the non-Gaussian and the new non-Gaussian parameters for water, urea and glucose molecules for a better view of the motional anomaly of the constituent particles.

The non-Gaussian $(\alpha_2(t))$ and new non-Gaussian $(\gamma(t))$ parameters are defined[27,28] as,

$$\alpha_2(t) = \frac{3\langle \delta r^4(t) \rangle}{5\langle \delta r^2(t) \rangle^2} - 1 \qquad \text{(Ad.1.2)}$$

$$\gamma(t) = \frac{1}{3}\langle \delta r^2(t) \rangle \langle \frac{1}{\delta r^2(t)} \rangle - 1 \qquad \text{(Ad.1.3)}$$

where, $\langle \delta r^2(t) \rangle = \langle \frac{1}{N}\sum_{i=1}^{N} |\Delta r_i(t)|^2 \rangle$ and $\langle \frac{1}{\delta r^2(t)} \rangle = \langle \frac{1}{N}\sum_{i=1}^{N} \frac{1}{|\Delta r_i(t)|^2} \rangle$. $\Delta r_i(t)$ is the displacement of i-th particle at time duration t from any arbitrary time origin. $\alpha_2(t)$ tracks those particles whose displacements are longer than the predictions from the Gaussian distribution of particle displacements. $\gamma(t)$, on the other hand, is dominated by the particles executing through the term $\langle \frac{1}{\delta r^2(t)} \rangle$. So, these two dynamic heterogeneity parameters provide information about relaxation rates in addition to collisional and diffusive relaxation timescales that are inherent to otherwise homogeneous systems.

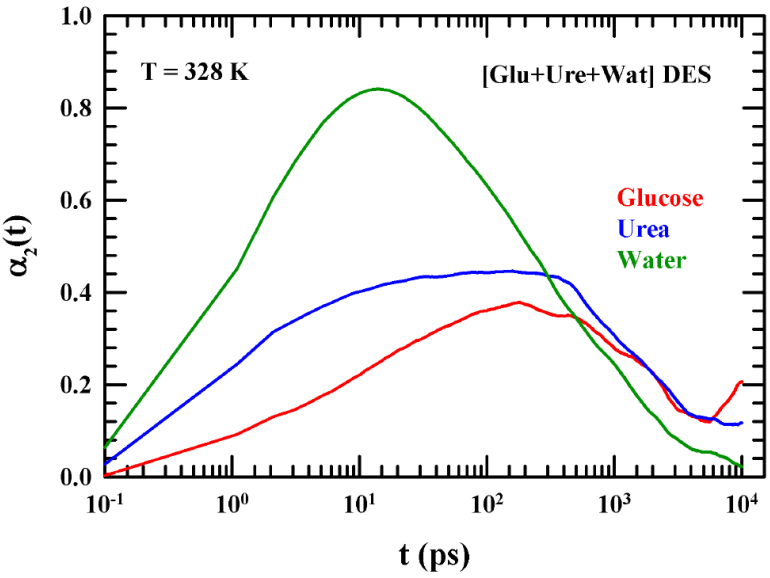

Figure Ad.1.4: Non-Gaussian parameters $(\alpha_2(t))$ for glucose, water and urea COM translational motion in the DES studied.

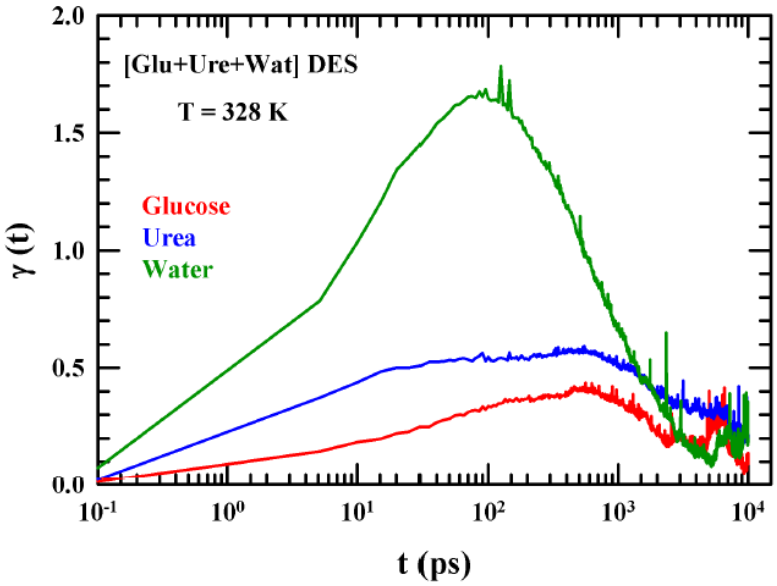

Figure Ad.1.5: New non-Gaussian parameters $(\gamma(t))$ for glucose, water and urea COM translational motion in the DES studied.

Figure Ad.1.4 and Figure Ad.1.5 depicts the non-Gaussian ($\alpha_2(t)$) and the new non-Gaussian parameters ($\gamma(t)$) respectively for constituent species of DES.

We find water becomes more heterogeneous within such crowded environment. Water non-Gaussian timescale is found to be τ_{NG}~$10ps$ and new non-Gaussian timescale τ_{NNG}~$100ps$ within the DES. These timescales are dramatically slower than those for neat ambient water[29,30] where both τ_{NG} and τ_{NNG} were found to be ~1 ps. For urea and glucose molecules τ_{NG}~$500ps$ whereas the τ_{NNG} is found to be in the nanosecond regme (~1 ns).

Ad. 1.3.2.3 Self-Scattering function and Four-point Dynamic Susceptibility

Next, we calculate Four-point dynamic susceptibility, $\chi_4(k,t)$ which measures the local mobility fluctuations and spatial correlations among the particles having similar mobilities at two space points over a certain period of time (t). $\chi_4(k,t)$ can be calculated from self-part of the scattering function, $F_s(k,t)$ at the nearest neighbour $k\sigma = 2\pi$ via the following description[31–33],

$$\chi_4(k,t) = N[\langle F_s(k,t)^2\rangle - \langle F_s(k,t)\rangle^2] \qquad \text{(Ad. 1.4)}$$

where $F_s(k,t) = \frac{1}{N}\sum_{i=1}^{N} cosk.\langle r_i(t) - r_i(0)\rangle$. Since the $\chi_4(k,t)$ tracks the correlation among particles with similar mobilities for a certain duration of time, the maximum time over which the particles remain correlated can be designated as t_4^{max} and it is obtained from the peak position of $\chi_4(k,t)$.

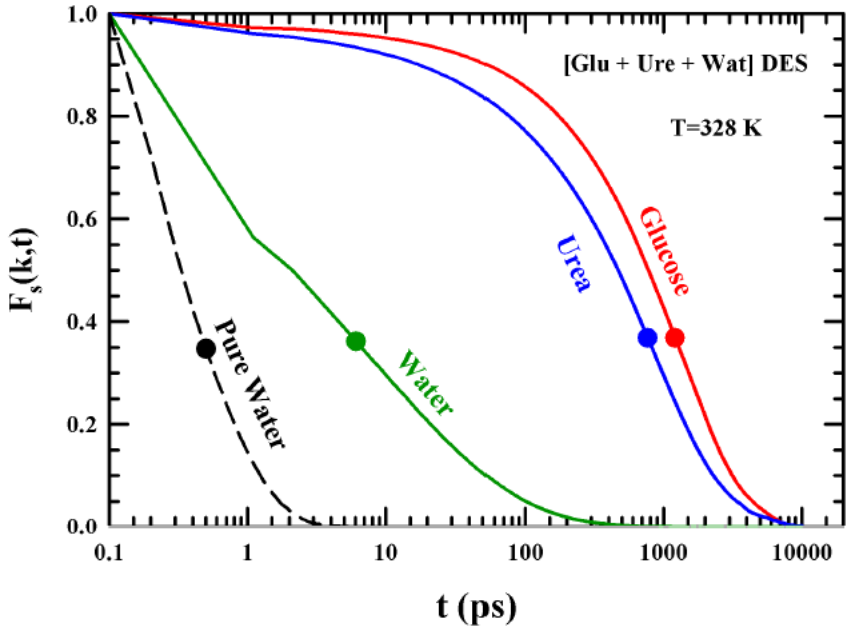

Figure Ad.1.6: Self-scattering function for glucose, water and urea COM in this DES. The same for neat ambient water is also shown for a comparison. Bullet marks indicate the 1/e decay of the self-dynamic structure factor.

Figure Ad.1.6 depicts self-scattering function (self-dynamic structure factor) for water, urea and glucose molecules. $F_s(k,t)$ for pure water is also presented for comparison. The $1/e$ decay times for these decays are identified as the α-relaxation time scale, τ_α and these are indicated by bullet marks. In general, this timescale indicates the time at which particles come out from cage and their displacements become truly random, initiating diffusive motion. For pure bulk water it is around 0.6 ps, whereas water in DES system possess a timescale (τ_α) of 6 ps. For urea τ_α is found to be around 1ns whereas glucose molecules are found to be even slower, $\tau_\alpha \sim$ 2 ns.

Figure Ad.1.7 represents four-point dynamic susceptibility $\chi_4(k,t)$ for all component molecules of DES.

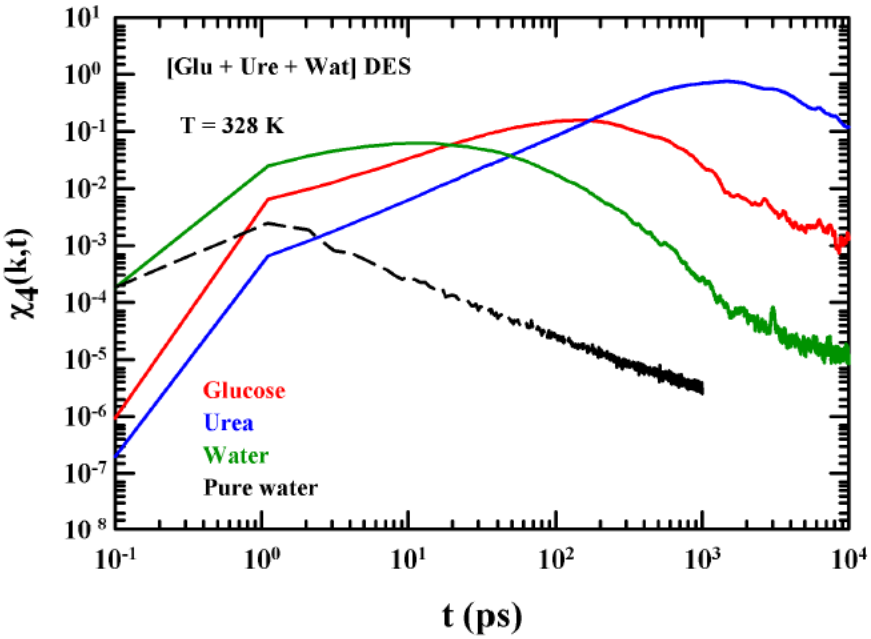

Figure Ad.1.7: Four-point dynamic susceptibility ($\chi_4(k,t)$) for glucose, water and urea COM translational motion in this DES.

This figure clearly depicts the fact that water molecules become more correlated in crowded environment of DES as t_4^{max} increases from 1 ps to 20 ps in DES. Urea and glucose molecules are found to be even more dynamically correlated than water molecules in DES. We find urea molecules are correlated for the longest duration ($t_4^{max} \sim 2ns$) among the three components constituting this DES.

Ad.1.3.2.4 Water hydrogen bond dynamics: Continuous and structural bond relaxations

Structural H-bond relaxation dynamics has been followed via the dynamic correlation function, $C_{HB}(t)$, [34–36]

$$C_{HB}(t) = \frac{<h(0)h(t)>}{<h>} \qquad \text{(Ad. 1.5)}$$

The continuous hydrogen bond lifetime is calculated from the time-correlation function, $S_{HB}(t)$,[34–36]

$$S_{HB}(t) = \frac{<h(0)H(t)>}{<h>} \qquad \text{(Ad. 1.6)}$$

Detailed description of these parameters has been discussed before in chapters 3 and 4.

Water-water continuous hydrogen bond continuous relaxations in this DES and in pure water are presented in Figure Ad.1.8. Multi-exponential fit parameters for the adequate description of the simulated $S_{HB}(t)$ for pure water and water in DES are summarized in table Ad.1.2.

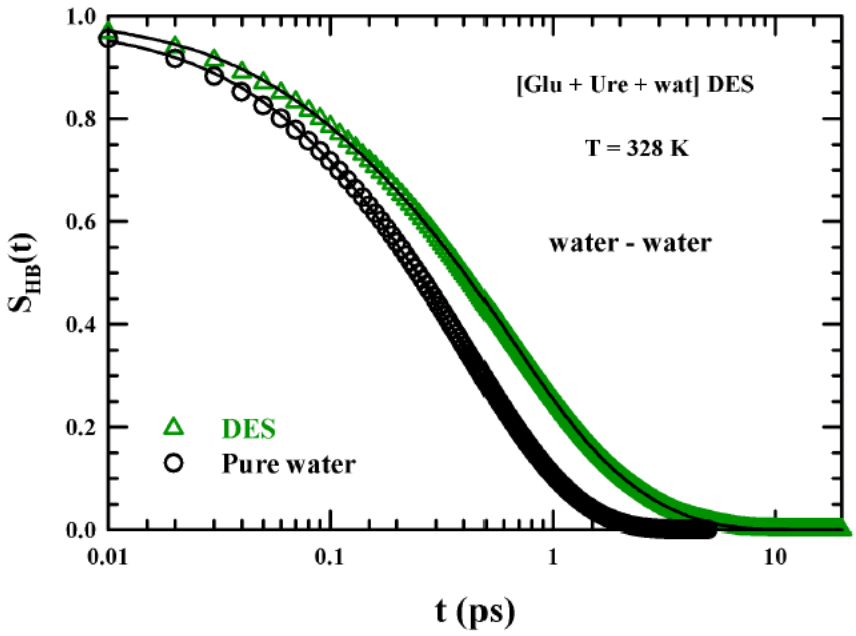

Figure Ad.1.8: Continuous water-water H-bond relaxation ($S_{HB}(t)$) in this DES and neat ambient water.

Table Ad.1.2: Multi-exponential fit parameters for continuous water-water hydrogen bonding relaxation for DES and pure water.

$S_{HB}(t)$	a_1	τ_1 (ps)	a_2	τ_2 (ps)	a_3	τ_3 (ps)	$< \tau_{WW}^{H} >$ (ps)
Neat ambient water (pure water)	0.18	0.09	0.80	0.49	--------	--------	0.42
Water in DES	0.15	0.08	0.53	0.53	0.32	1.63	0.82

The structural hydrogen bond relaxation ($C_{HB}(t)$) for water-water H-bonds are shown and compared with neat ambient water in figure Ad.1.9. The corresponding multi-exponential fit parameters and the average times are summarized in Table Ad.1.3. Structural water-water H-bonds are found to be much slower in this DES than in pure ambient water.

Table Ad.1.3: Multi-exponential fit parameters for Structural water-water H-bond relaxation dynamics for this DES and neat ambient water.

$C_{HB}(t)$	a_1	τ_1 (ps)	a_2	τ_2 (ps)	a_3	τ_3 (ps)	$< \tau_{WW}^{H} >$ (ps)
Neat ambient water (pure)	0.22	0.32	0.64	2.98	0.14	17.92	4.51
Water in DES	0.20	0.78	0.36	27.17	0.44	287.53	137.11

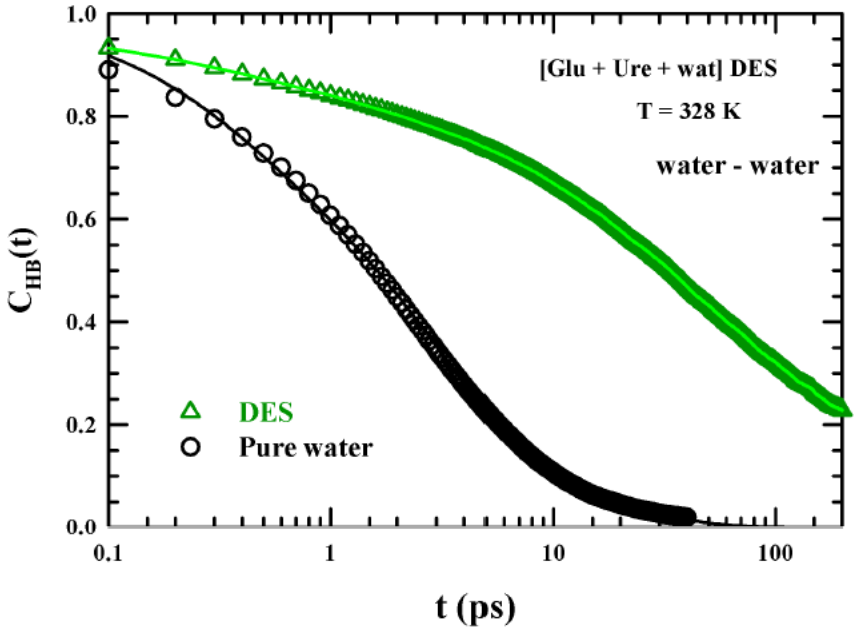

Figure Ad.1.9: Structural water-water hydrogen bonding relaxation $(C_{HB}(t))$ in this DES and neat ambient water.

References

[1] M.J. Earle and K.R. Seddon, Pure Appl. Chem. **72**, 1391 (2000).

[2] A.M. Scurto, K. Hutchenson, and B. Subramaniam, in *Gas-Expand. Liq. Crit. Media* (American Chemical Society, 2009), pp. 3–37.

[3] J.E. Lewis, R. Biswas, A.G. Robinson, and M. Maroncelli, J. Phys. Chem. B **105**, 3306 (2001).

[4] E.L. Smith, A.P. Abbott, and K.S. Ryder, Chem. Rev. **114**, 11060 (2014).

[5] A.P. Abbott, D. Boothby, G. Capper, D.L. Davies, and R.K. Rasheed, J. Am. Chem. Soc. **126**, 9142 (2004).

[6] Q. Zhang, K.D.O. Vigier, S. Royer, and F. Jérôme, Chem. Soc. Rev. **41**, 7108 (2012).

[7] Y. Dai, G.-J. Witkamp, R. Verpoorte, and Y.H. Choi, Anal. Chem. **85**, 6272 (2013).

[8] M. Faggian, S. Sut, B. Perissutti, V. Baldan, I. Grabnar, and S. Dall'Acqua, Mol. Basel Switz. **21**, (2016).

[9] A. Paiva, R. Craveiro, I. Aroso, M. Martins, R.L. Reis, and A.R.C. Duarte, ACS Sustain. Chem. Eng. **2**, 1063 (2014).

[10] Y. Dai, J. van Spronsen, G.-J. Witkamp, R. Verpoorte, and Y.H. Choi, Anal. Chim. Acta **766**, 61 (2013).

[11] E. Tarif, J. Mondal, and R. Biswas, J. Phys. Chem. B **123**, 9378 (2019).

[12] M. Allen and D. Tildesley, *Computer Simulation of Liquids* (1987).

[13] H. Berendsen, J. Grigera, and T. Straatsma, J. Phys. Chem. B **91**, 6269 (1987).

[14] L.S. Dodda, I. Cabeza de Vaca, J. Tirado-Rives, and W.L. Jorgensen, Nucleic Acids Res. **45**, W331 (2017).

[15] W.L. Jorgensen and J. Tirado-Rives, Proc. Natl. Acad. Sci. **102**, 6665 (2005).

[16] L.S. Dodda, J.Z. Vilseck, J. Tirado-Rives, and W.L. Jorgensen, J. Phys. Chem. B **121**, 3864 (2017).

[17] B. Doherty and O. Acevedo, J. Phys. Chem. B **122**, 9982 (2018).

[18] L. Martínez, R. Andrade, E.G. Birgin, and J.M. Martínez, J. Comput. Chem. **30**, 2157 (2009).

[19] D. Hess and E. Lindahl, Univ. Gron. **2010**, 1991 (2001).

[20] H.J. Berendsen, Jv. Postma, W.F. van Gunsteren, A. DiNola, and J.R. Haak, J. Chem. Phys. **81**, 3684 (1984).

[21] D. Van Der Spoel, E. Lindahl, B. Hess, G. Groenhof, A.E. Mark, and H.J. Berendsen, J. Comput. Chem. **26**, 1701 (2005).

[22] E. Lindahl, B. Hess, and D. Van Der Spoel, Mol. Model. Annu. **7**, 306 (2001).

[23] H.J. Berendsen, D. van der Spoel, and R. van Drunen, Comput. Phys. Commun. **91**, 43 (1995).

[24] H. Bekker, H. Berendsen, E. Dijkstra, S. Achterop, R. Van Drunen, D. Van der Spoel, A. Sijbers, H. Keegstra, B. Reitsma, and M. Renardus, in (World Scientific Singapore, 1993), pp. 252–256.

[25] A. Baksi and R. Biswas, J. Phys. Chem. B **124**, 11718 (2020).

[26] J.P. Hansen and I.R. McDonald, *Theory of Simple Liquids* (1986).

[27] C. Dasgupta, A. Indrani, S. Ramaswamy, and M. Phani, Eur. Lett **15**, 307 (1991).

[28] S.C. Glotzer, J. Non-Cryst. Solids **274**, 342 (2000).

[29] S. Indra and R. Biswas, J. Chem. Phys. **142**, 204501 (2015).

[30] A. Baksi, P.Kr. Ghorai, and R. Biswas, J. Phys. Chem. B **124**, 2848 (2020).

[31] C. Toninelli, M. Wyart, L. Berthier, G. Biroli, and J.-P. Bouchaud, Phys. Rev. E **71**, 041505 (2005).

[32] A. Rahman, Phys. Rev. **136**, A405 (1964).

[33] C. Bennemann, C. Donati, J. Baschnagel, and S.C. Glotzer, Nature **399**, 246 (1999).

[34] A. Luzar, Faraday Discuss **103**, 29 (1996).

[35] A. Chandra, Phys. Rev. Lett. **85**, 768 (2000).

[36] S. Balasubramanian, S. Pal, and B. Bagchi, Phys. Rev. Lett. **89**, 115505 (2002).